

Development of Hyperpolarised Xenon 129  
Production and MRI for a Clinical Setting

Robert Irwin

Thesis submitted to the University of Nottingham  
for the degree of Doctor of Philosophy

School of Medicine

July 2020

# Abstract

When the spin polarisation of a nuclear species' is increased far above levels observed at thermal equilibrium, it is said to be hyperpolarised (HP). These HP species can be created using many different methods for the purposes of nuclear magnetic resonance (NMR) and magnetic resonance imaging (MRI). HP Xenon  $^{129}\text{Xe}$  can be created using spin-exchange optical-pumping (SEOP), which uses circularly polarised light to polarise the electronic spins of alkali metal vapour. The polarised alkali metal electrons then transfer their polarisation to noble gas nuclei via Fermi contact two and three-body interactions. Other methods of HP are available such as dynamic nuclear polarization (DNP) and brute force (BF) polarisation.

One of the applications of HP  $^{129}\text{Xe}$  is clinical MRI imaging, which can be used to provide non-invasive structural and functional information about internal organs. This thesis focuses on  $^{129}\text{Xe}$  MRI for in-vivo lung imaging. This offers more sensitive localised information than spirometry, which can only provide an assessment of global lung function and does not provide localised structural or functional information. HP  $^{129}\text{Xe}$  MRI also does not use ionising radiation, unlike computerised tomography (CT) scans. CT and spirometry are the two most popular methods of assessing lung function and structure. This thesis examines the complete pathway of HP  $^{129}\text{Xe}$  production, from its polarisation to use in imaging, and starts by investigating the kinetics of  $^{129}\text{Xe}$  polarisation ( $P_{Xe}$ ) inside the optical cell where SEOP takes place. This analysis was conducted by measuring  $P_{Xe}$  using low-field NMR in tandem with in-situ Raman spectroscopy to measure the in-cell  $N_2$  gas temperature. The ability of  $^4\text{He}$  to reduce thermal gradients across the cell was found to have no significant effect on the  $N_2$  temperature and  $P_{Xe}$  when using an alkali metal with a high surface area within a cylindrical optical cell with a 1-inch diameter. Furthermore, the first comparison of internal gas temperatures during SEOP when using Rb and Cs as the alkali metals of choice was undertaken. It showed that Cs entered alkali metal runaway at an oven temperature of 120 C and above, with  $N_2$  temperatures elevated in excess of 330 C, whereas, under identical conditions, the  $N_2$  temperature in an Rb cell remained stable, slightly above oven temperature. The  $P_{Xe}$  measurements also exhibited the results seen in previous studies, namely that, under optimal conditions, Cs can achieve up to twice the  $P_{Xe}$  that could be produced with Rb.

Additionally, the upgrade, redesign and testing of a stopped-flow hyperpolariser (N-XeUS2) intended for clinical use is described. The N-XeUS2 is based on the XeNA, XeUS and N-XeUS designs, which were previously developed by the consortium (University of Nottingham, Southern Illinois University Carbondale and Vanderbilt University) to scale up HP  $^{129}\text{Xe}$  production for a clinical

setting. The upgrade and redesign were aimed at improving reliability, ease of use and cell lifetimes. This process involved redesigning the gas handling manifold, modifying the automation code and testing a 200 W laser at 794nm (Micro-channel cooled (MCC), QPC, Sylmar California, USA). The XeUS2 design was tested at Wayne State University, where the W-XeUS2 polariser was able to achieve a record  $P_{Xe}$ s in a 2000 Torr cell of  $59 \pm 1.5\%$ ,  $76 \pm 2\%$  and  $98 \pm 1.9\%$  at Xe partial pressures of 1500, 1000 and 500 Torr, respectively. A long-term quality assurance (QA) study was undertaken on the W-XeUS to investigate its cell lifetime. It was found that useable  $P_{Xe}$  levels could still be produced even after  $\approx 700$  optical cell fills, equivalent to one to two years of typical use. This was the first study of its type on this polariser design.

The work from later chapters presented in this thesis took place in the Queens Medical Centre (QMC) in Nottingham and focuses on producing and imaging HP  $^{129}\text{Xe}$  in a clinical setting. The HP  $^{129}\text{Xe}$  produced in the QMC was undertaken using a Polarean 9810 continuous-flow polariser. An investigation looked at the  $P_{Xe}$  that could be produced with a 3% Xe gas mix at different flow rates through the optical cell. At clinically relevant time scales, the Polarean 9810 could produce a 1 L sample in 28 minutes, with a  $P_{Xe}$  of  $\approx 16.7\%$ .

The HP  $^{129}\text{Xe}$  in the QMC was generated for use on both a 0.5 T MROpen Upright Paramed Medical Systems (Upright) scanner and a General Electric (GE) 1.5 T HDx multi-nuclear Flatbed MRI scanner. The Upright scanner's open geometry increases its tolerability, increasing the cohort of patients that can be imaged in any orientation. Using the Upright scanner and a small surface coil manufactured by Clinical MR Solutions (CMRS), the first HP  $^{129}\text{Xe}$  imaging study was performed. It showed that the coil and scanner together could resolve millimetre-level detail when imaging a phantom filled with HP  $^{129}\text{Xe}$ . The setup was also able to perform dissolved-phase NMR and could clearly resolve the NMR peaks of  $^{129}\text{Xe}$  dissolved in water, olive oil, tert-butanol and ethanol. These NMR and MRI results indicated that, once the coil is approved for human use, it could be used to perform initial in-vivo  $^{129}\text{Xe}$  MRI lung imaging on the Upright scanner.

A new flexible chest coil from CMRS (CMRS coil) designed for use with the GE 1.5 T flatbed MRI scanner was procured and tested to determine whether it could act as a suitable replacement for the previously rigid chest coil made by Rapid biomedical. In quadrature transmit array receive (QTAR) mode, a drop in signal from anterior to posterior was observed, making it unfit human for use. The coil was then switched to Quadrature Tx array Rx (QUAD T/R) mode, which gave more consistent results under initial testing. The flexible coil design allows for larger volunteers to be imaged increasing the limited cohort of patients that could tolerate the previous rigid coil.

# Acknowledgements

No PhD project is performed in a vacuum. Behind the words on the page and the numbers on the graph is the support of many people both inside and outside the lab.

I would, first of all, like to thank the James Tudor Foundation; without their support and funding, I would not have had the opportunity to carry out this project.

Next, I would like to thank my supervisors, Mike Barlow, Ian Hall and John Owers-Bradley, for their expertise, encouragement and guidance throughout my studies. Working with the HP  $^{129}\text{Xe}$  team has been nothing but a positive experience, and I cannot think of a more knowledgeable and lovely group of people to work with. My thanks go to Brett Haywood for operating the MRI scanner and the clinicians S. Safavi and J. Brooke, who ensured the safety of our volunteers. Additional thanks are owed to the late E. Hill, who was the Qualified Person who provided oversight for HP  $^{129}\text{Xe}$  production, and B. Sanders, who subsequently undertook this role. Gratitude must especially be paid to the volunteers that gave their precious time to make these investigations possible.

I would like to thank Jonathan Birchall for training me in not only how to use all of the equipment, in particular the complicated Polarean 9810 polariser, but also in how to use it safely. He offered his expertise, time and good humour not only in Nottingham but also at Wayne State University in Detroit. The productive collaboration in Detroit could not have occurred without Eduard Chekmenev, who acted as my supervisor during the visit and made me feel instantly part of the team.

Thanks must be given to my Mum, Dad and twin Ben, who provided unwavering love throughout my studies. An extra special thank you must be given to my girlfriend Maisie, whose love and support have been bottomless, especially during the write-up period, which occurred while we were isolating together during a global pandemic. A big thank you must also be given my friends for keeping me sane outside the lab, especially those I have had the pleasure of climbing with while in Nottingham.

Lastly, a special thank you must be given to my lab partner James Harkin, who was an absolute joy to work with and whose friendship is a distinct privilege.

# Contents

<b>1</b>	<b>Introduction</b>	<b>8</b>
1.1	Overview . . . . .	8
<b>2</b>	<b>NMR/MRI and hyperpolarisation review and techniques</b>	<b>11</b>
2.1	Nuclear magnetic resonance to magnetic resonance imaging . . . . .	11
2.1.1	Introduction . . . . .	11
2.1.2	Nuclear magnetic resonance . . . . .	11
2.1.3	NMR spectroscopy . . . . .	15
2.2	Magnetic resonance imaging . . . . .	16
2.2.1	MRI introduction . . . . .	16
2.2.2	MRI hardware . . . . .	16
2.2.3	MRI sequence . . . . .	17
2.3	Thermal polarisation . . . . .	25
2.4	Hyperpolarisation . . . . .	27
2.4.1	Introduction . . . . .	27
2.4.2	Brute force hyperpolarisation . . . . .	27
2.4.3	Dynamic nuclear polarisation . . . . .	27
2.4.4	Parahydrogen-induced polarisation . . . . .	29
2.4.5	Signal amplitude by reversible exchange . . . . .	30
2.4.6	Metastability-exchange optical pumping . . . . .	31
2.4.7	Spin exchange optical pumping . . . . .	32
2.4.8	Continuous-flow spin-exchange optical-pumping . . . . .	35
2.4.9	Buffer gases . . . . .	37
2.5	Hyperpolarised gas MRI . . . . .	37
2.5.1	Introduction . . . . .	37
2.5.2	Alternatives to MRI . . . . .	38
2.5.3	Conventional MRI imaging . . . . .	38
2.5.4	Hyperpolarised gas MRI imaging . . . . .	38
<b>3</b>	<b>Measuring in-cell temperature with Raman spectroscopy to understand optimal conditions of SEOP</b>	<b>43</b>
3.1	Introduction . . . . .	43
3.2	Theory . . . . .	44
3.2.1	Raman spectroscopy . . . . .	44
3.3	Materials and methods . . . . .	50
3.3.1	SEOP materials . . . . .	50
3.3.2	NMR methods . . . . .	56
3.3.3	Raman methods . . . . .	61

3.3.4	Cell cleaning and loading . . . . .	63
3.4	Raman SEOP experiments . . . . .	70
3.4.1	Introduction . . . . .	70
3.4.2	Data consistency . . . . .	71
3.4.3	General experimental protocol . . . . .	77
3.4.4	The effect of $^4\text{He}$ on managing $N_2$ temperature in a spread cell . . . . .	78
3.4.5	Caesium SEOP . . . . .	84
3.4.6	Comparison between Cs and Rb SEOP in a spread cell . . . . .	85
3.5	Conclusion . . . . .	94
<b>4</b>	<b>Upgrade and quality assurance of a N-XeUS2 stopped-flow xenon-rich SEOP polariser</b> . . . . .	<b>96</b>
4.1	Introduction . . . . .	96
4.2	Stopped-flow vs continuous-flow polarisers . . . . .	96
4.2.1	Operation . . . . .	96
4.2.2	Gas mixes . . . . .	97
4.3	XeNA . . . . .	99
4.4	XeUS . . . . .	101
4.4.1	Gas handling manifold . . . . .	101
4.4.2	Oven and TEC thermal management system . . . . .	101
4.4.3	Automation system . . . . .	103
4.4.4	XeUS performance . . . . .	104
4.5	N-XeUS . . . . .	104
4.5.1	Gas handling manifold . . . . .	104
4.5.2	$B_0$ field system . . . . .	105
4.6	N-XeUS2 . . . . .	105
4.6.1	Chassis . . . . .	106
4.6.2	Gas management system . . . . .	107
4.6.3	$B_0$ field . . . . .	110
4.6.4	Oven and TEC thermal management system . . . . .	110
4.6.5	Automation system . . . . .	111
4.6.6	Laser system . . . . .	114
4.6.7	NMR system . . . . .	118
4.7	N-XeUS2 performance . . . . .	123
4.7.1	Introduction . . . . .	123
4.7.2	Polariser performance for different binary gas mixes . . . . .	123
4.8	Long term quality assurance . . . . .	128
4.8.1	Introduction . . . . .	128
4.8.2	Methods . . . . .	129
4.8.3	Results . . . . .	131
4.8.4	Discussion . . . . .	136
4.9	New oven design . . . . .	136
4.9.1	Motivation . . . . .	136
4.9.2	Design and fabrication . . . . .	138
4.9.3	Installation and testing . . . . .	140
4.10	Future work . . . . .	141
4.10.1	Introduction . . . . .	141
4.10.2	New laser design . . . . .	141
4.10.3	Clinical work . . . . .	142

<b>5</b>	<b>Hyperpolarised <math>^{129}\text{Xe}</math> production for in-vivo clinical imaging using a continuous-flow polariser</b>	<b>143</b>
5.1	Polarean 9810 . . . . .	143
5.1.1	Gas management system . . . . .	143
5.1.2	SEOP cell and oven . . . . .	146
5.1.3	Hyperpolarised $^{129}\text{Xe}$ cryo-collection and storage . . . . .	148
5.1.4	$B_0$ Field . . . . .	150
5.1.5	Laser system . . . . .	150
5.1.6	Polarean 2881 polarisation measurement station . . . . .	152
5.1.7	Optimal operating conditions . . . . .	155
5.2	Conclusion . . . . .	157
<b>6</b>	<b>Clinical HP <math>^{129}\text{Xe}</math> MRI and NMR - lung, brain and kidney disease states</b>	<b>158</b>
6.1	Introduction . . . . .	158
6.2	Lung diseases . . . . .	158
6.2.1	HP $^3\text{He}$ vs HP $^{129}\text{Xe}$ MRI Imaging . . . . .	159
6.2.2	Cystic fibrosis . . . . .	159
6.2.3	Chronic obstructive pulmonary disease . . . . .	160
6.2.4	Asthma . . . . .	161
6.2.5	Idiopathic pulmonary fibrosis . . . . .	161
6.3	Brain diseases . . . . .	162
6.3.1	Stroke . . . . .	162
6.3.2	Alzheimer's disease . . . . .	163
6.4	Kidney disease . . . . .	164
6.5	Conclusion . . . . .	164
<b>7</b>	<b>HP <math>^{129}\text{Xe}</math> imaging results with a 0.5 T upright MRI scanner</b>	<b>166</b>
7.1	Introduction . . . . .	166
7.2	Imaging hardware . . . . .	166
7.2.1	0.5 T Paramed upright MRI scanner . . . . .	166
7.2.2	0.5 T Paramed upright receive coil . . . . .	168
7.3	Upright $^{129}\text{Xe}$ NMR spectroscopy . . . . .	170
7.3.1	$^{129}\text{Xe}$ dissolved phase NMR spectroscopy . . . . .	171
7.4	Upright $^{129}\text{Xe}$ MRI imaging . . . . .	173
7.4.1	Introduction . . . . .	173
7.4.2	Methods . . . . .	173
7.4.3	Sequence testing . . . . .	174
7.4.4	Flip angle optimisation . . . . .	175
7.4.5	Fine structure capabilities . . . . .	180
7.5	Discussion . . . . .	182
7.6	Future work - Pulseteq chest coil . . . . .	183
7.7	Conclusion . . . . .	184
<b>8</b>	<b>HP <math>^{129}\text{Xe}</math> imaging results with a 1.5 T flatbed MRI scanner</b>	<b>185</b>
8.1	Introduction . . . . .	185
8.2	Imaging hardware . . . . .	185
8.2.1	GE 1.5 T receive coils . . . . .	186
8.3	Imaging with the Clinical MR Solutions coil in QTAR mode . . . . .	195
8.3.1	Introduction . . . . .	195

8.3.2	Methods . . . . .	195
8.4	Imaging with the Clinical MR Solutions coil in QUAD T/R mode	207
8.4.1	Introduction . . . . .	207
8.4.2	Methods . . . . .	207
8.4.3	Discussion . . . . .	212
8.5	Conclusion . . . . .	213
<b>9</b>	<b>Conclusion</b>	<b>215</b>
9.1	Improving stopped-flow $^{129}\text{Xe}$ SEOP with Raman spectroscopy .	215
9.2	Upgrade and quality assurance of a N-XeUS2 stopped-flow xenon-rich SEOP polariser . . . . .	216
9.3	Production of hyperpolarised $^{129}\text{Xe}$ for in-vivo imaging using a continuous-flow polariser . . . . .	217
9.4	Hyperpolarised $^{129}\text{Xe}$ work on a Paramed 0.5 T upright scanner	217
9.5	Hyperpolarised $^{129}\text{Xe}$ MRI imaging on a General Electric 1.5 T flatbed scanner . . . . .	218
9.6	Overview . . . . .	218
9.7	Priorities for future work . . . . .	219
<b>Appendix A Publications</b>		<b>241</b>
<b>Appendix B N-XeUS2 automation system and gas handling manifold.</b>		<b>242</b>
<b>Appendix C Protocol for HP <math>^{129}\text{Xe}</math> clinical drug production</b>		<b>247</b>



# Chapter 1

## Introduction

### 1.1 Overview

This thesis focus is to contribute to the advancement of HP  $^{129}\text{Xe}$  MRI, focusing particularly on the imaging of the human lungs. The World Health Organisation (WHO) reports that respiratory diseases are the leading cause of death and disability around the world, with four million people dying prematurely each year as a result [1]. Chronic Obstructive Pulmonary Disease (COPD) is expected to rise to the fifth-largest burden to global health services this year [2]. Asthma, another respiratory disease, affects approximately 300 million people around the world, and idiopathic pulmonary fibrosis (IPF) was estimated to affect  $\approx 3$  million people worldwide in 2017 [3]. Patients who are diagnosed earlier are able to start treatment earlier, which can result in improved patient outcomes. This forms the motivation behind developing HP  $^{129}\text{Xe}$  MRI as a diagnostic and treatment monitoring tool.

Lung function is typically assessed by spirometry and structural changes assessed with high resolution computed tomography (CT). Spirometry only offers basic global information about lung function [4]. Its disadvantage is that respiratory diseases typically affect the lungs heterogeneously, with healthy and diseased tissue occupying different areas of the lung. This means a disease may not be affecting the overall lung function enough to be detected by spirometry, resulting in a delayed diagnosis. It is also not possible for spirometry to guide localised treatments such as tissue resection surgery [5]. CT scans use ionising radiation to generate high spatial resolution structural images of the lungs [6] and can also examine their perfusion [7]. Due to the increased risk of cancer associated with ionising radiation [8], the dose a patient receives should be limited and CT should be performed only when necessary [9]. This can prevent regular monitoring, which, in the case of chronic respiratory conditions, reduces the quality of disease management and the ability to assess treatment efficacy.

HP  $^{129}\text{Xe}$  MRI overcomes the issues inherent with CT by providing a non-ionising technique for investigating the lung's structure and function.  $^{129}\text{Xe}$  is an isotope of Xenon (Xe) with a 26% natural abundance and demonstrates many properties which make it the gas of choice for pulmonary MRI. Firstly, it is a noble gas and is therefore non-reactive and non-toxic [10]. This means it can be safely inhaled in a single breath-hold by patients, with no risk of

long-term adverse health effects. As it has a spin of  $\frac{1}{2}$ , it is an NMR active nucleus and therefore produces a signal that can be detected by an MRI scanner.  $^3\text{He}$  can also be used for HP MRI lung imaging but  $^{129}\text{Xe}$ 's affordability makes it economical for a clinical setting where consumption scales with patient throughput.

$^{129}\text{Xe}$ 's unique properties allow it to provide structural and functional information. Unlike  $^3\text{He}$ ,  $^{129}\text{Xe}$  can diffuse from the airways of the lungs and into the bloodstream using the same diffusion pathway as oxygen.  $^{129}\text{Xe}$  also possesses a very large chemical shift sensitivity, meaning its NMR signal shifts in frequency depending on its surroundings [11]. This means it is possible to ascertain the exact location of the  $^{129}\text{Xe}$  and determine locations of poor gas exchange in the lungs [12]. Through the provision of both structural and functional information, clinicians obtain more data for diagnostics, treatment monitoring and research for a wide range of pulmonary diseases.

Another thing which sets HP  $^{129}\text{Xe}$  MRI apart from  $^3\text{He}$  is that it is not just limited to the lungs as  $^{129}\text{Xe}$  can diffuse into other organs after being transported via the bloodstream. Progress has also been made into imaging perfusion within the human brain which may be used to detect stroke or cancer [13], in addition to preliminary work imaging the kidneys [14]. The utility of  $^{129}\text{Xe}$  MRI could increase further as scientists and clinicians find new and innovative ways of exploiting its properties.

$^{129}\text{Xe}$  is polarised using a technique known as SEOP. This is achieved by optically pumping alkali metal electron spins via angular momentum transfer from circularly polarised laser photons. The alkali metal electron spins then perform spin exchange with the  $^{129}\text{Xe}$  nuclei [15, 16] known as Fermi-contact via two and three-body collisions, yielding  $P_{\text{Xe}}$  levels  $10^5$  greater than the thermal polarisation. This is more than sufficient to compensate for its reduced signal density in the gas phase, which is exacerbated by its low natural abundance [17] and gyromagnetic ratio [18]. Hyperpolarisation makes  $^{129}\text{Xe}$  it suitable for a wide range of functions, including pulmonary imaging. HP  $^{129}\text{Xe}$  lung imaging has come a long way since 1994, where the first reported images were of an excised mouse lung by M. Albert et al. [19]. HP  $^{129}\text{Xe}$  is now being used in a wide range of in-vivo clinical studies across the world investigating different disease states.

As the field has developed, so too has clinical polariser technology, polarisers fall into two major design categories continuous- and stopped-flow. Continuous-flow polarisers flow the Xe gas mix through the cell continuously during SEOP. Whereas stopped-flow designs load the optical cell with the gas mix and seal it inside the cell during SEOP and releasing the gas mix to its target after SEOP is complete. The first  $^{129}\text{Xe}$  clinical scale polariser was a continuous-flow design developed by B. Driehuys et al. in the 1990s. This acted as a proof-of-concept, showing that  $^{129}\text{Xe}$  could be polarised to useable levels and in sufficient quantities, producing 1 L of HP  $^{129}\text{Xe}$  polarised to 5% in 1 hour[20]. Several teams have since produced various continuous-flow designs, making incremental but significant increases to the  $P_{\text{Xe}}$  produced [21],[22],[23]. Polarisers operating in the stopped-flow regime have also been developed for clinical imaging. Polarisers such as the XeUS and XeNA have taken advantage of high-powered lasers to achieve high levels of  $^{129}\text{Xe}$  bulk magnetisation using Xe rich gas mixes [24, 25].

In parallel with the production hardware, the hardware involved with imaging the HP  $^{129}\text{Xe}$  has also developed. The rigid chest coils previously used are

being replaced with more sensitive, flexible designs which have increased patient tolerability. As for the MRI scanner hardware, the prospect of using an upright scanner provided by Paramed is of particular interest in this thesis. The Upright scanner allows patients to be scanned in an upright orientation, meaning patients who previously could not be scanned in a conventional flatbed scanner can undergo  $^{129}\text{Xe}$  MRI imaging. These include patients in advanced stages of many pulmonary conditions who cannot breathe lying down and those with claustrophobia.

This thesis aims to investigate and improve the production and imaging of HP  $^{129}\text{Xe}$ . The first experimental section (Chapter 3), investigates HP  $^{129}\text{Xe}$  production using Rb and Cs to provide higher  $P_{\text{Xe}}$  for clinical imaging. These investigations used in-situ Raman spectroscopy, NMR spectroscopy and atomic absorption spectroscopy (AAS) to observe the kinetics of SEOP. The existing experimental protocol was improved, and  $^{129}\text{Xe}$  SEOP was investigated under a variety of experimental conditions including choice of alkali metal, gas mix, oven temperature and pump laser. The second section (Chapter 4) involves the redesign, rebuild and QA testing of a stopped-flow clinical polariser based on the XeUS design. The overall aim is to deliver a semi-automated stopped-flow polariser which can produce  $^{129}\text{Xe}$  with a high bulk magnetisation to replace the continuous-flow polariser in the QMC. This links to the third section, which examines the production and imaging of HP  $^{129}\text{Xe}$  in the QMC (Chapters 5-8), starting with the optimisation of the current Polarean 9810 clinical polariser to best exploit a richer 3% Xe gas mix. HP  $^{129}\text{Xe}$  was produced for initial Xe imaging on the Upright scanner, and a study using human volunteers to test a new flexible chest coil was performed on the GE 1.5 T flatbed scanner.

## Chapter 2

# NMR/MRI and hyperpolarisation review and techniques

### 2.1 Nuclear magnetic resonance to magnetic resonance imaging

#### 2.1.1 Introduction

HP  $^{129}\text{Xe}$  images are acquired using MRI. This chapter starts with the basic principles of NMR, moving through to generating MRI images.

#### 2.1.2 Nuclear magnetic resonance

##### Nuclear spin and polarisation

Nucleons (protons, neutrons and electrons) have an intrinsic quantum mechanical property called spin ( $I$ ) [26]. The nuclear spins of individual protons and neutrons have a spin of a half: either spin-up  $I = \frac{1}{2}$  or spin-down  $I = -\frac{1}{2}$ . An atomic nucleus is composed of neutrons and protons and therefore has a net spin that is dependent on the number of constituent nucleons. Neutrons and protons are fermions as they have a half-integer  $I$ , so their wavefunction must be antisymmetric under particle exchange according to the Pauli exclusion principle [27]. This means protons and neutrons fill up each energy level within a nucleus in proton-proton and neutron-neutron pairs before filling the next energy level. Within these pairs, one proton/neutron will be spin up and the other will be spin down, resulting in a net  $I$  of 0 for each pair. The net spin of a nucleus is therefore given by the number of unpaired nucleons within it. A nucleus with an even number of neutrons and protons will have a net spin of 0. If the sum of the protons and neutrons is odd, the nucleus will have a half-integer spin. Finally, a nucleus will have a net integer spin if both the number of neutrons and protons are odd [26].

The nucleus will have a magnetic moment ( $m$ ) associated with its  $I$  given by

Equation (2.1).

$$m = \gamma I \quad (2.1)$$

$m$  is a vector which is used to measure how prone the nucleus is to interacting with an external magnetic field.  $I$  and  $m$  are directly proportional and lie in the same direction and are related by the gyromagnetic ratio  $\gamma$ , which is unique to each atomic species. If the  $\gamma$  is positive, the vectors of  $m$  and  $I$  are parallel, and if  $\gamma$  is negative, they are antiparallel. If  $I$  is zero then  $m$  will also be zero and will not interact with an external magnetic field (NMR inactive). If  $I$  is non-zero so is  $m$  and the nucleus is NMR active. The size of the  $m$  of nuclei with equal  $I$  is proportional to the size of  $\gamma$ . Higher  $\gamma$  gives rise to higher NMR sensitivity.

Due to the Heisenberg uncertainty principle, it is not possible to know exactly what direction a nucleus's spin is pointing at a specific point in time. The spin state of a nucleus is an eigenstate of the angular momentum along a defined direction. An eigenstate is a measurable quantum property [28]. The number of nuclear spin states ( $N$ ) is given by Equation (2.2) and an example energy level-splitting diagram is shown in Figure 2.1.

$$N = 2I + 1 \quad (2.2)$$

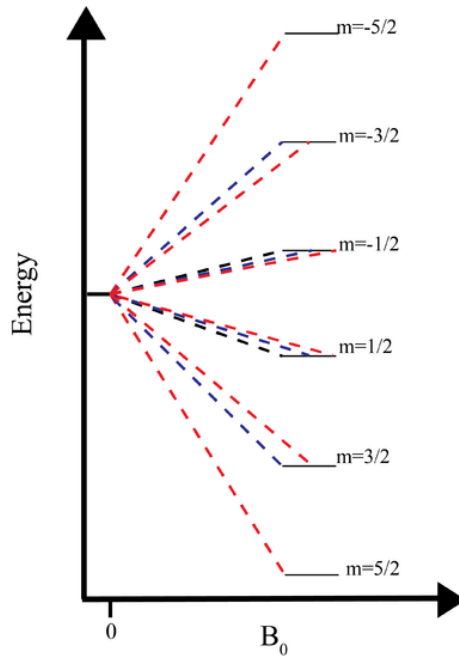


Figure 2.1: This figure shows the energy-level splitting for nuclei with  $I = \frac{1}{2}$  (black dashed lines),  $I = \frac{3}{2}$  (blue dashed lines) and  $I = \frac{5}{2}$  (red dashed lines). The energy-level splitting is dependent on the strength of the magnetic field [29].

Nuclei with the smallest non-zero spin ( $I = \frac{1}{2}$ ), such as  $^1H$  or  $^{129}Xe$ , have two possible spin states. This is when the magnetic moment either aligns parallel

to the magnetic field, also known as “spin-up” ( $I = \frac{1}{2}$ ), or anti-parallel, also known as “spin-down” ( $I = -\frac{1}{2}$ ). In a zero magnetic field, these two spin states are degenerate, meaning it is not possible to measure the difference between them. When subject to an external magnetic field ( $B_0$ ), the energy of the two spin states is separated via Zeeman splitting and can be measured. This energy difference between the two spin states scales with  $\gamma$  and  $B_0$  as shown in Equation (2.3) where  $\hbar$  is the Plank’s constant.

$$\Delta E = \gamma B_0 \hbar \tag{2.3}$$

The  $\Delta E$  is equivalent to the energy change given in Equation (2.4) of an atomic system when a photon is emitted due to relaxation.

$$\Delta E = \hbar \omega \tag{2.4}$$

$\omega$  is the frequency of the photon. From the above two equations, the frequency of precession of a nucleus about the  $B_0$  field can be found as shown in Equation (2.5).

$$\omega_L = \gamma B_0 \tag{2.5}$$

$$\tau = m B_0 \tag{2.6}$$

$\omega_L$  is the nuclei’s Larmor frequency, otherwise known as its NMR resonance frequency. This precession is due to the torque ( $\tau$ ) the  $B_0$  field exerts on the nuclei’s magnetic moment according to Equation (2.6). At this frequency the energy transferred to the nuclei from an NMR coil’s RF pulse is most efficient. This is because the alternating  $B_1$  field can generate an alternating current through an NMR coil perpendicular to the  $B_0$  field. It must oscillate at or near  $\omega_L$  to efficiently transfer energy to the nuclei and tip the magnetisation of the system into the transverse plane. If the  $B_1$ ’s frequency does not equal the  $\omega_L$ , it will shift in and out of phase with the nuclei spins and the energy transferred to the nuclei will be vastly reduced. When the frequency of  $B_1$  is close to  $\omega_L$ , resonance occurs, and energy transfer is more efficient, with maximal transfer occurring when the frequencies are equal.

The degree to which the nuclei are tipped into the transverse plane is dependent on the strength and length of the pulse. Stronger, longer pulses transfer more energy to the nuclei, resulting in a larger tipping angle.

The colinear magnetic moments of nuclei also tip into the transverse plane with the spins. The precession of these magnetic moments causes the generation of an alternating magnetic field in the transverse plane, which, according to Faraday’s law, generates a current in the coil. This makes it possible to detect the NMR signal from excited nuclei.

The NMR signal will gradually die away as the transverse magnetisation reduces due to relaxation. This is a process known as Free Induction Decay (FID), an example of which is shown in Figure 2.2.

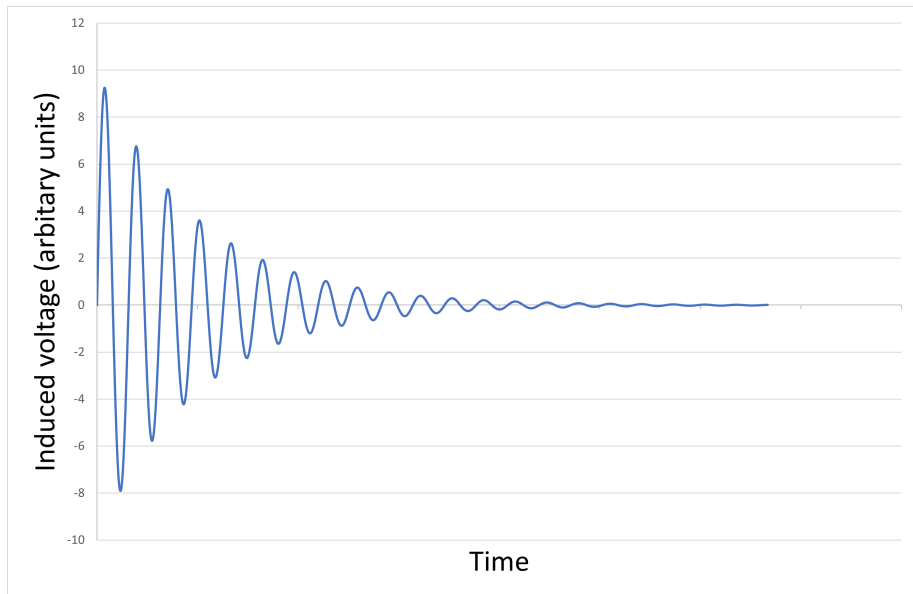


Figure 2.2: Example FID signal

### Spin-lattice relaxation

When energy is transferred to a nucleus and its magnetisation is tipped into the transverse plane or even further to be anti-parallel to  $B_0$ , the nucleus is in a higher unstable energy state. Without further input of energy into the system, the nuclei will relax and the longitudinal magnetisation  $M_z$ , parallel to  $B_0$ , will recover back to its original size.  $M_z$  increases with reducing energy as the nuclei statistically prefer the lower energy spin-up orientation which aligns with  $B_0$ . The overall net magnetisation  $M_0$  will eventually point in the direction of  $B_0$ , even though nuclei are mostly aligned in random directions due to the Boltzmann distribution of their energies [30]. The recovery of  $M_z$  to  $M_0$  is known as longitudinal or “spin-lattice” relaxation. This relaxation is the loss of energy from the spins to the surrounding lattice, i.e. other molecules and atoms. Energy transfer occurs through collisions, spin-rotation and electromagnetic interactions. The energy is finally lost from the system as heat. The time constant ( $T_1$ ) of longitudinal relaxation is the time taken for  $M_z$  to reach  $\frac{1}{e}$  of  $M_0$  from 0. After five  $T_1$  intervals,  $M_z$  has almost fully recovered to  $M_0$ .

The recovery of  $M_0$  is given by Equation (2.7).

$$M_z = M_0(1 - e^{-\frac{t}{T_1}}) \quad (2.7)$$

### Spin-spin relaxation

The decay of signal seen in the FID is the reduction in transverse magnetisation over time and it is known as transverse or “spin-spin” relaxation. If a 90-degree RF pulse is given to a nuclear species inside  $B_0$ , the original Boltzmann distribution is rotated 90 degrees, with the net magnetisation now pointing into the xy

plane ( $M_{xy}$ ). Implicitly longitudinal relaxation causes a reduction in transverse magnetisation as spins relax out of the transverse plane [31]. The net transverse magnetisation can also reduce without longitudinal relaxation due to dephasing of spins. This can happen due to nuclei being located in an environment where the local magnetic field is slightly different to  $B_0$  as a result of static field disturbances from other molecule/atoms. Therefore, according to Equation (2.5), nuclei will precess at slightly different frequencies and dephase with each other, resulting in the reduction of net  $M_{xy}$ . Transverse relaxation also occurs due to dipolar interactions between spins, where spins will swap longitudinal magnetisation, with one another which contributes to a loss of coherence between spins further, reducing  $M_{xy}$  [32].

The time constant for transverse relaxation ( $T_2$ ) is the time taken for  $M_{xy}$  to fall to  $\frac{1}{e}$  of its value after the RF pulse. The equations that describe the progression of  $M_x$ ,  $M_y$  and  $M_{xy}$  are given below in Equations (2.8), (2.9) and (2.10).

$$M_x = M_{eq} \sin(\omega_0 t) e^{-\frac{t}{T_2}} \quad (2.8)$$

$$M_y = -M_{eq} \cos(\omega_0 t) e^{-\frac{t}{T_2}} \quad (2.9)$$

$$M_{xy} = -M_{eq} e^{-\frac{t}{T_2}} \quad (2.10)$$

In a system with a perfectly homogeneous  $B_0$  field, transverse relaxation is dictated purely by the size of  $T_2$ . In the case where the magnetic field has some form of heterogeneity, there will be macroscopic differences in  $B_0$  in the field, so the  $\omega_L$  will differ slightly as a result. This difference will contribute to the dephasing of transverse spins and therefore accelerate the transverse relaxation. A new time constant,  $T_2^*$ , takes into account these inhomogeneities and is given by Equation (2.11), replacing  $T_2$ .

$$\frac{1}{T_2^*} = \frac{1}{T_2} + \frac{1}{T_{inhomogenaties}} \quad (2.11)$$

### 2.1.3 NMR spectroscopy

#### Signal processing

Turning the signal received by the detector coil into a usable NMR spectrum requires signal processing. From the FID signal, it is possible to find the Larmor frequency of the nuclei. High frequencies resulting from high  $B_0$  are usually electronically mixed down by a carrier frequency to the order of kHz so they can then be digitised by an analogue digital converter (ADC) and then Fourier transformed by the spectrometer. A homogeneous sample will have a single frequency. The signal, when Fourier transformed, results in a frequency spectrum with a Lorentzian peak about the Larmor frequency. If the sample is heterogeneous, the NMR signal detected will be an interference pattern of all the different nuclei. The resultant spectra are complex with multiple peaks at different frequencies, representing different elements and/or nuclei with differing chemical shifts. The frequency of the oscillations of an FID depends on the Larmor frequencies of the nuclei and therefore on the strength of  $B_0$ . In this thesis, the frequency can range from kHz to MHz for the low-field Raman work and MRI work at higher fields (0.5 T and 1.5 T respectively). The initial



magnitude of the NMR signal is dependent on the bulk magnetisation of the sample being excited, the flip angle of the exciting pulse and the sensitivity of the coil. Using NMR spectroscopy, it is possible to perform elemental analysis on materials with an unknown make-up.

## 2.2 Magnetic resonance imaging

### 2.2.1 MRI introduction

While MRI utilises the same basic physics as NMR, it uses gradient fields in addition to  $B_0$  to change the local magnetic field strength at different points and times in the MRI imaging sequence. This spatially encodes the nuclei of interest so that their signals can be used to create a final image or series of images of the ROI.

The first examples of imaging using nuclear magnetic resonance were performed by P. C. Lauterbur. Using a technique called “zeugmatography”, he was able to resolve a simple 2D proton image of water within two glass tubes, built up from 4 1D projections in the XY plane [33] he was later able to produce the first image of a tumour in a live mouse [34]. Sir Peter Mansfield proposed a method of exploiting spin echoes in time-dependent magnetic field gradients. He was able to observe and differentiate between signals from the different spins of the nuclei within a plane or multiple planes within the specimen [35]. The first NMR image of a human was of the cross-section of a finger created by Peter Mansfield at the University of Nottingham. This image was taken with A. Maudsley placing his fingers into the sample space of a conventional iron electromagnet. With increased sample space size inside the main magnet, larger parts of the human body could be imaged. The first full-body scan was performed by Damadian et al. [36], taking 5 hours to acquire a low-quality image. The field of MRI has moved on considerably since the early days, and this chapter will layout current MRI hardware and imaging sequences.

### 2.2.2 MRI hardware

#### Main magnet

The main magnet in an MRI scanner polarises the sample within it, or in the case of HP noble gases, maintains the polarisation of the gas. It also defines the quantisation axis. A superconducting magnet is the most common type of magnet used for clinical scanners [37]. For superconducting magnets, coils used to create the magnetic field are immersed in a coolant of liquid helium which brings the temperature down to 4.2 K. This eliminates the resistance in the wires and enables fields of up to 21.1T to be sustained [38]. This technology is used in the General Electric (GE) 1.5T flatbed scanner used in the QMC. Permanent magnetics are used for scanners with a weaker strength field,  $\approx 0.5T$  or lower. These can be cheaper to set up and run but have limitations due to their weaker field and cannot be turned off in the case of emergency. Another option is to use a high-temperature superconductor like magnesium diboride, as used in the Paramed 0.5T upright scanner in the QMC, preventing the need for liquid helium to be used as a cryogen [39].

## Shimming magnets

Even with modern manufacturing techniques and tolerances, producing an MR magnet with a homogeneous field is difficult. Once the magnet is installed, interference from metallic objects close by will further decrease field homogeneity. Shimming magnets are used to actively alter the field inside the bore of the magnet to keep it as homogeneous as possible [40]. Shimming can also be achieved passively with ferromagnetic material to improve the  $B_0$  field.

## Radio frequency coil

RF coils transmit RF pulses into the area of interest within the patient and/or receive the signal the excited nuclei give as they relax. Coils are more often receive-only than transmit/receive as the scanner itself can excite the nuclei. This allows the simpler receive-only coils to be used, although they have to be detuned during excitation so as not to interfere with the RF excitation pulse. RF coils come in a range of shapes and sizes to be used for imaging any part of the human body. RF coils come in two modalities: volume and surface. Volume coils are placed around the region of interest (ROI). Surface coils are placed onto or near the area of interest. The advantage of using surface coils is that their signal-to-noise ratio is higher (SNR). However, surface coils produce non-uniform RF that drops off in strength as the distance from the coil increases [41]. A volume coil still experiences these effects, but within their volume, the  $B_1$  is more uniform. The region of the patient being imaged is inside the volume coil, where a more uniform field can be maintained [37].

## Gradient coils

As discussed earlier in this section, the Larmor frequency of a nucleus depends on the strength of the magnetic field that the nuclei is in, Equation (2.5). In order to get positional data on the nuclei, the magnetic field must vary with position. A gradient coil is used to create a magnetic field that varies with position in one plane. By using three orthogonal gradient coils, the magnetic field can be varied in the x-, y- and z-planes. From this, the positional information can be used to generate a 3D image via MRI.

### 2.2.3 MRI sequence

#### Slice selection

When the z-gradient coil is switched on (z axis defined arbitrarily in line with  $B_0$  generated by the main magnet), it generates a gradient field in line with  $B_0$ .  $B_z$  is higher at the head than the feet or vice versa depending on the direction of the gradient. The nuclei experience different  $B_z$  strengths, which means they have different Larmor frequencies spinning faster with a stronger  $B_z$ . The slice selection gradient is turned on during the application of the RF pulse so only one slice is excited, and during rephasing [42]. A specific slice has a centre frequency ( $F_c$ ) that determines the position of the slice. The span of frequencies ( $\Delta F$ ) that makes up this slice is determined by the slice thickness ( $\Delta z$ ). Figure 2.3 shows the range of frequency excited by different RF pulses. Gaussian and sinc pulses are the most commonly used for slice-selective applications, with

the sync pulses giving a more uniform excitation across the slice. If the RF coil transmits the RF pulse at a specific frequency, only the nuclei with that exact Larmor frequency are excited. A long rectangular wave only excites a single frequency, and normally a short, strong rectangular pulse is used to excite an entire sample with no gradients applied [43]. A sync pulse is a sine wave which is amplitude modulated with the centre frequency of the slice acting as its base frequency given in Equation (2.12) [42].

$$B_1(t) = K \frac{\sin(\Delta F \pi t)}{\Delta F \pi t} \sin(2\pi F_c t) \quad (2.12)$$

- $B_1$  Magnetic field strength over time:  $B_1(t)$
- Frequency span:  $\Delta F$
- Central frequency:  $F_c$
- Time:  $t$
- Pulse amplitude:  $K$

In a sync pulse, the range of frequencies within a slice is equal to the bandwidth of the transmitted RF pulse. An ideal sync pulse would excite all the nuclei in a slice uniformly and do not affect nuclei outside the selected slice. An ideal sync pulse is not possible as it would require an infinite number of side lobes, requiring an infinite transmission time. Thus, the number of side lobes are limited and digitally filtered to get as close as possible to an ideal sync pulse [42]. Therefore, when the excited nuclei relax from the sync pulse, only that small slice along the z-axis in the x-y plane gives off a signal. This allows the operator to choose which point(s) along the z-axis of the body are excited, known as slice selection [37].

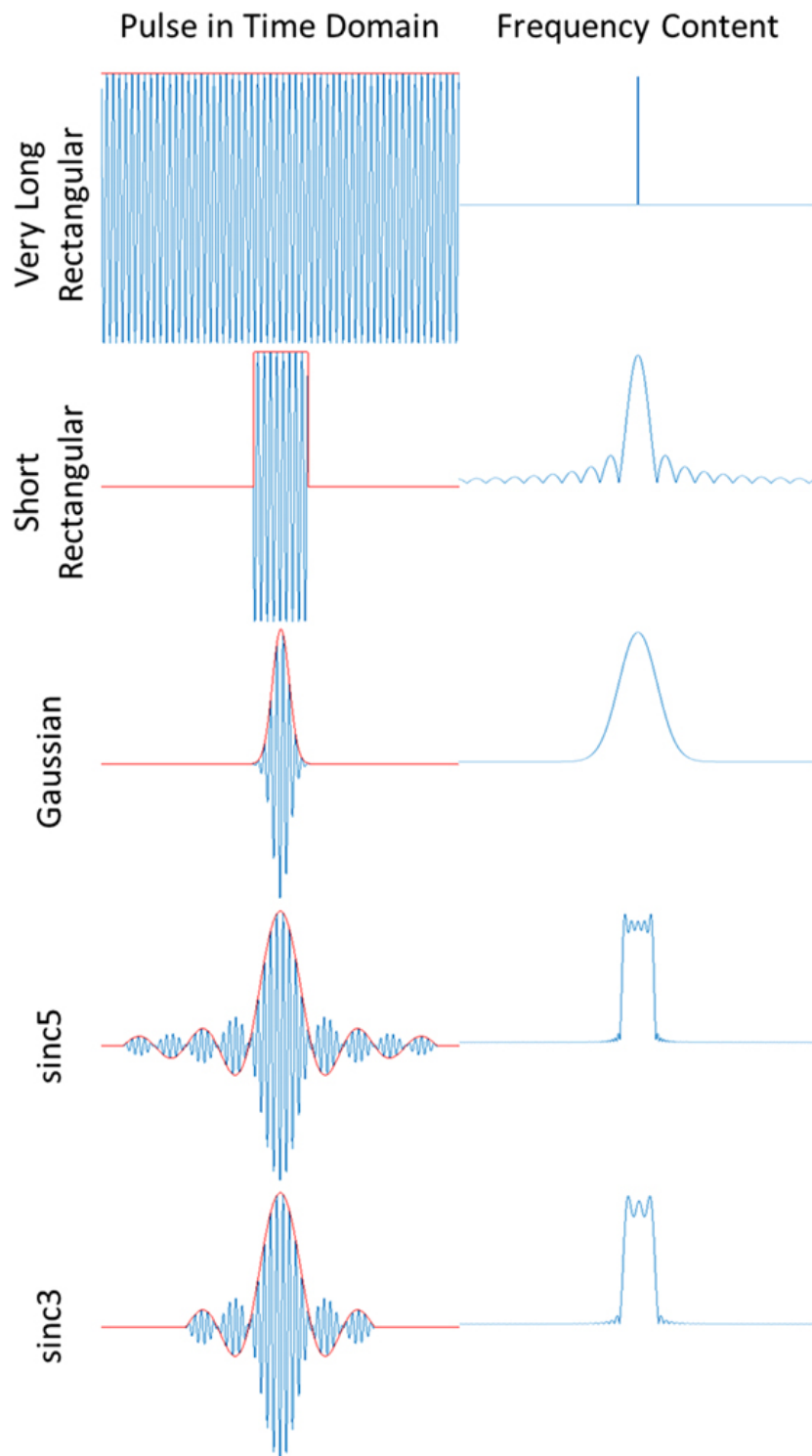


Figure 2.3: The slice excitation profiles from different RF excitation pulse shapes [43]

## Phase encoding

Slice selection makes it possible to encode the nuclei's spatial information in the z-axis. The next step is to encode spatial information along the y-axis by changing the phase of the RF signal produced by the excited protons, which runs anterior to posterior. The phase-encoding gradient (GPE) in the y-direction is only turned on for a very short time. This makes the nuclei spin at a frequency proportional to field strength along the gradient. Once the GPE is off, all the nuclei in the slice go back to being exposed to the same magnetic field strength. Therefore, the nuclei all precess at the same frequency. However, because of the GPE, the nuclei that were precessing quicker are now ahead of the nuclei that were precessing more slowly. This causes the nuclei to be phase-shifted relative to one another depending on their position in the y-axis [44]. See Figure 2.4 for a simple example. With a single-phase encoding step, it is not possible to discern the location of nuclei in the y-axis. Signals with different phases added together result in a final signal where the signals from each nucleus constructively and destructively interfere. However, from this, it is not possible to discern the location of the individual contributions along the phase-encoding axis. Exciting the same slice with a different phase-encoding gradient now means the final signal has been changed because a different phase has been introduced between the nuclei. The differences in the final signal and knowledge of the phase encoding gradient strength make it possible to discern the contribution and position of the nuclei along the y-axis.

Each line of pixels in the final MR image requires a unique phase-encoding gradient for each phase-encoding step. The MR signal is sampled from each phase-encoding step at a regular frequency. A fixed frequency-encoding gradient is also applied during readout. Frequency encoding is explained further in the next section. Each time the signal is sampled, it will have both real and imaginary components with unique phase and frequency information which fill a frequency domain matrix known as k-space. Each point in k-space holds all the specific frequency and phase information for each pixel in the final image. The centre of k-space holds the contrast information and the edges of k-space hold the high-resolution information for the final image. K-space can be filled in any order and does not need to be totally filled depending on the contrast, resolution and acquisition speed required. The most common and simplest method of filling k-space is line by line, which is known as Cartesian filling. Each phase-encoding step fills an entire line in k-space. As a simplification of Cartesian, k-space filling is shown in Figure 2.5. Other filling methods include radial, spiral and zig-zag, among other compressed sense methods where k-space is under-sampled for various reasons, including faster acquisition speed and mitigation of motion artifacts. Once k-space has been filled, a 2DFT converts the k-space data into the final image [45]. Now that the nuclei have been phase encoded, they have spatial information in both the y- and z-axis.

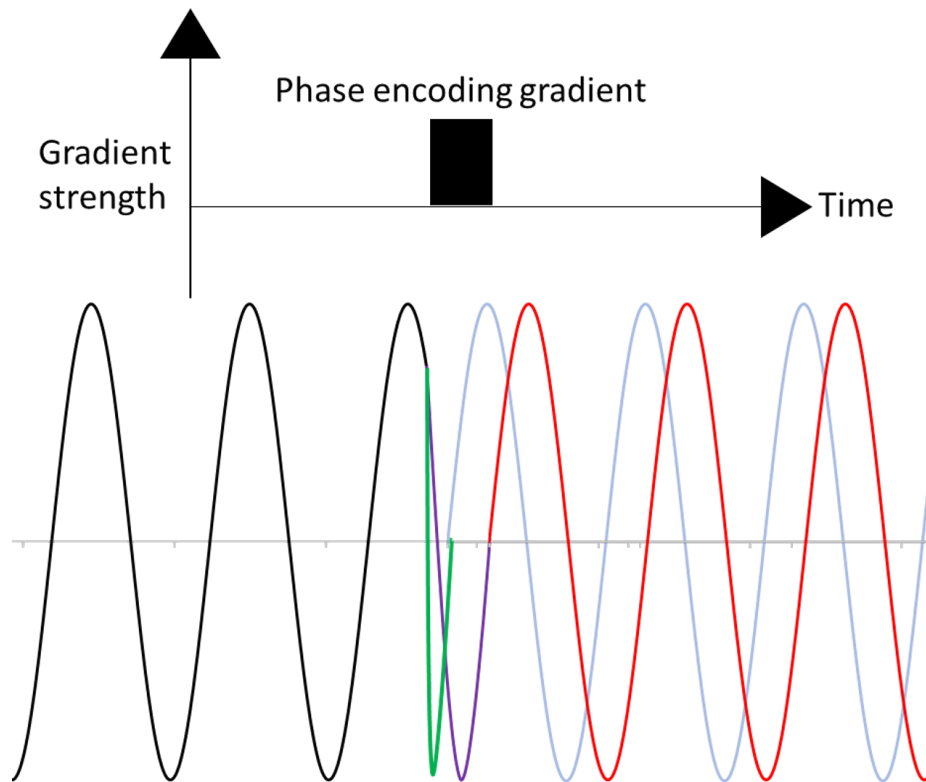


Figure 2.4: Phase shift example: The black line is the original precession frequency of the slice. An RF gradient is applied, and the green and purple lines show where the precession frequency has changed depending on the position along the phase-encoding direction. When the RF gradient is switched off, the nuclei return to their original frequency (red and blue lines) with an acquired phase shift between nuclei depending on their position.

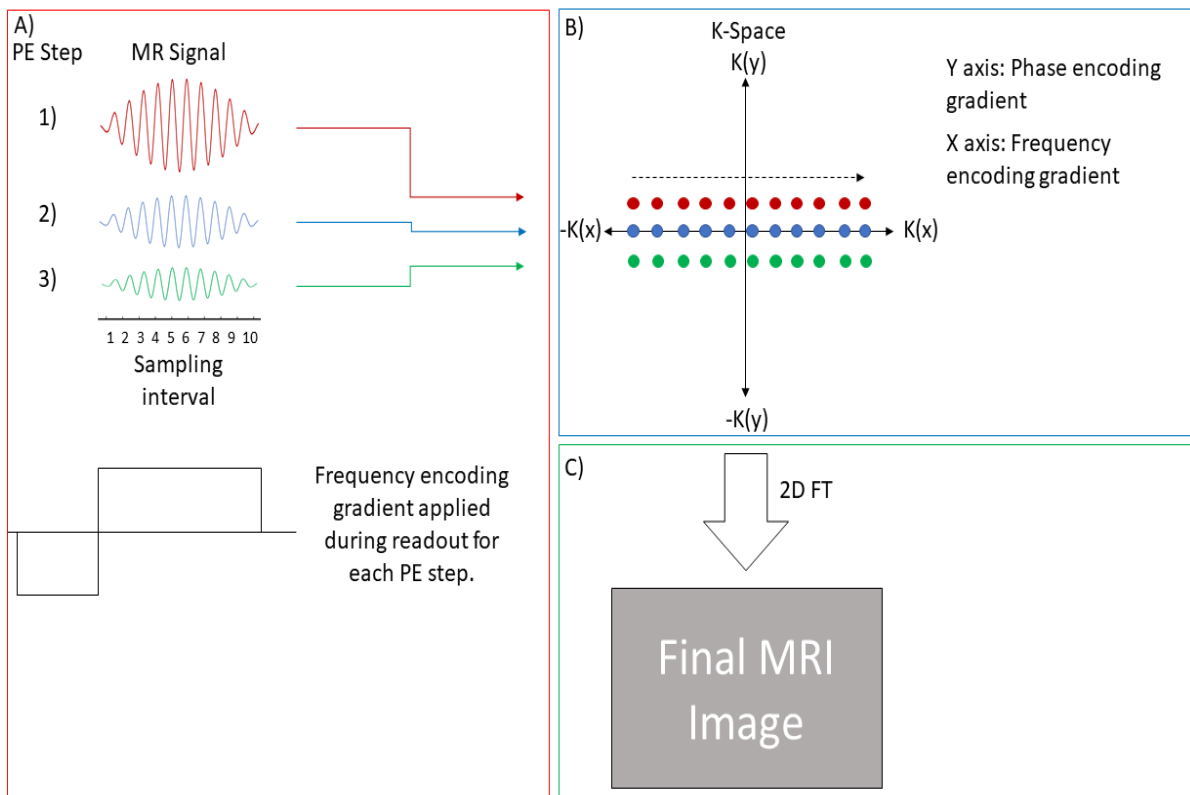


Figure 2.5: A simplification of cartesian k-space filling for three different phase encoding steps. A) Each phase-encoding step will introduce a different phase between the nuclei and therefore have a unique echo. These echoes are sampled at a set frequency while the frequency-encoding gradient is applied. B) Each sample of the signal has a unique phase and frequency value and fills a point in k-space. Every phase-encoding step fills a new line of k-space. C) Once k-space has been filled, a 2DFT converts the frequency and phase information into the final image.

### Frequency encoding

This is the final positional encoding step, acquiring the spatial information along the x-axis. The gradient coil now varies its strength along the x-axis during readout. Therefore, the Larmor frequency of the slice selected varies along the x-axis. This makes it possible to pinpoint where a signal came from on the x-axis. Combining all three positional encoding steps, the precise region where an RF signal originates can be determined. This is because every voxel now has a different frequency and phase [37].

### Pulse sequence

A pulse sequence is a series of different pulses and changing magnetic gradients that provide the spatial information to generate an MRI image. It is comprised of RF pulses, the switching of gradient coils, and signal collection. Using the

correct pulse sequence and optimising it is vital for imaging different regions and pathologies. Whether a sequence is  $T_1$  or  $T_2$  weighted dictates if the contrast and brightness of the image is governed by the  $T_1$  relaxation properties of the tissue or the  $T_2$  properties [46]. Adjusting pulse sequence parameters can reduce the signal from fat, so it is easier to see the pathology of the patient [47]. Water signals can also be suppressed [48]. It is also possible to image tissue using diffusion-weighted imaging (DWI) [49]. Molecules such as water can be used in DWI to detect and access the size of tumours [50] or identify a stroke [51]. It is very important to have the right sequence for the job. Pulse sequences vary in complexity. To better understand pulse sequences, two fundamental pulse sequences are discussed below [37].

### Spin-echo sequence

A spin-echo (SE) sequence is one of the most frequently used types of pulse sequences. A  $90^\circ$  RF pulse is used to excite the protons. Immediately after the RF pulse, all proton vectors in the x-y plane are in phase, and the signal is at its maximum. After a  $90^\circ$  pulse,  $T_2^*$  relaxation causes the nuclei to dephase, reducing the overall magnitude of the signal. After a time (t), a  $180^\circ$  pulse is then applied, rotating the magnetisation of the nuclei by 180 degrees. Protons that were precessing faster and in front while dephasing are now behind and vice versa for slower spins that were lagging behind. This means the faster-precessing nuclei catch up to the slower-precessing nuclei. After another t, the proton vectors will all be in phase with one another. This means the x-y magnetisation lost by  $T_{inhomogeneities}$  relaxation is regained as it is symmetrically reversible and the signal is at its maximum, giving a spin-echo that can be detected. The signal is not as high as after the initial  $90^\circ$  RF pulse because of non-recoverable  $T_2$  relaxation. There can be further losses in the signal of the spin-echo above the  $T_2$  relaxation due to random diffusion of the nuclei. Should nuclei diffuse to other regions with different magnetic field strengths, the exact rephasing process described above would not occur as nuclei that diffused will precess at different frequencies between the  $90^\circ$  and  $180^\circ$  RF pulses [52]. The time between the  $90^\circ$  RF pulse and the echo is the echo time (TE). The  $180^\circ$  is applied at  $\frac{TE}{2}$ . A single TE sequence is given below in Figure 2.6.

The magnetisation in the z-axis is regained via the  $T_1$  relaxation process. However, within a live patient, the  $T_1$  time constant is longer than  $T_2$ . As a result, z-magnetisation is recovered over a longer period. This means that there is a minimum repetition time (TR) between  $90^\circ$  pulses to regain enough magnetisation for there to be no degradation in the signal strength. TR is an influential variable on the contrast of the final image and the image acquisition time. SE sequences or sequences based on the fundamental SE sequence can image a range of pathologies.  $T_1$  weighted SE can be used after a Gadolinium (Gd) contrast agent has been administered to a patient.  $T_1$  relaxation drops with increased concentrations of Gd and can be used for lesion detection as there is signal enhancement from the uptake of the Gd contrast agent [53]. SE imaging allows imaging with  $T_1$ ,  $T_2$  and proton density contrast. SE sequence variants are used to image almost all regions of the body [53]. SE can also be used to produce Diffusion weighted (DW) images which is explored in greater depth in Section 2.5.4.



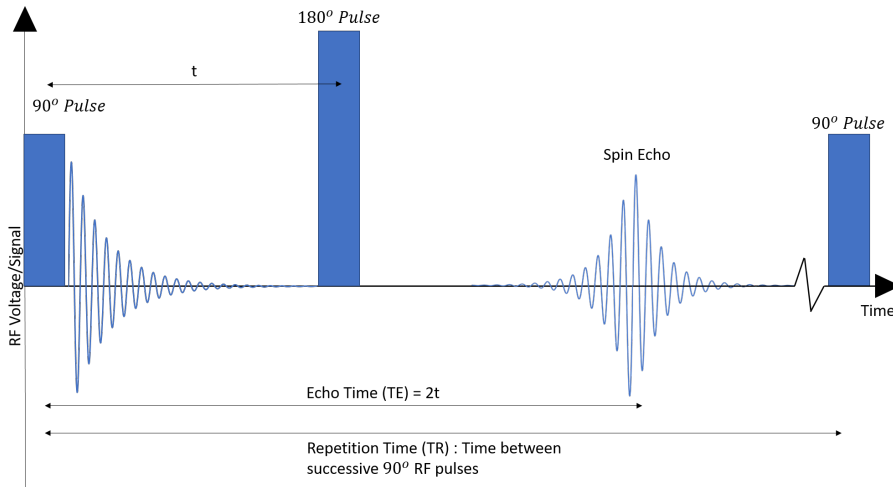


Figure 2.6: Graph to show the RF pulses and signal from a single spin-echo cycle

### Gradient-echo sequence

In a gradient-echo (GE) sequence, gradient fields are used to dephase and rephase transverse magnetisation. The gradient speeds up the dephasing of the transverse magnetisation by increasing  $T_2^*$  relaxation. A rephasing gradient is then applied to the sample after a set time. The rephasing gradient has the same strength as the dephasing gradient but with the opposite polarity. This rephasing gradient recovers the signal lost by the dephasing gradient, causing a gradient echo, as shown in Figure 2.7. This echo is smaller than the original signal, as  $T_2$  and  $T_2^*$  are unaffected. The flip angle of the GE sequence does not have to be  $90^\circ$  like the SE sequence. Instead, it can take any value [37]. If a  $90^\circ$  pulse is not used, not all the longitudinal magnetisation is killed, so the build-up time to recover this magnetisation is quicker. The FA of the first pulse is typically  $90^\circ$  in proton imaging, where magnetisation is recoverable. For HP work where the magnetisation is non-recoverable, a lower flip angle is used.[37]. Smaller flip angles only partially tip the z-magnetisation into the x-y plane so can preserve magnetisation.

If the TR is short, the protons do not have time to fully recover between pulses. The maximum signal is achieved when the FA is equal to the Ernst angle [54] and allows more rapid TR while maximising signal. As a result, subsequent pulses can be taken closer together, reducing scan times. Moreover, GE sequences can be weighted to select the contrast. Unlike SE, the local inhomogeneities in the magnetic field are not taken into account and corrected. This leads to artefacts in the final image, which can make it harder to interpret.

$$\alpha_E = \arccos\left(e^{-\frac{TR}{T_1}}\right) \quad (2.13)$$

- Repetition time: TR
- Longitudinal relaxation time constant:  $T_1$

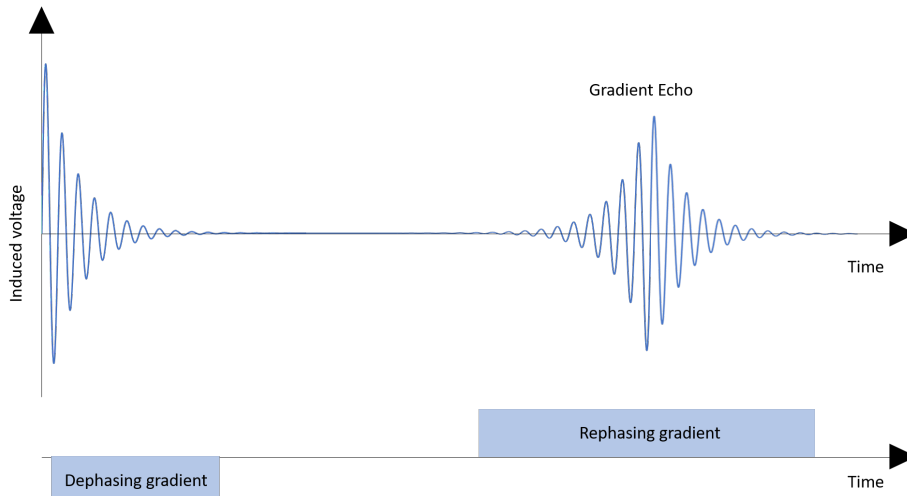


Figure 2.7: A diagram to show how gradient-echo sequence is performed

Fast GE is the basis for a wide range of clinical applications and can create good-quality images with fast acquisition times [55].  $T_2^*$  weighted GE sequence sensitivity can be used in functional MRI (fMRI) in which blood oxygenation levels lead to  $T_2^*$  changes. Therefore, it can be used to detect microbleeds in the brain after a stroke [56] and can also map cerebral blood flow [57]. RF-spoiled GE imaging can be used to assess myocardial perfusion [58]. Many pathologies can be observed by using sequences based on the basic GE sequence.

### 2.3 Thermal polarisation

The nuclear spin numbers of  $^1H$  and  $^{129}Xe$ , which are of particular interest to this thesis, are both  $\frac{1}{2}$ . This means the number of possible orientations those nuclei can occupy in an external magnetic field is two. The two directions are either parallel to the field (spin-up) or anti-parallel (spin-down). Parallel nuclei have the lower energy state of the two. The difference between these populations is what dictates the polarisation ( $P$ ) of the population as a whole.

$$P = \frac{N_{\uparrow} - N_{\downarrow}}{N_{\uparrow} + N_{\downarrow}} \quad (2.14)$$

$N_{\uparrow}$  and  $N_{\downarrow}$  respectively represent the  $m = \frac{1}{2}$  and  $m = -\frac{1}{2}$  magnetic quantum numbers,  $m = \frac{1}{2}$  being the parallel energy state and  $m = -\frac{1}{2}$  anti parallel. These are the only two energy levels that nuclei with  $I = \frac{1}{2}$  can take according to Equation (2.2).

For a  $I = \frac{1}{2}$  nuclei, the difference in energy between the two energy levels is given as a product of the field strength ( $B_0$ ) and the gyromagnetic ratio of the nuclei as described in Equation (2.3). The signal observed during NMR and MRI experiments is from the bulk magnetisation  $M_o$  of the sample. This is a product of the polarisation of the sample and the number of nuclear spins ( $N_s$ ).

$$M_o = \frac{1}{2} N_s \gamma \hbar P \quad (2.15)$$

When performing NMR or MRI on a spin system at thermal equilibrium, the polarisation is dictated by the  $B_0$  field strength and the temperature (T) of the system. For a system where  $I = \frac{1}{2}$ , P is given by Equation (2.16).

$$P = \tanh\left(\frac{\gamma\hbar B_0}{2kT}\right) \quad (2.16)$$

- Boltzman constant: k
- Temperature: T
- Magnetic field strength:  $B_0$
- Thermal polarisation: P

When x approaches zero  $\tanh(x)$  approaches x. Therefore, Equation (2.16) can be approximated as (2.17).

$$P \approx \left(\frac{\gamma\hbar B_0}{2kT}\right) \quad (2.17)$$

Therefore, according to Equation (2.14):

$$\left(\frac{\gamma\hbar B_0}{2kT}\right) \approx \frac{N_{\uparrow} - N_{\downarrow}}{N_{\uparrow} + N_{\downarrow}} \quad (2.18)$$

It is possible to calculate the ratio of  $N_{\uparrow}$  to  $N_{\downarrow}$  within a system at thermal equilibrium using Boltzmann statistics. This ratio is a function of  $\Delta E$ , T and k.

$$\frac{N_{\uparrow}}{N_{\downarrow}} = e^{\Delta E/(kT)} \quad (2.19)$$

This can be approximated to the first two terms of the exponential series, meaning:

$$e^{\Delta E/(kT)} \approx 1 - \frac{\Delta E}{kT} \quad (2.20)$$

In a magnetic field of 1 Tesla  $\Delta E = -1.76 \times 10^{-7} eV$  at room temperature [59], the ratio is 0.9999956. The excess of protons in the  $N_{\uparrow}$  is therefore approximately 4 in one million, giving a very small thermal polarisation. However, the acquired signal is not based purely on polarisation, and it is also based on the number of nuclear spins i.e. molar concentration. For example, in proton MRI imaging of a human body, the number of nuclear spins is high. This means the bulk magnetisation is enough to yield a sufficient signal for imaging. As gases like  $^{129}\text{Xe}$  have a much lower density than a solid, a few methods can be employed in order get the bulk magnetisation required to produce a useable signal from thermal polarisation. The magnetic field strength can be increased. Normal clinical scanners have a field strength of between 0.2T and 3T, with some experimental scanners capable of >12T. The higher the field, the higher the costs of the scanner or system and the physiological effects on the human body increase at high B fields, reducing patient acceptability [60].

Another option is to lower the temperature to almost absolute zero. This however increases experimental complexity and cost. It is also not possible

to image living subjects at this temperature. The other option is to average numerous scans to bring the NMR water signal out of the noise floor, but this can be very time consuming and impractical for human subjects using these methods together is a known as brute force polarisation (BFP) [61]. The next section discusses other methods, which brings the system out of thermal equilibrium to achieve polarisation far in excess of thermal levels.

## 2.4 Hyperpolarisation

### 2.4.1 Introduction

When a spin system is driven out of thermal equilibrium, it enters a state called hyperpolarisation. The intensity of the signals from HP systems is larger than thermal polarisation by several orders of magnitude. This is used to overcome the sensitivity problem that many NMR/MRI techniques face. There are many methods used to achieve hyperpolarisation of gases and liquids, BFP [61], dynamic nuclear polarisation (DNP) [62], signal amplification by reversible exchange (SABRE) [62], parahydrogen induced polarisation (PHIP) [62, 63, 64] and metastability exchange optical pumping (MEOP) [65, 66]. These techniques are described below but SEOP is discussed in greater detail in this section as it is the hyperpolarisation technique used in this thesis.

### 2.4.2 Brute force hyperpolarisation

In BFP, the sample is cooled to a very low temperature in a high strength magnetic field. A high nuclear spin can be achieved under these conditions according to Equation (2.17). This is currently still thermal polarisation (pre-polarisation), albeit at more extreme conditions. The sample is considered hyperpolarised when it is returned to standard temperature and pressure conditions. This comes with its challenges, as polarisation losses must be limited while transferring the material from the magnetic field where it is polarised to the field where it is detected. The time between dissolution and detection must therefore be kept to a minimum.

Large enhancements have been found when the pre-polarisation  $B_0$  field is maximised and the temperature is very low. For example, the  $^{13}\text{C}$  polarisation was found to be greater than 0.1% using a  $B_0 = 14\text{T}$  at a temperature of 2.3K. This is using small molecule metabolites such as 1- $^{13}\text{C}$ -pyruvic acid [67]. Furthermore, the timescale of polarisation build-up under low temperatures is  $\approx 10^1$  to  $\approx 10^2$  hours, which can be reduced by the use of nanoparticle agents [67]. Even though  $^{13}\text{C}$  is the main molecule of interest due to its use in imaging metabolic cancer [68], BFP can be used to hyperpolarise any nuclei with a non-zero spin.

### 2.4.3 Dynamic nuclear polarisation

DNP is another technique that can be used to hyperpolarise  $^{13}\text{C}$ . DNP was first performed on liquids by Albert Overhauser [69]. The core of DNP is based around a mechanism called the nuclear Overhauser effect, which transfers the higher electron spin-polarisation to a nuclear spin using microwave radiation.

This in turn hyperpolarises the nuclear spins of the target nuclei. The theoretical maximum of this polarisation enhancement is given by Equation (2.21).

$$En_{max} = \frac{\gamma_e}{\gamma_n} \quad (2.21)$$

- Gyromagnetic ratio of the electron:  $\gamma_e$
- Gyromagnetic ratio of the nucleus:  $\gamma_n$

For protons, the maximum enhancement factor is 660 and can be even higher for other nuclei. DNP can occur in liquids and solids, with one of the methods of spin transfer in solids being called the “solid effect”. The solid effect is best described as a three-step process. The electron spins are polarised via brute force methods, lower temperatures  $<1.5\text{K}$  and higher magnet field strengths. The polarisation is then transferred to the local nuclear spins via microwave pumping. Nuclear spins transfer from local nuclei to those further away via nuclear spin diffusion. This builds up nuclear polarisation while competing against nuclear spin-lattice relaxation [70], as shown in Figure 2.8. Once the nuclei are polarised, the sample is removed from the polariser and rapidly thawed into a liquid. From there, it is transported and injected into its target, known as dissolution DNP. Dissolution DNP was the first method used to image prostate cancer in-vivo using  $^{13}\text{C}$ -pyruvate [68]. DNP is currently able to achieve between 15-20% polarisation in  $^{13}\text{C}$ -pyruvate. The disadvantage of DNP is that it is costly, requiring bespoke machines and using specialised components to ensure samples are sterile when they are delivered in-vivo. This makes scaling up production very hard. Additional complications arise because of the fast  $T^2$  relaxation of the liquid samples, which means they have to be delivered to the patient very quickly. Any mistakes or delays can therefore render the samples unusable.

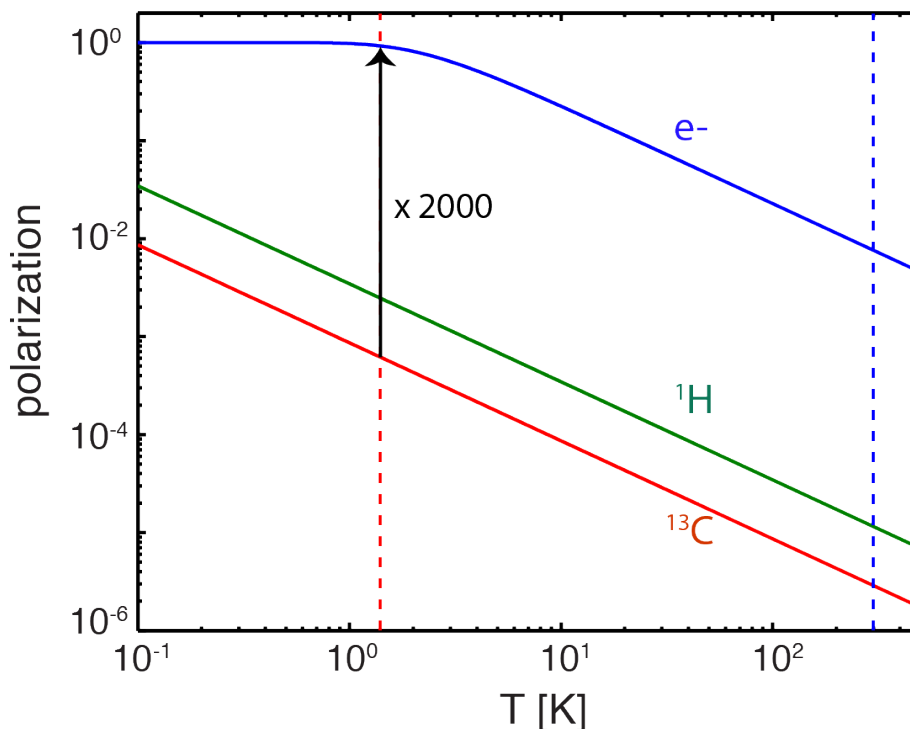


Figure 2.8: This figure shows the difference in polarisation between electrons and  $^1\text{H}$  and  $^{13}\text{C}$  nuclei. DNP allows the exchange in polarisation from electron spins to nuclear spins [71]

#### 2.4.4 Parahydrogen-induced polarisation

Molecular hydrogen ( $\text{H}_2$ ), the basis for PHIP, does not exist in one state. It can be one of four nuclear spin isomers in two different states: ortho and para. This is determined by the symmetrisation principle in quantum mechanics [72], which dictates that the overall wave function has to be antisymmetric under the exchange of nuclei. The  $\text{H}_2$  antisymmetric rotational states are associated with symmetric nuclear spin states, otherwise known as “ortho”. The opposite is true of symmetric rotational states that must be associated with antisymmetric nuclear spin states, known as “para”. Orthohydrogen can be any of three spin state terms:  $\uparrow\uparrow, \uparrow\downarrow + \downarrow\uparrow, \downarrow\downarrow$ . Parahydrogen can only occupy one spin state:  $\uparrow\downarrow + \downarrow\uparrow$ . These four states are equally populated at room temperature according to the Boltzmann distribution. The ratio of orthohydrogen to parahydrogen is 3:1 [73]. Reducing the temperature in the presence of a catalyst allows the  $\text{H}_2$  population in the higher energy ortho states to move the lower energy para states [74]; see Figure 2.9. As the transition between ortho and para states is forbidden once the catalyst is removed, the parahydrogen molecules are long-lived so there is time to attach them to a suitable target molecule and then use the molecule for various experiments.

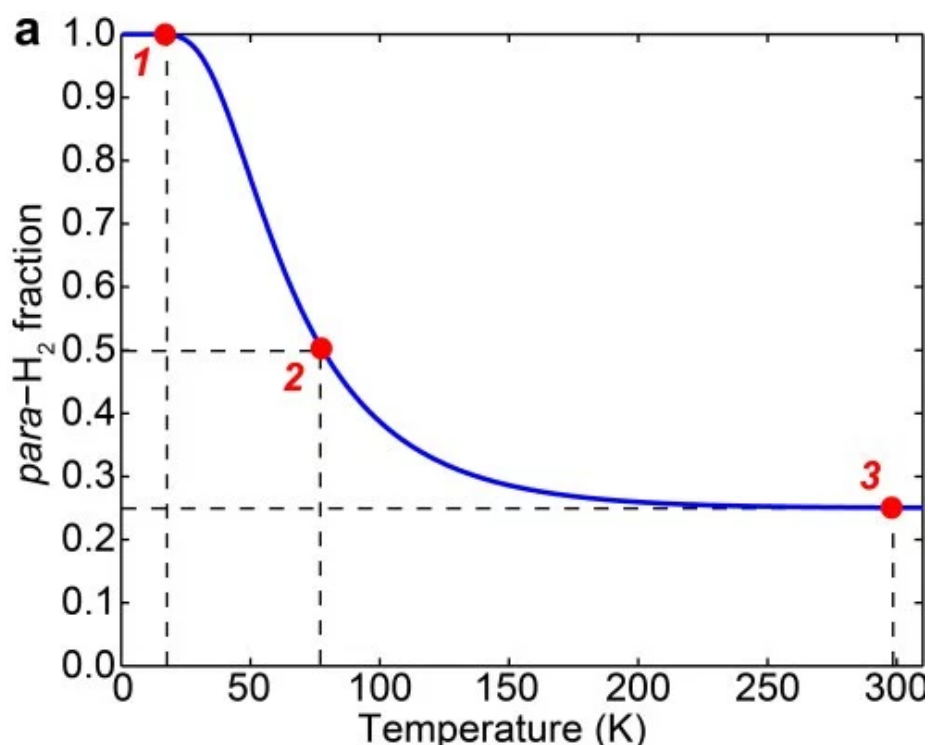


Figure 2.9: Parahydrogen fraction at different temperatures, with a suitable catalyst present. 1) At low temperatures, the composition is almost purely parahydrogen. 2) As the temperature is increased, the 3:1 ratio is reached asymptotically. 3) 3:1 ratio at room temperature [75]

A large population of parahydrogen is useful for polarisation because the singlet nuclear spin order of parahydrogen can be converted into nuclear spin magnetisation. This is achieved by adding the parahydrogen to a molecule that has an unsaturated carbon-carbon bond for the hydrogenation reaction to take place. The polarisation build-up rate is limited by the reaction rate between the parahydrogen and carbon molecules. A catalyst is used to increase the reaction speed so it occurs on a reasonable time scale. Typically, the catalyst contains rhodium [76]. In contrast to many hyperpolarisation methods, the equipment used for PHIP can be made with off-the-shelf components simply and cheaply, an example of which can be found in a paper by S. Kadlecik et al. [77].

#### 2.4.5 Signal amplitude by reversible exchange

A variant of PHIP is SABRE, which uses a metal catalyst to transfer the polarisation from parahydrogen to hyperpolarised substrate. The transfer occurs through the scalar coupling network [78]. Critically, this does not chemically change the target molecules [79]. Figure 2.10 shows how the SABRE catalytic cycle works.

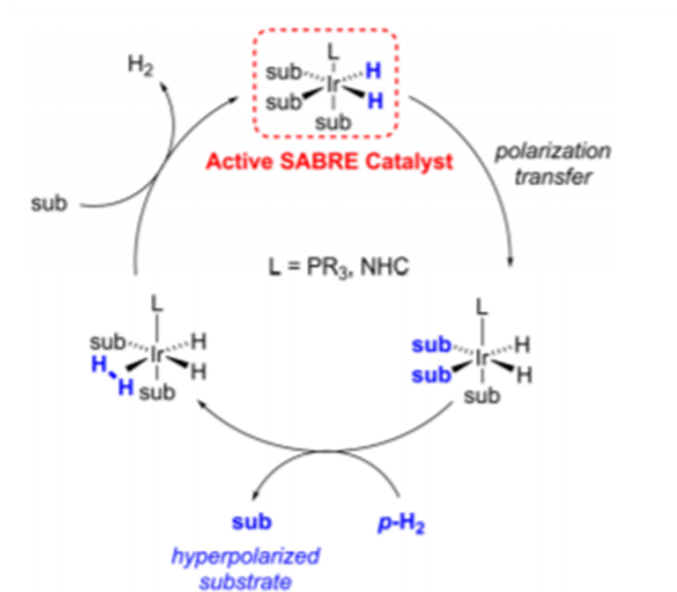


Figure 2.10: Diagram of a SABRE cycle. [80]

The problem is that most of the catalysts that work with substrates of biological relevance are heavy metals, which is a significant issue for SABRE for in-vivo applications. This means the catalyst is toxic, which has been a limiting step for in-vivo work [81]. There have been recent efforts to remove the toxic catalysts from the substrate without losing hyperpolarisation. Work by B. Kidd et al. has reported being able to remove an iridium catalyst from hyperpolarised metronidazole using  $\text{SiO}_2$  microparticles, all while preserving the hyperpolarisation [82]. This means SABRE is moving closer to becoming practical for a clinical setting.

## 2.4.6 Metastability-exchange optical pumping

MEOP is used to hyperpolarise  $\text{He}^3$  and  $^{21}\text{Ne}$  [83]. MEOP occurs in a uniform magnetic field, and the optical pumping is performed using circularly polarised light. A percentage of the  $\text{He}^3$  is promoted into a higher-energy state using a secondary laser. The excited nuclei then relax via a radiation cascade to the  $2^3\text{S}_1$  metastable state. The pumping laser is set to a frequency of 1083 nm, which allows the transition between the metastable state and an excited state to be optically pumped using the same mechanics as SEOP. Optical pumping is described in 2.4.7. This hyperpolarises the metastable  $\text{He}^3$ . The polarisation is transferred from the metastable  $\text{He}^3$  to the  $\text{He}^3$  population in the ground state via metastability exchange collisions [65].

The issue with MEOP is that, to allow RF discharge to create the metastable states, it has to be performed under gas low-pressures [65]. Polarisation losses occur when re-compressing the gas to a workable pressure for in-vivo work [84] or neutron scattering experiments [85] and the equipment required to perform this re-compression adds to the complexity and cost of the technique. Additionally,



MEOP can only be used to polarise  $\text{He}^3$ . Although HP  $\text{He}^3$  is popular for use in HP noble gas MRI,  $^{129}\text{Xe}$  does provide some advantages over  $\text{He}^3$ . A detailed comparison between the two gases is set out in Section 2.5.4

### 2.4.7 Spin exchange optical pumping

The most common method used to hyperpolarise  $^{129}\text{Xe}$  is SEOP. This is the hyperpolarisation method used throughout the work in this thesis; thus, SEOP is discussed in greater detail.

In SEOP, an alkali metal vapour, typically rubidium (Rb), acts as an intermediate step between the polarising laser light and  $^{129}\text{Xe}$ . Rb has a low melting point of 39 C and can be easily vaporised at moderate temperatures under pressure. If this occurs in a magnetic field and the Rb vapour irradiated with circularly polarised light, it is possible to polarise Rb electrons [15]. The Rb electrons absorb the circularly polarised photons when they are resonant with the  $D_1$  transition line 794.77nm at atmospheric pressure [86]. In this interaction, angular momentum also needs to be conserved in addition to energy. The ground state and its excited state both have a total angular momentum of  $\frac{1}{2}$ . The Rb  $5^2S_{\frac{1}{2}}$  ground state and  $5^2P_{\frac{1}{2}}$  excited state are split by the static magnetic field because of the Zeeman effect, so both ground and excited states can be spin up or spin down [16]. Depending on whether the light is circularly polarised left-handedly or right-handedly, one of the ground states, ( $m_j = \frac{1}{2}$ ) or ( $m_j = -\frac{1}{2}$ ) electron population will absorb the resonant photons. This is because of momentum conservation. A circularly polarised photon has the  $+\hbar$  angular momentum and can therefore only excite a spin down electron in the ground state and, as momentum is conserved, the electron is excited to a spin-up excited energy state. It is not possible to excite the spin-up ground state electrons as angular momentum is not conserved. The inverse is true if the photon is circularly polarised in the other direction. This means only one spin-up or spin-down electron population can be excited with the magnetic field applied.

The populations of the two virtual excited states equilibrate due to collisional mixing. Eventually, these electrons relax back down into the corresponding ground states. Only one ground state is being excited, so electrons build up in the opposing ground state, and the stimulated ground state's electrons are depleted. It is easiest to visualise this as filling two half-full buckets at the same rate using the water taken from one of the buckets. Eventually, one bucket is empty and the other full. An energy level diagram is shown in Figure 2.11. Optical pumping can create near-unity polarisation of Rb electrons.

The Rb polarisation rate is given by:

$$P_{Rb} = \frac{\gamma_{OP}}{\gamma_{OP} + \Gamma_{SD}} \quad (2.22)$$

- Optical pumping rate:  $\gamma_{OP}$
- Spin destruction rate:  $\Gamma_{SD}$

The spin destruction rate is depolarisation rate of the Rb from binary collisions and van der Waals molecule formation. The amount that the binary collisions contribute to spin destruction is given by Equation (2.23) [87].

$$\Gamma_{SD}^{binary} = \sum_i [G_i] \kappa_{SD}^{Rb-i} \quad (2.23)$$

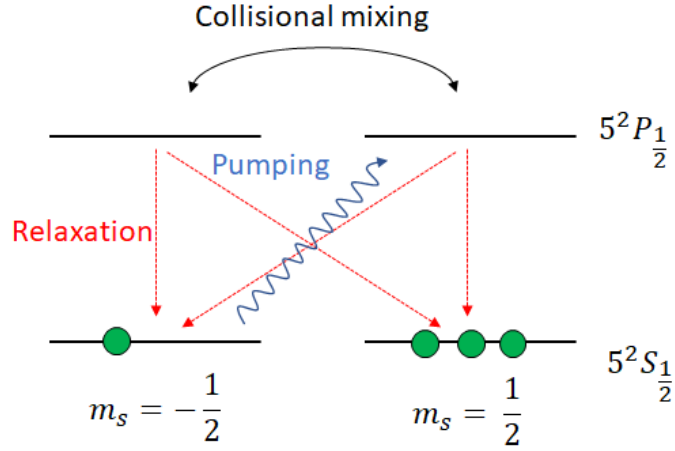


Figure 2.11: Energy-level diagram for Rb optical pumping

- The spin destruction coefficient with nuclei “i”:  $\kappa_{SD}^{Rb-i}$
- Atomic number density of each gas:  $[G_i]$

The highest spin destruction coefficients in a typical cell are between Rb and Rb. The next highest is Rb and  $^{129}\text{Xe}$ . The buffer gases  $\text{N}_2$  and  $^4\text{He}$  have spin destruction coefficients 3 and 4 orders of magnitude lower respectively. This means that for a reduced SD rate, it is best to have a gas mix that is as low in  $^{129}\text{Xe}$  as possible. This will increase the final polarisation but at the cost of bulk magnetisation.

The contribution of spin destruction from van der Waals molecule formation has a pressure-dependent component. The interaction time is decreased by buffer gas pressure. This is because collisions that cause molecule break up increase. For a gas mix with Xe,  $\text{N}_2$  and  $^4\text{He}$ , the van der Waals spin destruction is given by Equation (2.24) [87].

$$\Gamma_{DS}^{vdW} = \left( \frac{66183}{1 + 0.92 \frac{[\text{N}_2]}{[^{129}\text{Xe}]} + 0.31 \frac{[\text{He}]}{[^{129}\text{Xe}]}} \right) \left( \frac{T}{423\text{K}} \right)^{-2.5} \quad (2.24)$$

- Gas number density of X:  $[X]$

The total optical pumping rate of the Rb is given by Equation 2.25 [88].

$$\gamma_{OP}(z, r, \nu) = \int_0^\infty \Phi(z, r, \nu) \sigma_o(\nu) d\nu \quad (2.25)$$

- Photon flux at position  $(z, r)$  in the cell per unit frequency:  $\Phi(z, r, \nu)$
- alkali line absorption cross section:  $\sigma_o$

$$\sigma_o = \frac{2c r_e f}{\gamma} \quad (2.26)$$

- Speed of light:  $c$

- Electron radius:  $r_e$
- Oscillator strength:  $f$
- Lorentzian:  $\gamma$

The FWHM of  $\gamma$  is dependent on the gas mix and pressure inside the cell. The Rb cross-section can be pressure broadened, which means that at higher pressures its FWHM gets larger [89]. This means a greater range of photon frequencies can be absorbed, increasing the optical pumping rate. This is more useful with broadband lasers, as frequency narrowed lasers were uncommon in the early days SEOP development.

The second step of SEOP is spin exchange. The polarised Rb transfers its polarisation to the nuclei of  $^{129}\text{Xe}$  via spin-exchange collisions. These collisions are either binary collisions or molecular collisions. Binary collisions are just between Rb and  $^{129}\text{Xe}$ . An interaction between a spin-up Rb electron and spin-down  $^{129}\text{Xe}$  nuclei will, via a fermi hyperfine interaction, cause the spin directions to swap. The previously polarised Rb is now spin-down and can be polarised again by photons from the pump laser. Molecular collisions involve Rb,  $^{129}\text{Xe}$  and  $\text{N}_2$ . These collisions form weakly bonded van der Waals molecules between Rb and  $^{129}\text{Xe}$ . Another collision with  $\text{N}_2$  breaks up the short-lived van der Waals molecule and has the same effect as the binary collisions. See Figure 2.12

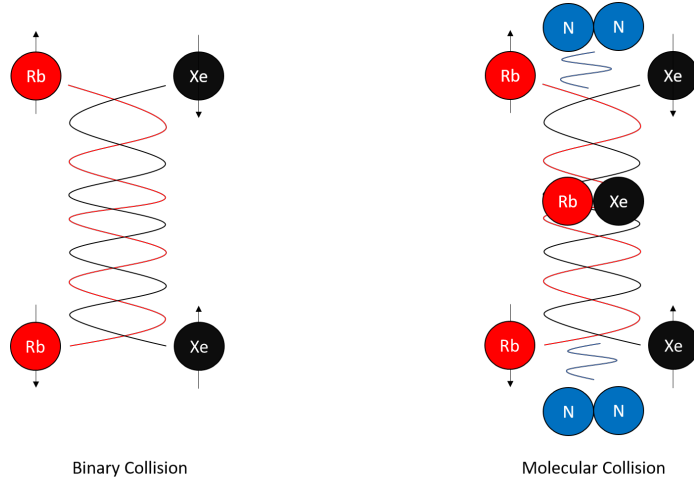


Figure 2.12: Binary collisions and molecular collisions

The sum of these two collisions dictates the polarisation build-up rate.

$$\gamma_{SE} = \gamma_{SE}^{bin} + \gamma_{SE}^{vdW} \quad (2.27)$$

After the Rb exchanges its spin to the  $^{129}\text{Xe}$  via these collisions, it can then be repolarised and then undergo collisions with another  $^{129}\text{Xe}$  nuclei. This allows the  $P_{Xe}$  to build up as this cycle repeats (see Equation (2.28)) [20].

$$P_{Xe}(t) = \frac{\gamma_{SE}}{\gamma_{SE} + \Gamma_1} (P_{Rb}) (1 - e^{-t(\gamma_{SE} + \Gamma_1)}) \quad (2.28)$$

- Time in cell:  $t$
- Relaxation rate in the cell:  $\Gamma_1$

The relaxation rate is partly dictated by the dipole interactions of  $^{129}\text{Xe}$  with paramagnetic centres in the walls of the cell. This can be found as the inverse of the  $T_1$  relaxation constant of the cell. The  $T_1$  time of the cells can be increased with siliconising fluid, which forms a siloconised surface on the inner cell wall, which act as a barrier between the polarised  $^{129}\text{Xe}$  and paramagnetic centres in the glass. This has the effect of increasing the speed of polarisation and also increases the time the HP  $^{129}\text{Xe}$  can be left in the cell before extraction after SEOP has ceased.

### 2.4.8 Continuous-flow spin-exchange optical-pumping

The physics of SEOP are universal regardless of whether the polariser is operating continuous- or stopped-flow. There are some extra considerations in a continuous-flow polariser, where the gas is constantly flowing through the optical cell during SEOP, which can affect the final  $P_{Xe}$  which are not present in a stopped-flow polariser, where the entire gas mix remains in the optical cell during SEOP.

The final polarisation ( $P_{Xe}$ ) after a time ( $t$ ) in a continuous-flow polariser is the polarisation of the gas after it leaves a cell, which depends on the residence time inside the cell ( $t_{cell}$ ) [90].

$$P_{Xe}(t_{cell}) = \frac{\gamma_{SE}}{\gamma_{SE} + \Gamma_1} (P_{Rb}) (1 - e^{-t_{cell}(\gamma_{SE} + \Gamma_1)}) \quad (2.29)$$

$t_{cell}$  is dependent on the volume of the cell ( $V_{cell}$ ), the flow rate of the gas ( $F$ ) and the pressure of gas in the cell ( $p_{cell}$ ). This relationship is given by Equation (2.30), and the standard pressure ( $p_s$ ) is defined as 760 Torr for all gases, which is approximately Earth's atmospheric pressure at sea level [91].

$$t_{cell} = \frac{V_{cell} p_{cell}}{F p_s} \quad (2.30)$$

The spin up time  $\tau_{SU}$  is given as:

$$\tau_{SU} = \frac{1}{\gamma_{SE} + \Gamma_{SD}} \quad (2.31)$$

Therefore using 2.30 and 2.31, 2.29 can be rearranged in terms of flow rate [90].

$$P_{Xe}(F) = \frac{\gamma_{SE}}{\tau_{SU}} (P_{Rb}) (1 - e^{-\frac{V_{cell} p_{cell}}{F p_s \tau_{SU}}}) \quad (2.32)$$

This gives a critical flow rate, where the the  $t_{cell}$  is the same as  $\tau_{SU}$ .

$$F_{crit} = \frac{V_{cell} p_{cell}}{\tau_{SU} p_s} \quad (2.33)$$

Substituting 2.33 into 2.32 gives [90]:

$$P_{Xe}(F) = \frac{\gamma_{SE}}{\tau_{SU}} (P_{Rb}) (1 - e^{-\frac{F_{crit}}{F}}) \quad (2.34)$$

The polarisation that can be achieved is maximal when the flow rate is zero. The faster the flow rate, the lower the residence time in the cell. This decreases to 0.63 of the maximum polarisation when the flow rate is equal to  $F_{crit}$ . With increasing temperatures, Rb vapour density increases and so does  $\gamma_{SE}$  and the size of  $F_{crit}$ . At higher temperatures, spin destruction and  $^{129}\text{Xe}$   $T_1$  relaxation also increases and the maximum polarisation that can be achieved decreases. Therefore, there is an optimum regime where the required gas volume can be collected in a reasonable amount of time with sufficient polarisation [90].

Equation (2.34) gives the polarisation leaving the cell, although this is not the final polarisation seen in the bag. During the cryo-collection and storage process, the HP  $^{129}\text{Xe}$  is depolarising. The formula for  $T_1$  relaxation must be modified to account for the storage time of the gas being longer at the start of the collection compared to at the end [92].  $T_{1s}$  is the  $T_1$  relaxation time of  $^{129}\text{Xe}$  in solid form (150 minutes in the 9810 storage field [92]) and the total collection time is given by  $t_c$ , which is the time gas is flowing through the cell and being cryo-collected.

$$P_{Xe}(t_c) = \int_0^{t_c} \frac{t}{t_c} P_0 e^{-\frac{t}{T_{1s}}} dt \quad (2.35)$$

This can be solved to give.

$$P_{Xe}(t_c) = P_0 \frac{T_{1s}}{t_c} (1 - e^{-\frac{t_c}{T_{1s}}}) \quad (2.36)$$

As before  $t_c$  and  $T_{1s}$  can be re-arranged in terms of flowrates.

$$F_c = \frac{V_{cell} p_{cell}}{t_c p_s} \quad (2.37)$$

$$F_{T1} = \frac{V_{cell} p_{cell}}{T_{1s} p_s} \quad (2.38)$$

The relaxation of  $^{129}\text{Xe}$  can therefore also be expressed in terms of flowrate.

$$P_{Xe}(F) = P_0 \frac{F_{T1}}{F} (1 - e^{-\frac{F_{T1}}{F}}) \quad (2.39)$$

Putting both the polarisation from Equation (2.34) and relaxation in Equation (2.39) together gives.

$$P_{Xe}(F) = \frac{\gamma_{SE}}{\tau_{SU}} (P_{Rb}) (1 - e^{-\frac{F_{crit}}{F}}) \frac{F_{T1}}{F} (1 - e^{-\frac{F_{T1}}{F}}) \quad (2.40)$$

This can be approximated to:

$$P_{Xe}(F) \approx (P_{Rb}) (1 - e^{-\frac{F_{crit}}{F}}) (1 - e^{-\frac{F_{T1}}{F}}) \quad (2.41)$$

Equation (2.41) does not take into account the reduced  $T_1$  time when the  $^{129}\text{Xe}$  is depositing from a gas to a solid and back [93], nor the relaxation in earth's field when passing through the outlet manifold. Therefore, given the time limitations of a clinical environment, finding the optimal settings for a continuous-flow polariser requires a practical investigation.

## 2.4.9 Buffer gases

Historically in  $^{129}\text{Xe}$  SEOP, two buffer gases were also added to the gas mix:  $N_2$  and  $^4\text{He}$ . The main purpose of  $N_2$  is to perform radiation trapping, which reduces the depolarisation of alkali metals by collisionally quenching the emission of resonant photons from the relaxation of excited alkali metal atoms. Due to the random relaxation of excited alkali metal, the polarisation of the emitted photons is also random, meaning the emitted photons can go on to depolarise polarised alkali metal vapor if the  $N_2$  is not present in sufficient quantities.  $N_2$  can also be used to pressure-broaden the absorption lines of the alkali metal. However, the increased number of  $N_2$  atoms also contributes to increased spin-destruction. Pressure broadening allows for better coupling between the OP laser and the alkali metal  $D_1$  or  $D_2$  lines.  $^4\text{He}$  was also added in large amounts ( $\approx 6 - 10$  amg) to collisionally broaden the absorption lines of the alkali metal. It has a smaller spin-destruction rate ( $3.45 \times 10^{-19} \text{cm}^3 \text{s}^{-1}$ ) compared to  $N_2$  ( $3.44 \times 10^{-18} \text{cm}^3 \text{s}^{-1}$ ) [94]. The broadening effects of the buffer gas were much more important early in the exploration of SEOP when OP laser linewidths were  $\approx 10$  times wider than those that can be achieved with current laser technology. Now that OP laser line widths are close to the  $D_1$  linewidths, the utility of  $^4\text{He}$  in pressure broadening to achieve optimal polarisation is greatly diminished.

Each transition has a natural linewidth at absolute zero, given by the Heisenberg uncertainty principle shown in Equation 2.42 [95].

$$\Delta E \Delta t \geq \frac{\hbar}{2} \quad (2.42)$$

- Energy uncertainty  $\Delta E$
- Lifetime of the state  $\Delta t$
- Reduced Plank constant  $\hbar$

At non-zero temperature, the Rb vapour atoms will have random thermal motion, so will see either red- or blue-shifted photons, further broadening the line width as the Rb vapour temperature rises. With increased gas pressure, there are also more collisions with the Rb so  $\Delta t$  reduces and further increases  $\Delta E$ , pressure broadening the linewidth.

## 2.5 Hyperpolarised gas MRI

### 2.5.1 Introduction

This section looks into the background of HP gas MRI development, in particular looking at alternate ways of obtaining functional and structural information about the lungs and why different methods are needed. It then covers why HP gas MRI is used in place of conventional proton MRI in certain situations and which gases are best suited for this role. Finally, the most common MRI sequences used in HP  $^{129}\text{Xe}$  imaging are discussed.

### 2.5.2 Alternatives to MRI

The current standard procedure to measure lung function is spirometry. This involves patients exhaling into a tube with basic monitoring equipment attached. The most common measurements are forced expiratory volume in one second (FEV1), the amount of air forcibly exhaled in one second and forced vital capacity (FVC), which is the total amount of air a patient can force from their lungs [4]. Spirometry is only able to give a global measurement of lung function for clinical staff to interpret, so cannot give any localised structural, or functional information. It can only detect substantial changes in lung function, which may delay detection of lung diseases limiting the treatment options available.

Another method used for lung imaging is CT. CT works by combining a set of x-ray images that pass through the body at different angles. These x-rays are combined by using a computer to build up a series of image slices through the body.

Although CT scans can produce high-resolution images of the lung tissue and structure, x-rays are a form of ionising radiation. As the major lung and brain diseases are chronic, many images need to be taken over the patients' lifetimes, which increases the risk of side-effects caused by ionising radiation, such as cancer. As limiting radiation exposure is a priority in health care, the amount of times a patient can be imaged is limited, and the cohort that can be imaged with CT is also reduced.

### 2.5.3 Conventional MRI imaging

Conventional MRI in-vivo images protons within the body, which are abundant in tissue. Compared to other organs and tissues in the body, however, lungs have a very low proton density [96] and the airways even less. This is why, in conventional proton MRI images, the lungs are dark areas lacking in signal. The lungs' inherent heterogeneous structure also induces magnetic field inhomogeneities, leading to a short  $T_2^*$  [97]. This creates magnetic susceptibility artefacts, further reducing image quality. It is not possible to image the gas in the lungs with conventional proton MRI either as there are so few protons to image.

### 2.5.4 Hyperpolarised gas MRI imaging

#### Gases

Many of the problems conventional proton MRI have in the lungs can be circumvented using an external gas acting as a contrast agent. If a gas is inhaled, it can be used to image the airways of the lungs instead of the lung tissue itself. The problem with using a gas as a contrast agent is that its density is  $\approx 1000$  times smaller than protons found in human the tissue. Therefore hyperpolarisation is needed to increase the bulk magnetisation and get a useable signal from the lungs. The first time HP MRI was performed in 1994 was ex-vivo using  $^{129}\text{Xe}$  [98].  $^{129}\text{Xe}$  is a noble gas that provides an unreactive and safe target for hyperpolarisation. Three years later, the first HP  $^{129}\text{Xe}$  study was conducted in humans [99].

Despite  $^{129}\text{Xe}$  being the first to be imaged, the results were limited due to the low polarisation that could be achieved at the time; typically only a

few percent [100]. This led to an initial switch in research focus to another noble gas,  ${}^3\text{He}$ .  ${}^3\text{He}$  polarisation technology at the time offered an order-of-magnitude improvement in polarisation, over  ${}^{129}\text{Xe}$ , providing a greater bulk magnetisation. Another advantage  ${}^3\text{He}$  had over  ${}^{129}\text{Xe}$  is that, unlike  ${}^{129}\text{Xe}$ , it did not cause any side effects when inhaled. Xe acts as a mild anaesthetic which can cause transient dizziness for a few minutes after inhalation [101]. By 1996  ${}^3\text{He}$  had been used for clinical research, which rapidly increased in scale and scope and provided clinically relevant data [102].  ${}^3\text{He}$  is now no longer the gas of choice for HP MRI imaging for a few different reasons. The main reason, it is prohibitively expensive to procure for academic use and as a medical consumable. This is because  ${}^3\text{He}$  comes exclusively from tritium decay, which only comes from the historical production of US nuclear missiles, so there is a finite supply. The US government has earmarked  ${}^3\text{He}$  for use in neutron detectors to detect illegally transported plutonium. These factors combined, along with increasing demand, has resulted in 1 litre of  ${}^3\text{He}$  costing up to \$ 2000 [103].

The cost of Xe is much more economical [104]. Development in polariser technology has also increased the polarisation that can be achieved with  ${}^{129}\text{Xe}$  using SEOP. This makes it a viable alternative to  ${}^3\text{He}$ .  ${}^{129}\text{Xe}$  also has some other characteristics that increase its utility in HP-gas MRI. Unlike  ${}^3\text{He}$ ,  ${}^{129}\text{Xe}$  can dissolve into pulmonary tissue, and it does so via the same pathway as oxygen, eventually binding with red blood cells (RBCs) [105]. This means  ${}^{129}\text{Xe}$  can be transported via the bloodstream to other organs in the body such as the brain and liver, increasing the number of sites that can be imaged. Due to its large electron cloud, Xe also has a large chemical shift. This means it is possible to discern where the Xe is located as different tissues since the blood and airways of the lungs cause a different chemical shift in the  ${}^{129}\text{Xe}$  [11]. The chemical shift is given by Equation (2.43) [106].

$$\delta = \frac{\nu_{sample} - \nu_{ref}}{\nu_{ref}} \quad (2.43)$$

- $\nu_{sample}$  resonant frequency of a sample
- $\nu_{ref}$  resonant frequency of a standard reference compound

$\delta$  is expressed as parts per million (ppm). This chemical shift is expressed in this form is independent to the strength of the magnetic field. Although  $\nu_{sample}$  scales with frequency, the difference in frequency increases as the magnetic field strength is increased. Therefore, the higher the magnetic field, the higher the resolution of any NMR spectra.

### Ventilation imaging

The simplest clinically relevant form of imaging HP gases is ventilation imaging. This is where the size of the signal produced by the gas is proportional to the density of the HP gas. This allows a map of the lungs to be created that show ventilation defects where the gas is not able to travel. This lack of signal could be caused by several different conditions like COPD, Asthma or CF. Ventilation images make it possible to quantify how the condition is affecting the ventilation ability of the lungs.  ${}^{129}\text{Xe}$  has a greater sensitivity to ventilation defects compared to  ${}^3\text{He}$  as it is denser and has a lower diffusion coefficient [107].



The sequences used in HP MRI need to be designed to fit into the time scale of a typical breath-hold of  $\approx 10$ s. As the polarisation in HP is non-recoverable, it is essential to exploit the signal as quickly and efficiently as possible to get the best images. The most widely used sequences are Fast Gradient Echo Sequences (FGE) [108]. These use short echo times with a short TR. Typically, these have a low flip angle so as not to deplete the polarisation before the entire image has been built up. Figure 2.13 shows the difference between a healthy lung and one with COPD and shows the ventilation defects caused by COPD.

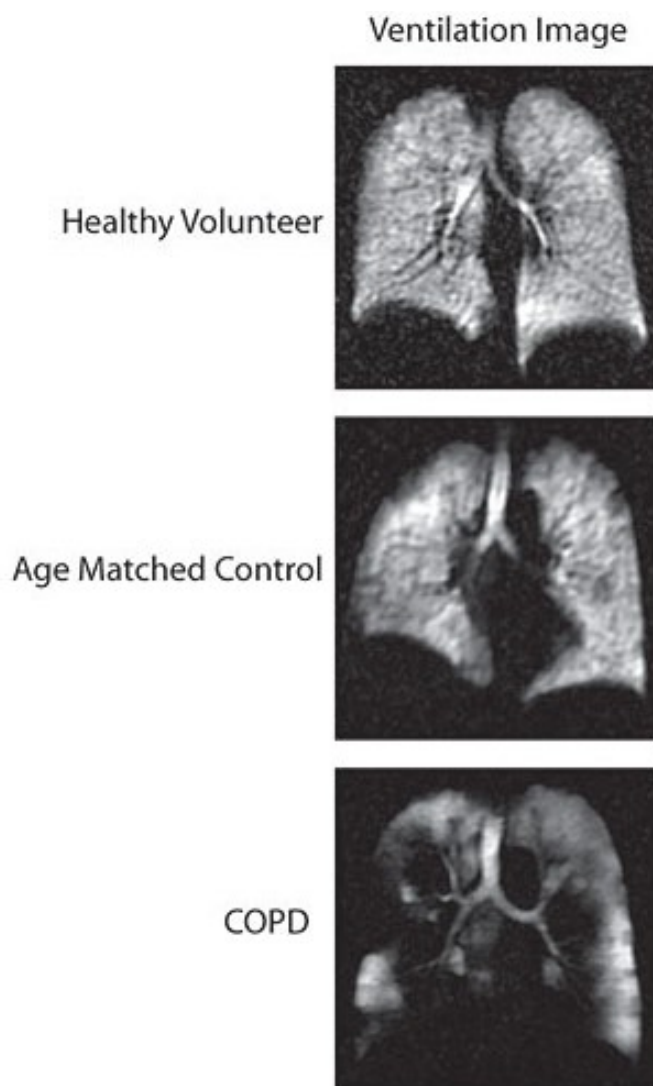


Figure 2.13: Comparison of HP MRI ventilation imaging between a patient with COPD and a healthy volunteer. [109]

## Diffusion-weighted imaging

Diffusion-weighted imaging (DWI) with HP gas allows an image to be built up, showing how the gas is able to diffuse through the structures in the lungs. This is visualised with an apparent diffusion coefficient (ADC) image of the lungs. This is because there is restricted diffusion between the microstructure of the lungs, such as the alveoli. An ADC image is built up by acquiring images of the HP gas both with and without diffusion-sensitising gradients applied. Diffusion-sensitising gradients are a pair of gradients of equal magnitude with opposite polarity. If a nucleus remains in the same place between the application of these two pulses, it will have no net shift in phase. When particles move between these two pulses, they will experience a phase shift. This is because they will not experience the same gradient strength on the reversed gradient. The degree to which the final image is sensitive to molecular motion can be changed by adjusting the strength of the diffusion gradient pulses and the time between them. This is given by the b-value, shown in Equation (2.44).

$$b = \gamma^2 G^2 \delta^2 \left( \Delta - \frac{\delta}{3} \right) \quad (2.44)$$

- Gyromagnetic ratio:  $\gamma$
- Magnitude of the DW gradient pulses:  $G$
- Length of the DW gradient pulses:  $\delta$
- Time between the two DW gradient pulses:  $\Delta$

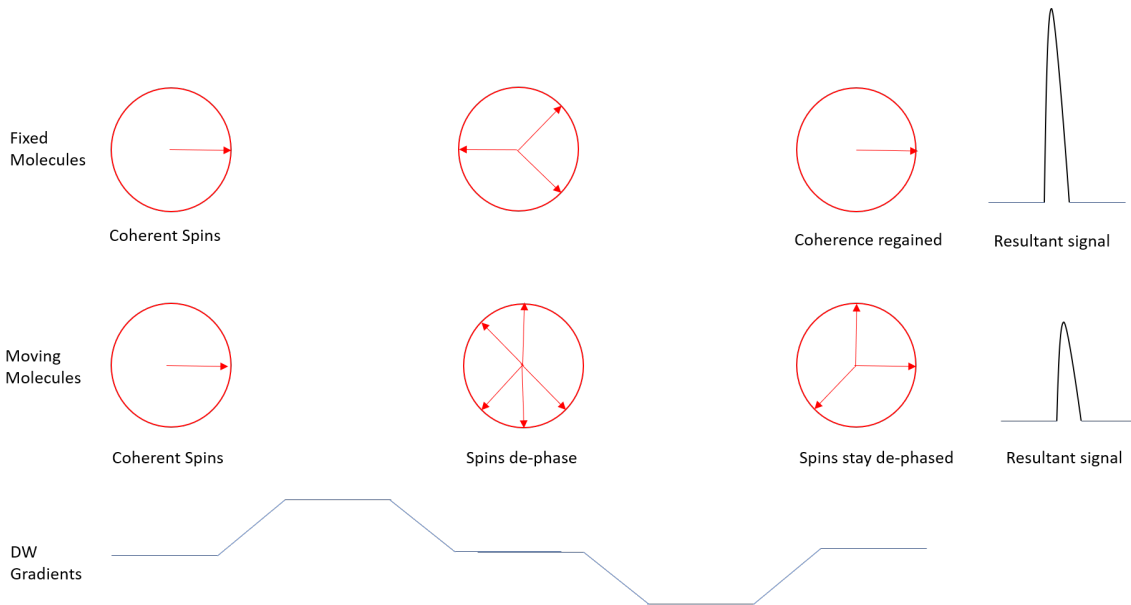


Figure 2.14: How DW gradients create dephasing in moving molecules

The lower the b-value, the less sensitive to diffusion the image will be. Higher b-value images will be more sensitive but there will be less signal as most of

the signal will be lost from molecular motion. Getting an ADC image requires comparing an image with a b-value of 0 and a b-value  $>0$  on a pixel-by-pixel basis [105].

$$S_D = S_{b=0}e^{-bD} \quad (2.45)$$

$$D = \frac{-1}{b} \ln \frac{S_D}{S_{b=0}} \quad (2.46)$$

- Signal intensity of image with non-zero DW gradient applied:  $S_D$
- Signal intensity of image with zero DW gradient applied:  $S_{b=0}$
- Apparent diffusion coefficient

In normal-functioning lungs, the diffusion is restricted between gas in neighbouring alveoli due to the structure of the alveoli. In diseases like emphysema, the gases are more able to diffuse as the internal lung structure has been enlarged, meaning higher ADC values will be seen than in a healthy lung [105]. The lungs of COPD patients can also exhibit elevated ADC values.

### Dissolved phase imaging

This type of HP-gas MRI can only be achieved with  $^{129}\text{Xe}$ , which can dissolve in pulmonary tissue. The chemical shift Xe experienced in the alveolar-capillary membrane is 198ppm and 217ppm in RBC. Compared to the gas phase, the dissolved phase intensity is  $\approx 2\%$ , and  $T_2^*$  relaxation is much quicker [110]. The chemical shift is also distinct but still fairly close at common clinical scanner field strengths ( $\approx 3.8\text{kHz}$  at 1.5T). This means that, to only excite the  $^{129}\text{Xe}$  in the dissolved phase, the RF excitation pulses must be well defined in frequency so as not to excite the gas phase  $^{129}\text{Xe}$ .

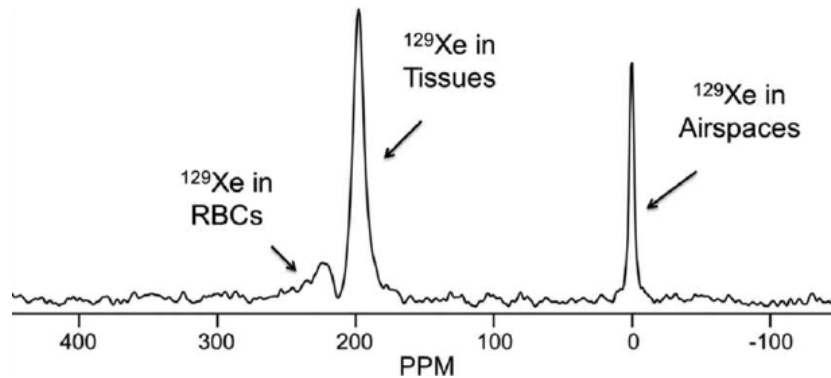


Figure 2.15: NMR Spectrum showing dissolved and gas-phase HP  $^{129}\text{Xe}$ , adapted from [111]

## Chapter 3

# Measuring in-cell temperature with Raman spectroscopy to understand optimal conditions of SEOP

### 3.1 Introduction

The polarisation of HP  $^{129}\text{Xe}$  must be maximised to produce the highest SNR images when performing MRI. The higher the SNR, the clearer the images and the more detail can be discerned, which are easier for clinicians to interpret leading to better diagnosis. To produce high SNR images, the bulk magnetisation of the HP  $^{129}\text{Xe}$  also needs to be high. The bulk magnetisation is the product of the percentage polarisation of HP  $^{129}\text{Xe}$  and the number of  $^{129}\text{Xe}$  nuclei within the gas mix. The number of nuclei scales linearly with the partial pressure of  $^{129}\text{Xe}$ .

To achieve a  $P_{Xe}$ , the conditions inside the optical cell where SEOP takes place must be optimised. One condition that can drastically affect the final  $P_{Xe}$  achieved using SEOP is temperature. The internal cell temperature plays a significant role in the final  $P_{Xe}$  as it determines whether SEOP of  $^{129}\text{Xe}$  is occurring in steady-state or runaway conditions. Under steady-state conditions, the  $P_{Xe}$  builds up at a relatively constant rate ( $\gamma_{SEOP}$ ) throughout a run and plateaus as the maximum  $P_{Xe}$  is reached. SEOP occurring in steady-state conditions is typically stable and less sensitive to fluctuations in pump laser power and oven temperature. Runaway conditions, on the other hand, are much less stable, and although they exhibit a greater initial  $\gamma_{SEOP}$ , they have larger spin-destruction effects compared to steady-state conditions, so the maximum  $P_{Xe}$  is more limited.

Runaway is entered as a result of a positive feedback loop between in-cell temperature, alkali metal vapour density and pump laser absorption. As described in Section 2.4.9,  $N_2$  collisionally quenches the emission of unpolarised photons during spin-exchange. This quenching causes energy to build up inside the  $N_2$  atoms, which becomes heat energy and increases the in-cell temperature.

An increase in in-cell temperature results in an increased alkali metal vapour density, which in turn absorbs more laser pump light. This creates the positive feedback loop, which becomes uncontrollable, hence the term runaway. This feedback loop continues to raise the alkali metal vapour density, making the cell less transparent to the pump laser. This means less alkali metal vapour atoms will be optically pumped, reducing the overall alkali metal polarisation and in turn  $P_{Xe}$ . Runaway conditions are characterised by an initial sharp increase in  $P_{Xe}$ , taking advantage of the high alkali metal vapour density and polarisation. The  $P_{Xe}$  peaks and starts to reduce as the feedback loop causes the cell to become more opaque to the pump laser, increasing spin destruction effects which outpace the  $\gamma_{SE}$ .

The optimal oven temperature, and therefore in-cell temperature, for a cell undergoing SEOP is where the cell reaches the maximum  $P_{Xe}$  while still under steady-state conditions. Higher peak  $P_{Xe}$  can be achieved in runaway regimes, but they are short-lived. Optimal in-cell temperatures sit near the limit of steady-state conditions before they enter runaway. Near this limit, the temperature is able to produce a high enough alkali metal vapour density for high alkali metal polarisation and thus high  $\gamma_{SEOP}$  and  $P_{Xe}$ . There is a fine line between steady-state and runaway conditions, meaning it is advantageous to measure the internal cell temperature when trying to determine the optimal SEOP conditions.

Although the temperature of the cell can be measured externally with a thermocouple, this does not give an accurate representation of the temperature within the gas volume inside the cell. Furthermore, a thermocouple can only measure the temperature at a single location, which gives an estimated global value. To better understand the conditions within the cell, the internal gas temperature needs to be interrogated. This can be achieved using a technique called Raman spectroscopy, which measures the  $N_2$  gas temperature directly, allowing a more accurate comparison of internal cell temperature under a variety of SEOP conditions. It is also possible to measure how the  $P_{Xe}$  changes with internal cell temperature by measuring it concurrently using NMR.

This chapter starts by covering the theory behind calculating the internal  $N_2$  gas temperature using Raman spectroscopy at different locations throughout the cell. It then goes on to describe the methods and equipment used in the experiment set out in this chapter. Lastly, the results of each experiment are discussed, investigating the effects of different gas mixes, alkali metal species and lasers on the internal cell temperature and  $P_{Xe}$ .

## 3.2 Theory

### 3.2.1 Raman spectroscopy

#### Raman scattering

When a photon of a specific frequency is scattered by a molecule transfers energy to the molecule's electron cloud. This distorts the cloud and excites the molecule into a higher vibrational or rotational energy state. The vibrational energy states occur due to intermolecular bonds behaving like harmonic oscillators. The rotational energy states occur due to the rotation about the molecule's centre

of mass. These higher virtual energy states are unstable, and the molecule will eventually relax back to a lower-energy state. When this relaxation occurs, the photon is re-radiated. In most cases, the molecule relaxes back to its original energy state, causing the radiated photon to have the same energy and frequency as the original incident photon. The photon's energy is conserved, so it is said to have scattered elastically, known as Rayleigh scattering [112].

When a molecule returns to a different vibrational or rotational energy state, the radiated photon has a different energy and frequency to the incident photon. This phenomenon is known as Raman scattering, first discovered by CV Raman in 1928 [113]. Raman scattering comes in two forms: Stokes and anti-Stokes Raman scattering. Stokes Raman scattering is when a molecule returns to a rovibrational state with a higher energy [113]. As the total energy of the molecule-photon system is conserved, the radiated photon has a lower energy. Anti-Stokes scattering is when the molecule relaxes to a lower energy rovibrational state than its original [113]. The radiated photon, therefore, has more energy than the incident photon. A diagram showing Rayleigh and Raman scattering is shown in Figure 3.1 [114].

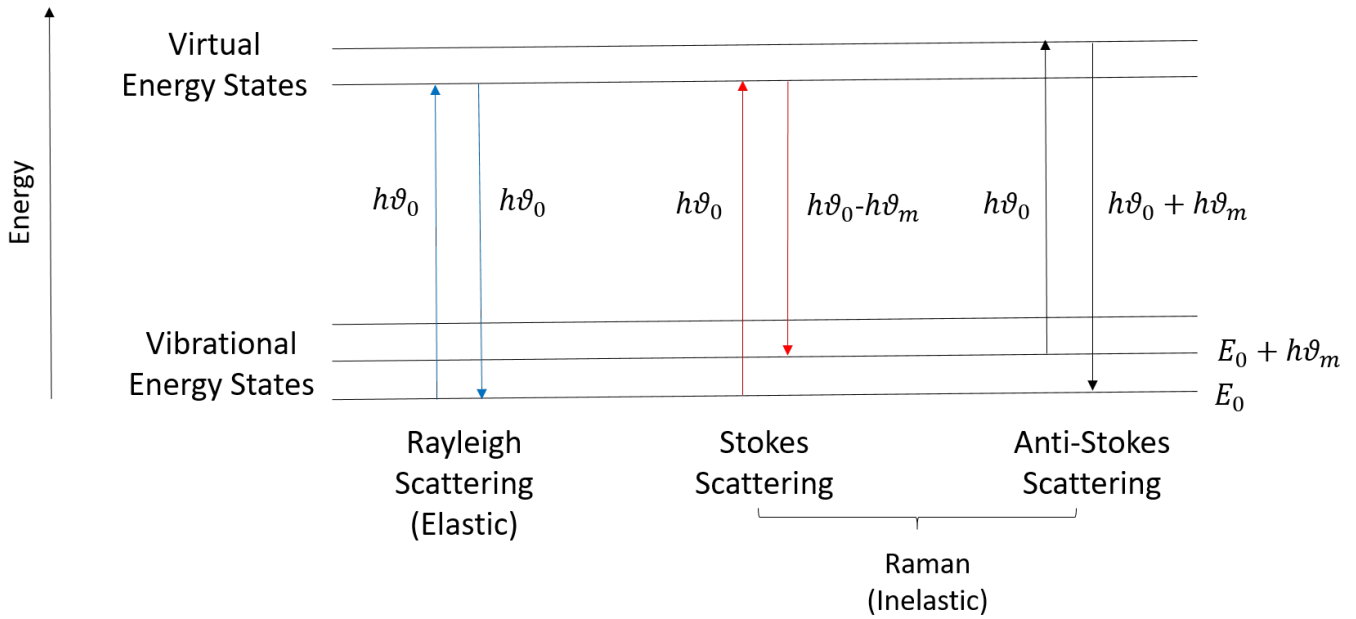


Figure 3.1: Diagram of the Rayleigh and Raman scattering processes [114]

### Raman spectra

A Raman spectrometer detects photons scattered by a sample and creates a Raman spectrum by plotting the light intensity of the scattered photons against the size of the “Raman shift” between scattered and incident photons. The size of the Raman shift is shown in Equation (3.1).  $\lambda_2$  and  $\lambda_1$  are the wavelengths of the scattered and incident light, respectively, in nanometres.

$$Raman.Shift(cm^{-1}) = \left(\frac{1}{\lambda_1} - \frac{1}{\lambda_2}\right)[114] \quad (3.1)$$

Raman shift is used because the wavenumber ( $1/\lambda$ ) scales linearly with energy. The resultant spectrum is therefore independent of the incident light's wavelength [114].

### Measuring $N_2$ temperature using Raman spectroscopy

In a Raman spectrum, the vast majority of photons are Rayleigh scattered, up to  $10^8$  times the number Raman scattered. The ratio of Stokes to anti-Stokes Raman scattering depends on the energy state populations of the sample molecules. At room temperature, the ground state is the most energetically favourable, so has the highest population. When a ground-state electron is excited, there is no lower energy state to relax back into, and the photon, therefore, can only experience Stokes scattering. At ambient temperature, there is a slight excess of electrons in the ground state, so the intensity of the Stokes peaks is higher than that of the anti-Stokes peaks since more molecules cannot experience anti-Stokes scattering. This discrepancy reduces as temperature increases as molecules inhabit higher energy levels and the populations of in the lower energy levels reduce. This results in a change in peak heights in the rotational Raman spectrum as shown in Figure 3.3.

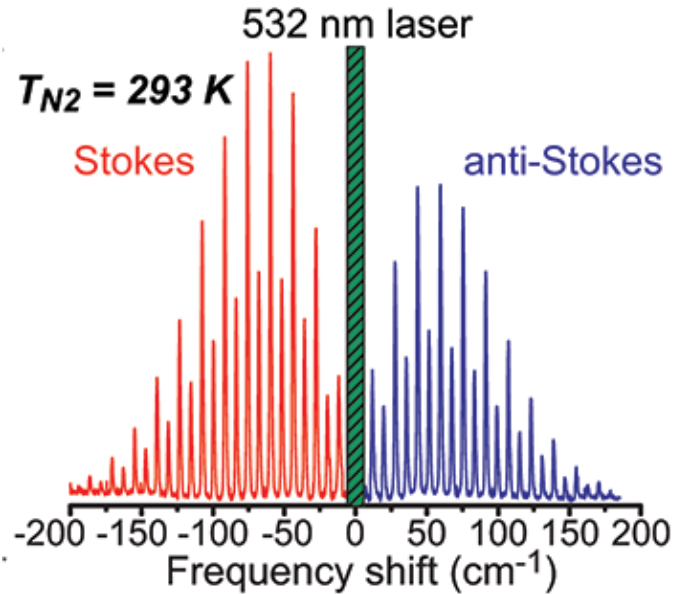


Figure 3.2: An example  $N_2$  Raman spectra taken at 293 K [115]

A feature of the  $N_2$  Raman spectrum is the alternation of half- and full-height peaks, which occur because  $^{14}\text{N}$  is a boson. The peaks are a result of the exchange interaction/quantum mechanical selection rules that are dependent on a molecule's molecular spin quantum number (I). These rules are governed by the Pauli exclusion principle, which states that no identical fermions can have

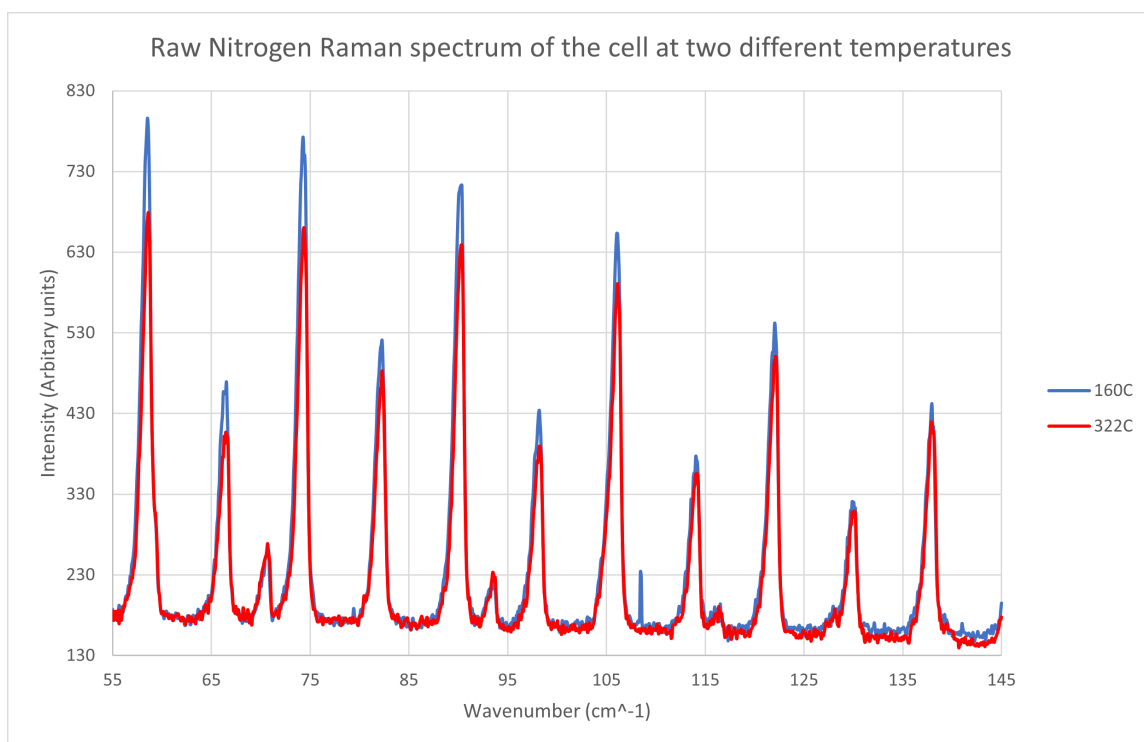


Figure 3.3: Two raw  $N_2$  Raman spectrum taken at 160 C and 322 C to show how the increase in temperature changes the relative peak heights of the rotational Raman peaks



the same quantum state. In a system, no two fermions can have the same value for all four of their quantum numbers at the same time [27]. The I value of a boson can only be an integer value or zero, while fermions can only be a half-integer I. Under particle exchange, the total wave-function of a fermion has to be anti-symmetric. A boson's wave function under particle exchange meanwhile must be symmetric. The total wave function for  $N_2$  is given below.

$$\Psi_{tot}(R_1R_2r_ar_aI_1I_2s_as_b) = \psi_e(r_ar_b)\chi_e(s_as_b)\psi_n(R_1R_2)\chi_n(I_1I_2) \quad (3.2)$$

- $r_ar_b$ : Electron locations
- $\psi_e(r_ar_b)$ : Electronic spatial component of the molecular wave function
- $s_as_b$ : Electron spins
- $\chi_e(s_as_b)$ : Electron spin component of the molecular wavefunction
- $R_1R_2$ : Nuclear coordinates
- $\psi_n(R_1R_2)$ : Nuclear spatial component of the molecular wavefunction
- $I_1I_2$ : Nuclear spin coordinates
- $\chi_n(I_1I_2)$ : Nuclear spin component of the molecular wavefunction

$\psi_n(R_1R_2)$  is the product of the rotational and vibrational terms. Under particle exchange, the vibrational term is symmetric in the ground state and reduces to zero. The resultant spectra of  $N_2$  is therefore purely rotational.

$$\phi_n = \phi_n^{vib}\phi_n^{rot} \quad (3.3)$$

$^{14}N$  has an I=1, meaning the molecular spin ( $I_{tot}$ ) of  $N_2$  can take three values: 0, 1 and 2 [116]. The electronic contribution of the molecular wave function must be symmetric under particle exchange, and, since the total wave function of a boson is symmetric, the nuclear component must also be symmetric. Thus, the rotational angular momentum quantum number (J) is even when  $I_{tot}$  is even (0 or 2). This results in a total spin multiplicity ( $\Sigma(2(I_{tot}) + 1)$ ) of  $(2(2) + 1) + (2(0) + 1) = 5 + 1 = 6$  [116]. When I is odd (1), only odd J values are allowed, and the spin multiplicity is  $2(1) + 1 = 3$ . This is displayed in the  $N_2$  Raman spectrum as the 2:1 ratio between even and odd J peaks [116].

The first in-depth analysis of the rotational temperature using Raman spectroscopy of  $N_2$  was carried out by Hickman et al. [117]. In  $N_2$  the rotational temperature is equal to its translational temperature. The technique compares line intensity (I(J)) from a transition (J) against the signal received by the spectrometer.

$$S(J) = GI(J) \quad (3.4)$$

In Equation (3.4), G is a constant of proportionality which contains all experimental constants, described by D. Walter et al. [118]. These include:

- Cross-section of the transition
- Nitrogen gas volume

- Photon scattering cross-section
- Probe-beam intensity

The line intensity of the ro-vibrational spectrum from a  $J$  to  $J'$  state conforms to the following relationship:

$$I(J) \propto v^4 g(2J+1) P_{J \rightarrow J'} e^{-\frac{BJ(J+1)}{k_B T}} \quad (3.5)$$

- $v$ : Frequency of the rotational line
- $J$ : Rotational angular momentum quantum number
- $g$ : Ground state degeneracy from nuclear spin
- $B$ : Nitrogen's rotational constant
- $k_B$ : Boltzmann constant

The rotational transitions  $N_2$  obey the following selection rule,  $\Delta J = +2$ , as the spectra is purely from Stokes scattering, for anti-Stokes scattering  $\Delta J = -2$ .

$$P_{J \rightarrow J'} = \frac{(3(J+1)(J+2))}{(2(2J+3)(2J+1))} \quad (3.6)$$

It is possible to eliminate the proportionality constant in equation (3.5), defined as  $1/G$ . This is the same  $G$  stated in (3.4), which cancels down to Equation (3.7).

$$S(J) = I(J)G \quad (3.7)$$

Substituting in the values from equations (3.6) and (3.5) gives:

$$S(J) = v^4 g(2J+1) e^{-\frac{BJ(J+1)}{k_B T}} \frac{(3(J+1)(J+2))}{(2(2J+3)(2J+1))} \quad (3.8)$$

Which can cancel to:

$$S(J) = v^4 g e^{-\frac{BJ(J+1)}{k_B T}} \frac{(3(J+1)(J+2))}{(2(2J+3))} \quad (3.9)$$

Equation (3.9) can be simplified using:

$$f(J) = \frac{(3(J+1)(J+2))}{(2(2J+3))} \quad (3.10)$$

This leads to the simplified version of (3.8):

$$S(J) = v^4 g f(J) e^{-\frac{BJ(J+1)}{k_B T}} \quad (3.11)$$

This can be rearranged to give:

$$-J(J+1) \frac{Bhc}{k_b T} = \ln \frac{S(J)}{gf(J)} + 4 \ln \frac{1}{v} \quad (3.12)$$

This equation can be compared to a straight line on a xy plot, rearranging (3.12) to the same format as  $y = mx + c$  with  $g=1$  will give:

$$\ln \frac{S(J)}{f(J)} = -\frac{Bhc}{k_B T} J(J+1) - 4 \ln \frac{1}{v} \quad (3.13)$$

Plotting  $\ln \frac{S(J)}{f(J)}$  against  $J(J+1)$  even Stokes line peaks ( $J = 6, 8, 10, 12, 14, 16$ ) will give a graph similar to 3.4. The slope of the line is equal to  $-\frac{Bhc}{k_b T}$ . It is then possible to calculate the temperature ( $T$ ) of a  $N_2$  gas using Raman spectroscopy. The odd peaks are not used as they would have to be scaled up by 2 and so would the resultant noise. This would reduce the SNR of the system and increasing the uncertainty in the final measurement which is  $\frac{1}{SNR}$  [117].

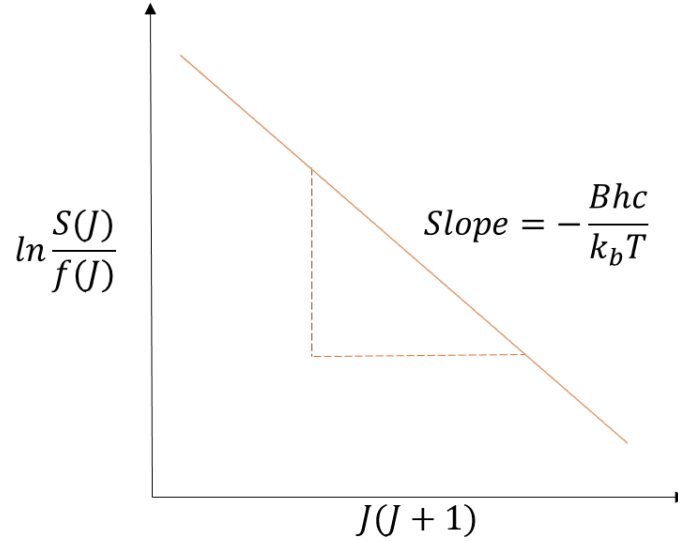


Figure 3.4: Illustration of how the  $N_2$  Raman temperature can be calculated [115]

### 3.3 Materials and methods

#### 3.3.1 SEOP materials

##### Lasers and optics

Three OP lasers are used in the experiments detailed in this chapter: A 30 W laser at 794 nm (Integra, Spectra physics, Irvine, USA), another 30 W laser at 794 nm (Ultra100 BrightLock, QPC, Sylmar California, USA) and a 50 W laser (Ultra100 BrightLock, QPC, Sylmar California, USA). All three OP lasers are frequency narrowed to  $\approx 0.3$  nm FWHM. The QPC lasers are powered by a Sorensen-XG programmable power supply, and the Integra has an internal power supply controlled remotely via the Integrasoft software. The temperature of the QPC lasers is controlled by an external water chiller that flows water through

integrated cooling plates in the lasers' base. By thermally tuning an on-chip grating, the central wavelength can be adjusted by  $\pm 1$  nm to better match the laser's output with the Rb/Cs  $D_1$  lines. The Integra's parameters are adjusted via Integrasoft, and it is also thermally tuned by laser power heating its glass variable Bragg grating (VGB) to adjust the laser's central wavelength.

The appropriate OP laser was selected for each experiment. The first test examined the consistency of the experimental setup using the Rb BrightLock laser. This laser was also used in the experiment that investigated the ability of  $^4\text{He}$  to suppress Rb runaway during SEOP. For the Cs vs Rb Raman experiments, the Cs BrightLock was used to optically pump the Cs, and the Rb was optically pumped using the Integra.

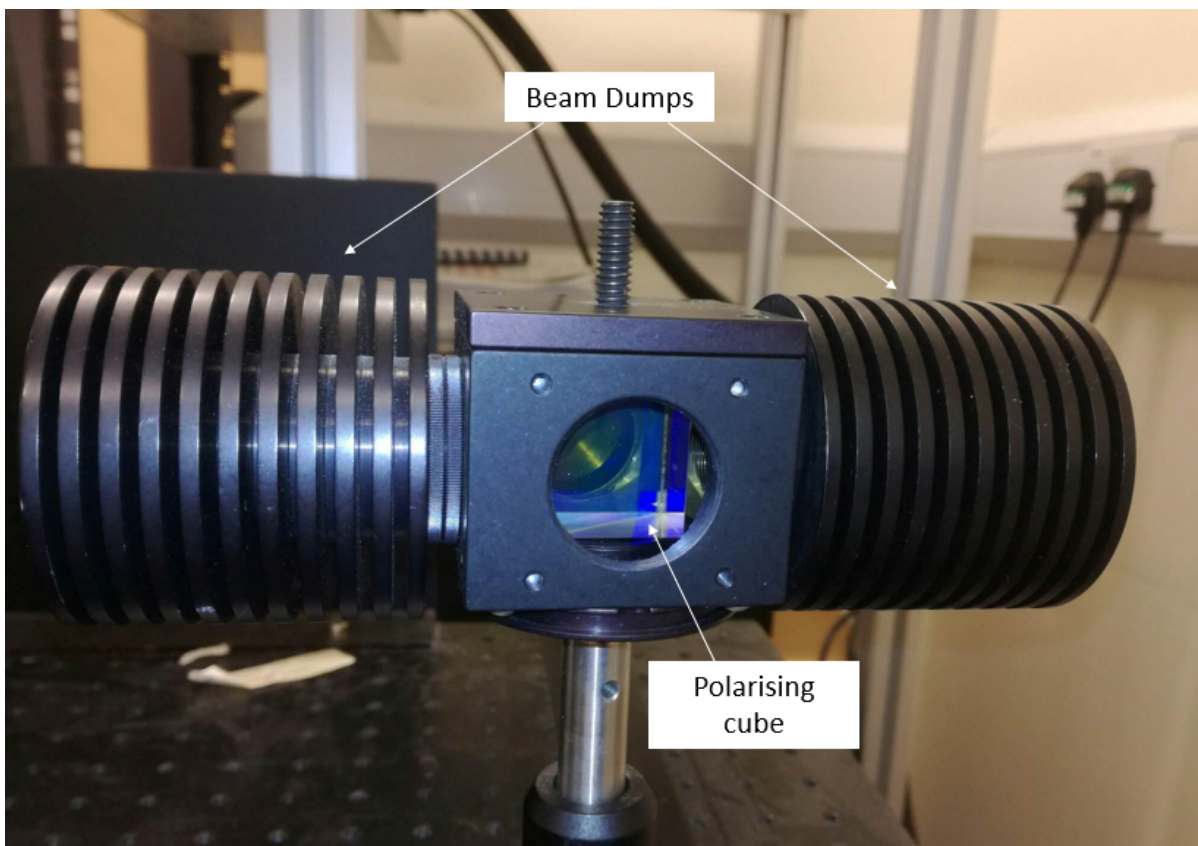


Figure 3.5: Polarising cube with beam dumps sitting at 90 degrees either side. Only one Beam dump is used to capture rejected OP laser light. The other is to balance the setup to ensure the weight is not all on one side and no spurious reflections exit that hole in the polarising cube holder.

After the laser light leaves the pump laser cavity, it passes through an optical fibre. Upon leaving the fibre, the photons then pass through a collimating lens to give the beam a 1-inch diameter. The diameter of the beam now matches the diameter of the inner cell of the Rosen cell, therefore uniformly illuminating the gas mix across the cell's diameter. After collimation, the photons need to be circularly polarised to perform SEOP, as shown in Section 2.4.7. The collimated

light passes through a polarising cube that cleans up the linear polarisation of the laser light. This light then passes through the  $\frac{\lambda}{4}$  wave-plate. The wave plate converts the linearly polarised light into circularly polarised light before it reaches the cell. The  $\frac{\lambda}{4}$  wave plate/polarising cube set-up is shown in Figure 3.6.

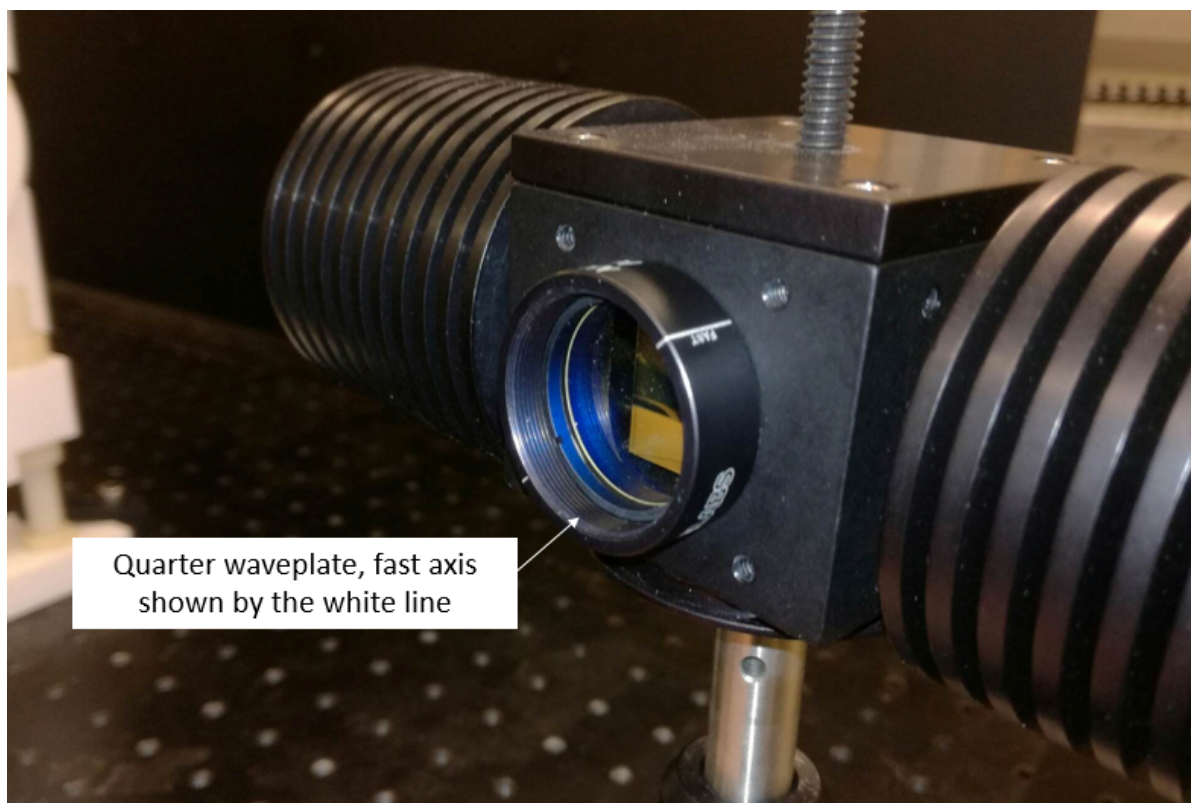


Figure 3.6:  $\frac{\lambda}{4}$  placed after the polarising cube in the optical train. It turns the linearly polarised light into circularly polarised light for OP

### **$B_0$ field and NMR spectroscopy**

The homogeneous magnetic field required for SEOP is provided by two coils set up in a Helmholtz pair. Each coil has 197 turns and a 32-inch diameter and is powered by a Sorenson XG20-81 programmable power supply. The XG20-81 provides an 8.9 A current to coils to achieve the desired  $B_0$  field strength for  $^{129}\text{Xe}$  NMR spectroscopy. When collecting a water signal, the current is adjusted to 2.5 A. This is to ensure the Larmor frequency of  $^{129}\text{Xe}$  is the same as the optimum frequency of the NMR search coils (34.4 kHz). The gyromagnetic ratios of  $^1\text{H}$  and  $^{129}\text{Xe}$  are known:  $42.5759 \frac{\delta}{\text{MHz}\cdot\text{T}^{-1}}$  and  $-11.7769 \frac{\delta}{\text{MHz}\cdot\text{T}^{-1}}$ , respectively. The  $B_0$  strength is altered by adjusting the current going through the coils the ratio of the gyromagnetic ratios so that both nuclei can be pulsed at the optimum frequency of the search coil (34.4 kHz). The corresponding  $B_0$  field strength for  $^1\text{H}$  and  $^{129}\text{Xe}$  are 8.1 G and 29.2 G, respectively.

NMR spectroscopy is performed by three 1-inch diameter 350-turn surface coils. These are mounted in a 3D-printed plastic housing so that they fit into the optical cell (see Figure 3.7). NMR signals can be acquired at the front, middle and back of the optical cell. The NMR coils are connected to a Magritek Kea2 spectrometer, which is controlled via USB using a software package called "Prospa". The search coils both transmit NMR pulses to excite the HP  $^{129}\text{Xe}$  and receive the resultant NMR signal produced by the  $^{129}\text{Xe}$  using the Kea2 "1Pulse" experiment. When Prospa receives the NMR signal via the Kea2, it is saved to the computer for analysis.

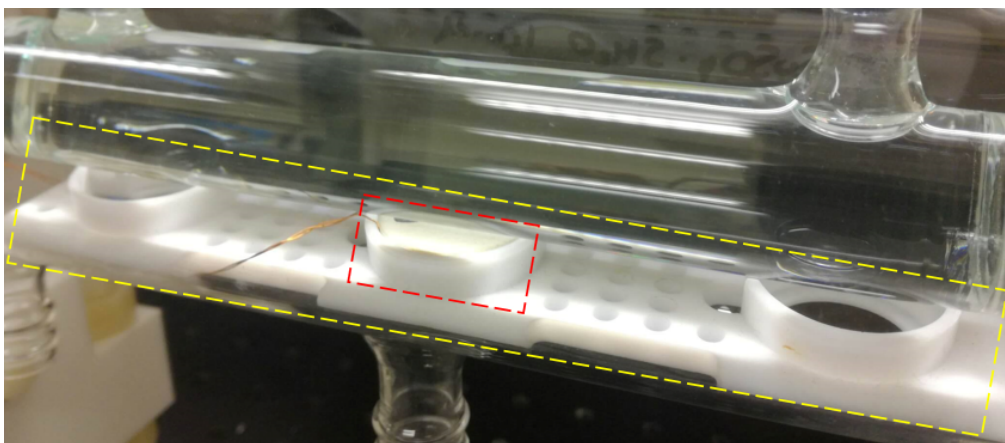


Figure 3.7: NMR coil holder (yellow box), containing a single NMR coil (red box) in a cell filled with doped water used to obtain a reference signal.

### Optical cell and oven

The final components of the SEOP apparatus are the optical cell and oven system. The optical cell is a variation of a Pyrex Rosen cell [119] and comprises three main parts: the inner and outer cylindrical sections and the valve stems.

The inner cell is 16.5 cm long and has a diameter of 2.5 cm, while the outer cell has a length of 28 cm and a diameter of 6.5 cm. The inner cell is where the Rb/Cs is loaded, and it is filled with the gas mix, providing a sealed environment for SEOP. Flat optical windows are situated at either end of the inner cell to minimise light diffraction and maximise the light transmitted to the alkali metal vapour. The cell is mounted in an adjustable plastic mounting system which aligns the cell with the pump laser. Since the mounting system can be left in place, realignment is not needed should the cell be replaced or removed for gas filling.

The outer cell is capped off with two circular anti-reflection coated windows mounted in a plastic frame, which act to reduce optical losses when transmitting light to the cell. The windows act as an interface between the cell and the mounting system. They also enclose the outer cell so it can be used as the oven for the inner cell.

To transform the outer cell into an oven, a compressor is used to force air through a heat pipe and into the outer cell via a stem on its underside.

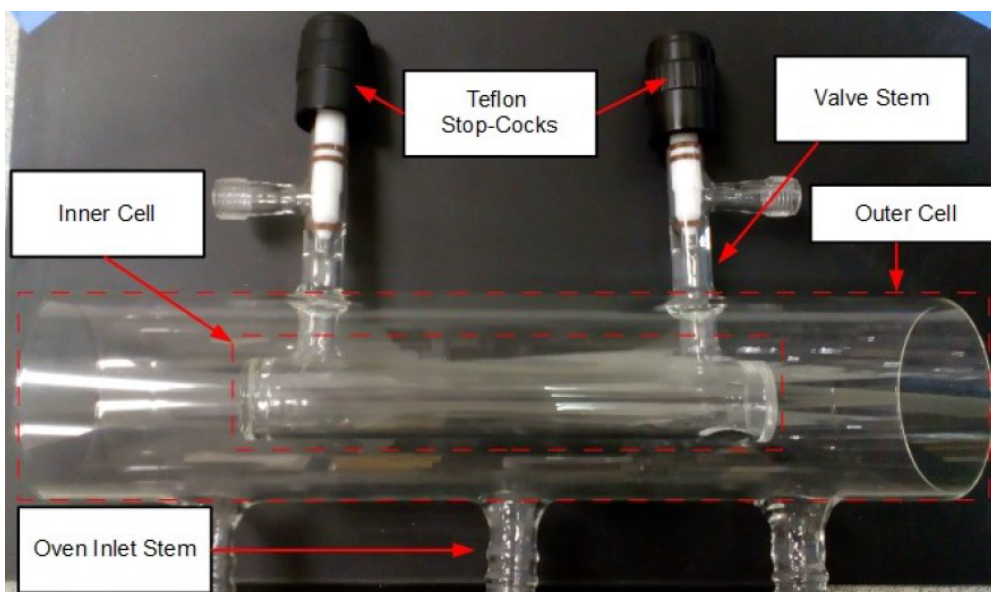


Figure 3.8: A typical Rosen cell used in the SEOP experiments

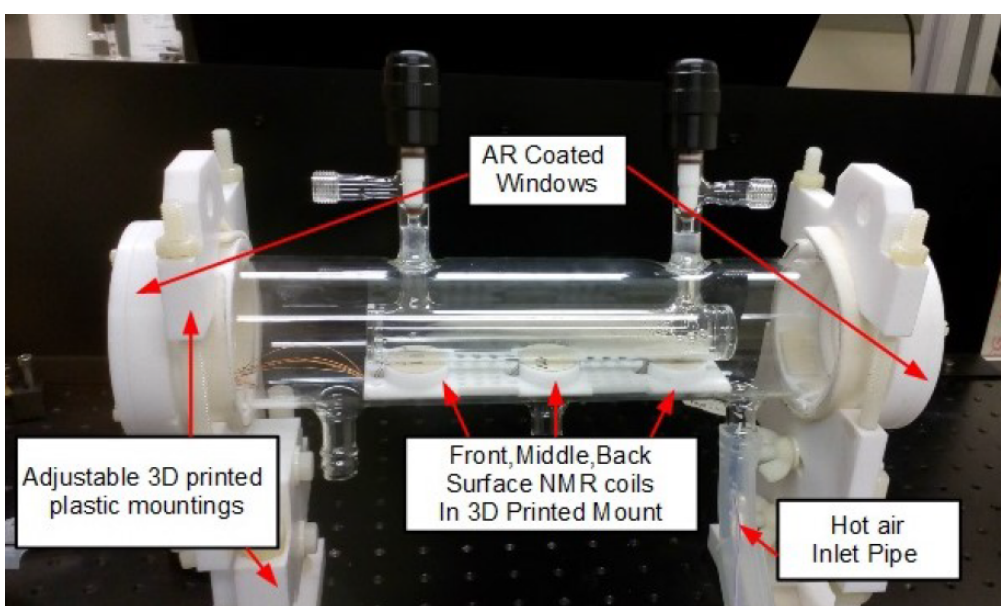


Figure 3.9: A loaded and mounted Rosen cell ready for SEOP

The temperature of the hot air is controlled by a heat pipe controller based around a CAL9000 temperature controller, a proportional–integral–derivative (PID) controller. The CAL9000 in this setup only uses the "P". It continuously calculates the difference between the setpoint and the current measured value and then applies a correction to reach that set point [120]. The oven temperature set point can then be reached with minimal over/undershoot based on feedback

from a PT100 temperature sensor. The sensor is placed in the middle inlet stem at the bottom of the outer cell, where the hot air inlet pipe is connected. When the oven temperature is raised, the Rb/Cs is vaporised and can be optically pumped via the OP laser.

### Raman materials

The Raman portion of the experiment is based on the setup presented in the thesis of H. Newton [121], book chapter by J. Birchall [115] and a paper by H. Newton [122]. It is built around a 5W laser at 532 nm (Verdi-V5, Coherent, Santa Clara, USA). Raman scattering efficiency increases with  $\frac{1}{\lambda^4}$  which reduces the scan time required to collect spectrum with useable SNR [123]. Short wavelengths also come with increased spatial resolution, which is needed for the  $N_2$  rotational Raman spectra measured where the peaks are close together. Shorter wavelengths produce more autofluorescence from the target compared to longer wavelengths increasing SNR. [123] 532 nm was selected as it offered the best compromise between the two.

After leaving the Verdi, the photons pass through an optical fibre to an in-line Ondax probe head, shown in Figure 3.10. A 1-inch lens focuses the photons into the centre of the inner cell, where they scatter off the  $N_2$  in the gas mix. The scattered photons are then collected via the same optical path as the incident photons. The ultra NB notch filters within the probe head attenuate the photons that have been Rayleigh scattered from the  $N_2$ . Rayleigh-scattered photons make up the vast majority of the spectra [124]. These Rayleigh-scattered photons need to be attenuated, or the Raman spectrometer’s charge-coupled device (CCD) would become saturated, leaving the Raman scattered photons undetectable. The photons then pass through a beam splitter, directing them into a fibre optic cable linked to the spectrometer’s CCD for detection.

The probe head is orthogonal to the main pump beam so the temperature can be measured at different positions along the length of the cell. Vertical alignment of the Ondax Raman probe head is performed by a ThorLabs height-adjustable platform.

The adjustable platform is then mounted to a ThorLabs’ LTS300(/M) Linear Translation Stage (LTS) with an integrated controller. The LTS moves the probe head horizontally to any part of the cell with a 0.01 mm accuracy. Throughout an SEOP experiment, the stage can automatically move the Ondax raman probe head using the “Move sequencer” on the ThorLabs’ inbuilt software. The stage, however, must be placed outside of the Helmholtz coils as it has ferrous components that significantly disturb the homogeneity of the field. The LTS therefore had to be mounted off the bench using a sliding ThorLabs optical breadboard. The breadboard can move the probe head perpendicular to the cell to measure the gas temperature across the cell’s diameter. To compensate for being mounted outside of the magnetic field, the 50 mm focal-length plano-convex lens had to be mounted on the end of a lens tube, keeping the Verdi laser’s focal point in the inner cell.

The probe head is connected to a Horiba Jobin Yvon U1000 double one-metre spectrometer with Andor Newton EM CCD via an optical fibre. The Horiba is controlled via the software “LabSpec”, which can be used to save, edit and export the resultant Raman spectra.



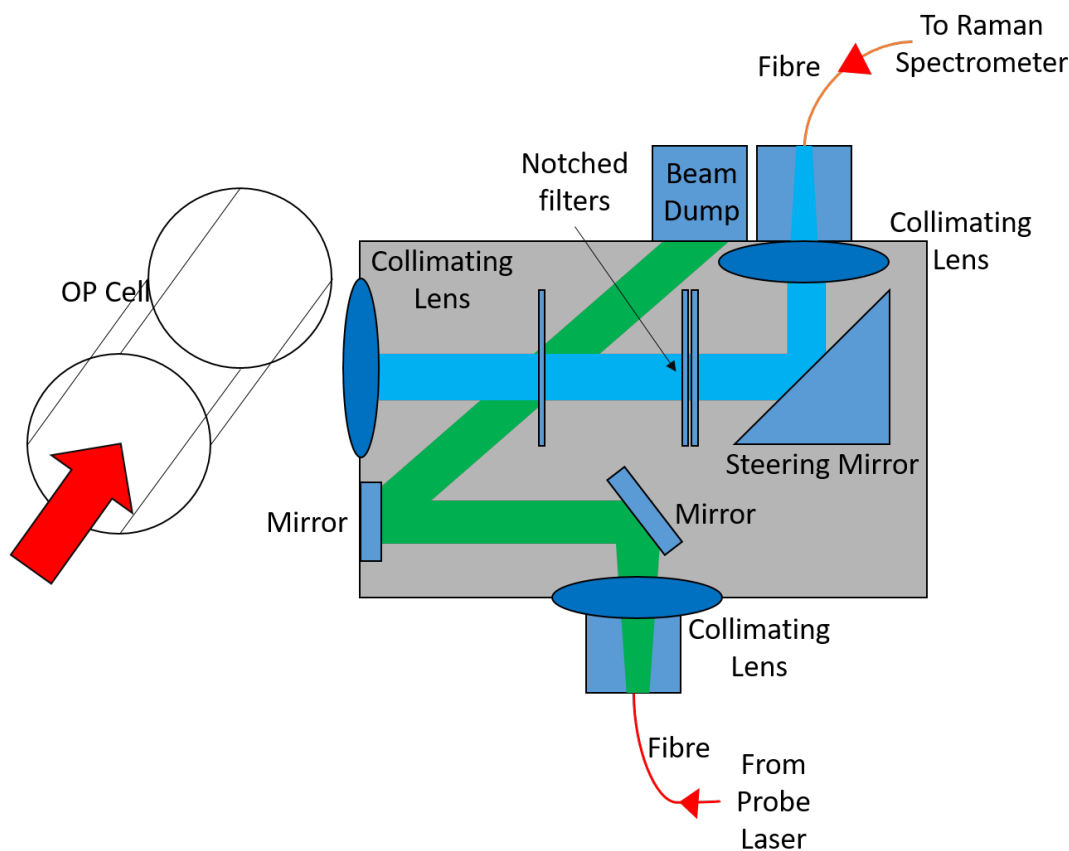


Figure 3.10: Ondax head schematic

### 3.3.2 NMR methods

#### Data collection

The NMR surface coils are inserted into the outer cell underneath the inner cell. Using the Prospa V3.1 software, the user can then select the appropriate settings for the Kea2 pulse/receive sequence, and a directory is created for the experimental data to be saved. The NMR spectrum can now be collected by toggling the three-way switch to the appropriate coil and running the desired sequence. It is important to have a long enough delay time between transmitting the NMR pulse and receiving the signal so that the coil does not pick up the ringdown from its own transmission pulse. A  $3000 \mu\text{s}$  acquisition delay (delay time) was selected as it marginally longer than the coil's ringdown time and the  $T_2^*$  of the  $^{129}\text{Xe}$  was long enough to still be able to detect NMR signals with high SNRs.

In later Raman experiments, the NMR data acquisition, the saving of the spectra in the correct folder and the coil switching have all been automated. This modification was carried out by W. Hardiman and J. Botham for their final year Master's project and details can be found in their final report [125]. It is

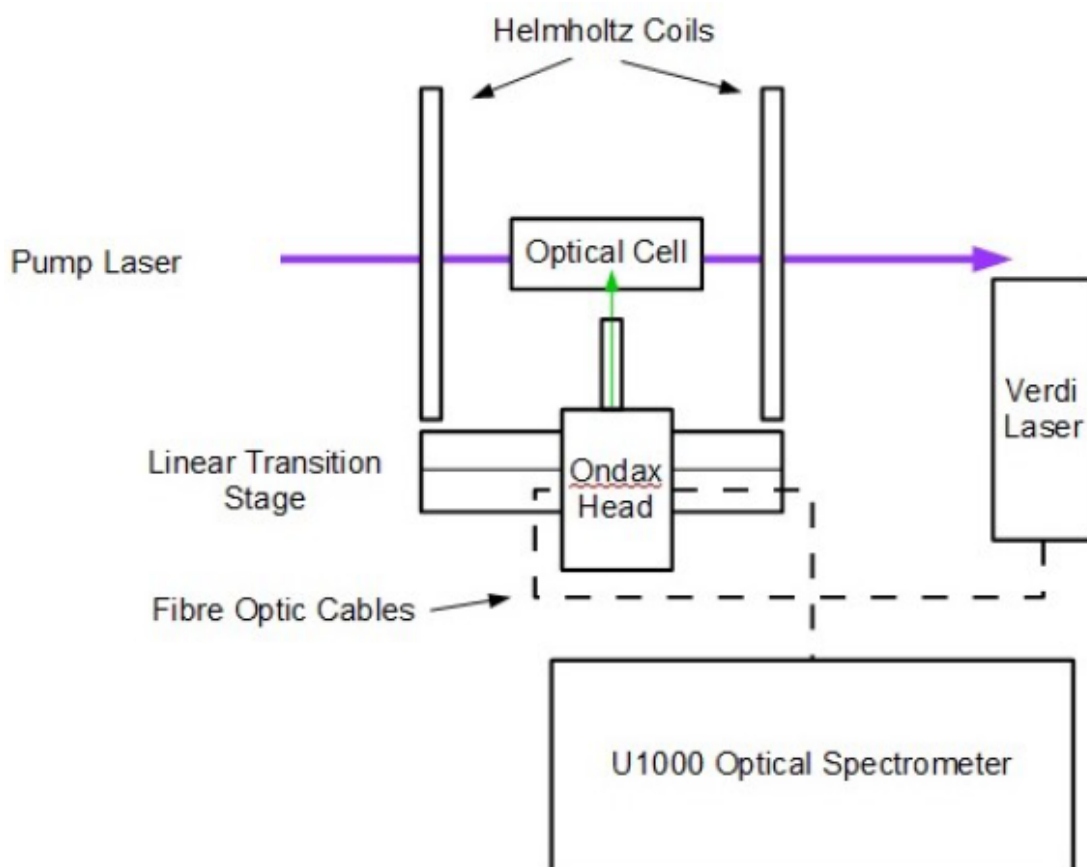


Figure 3.11: Diagram of the Raman setup

based around an Arduino Mega 2560 and an automated Mini Circuits MSP4TA-18+ switch, all controlled via an app created in MATLAB. The automation eliminates human error and effort when switching between coils.

### Obtaining a water signal

In order to calculate the percentage polarisation of the HP  $^{129}\text{Xe}$ , it is necessary to compare the NMR signal from the HP  $^{129}\text{Xe}$  to a reference proton ( $^1\text{H}$ ) signal. The  $^1\text{H}$  spectra must be taken at thermal equilibrium. The  $^1\text{H}$  signal is acquired using a water sample doped with 10 mM copper sulphate ( $\text{CuSO}_4$ ) ( $\approx 0.11$  g). The NMR signal comes from  $^1\text{H}$  in the water ( $\text{H}_2\text{O}$ ), the  $\text{CuSO}_4$  acts to decrease the  $^1\text{H}$   $T_1$  relaxation time [126] to  $\approx 0.15\text{s}$ . As the nuclear spins of the  $^1\text{H}$  recover quicker, the time between acquisitions can be reduced. The Helmholtz coils produce a low  $B_0$  field strength, resulting in a very low  $^1\text{H}$  polarisation. The  $^1\text{H}$  NMR signal will therefore have a very low SNR, so multiple pulses need to be averaged to bring the signal out of the noise floor. An NMR signal is acquired every 0.6 s, equivalent to 4  $T_1$ s, allowing the  $^1\text{H}$  nuclei to fully relax between acquisitions. As each NMR pulse will have

the maximum signal from the  $^1H$ , fewer pulses have to be averaged to get an acceptable SNR. A reference water signal with acceptable SNR can be produced after  $\approx 10^5$  acquisitions. The water sample used is housed within the same Rosen cell as that used for  $^{129}Xe$  SEOP. This ensures that the volume and geometry of the water and  $^{129}Xe$  excited by the search coil is the same.

### Flip angle calibration

Flip angle calibrations require signals to be acquired at a range of pulse lengths or RF amplitudes (sweeps). A  $^1H$  flip angle calibration was performed using the Kea2 controlled by Prospa using the function ‘‘Pulse duration sweep’’. The signals from a sweep of RF pulses with different pulse durations are plotted on a sine curve to determine how the strength/length of the NMR pulse corresponds to the resultant flip angle of the affected nuclei. This sweep used the central surface coils to send pulses with lengths of  $\approx 80 \mu s$  to  $\approx 325 \mu s$ . After each acquisition in the sweep, the pulse length was increased by  $14.4 \mu s$  in order to get a larger enough number of points to fit the sine curve but which still allows the sweep to be taken in a reasonable amount of time. Due to limited time, the number of acquisitions is reduced to the order of  $10^4$  when acquiring multiple spectra for a flip angle calibration. Parameters common to all individual pulses within the sweep can be found below.

- Pulse amplitude: -6 dB
- Pulse acquisition delay time:  $3000 \mu s$
- Dwell time:  $20 \mu s$
- Number of points: 512
- Filter: Exponential

Figure 3.12 shows the resultant points fitted to a sine curve (adjusted  $R^2 = 0.99891$ ), with a pulse length of  $83 \mu s$  equating to a  $46^\circ$  flip angle pulse.

The for the pulse duration sweep for  $^{129}Xe$  to be accurate it must be taken when the polarisation is at a steady state, so the polarisation available for each pulse in the sweep is the same. As a fraction of the  $^{129}Xe$  is depolarised by the NMR pulse, the time between pulses must be long enough for the polarisation to recover via SEOP back to steady state, so the resultant signal’s peak height is only dependent on NMR pulse duration.

The cell was loaded with a 0.3 g bead of Rb and filled with a Xe/ $N_2$  gas mix. The gas mix underwent SEOP at an oven temperature of 160 C to build  $P_{Xe}$  up to a steady-state. The  $^{129}Xe$  was then subject to pulses with lengths from  $100 \mu s$  to  $450 \mu s$  in  $25 \mu s$  increments. All other parameters are equal to those listed for the water pulse duration sweep with  $\approx 30$  s between pulses. Even at high flip angles, the surface coil only stimulates  $^{129}Xe$  nuclei above the coil, meaning only a small fraction of the total number in the cell are depolarised. The time for the polarisation to recover is therefore short. The pulse duration sweep can be seen in Figure 3.12.

The  $^{129}Xe$  pulse duration sweep was also fitted to a sine curve (adjusted  $R^2 = 0.991$ ). A pulse duration of  $300 \mu s$ , equivalent to a  $70^\circ$  flip angle, was used for the following Raman experiments.  $300 \mu s$  was chosen as it strikes a

balance between maximising the  $^{129}\text{Xe}$  signal while not totally depolarising the probed nuclei. NMR pulses can be taken closer together without significantly slowing down polarisation build-up, offering a greater temporal resolution in the polarisation build-up curve.

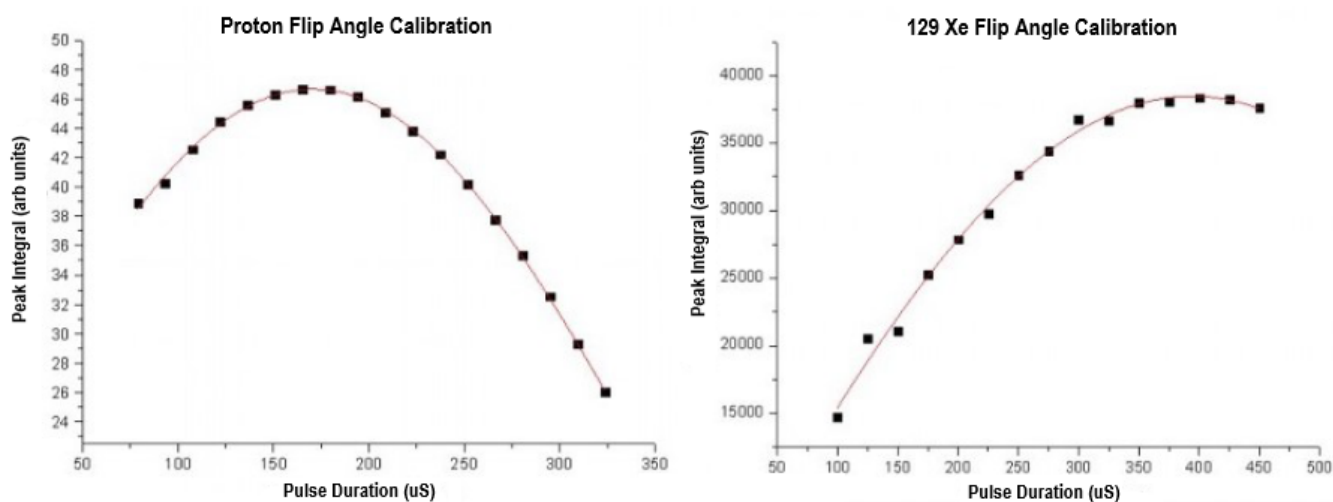


Figure 3.12: Flip angle calibration for  $^1\text{H}$  (left) and  $^{129}\text{Xe}$  (right)

The spectrum for the water signal used in these calculations is shown below in Figure 3.13.

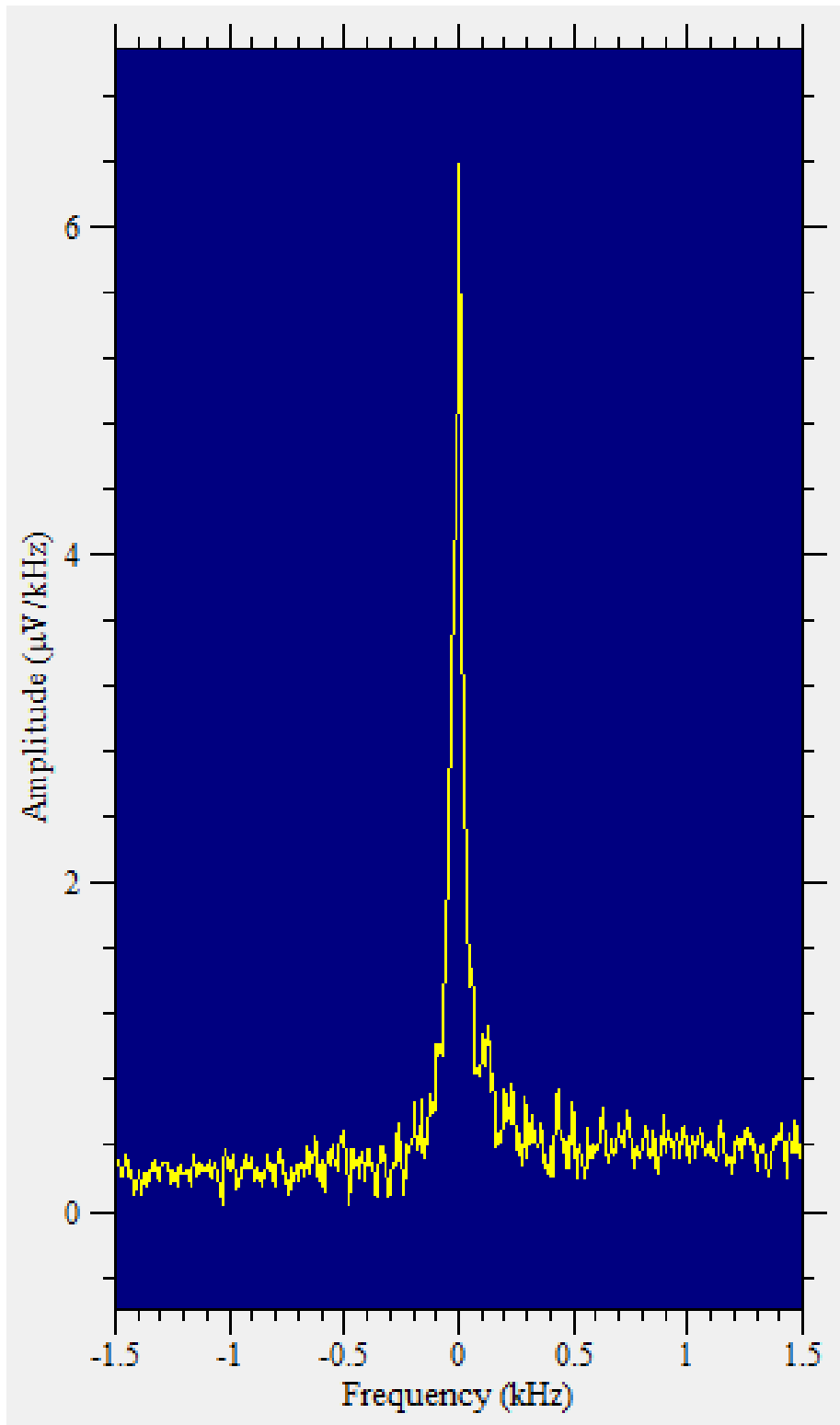


Figure 3.13: Water signal for use in  $P_{X_e}$  calculation

After the flip angle calibration is performed and the reference proton signal obtained, it is possible to calculate the percentage polarisation of the  $^{129}\text{Xe}$  within the cell by comparing it to the proton reference signal using Equation (3.14).

$$P_{Xe} = \epsilon_{enhance}(C_{T_2}P_{thermal}100) \quad (3.14)$$

- $P_{Xe}$  : Xenon polarisation
- $\epsilon_{enhance}$ : Enhancement factor
- $C_{T_2}$ : Compensation factor to account for  $T_2^*$  and acquisition delay [24]
- $P_{thermal}$ : Thermal proton polarisation

$\epsilon_{enhance}$  shows how much the HP  $^{129}\text{Xe}$  has been enhanced when compared to signal obtained from the thermal protons and is given by Equation (3.15).

$$\epsilon_{enhance} = \frac{C_H \sin(\alpha_H) \gamma_H S_{Xe}}{C_{Xe} \sin(\alpha_{Xe}) \gamma_{Xe} S_H} [87] \quad (3.15)$$

- $C_{H,Xe}$  : Molar concentration of H,  $^{129}\text{Xe}$
- $\alpha_{H,Xe}$  Flip angle of H,  $^{129}\text{Xe}$
- $\gamma_{H,Xe}$  Gyromagnetic ratio of H,  $^{129}\text{Xe}$
- $S_{H,Xe}$  Signal intensity H,  $^{129}\text{Xe}$

The uncertainty in the final polarisation value is determined by the largest source of error: the noise of the water signal. The error is therefore calculated from the water signal's SNR given by Equation (3.16).

$$Error_{P_{Xe}} = \frac{P_{Xe}}{SNR_{watersignal}} \quad (3.16)$$

### 3.3.3 Raman methods

#### Data collection

Raman spectra acquisition is controlled via Labspec, which controls the shutter on the CCD. The time the shutter is open can be increased so that more scattered light is incident on the CCD, increasing the SNR. This time is limited, as too much light saturates the CCD. To get a high temporal resolution for the temperature measurements, the acquisition time should also be kept short. Otherwise, short term temperature fluctuations cannot be observed. The acquisition time is on the order of tens of seconds for the  $N_2$  temperature measurements in these experiments.

Multiple spectra are acquired using a Labspec mode called "mapping acquisition". Mapping acquisition allows the user to program a sequence of acquisitions to work in time with the move sequencer of the LTS. With the stage and spectrometer working in tandem, it is possible to record the temperature at different locations in the cell and at different times during a run.

## Data Processing

Once all the Raman spectra are recorded, they can be used to calculate the  $N_2$  temperature throughout the experimental run. This process uses the theory from Hickman et al. [117] discussed in Section 3.2.1.

Each Raman spectrum requires some pre-processing before the  $N_2$  temperature can be calculated. Not all the peaks in the Raman spectra are from the  $N_2$  in the inner cell. The laser beam from the Verdi travels through the atmosphere before it reaches the inner cell. Although the beam is focused inside the cell, a non-negligible portion of light reaching the CCD is scattered by the atmosphere. There will therefore be components of the Raman spectra from light scattered by atmospheric  $O_2$  and  $N_2$ . If not accounted for, these components can result in an inaccurate temperature calculation. Removing the atmospheric contribution requires background spectra to be taken for each oven temperature used. This is performed using an evacuated cell ( $\approx 10^{-5}$  Torr), so the distortion of the light by the cell and the temperature of the air in the outer cell are kept consistent between the background and actual spectra. To achieve a high SNR the background spectra are acquired for 30 minutes. Two background spectra are recorded and the lower intensity of the two spectra at each in the Raman wavelength is used in the final background spectra, this is to negate the effect of potential random background noise. The  $O_2$  peaks from both the background and actual spectra should be equal and in the same place. As the acquisition time for the actual spectra is 25 seconds, and the background spectra 30 minutes, the background spectrum's  $O_2$  peak intensity is much higher. The background spectra are therefore scaled so that the  $O_2$  peak heights are the same as the actual spectra. The scaled background spectrum's  $O_2$  peaks are then aligned with the actual spectrum's  $O_2$  peaks. Finally, the aligned and scaled background spectra are subtracted from the actual spectra.

The peaks in the final Raman spectrum are only from the  $N_2$  in the inner cell. The MATLAB code can pick out the  $N_2$  peaks and plots  $F(J)$  against  $J(J+1)$  and calculate the gradient and the  $N_2$  temperature. The MATLAB code enables multiple Raman spectra to be processed and the resulting temperature data to be written into a single matrix to aid analysis.

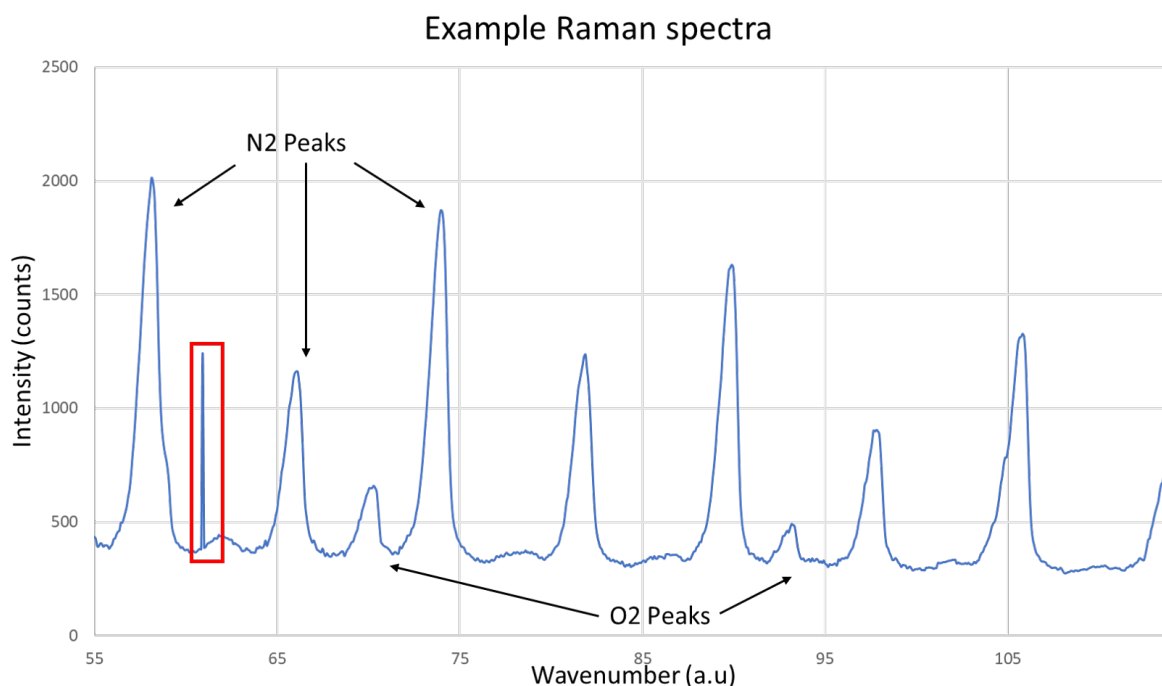


Figure 3.14: An example Raman spectra taken on a cell at with a 100 C oven temperature with the cosmic ray highlighted in red.  $N_2$  and  $O_2$  labelled

One part of the workflow has to be performed manually. During Raman spectra acquisitions, cosmic rays may hit the CCD. This produces a sharp, intense spike on the spectrum, as shown in Figure (3.14). Such a spike could be mistaken for an  $N_2$  peak by the analysis code and in turn affect the temperature calculation. Since cosmic rays pass straight through any shielding on the CCD and even the building the lab occupies, it is not practical to mechanically shield the CCD. Cosmic rays also occur randomly, so there is no way to remove them via a automated process reliably. The simplest way to remove cosmic rays without affecting the rest of the spectrum is manually using the “spike removal tool” in LabSpec. The spectrum is saved before and after cosmic ray removal to ensure the removal of the spike has not affected the size or location of any Raman peaks. Every spectrum is inspected and any cosmic ray spikes are removed before the spectrum is processed in MATLAB.

### 3.3.4 Cell cleaning and loading

#### Introduction

Alkali metals such as Rb/Cs are highly reactive with  $H_2O$  and  $O_2$  [127] these reactions are said to poison the alkali metal. The  $O_2$  can react with the Rb/Cs and caused its surface to oxidise into  $Rb_2O/Cs_2O$ . Both have a vastly increased melting point [128] and can also increase relaxation within the cell due to electromagnetic impurities [129]. In large enough quantities,  $O_2$  can vastly reduce the polarisation achieved via SEOP. Even small amounts of impurities can poison



the Rb/Cs and inhibit polarisation. This risk is highest when the cell is being loaded with a new gas mix, but overtime atmospheric impurities can leech into the cell through the stopcocks. This means that occasionally the cells need to be cleaned and loaded with fresh alkali metal. Cleaning and loading must be undertaken under controlled conditions, in an  $N_2$ -rich atmosphere. If the alkali metals are exposed to  $H_2O$  or  $O_2$ , the resultant reaction could cause a fire or even an explosion. Besides safety, these controlled conditions ensure there are no impurities introduced when loading a cell with fresh alkali metal, maximising cell lifetimes. The process for cleaning and loading a cell is outlined in this section.

### Alkali metal cleaning with tert-butanol and methanol

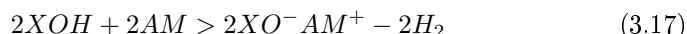
Cell cleaning is performed in a Plas-Lab glove box. The glove box provides an  $N_2$ -rich environment for cell cleaning, ensuring the Rb/Cs has no  $H_2O$  and  $O_2$  with which to react. After the cell, cleaning chemicals and equipment have been loaded and the glove box is sealed, three purge/evacuate cycles of  $N_2$  are performed on the glove box. This reduces the fraction of atmospheric  $O_2$  and other contaminants in the glove box to a negligible level, replacing them with unreactive  $N_2$ .



Figure 3.15: Plas-Lab Glovebox

After the glovebox has been purged and evacuated with  $N_2$  three times, it is safe to remove the stopcocks from the cell and begin the cleaning process. A solution of tert-butanol is pipetted a few drops at a time into the inner cell. The subsequent reaction of the tert-butanol with the Rb/Cs produces a stable alkoxide salt, and hydrogen gas is shown in Equation (3.17). In Equation, (3.17) X is the hydrocarbon chain of alcohol used, and AM is the alkali metal, either Cs or Rb. Tert-butanol is used as it has a small reaction cross-section with Rb/Cs owing to the alcohol compounds longer hydrocarbon chain. The smaller cross-section means the reaction is slower and more controlled, making it safer when there is a larger amount of Rb/Cs present. Throughout the cleaning

process, the glovebox is filled and evacuated with  $N_2$  to remove the hydrogen gas produced, which poses a fire risk if allowed to build up. When no more Rb/Cs is visible, a final wash is performed with pure methanol which has a larger reaction cross-section than tert-butanol as it has a shorter hydrocarbon carbon chain. Methanol is therefore able to react more readily with any remaining Rb/Cs. The methanol wash is to ensure there are no Rb/Cs traces left within the cell and is only used in the last step, as the rapid reaction with a large amount of Rb/Cs could become uncontrollable, damaging the cell, glovebox and potentially harming the user. It would also produce hydrogen gas at a such a rate that it may build up to dangerous levels inside the glovebox.



### Base bath

After the cell has been removed from the glove box, it is left in a base bath solution of potassium hydroxide and methanol  $KOH/CH_3OH$  overnight. This ensures that any remaining Rb/Cs that had not been removed by the tert-butanol and methanol rinses react with base bath solution and be removed from the cell. The base bath solution is highly alkaline and could cause burns if it touches exposed skin, meaning appropriate safety equipment must be worn, including gloves and lab coats to protect the skin and safety glasses to protect the eyes. All glassware is loaded and removed from the bath via tongs. Care must be taken to fill the inner cell with the solution, leaving no air bubbles. When removed from the bath, the cell is washed with distilled water to remove the  $KOH/CH_3OH$  solution.

### Sonic bath

The final cleaning step involves sonicating the cell in a Bandelin Sonorex sonic bath filled with equal parts methanol and distilled water. This removes any traces of base bath solution left in the cell. The cell is suspended in the solution via a flexible wire mounted to a clamp stand. When the base bath is switched on, the cell must not touch the sides of the bath as direct contact with the vibrating surfaces may damage it. The outer cell is submerged, and the inner cell is filled with the solution before being sonicated for one hour. The ultrasonic vibrations ensure that the solution can get to every surface and react with any remaining base bath solution. After an hour, the cell is removed from the sonic bath, and the inner cell is given a methanol rinse to assist the drying process before it is placed in a drying oven overnight at a temperature of 80C.

### Cell loading

#### Testing cell integrity

Before Rb/Cs loading can take place, both valve stems must be checked to ensure the cell can hold a vacuum. This is performed using the gas handling manifold.

Each component of the manifold is sealed from the atmosphere and from one other using Swagelok valves. This means that each section can be isolated



Figure 3.16: Bandelin Sonorex sonic bath

and evacuated by the vacuum pumps to remove any impurities in the gas lines. The system has two pumps: a rotary pump to bring the system down to a  $10^{-3}$  Torr vacuum level and a turbo pump which can achieve below  $10^{-5}$  Torr. The rotary pump is used to reduce the pressure before switching to the turbo pump, as exposing the turbo pump to high pressures can cause it to be damaged. Both pumps cannot be connected to the manifold at the same time as the turbo pump is powerful enough to suck up oil from the rotary pump. The rotary pump must therefore be disconnected before switching over to the turbo pump.

The cell is vacuum tested by connecting the manifold to one of the two valve stems. Both stopcocks are closed, denoted by the O-ring wetting on the inside of the stem. The stopcock in the valve stem connected to the manifold is then loosened, allowing the rotary pump and then turbo pump to vacuum down the cell. Once the cell has been vacuumed down to  $10^{-5}$  Torr, it is closed for a few minutes and then opened. If the vacuum level does not rise when opened, the valves can hold the vacuum and the cell is fit for purpose.

### Cell coating

One form of spin destruction can occur when polarised  $^{129}\text{Xe}$  nuclei interact with paramagnetic impurities in the glass cell wall. To reduce the relaxation contribution from these interactions, the walls of the inner cell are coated with a product called SurfaSil<sup>TM</sup>. SurfaSil<sup>TM</sup> is a siliconising fluid which acts as a barrier between HP  $^{129}\text{Xe}$  and the glass walls of the cell in order to minimize dipole interactions between polarised  $^{129}\text{Xe}$  nuclei and these paramagnetic centres.

The coating process requires two alternating rinses, one with pure hexane and the other with a 9:1 hexane/SurfaSil<sup>TM</sup> solution. The inner cell undergoes an initial wash with hexane to remove any remaining impurities in the cell. After this, it is decanted into a waste container. The SurfaSil<sup>TM</sup> solution is then poured into the inner cell and agitated, with each part of the inner cell being submerged for at least 30 seconds. The SurfaSil<sup>TM</sup> solution is poured out to waste, and the inner cell is rinsed with hexane to remove any SurfaSil<sup>TM</sup>

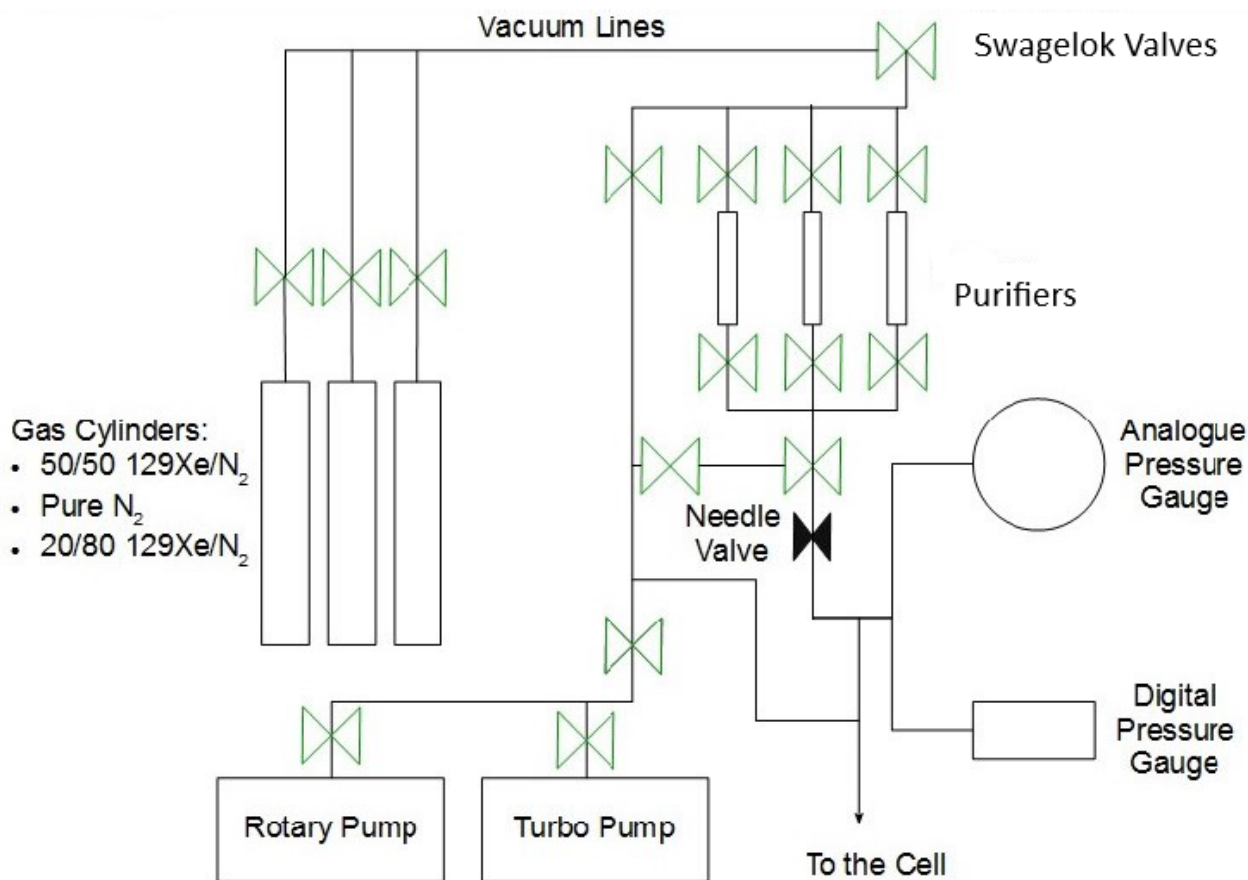


Figure 3.17: Diagram of the gas handling manifold

that has not bonded with the glass. To ensure the entire cell has been coated with SurfaSil<sup>TM</sup>, this cycle is repeated two more times. This process must be performed in a fume cupboard as a small amount of HCl is released when SurfaSil<sup>TM</sup> reacts with the glass. The coated cell is then placed in the drying oven overnight at 80C before the alkali metal loading can take place.

#### Alkali metal loading

The next step is loading the Rb/Cs into the cell. Due to the high reactivity of Rb/Cs, the cell is loaded with the alkali metal of choice in an . The  $\text{O}_2$  and  $\text{H}_2\text{O}$  content of the atmosphere inside the cabinet is closely monitored. For alkali metal loading to proceed, the  $\text{O}_2$  and  $\text{H}_2\text{O}$  must be below ten ppm and two ppm, respectively. This is to ensure a safe working environment and to prevent alkali metal poisoning.

The following equipment is transferred into the cabinet for alkali metal loading:

- Pipettes

- Pipette bulbs
- Foil
- Sealable waste container
- Evacuated cell
- Schlenk tube filled with Rb/Cs
- Heat gun
- Clamp stand

The empty cell and Schlenk tube containing the alkali metal are mounted in the clamp stand. Following this, the Schlenk tube and cell valve stems are positioned vertically. Foil is placed under the stand and glassware to allow easy clean-up of any spills. The Schlenk tube is heated with the hairdryer to melt the alkali metal. The pipette is also heated to stop the alkali metal solidifying inside it during the transfer of the alkali metal from the Schlenk tube to the cell. Care must be taken not to damage the pipette or get the alkali metal on the inner cell windows during transfer. Should the alkali metal be left on the cell windows, it can block the transmission of the laser photons into or out of the cell causing localised heating of the glass which has the potential to cause structural damage to the cell. Once loading is complete, the cell is sealed by closing both stopcocks. All items contaminated with the alkali metal must be placed in a sealable container and safely disposed of by cleaning them via the same protocol as described during cell cleaning. The cell can now be removed from the cabinet for gas loading.



Figure 3.18: MBRAUN MB200B ECO sealed environment cabinet

## Gas loading and cell evacuation

During gas filling, each section of the manifold undergoes  $N_2$  purge/evacuation cycles to reduce impurities in the gas lines to negligible amounts. The exception is the NuPure “THE ELIMINATOR CAG”s (getters), which are isolated from the manifold until gas is flowing through them. This is to limit their gas throughput, which increases their useful lifetimes. When all the lines have been evacuated, the vacuum line and all Swagelok valves are closed in order to maintain the vacuum.  $^{129}\text{Xe}$  gas mix,  $N_2$  or  $^4\text{He}$  may then flow at a controlled rate from their cylinders through the regulator, getters, filling lines and then into the cell itself. The flow rate into the cell is controlled via a needle valve. Cell pressure is monitored by digital and analogue pressure gauges for pressures below and above 1200 Torr, respectively. The components of the gas mix are loaded from their cylinders in order of ascending partial pressure. This is to ensure the cell always has a lower pressure than the manifold, which stops back-flow, and to ensure the lower partial pressure gases, typically the Xe fraction, can be filled more accurately using the digital pressure gauge. The evacuate purge cycles also occur when switching between cylinders, so the exact partial pressure of each component of the gas mix is known. In all experiments in this chapter all cells are filled to a total pressure of 2000 Torr for consistency and to prevent overpressuring the cell which might result in cell failure.



Figure 3.19: Cell connected to gas filling rig via valve stem

## 3.4 Raman SEOP experiments

### 3.4.1 Introduction

The goal of these experiments is to use Raman spectroscopy to better understand the in-cell thermal dynamics during SEOP under different conditions. The results from which are intended to inform users of stopped-flow polarisers of how to exploit different variables best to achieve optimal conditions for SEOP. Optimal SEOP conditions lead to a higher  $^{129}\text{Xe}$  magnetisation and polarisation, so there will be more signal available during MRI imaging. This will produce higher-quality images allowing clinicians to make more informed decisions when treating patients.

The repeatability of these experiments was first investigated and improved. The general experimental protocol for these experiments is then outlined to reduce repetition within the chapter. Following this initial work, the experiments in the chapter are discussed. These include the effect of  $^4\text{He}$  buffer gas on in-cell temperature, and the in-cell temperature comparison between Cs and Rb SEOP.

### 3.4.2 Data consistency

It was necessary to investigate how much the  $P_{Xe}$  changed when all other variables were kept the same. The results needed to be consistent, otherwise it would not be possible to determine if changing independent variables had a significant effect on the dependent ones (i.e. the  $P_{Xe}$  and in-cell temperature).

A freshly cleaned cell was loaded with a bead of Rb, then filled with a 1000 Torr  $Xe/1000$  Torr  $N_2$  gas mix. The cell was heated to an oven temperature of 130 C and the temperature was allowed to stabilise for 20 minutes before experiments began. The Rb vapour was then optically pumped using the 50W QPC Rb BrightLock laser. NMR was taken every five minutes for 60 minutes with the middle surface coil. At the end of each 60-minute run, the pump laser was blocked. The  $P_{Xe}$  was then destroyed using a series of 1000 NMR crusher pulses. The repetition time between crusher pulses was 0.5 seconds and the pulse duration was 400  $\mu\text{s}$ , which equated to  $\approx 90^\circ$  flip angle to maximise the depolarisation from each pulse. The NMR signal was monitored during crushing and, if any NMR signal remained, the crusher sequence was repeated.

As the polarisation of the  $^{129}\text{Xe}$  is non-recoverable, it is possible to completely depolarise the HP  $^{129}\text{Xe}$  within the cell using successive NMR pulses. This can only happen if the pump laser is blocked and not able to re-polarise the  $^{129}\text{Xe}$ . All three NMR coils produce high flip angle NMR crusher pulses. The NMR crusher pulses continued until the  $^{129}\text{Xe}$  NMR signal had dropped below the noise floor. Relaxation would occur through the normal relaxation mechanisms, however this would not be practical given experimental time constraints, as  $T_1$  relaxation time would be on the order of hours [24]. NMR crusher pulses completely depolarised the  $^{129}\text{Xe}$  on the order of minutes, once they had finished, the experiment was repeated.

In total, nine repeats were taken: two on the first day, six the day after, and a final run was taken two days later. Between the 8<sup>th</sup> and 9<sup>th</sup> runs, the cell was run at a variety of oven temperatures and cooled to room temperature several times. The NMR signal build-up during each run is shown in Figure 3.20.

Both the NMR signal and build-up rate increased from Run 1 to Run 9. However, there was a slight dip in the final polarisation between Run 2 and Run 3. As this was the first run of the day, it is possible that the oven temperature was not given enough time to stabilise, and only the area close to the thermocouple was up to temperature. This could have resulted in a lower starting Rb vapour density, meaning a slower initial polarisation build-up occurred. The  $^{129}\text{Xe}$  NMR signal increased between each subsequent run, and this increased the most between Run 8 and 9. The final NMR values are shown in Figure 3.21. The increasing polarisation, despite all other variables remaining unchanged, could have come from several sources.



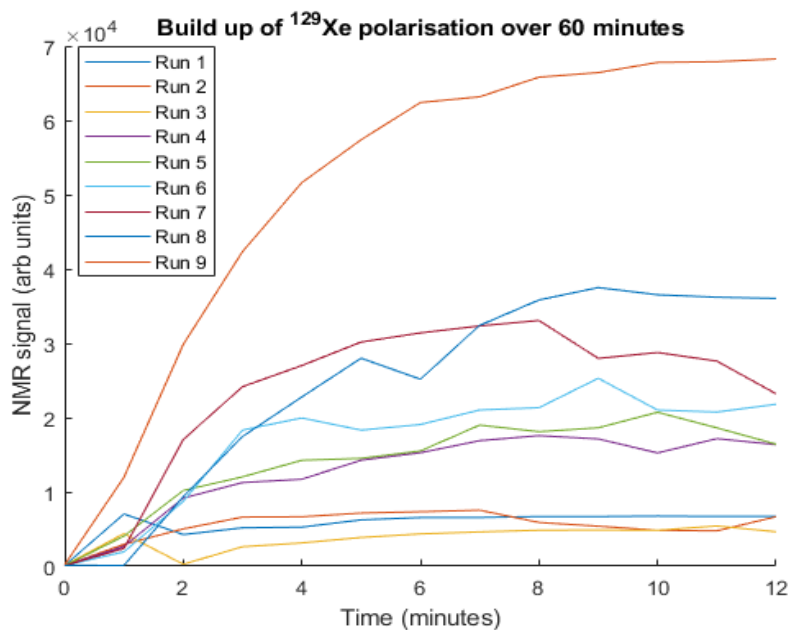


Figure 3.20: Build up of NMR signal (area under the FFT FID peak) from HP  $^{129}\text{Xe}$  at 130 C oven temperature to test the consistency over nine different runs

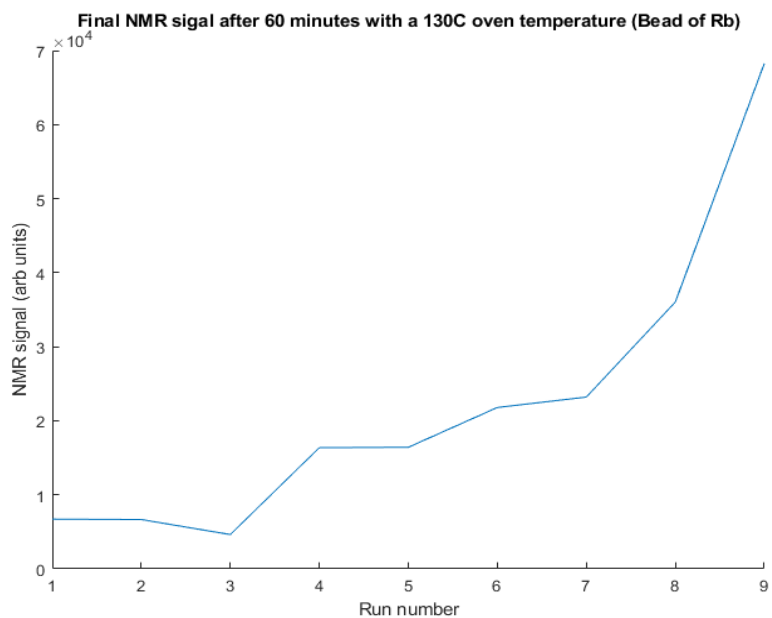


Figure 3.21: Final NMR signal (area under the FFT FID peak) from HP  $^{129}\text{Xe}$  at 130 C oven temperature to test the consistency over nine different runs

## Methods to improve consistency

The lack of repeatability could be due to atmospheric  $O_2$  being introduced into the gas mix when filling the cell. This could be a result of improperly evacuating the manifold or a poor seal when filling the cell. In small quantities, a thin oxidised film can form over the surface of the Rb bead. As a result of successive heating and cooling cycles, these oxidised areas can move from the surface of the bead to the interior. The surface Rb is vaporised first, so a surface layer of “fresh” unoxidised Rb can give a higher Rb vapour density at lower oven temperatures and result in increased  $P_{Xe}$ .

The other possibility is that vaporised Rb condenses over a large surface area when it cools. The Rb surface area increases with successive heating and cooling cycles, plating the cell walls. As Rb vapour density increases with the Rb surface area at a given oven temperature, final  $P_{Xe}$  then increases from run to run as a result of this plating.

Both sources of polarisation variability are linked to Rb vapour density, and two different solutions were proposed to improve the comparability between runs. The first is to account for the difference in Rb vapour density by measuring it directly and then using this measurement to scale the resultant polarisation. The second is to accelerate the plating process artificially, increasing the surface area of the Rb. A larger Rb surface area may have a smaller percentage change after each heating and cooling cycle, giving a more consistent Rb surface area and, as a result, a more consistent  $P_{Xe}$ .

## Atomic absorption spectroscopy

Rb vapour density was measured using AAS, which measures the absorption of unpolarised light by an atomic element(s) [130]. The amount of light absorbed is proportional to the vapour density of the specific element(s).

The Rb vapour density can be measured by comparing the absorption of a light source with the cell at room temperature, where a Rb vapour density of 0 is assumed as Rb’s melting point of 39.3 C [131], to the absorption through the cell at a high oven temperature [132]. Absorption can be measured on either the Rb  $D_1$  line at 794.77 nm [86] or the Rb  $D_2$  line at 780.23 nm [86]. As the pump laser is tuned to the Rb  $D_1$ , even a perpendicular optical fibre would be able to pick up any unexpected reflections due to the power of the laser. For this reason, the Rb  $D_2$  line was used for the AAS.

A Photodigm A15-138 laser diode tuned to the Rb  $D_2$  was first tested for AAS. However, the diode’s output power had poor stability, even when driven by a range of different power supplies. Poor stability made it difficult to determine if the power reduction detected was due to absorption by the Rb vapour or from a drop in output power of the diode. The choice was made to switch from the laser diode to a Quartz Tungsten-Halogen Lamp from Thorlabs, which offered a more stable output at Rb  $D_2$  line. The output spectrum was measured with an optical fibre, with a cosine head connected to an Ocean Optics HR2000 spectrometer. The fibre was placed on the opposite side of the cell from the halogen lamp and was attached to the Ondax head lens tube so that it did not interfere with Raman data collection.

AAS was tested on a cell loaded with Rb and filled with a 400 Torr  $Xe$ /1600 Torr  $N_2$  gas mix. The cell was then heated to an oven temperature of 160

C with no pump laser. Once the thermocouple measured an oven temperature of 160 C, the cell temperature was allowed to stabilise for 30 minutes, and the absorption spectrum was recorded. The absorption spectrum is shown in Figure 3.22, which shows the absorption on the Rb  $D_1$  and Rb  $D_2$  lines relative to the spectra recorded at room temperature.

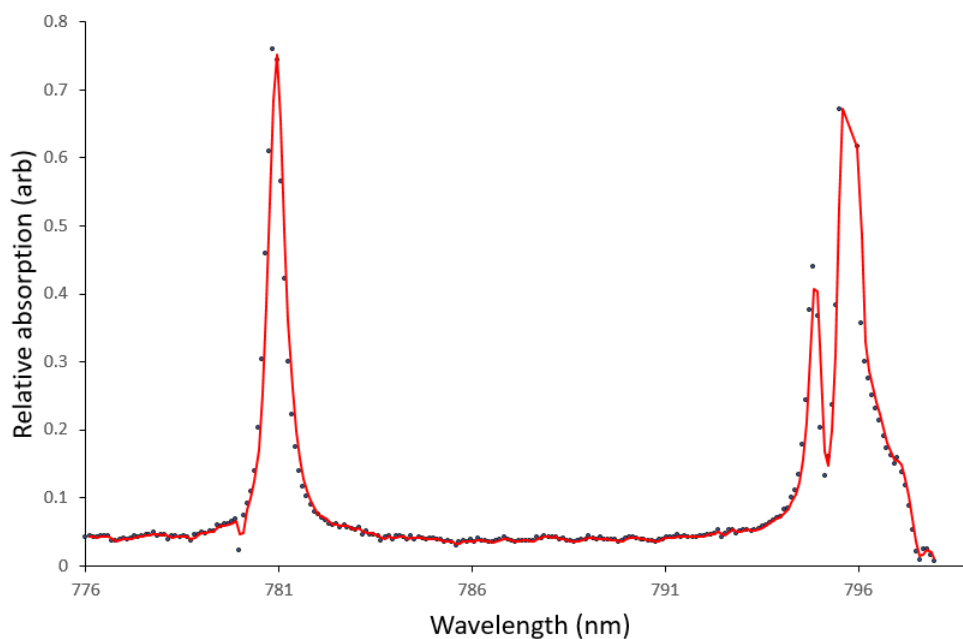


Figure 3.22: Rb absorption spectra showing absorption of photons from the halogen lamp light source by the Rb  $D_1$  line (right) and  $D_2$  line (left) with laser off.

For the next set of experiments, the laser was unblocked and, over the course of six, 60-minute SEOP runs, the absorption and polarisation were recorded. These six runs were performed in sets of three on two successive days. Each set used the following oven temperatures: 100 C, 110 C and 120 C. Between each run, the polarisation was depleted using a series of NMR crusher pulses as described in Section 3.4.2. The results of these six runs are shown in Figure 3.23. These runs showed how stable the Rb vapour density is in a steady-state cell. They also exhibited the previously observed increase in polarisation under the same starting conditions on consecutive days. The AAS confirms that the vapour density does increase with successive heating and cooling cycles.

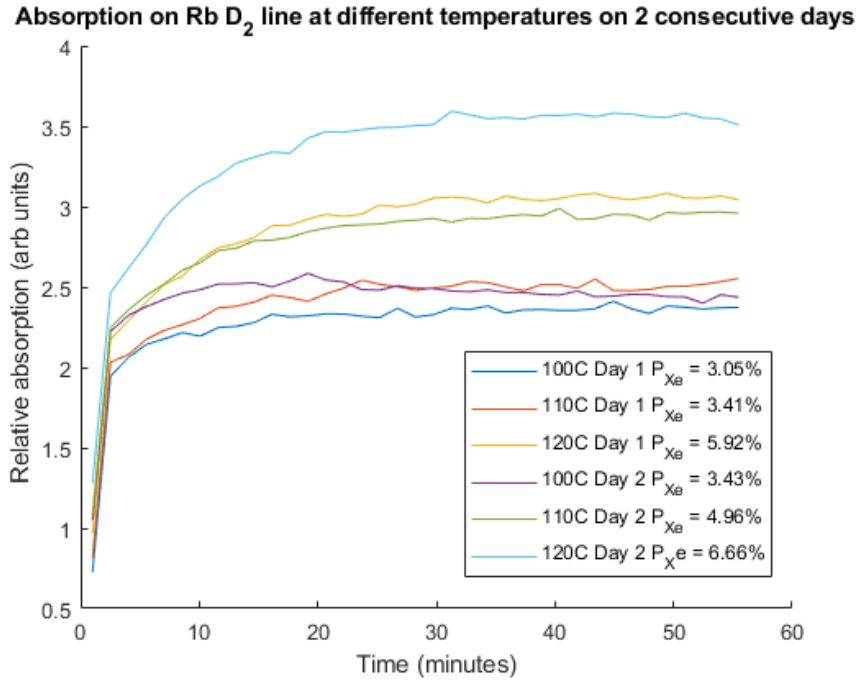


Figure 3.23: Rb  $D_2$  absorption relative to a cold cell spectrum during SEOP on the Rb  $D_2$  line. The oven temperature, day and percentage  $P_{Xe}$  is displayed in the legend on the right.

For a fair comparison between runs, AAS relies on the lamp, fibre and optical cell remaining in the exact same orientation relative to one other for each run. As the cell is free to rotate in its housing, it can be hard to keep it in a fixed position. Cell movement can occur when evacuating or filling the cell with new gas mixes or if the optical bench is knocked, which can often happen with many users in the lab. Cell rotation changes the refraction and reflection of light through the inner and outer cell walls, glass defects and plated Rb. A solution would be to make a device that does not allow for rotation. Due to the complexity of creating a device which prevents any cell movement but does not interfere with Raman or NMR data collection, the decision was made to explore other ways of improving experimental repeatability and they are discussed below.

### Accelerating the alkali metal plating process

To increase the alkali metal's surface area, it must be artificially spread on the walls of the cell, creating what is henceforth referred to as a "spread cell". Alkali metal spreading must be carried out in an evacuated cell, vacuumed down to  $\approx 10^{-5}$  Torr. Evacuation is necessary because a lower pressure in the cell requires less energy for the alkali metal to vaporise [133]. It also increases the free scattering length within the cell, enabling better diffusion of the alkali metal throughout the cells volume [134]. The heat gun is focused on the alkali metal bead itself, on the inner cell windows and on one side of the inner cell. This process quickly plates the alkali metal onto the cell walls. The windows are

heated so that the alkali metal does not condense there, allowing the pump laser to pass through the front and back optical windows unimpeded. The side of the inner cell nearest the Raman head is heated to prevent condensation so that the Raman laser can still enter the cell. The alkali metal instead condenses on the opposite side of the cell, which has not been heated. An example spread cell can be seen in Figure 3.24.

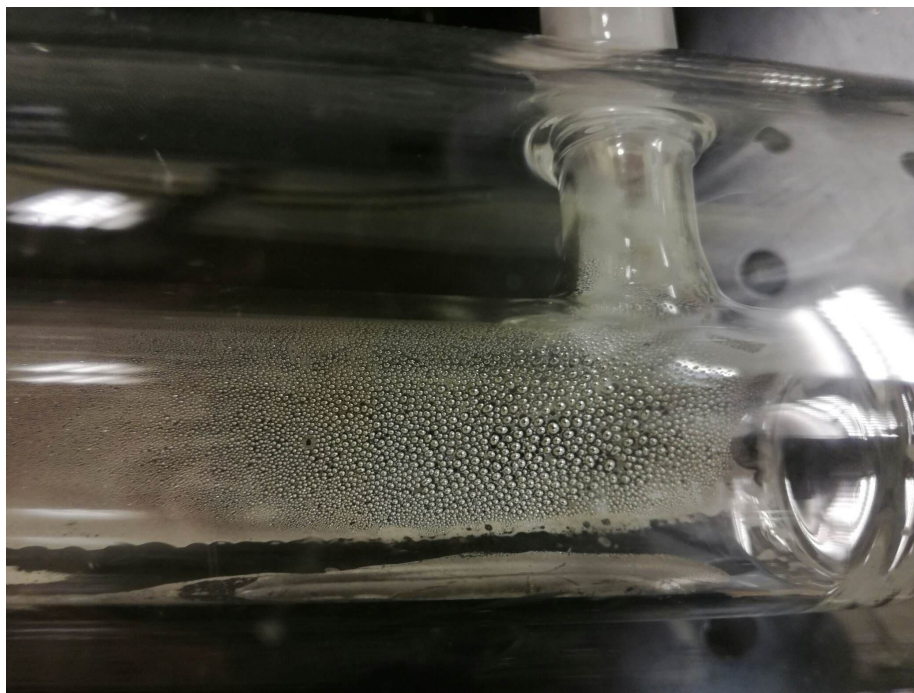


Figure 3.24: Example of a Rb spread cell

The spread cell was refilled with the same 400 Torr  $Xe$  and 1600 Torr  $N_2$  gas mix. Seven runs were performed at a 100 C oven temperature using the same procedure as the first repeatability experiments. Four runs were taken on the first day and three runs on the second, the results of which are shown in Figure 3.25. Although there was a downward trend there was a significant 4.94-fold decrease in percentage standard deviation in the spread cell compared to the "unspread cell". In the unspread cell, the Rb has not been spread artificially but rather left in the large droplet it forms as it is loaded into the cell. The variation in the unspread cell comes from the Rb spreading out due to repeated heating and cooling cycles. Eventually, the consistency of the unspread cell may improve as it reaches the Rb surface similar to that of a spread cell. However, it is not practical to spend the time required to bed in each cell when the Rb can easily be spread with a heat gun. Due to their increased consistency, spread cells were chosen for all further experiments detailed in this chapter.

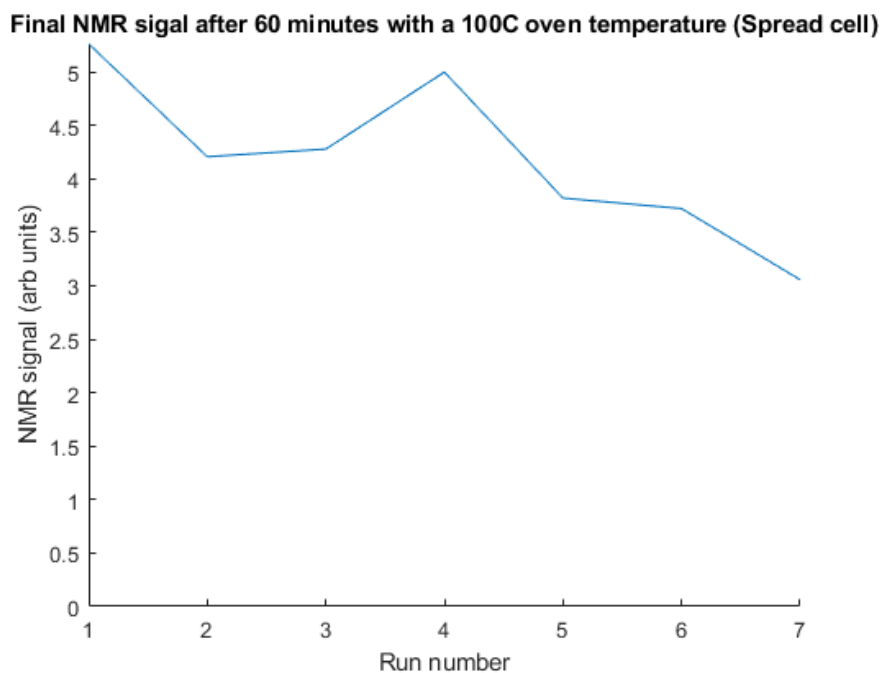


Figure 3.25: Final NMR signal (area under the FFT FID peak) from HP  $^{129}\text{Xe}$  at 100 C oven temperature to test the consistency over seven different runs in a spread cell

### 3.4.3 General experimental protocol

This section describes the generalities of the Raman SEOP experiments to reduce repetition within the chapter. Any differences in the experimental protocol specific to an experiment are discussed in that experiment's section.

In all Raman experiments, both the pump and Raman lasers are brought up to power and blocked until needed. The pump laser is blocked by a power meter and the Raman laser by an internal shutter in the laser. The pump lasers output frequency is adjusted using the water chiller so that its output is resonant with  $D_1$  of the alkali metal being used. When the cell is up to temperature, both lasers are unblocked, and the run begins.

Raman and NMR measurements are taken at the front, middle and back of the cell. Raman data is measured above each NMR coil so that both measurements are taken at the same location. Both Raman and NMR acquisitions are taken at regular intervals of 90 seconds and 60 seconds respectively throughout the experimental run. The interval of 60 seconds was chosen as a compromise to ensure high temporal resolution in the NMR build-up curves while minimising  $^{129}\text{Xe}$  depolarisation from quick successive NMR pulses. A gap of 90 seconds was chosen for the Raman as that is the time it takes to collect the spectra from all three positions. The minimum time between successive Raman acquisitions in the same position is therefore 90 seconds. The Raman laser's location is changed with the LTS, while the NMR acquisition location is changed by switching between the three surface coils. At the end of each run, a 1D temper-

ature map (1DTM) is taken. The 1DTM measures the temperature of the gas inside the cell from front to back at 10 mm intervals, showing the temperature variation along the cell under steady-state polarisation conditions. After an experiment is complete, both lasers are blocked, and the NMR crusher pulses are initiated.

If multiple oven temperatures are being investigated, the experiments are performed in ascending temperature order. This is more time-efficient as it is quicker to increase the temperature of the cell than to reduce it, as this set-up does not employ active cooling.

### 3.4.4 The effect of $^4\text{He}$ on managing $\text{N}_2$ temperature in a spread cell

#### Introduction

The reasons for  $^4\text{He}$ 's use in the buffer gas mix is discussed in Section 2.4.9 but it has another property that may be of use for SEOP, namely a high thermal conductivity of  $0.1513\text{Wm}^{-1}\text{K}^{-1}$ . This is significantly higher when compared to Xe and  $\text{N}_2$ , which have thermal conductivities of  $5.56 \times 10^{-3}\text{Wm}^{-1}\text{K}^{-1}$  and  $25.83 \times 10^{-3}\text{Wm}^{-1}\text{K}^{-1}$ , respectively [94]. Rich Xe gas mixes for stopped-flow SEOP could benefit from increased thermal dissipation within the cell. This is because rich mixes have a low thermal conductivity due to their large Xe fraction and the gas mix is resident in the cell for a longer amount of time compared to continuous-flow polarisers. Richer Xe mixes also allow for an increased spin-exchange rate between the Rb and  $^{129}\text{Xe}$  so more laser light is absorbed by the Rb compared to leaner mixes, resulting in more energy building up in the system. All these factors make thermal runaway more likely.  $^4\text{He}$  may be able to improve heat dissipation from the front of the cell by improving heat conduction throughout the gas mix, and therefore suppressing thermal runaway at higher oven temperatures. This could enable cells to be run at higher temperatures, increasing the ultimate polarisation of  $^{129}\text{Xe}$  and reducing polarisation build-up times.

A previous investigation into the thermal management of  $^4\text{He}$  was undertaken by H. Newton et al. They used an unspread cell filled with 100 Torr Xe with increasing fractions of  $^4\text{He}$  in the  $^4\text{He}/\text{N}_2$  buffer gas mix, up to a total pressure of 2000 Torr. The investigation showed that a fraction of  $^4\text{He}$  at a partial pressure of 1400 Torr was able to reduce the gas temperature by 100 C and suppress the onset of Rb runaway [135]. This, however, did not result in a higher  $P_{\text{Xe}}$  and, contrary to prediction, the polarisation decreased in this experiment [135].

The experiments detailed below were undertaken to investigate whether  $^4\text{He}$  could suppress thermal runaway in a spread cell. This is because clinical stopped-flow polarisers use spread cells to take advantage of higher Rb vapour densities at lower temperatures. As the alkali metal vapour density is higher in a spread cell and as a result absorbs more energy from the OP laser, the effect from the  $^4\text{He}$  may be reduced.

## Methods

The experiments used gas mixes with a total pressure of 2000 Torr with 10% (200 Torr) Xe. Three buffer gas mixes were used with increasing fractions of  $^4\text{He}$ . The first buffer gas mix was 1800 Torr of pure  $\text{N}_2$ , which acted as the control. The two other buffer gas mixes were 200 Torr  $^4\text{He}$  / 1600 Torr  $\text{N}_2$  and 500 Torr  $^4\text{He}$  / 1300 Torr  $\text{N}_2$ . The first set of experiments used the general experimental protocol detailed above. SEOP was performed for 11 minutes, and a 1DTM was collected at the end of each experiment. The first set of experiments only used an 11-minute build-up time because of time constraints from an upcoming conference, the International Xenon Symposium (XeMAT). After the conference, the same set of gas mixes were repeated with a 31-minute build-up time to allow the polarisation to reach steady-state and confirm the findings of the initial experiments. Each gas mix was run at three different oven temperatures: 80 C, 120 C and 160 C. These temperatures were chosen as they would show how  $^4\text{He}$  affected the  $\text{N}_2$  temperature both in steady-state and runaway conditions. The laser used in the experiment was a BrightLock Ultra100 Rb laser tuned to the Rb  $D_1$  line. The laser produced  $\approx 30\text{W}$  of on-resonance power at the time of the experiment.

## Results

The initial 11-minute experiments showed that, for all oven temperatures, the  $^4\text{He}$  fraction had no significant effect on the average  $\text{N}_2$  temperature within the cell or the temperature variation across the cell. The  $P_{Xe}$  achieved after 11 minutes was also unaffected.

At 80 C, the  $P_{Xe}$  was  $13.2\% \pm 3\%$ ,  $11.0\% \pm 2\%$  and  $10.4\% \pm 2\%$  for 200 Torr  $^{129}\text{Xe}$  / 1800 Torr  $\text{N}_2$ , 200 Torr  $^{129}\text{Xe}$  / 1600 Torr  $\text{N}_2$  / 200 Torr  $^4\text{He}$  and 200 Torr  $^{129}\text{Xe}$  / 1300 Torr  $\text{N}_2$  / 500 Torr  $^4\text{He}$  gas mixes, respectively after 11 minutes. At 160 C, the final polarisation was  $16.0\% \pm 3\%$ ,  $16.6\% \pm 2\%$  and  $15.7\% \pm 3\%$  for the same gas mixes. At 160 C, the polarisation levels peaked and then reduced, a sign of Rb runaway. Runaway occurred for all buffer gas mixes, showing  $^4\text{He}$  was not able to suppress it. The  $^4\text{He}$  fraction did not significantly affect the final  $P_{Xe}$  either, as shown in Figure 3.26.



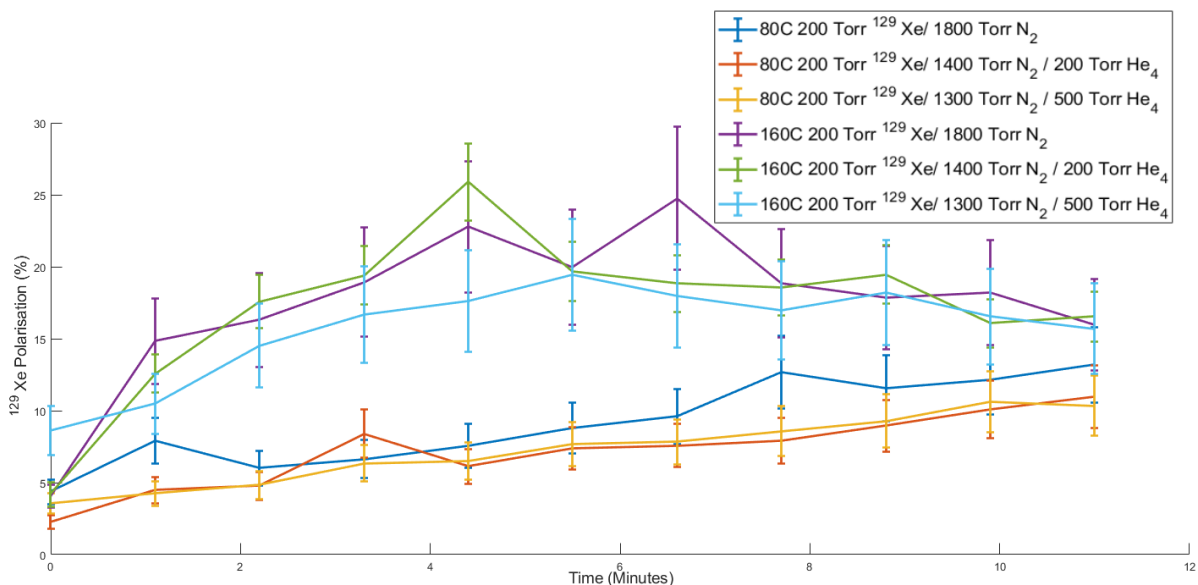


Figure 3.26: Polarisation build-up at different  ${}^4\text{He}$  fractions in the buffer gas mix. 2000 Torr gas mix with 200 Torr Xe at 80 C and 160 C oven temperature in a spread cell

At an oven temperature of 80 C, the average temperatures for the three buffer gas mixes across the 1DTM were  $84\text{C} \pm 5\text{C}$ ,  $76\text{C} \pm 4\text{C}$  and  $84 \pm 5\text{C}$  in order of increasing  ${}^4\text{He}$  fraction. In the same order of gas mixes, the average  $\text{N}_2$  temperatures for a 120 C oven temperature were  $129\text{C} \pm 8\text{C}$ ,  $121\text{C} \pm 10\text{C}$  and  $127\text{C} \pm 9\text{C}$ . Lastly, the average  $\text{N}_2$  temperatures for the 160 C oven temperature were  $172\text{C} \pm 22\text{C}$ ,  $153\text{C} \pm 17\text{C}$  and  $164\text{C} \pm 13\text{C}$ . Figure 3.27 shows that there are two points in the 160C 1DTM (green and purple lines) where the temperature is higher than those around them. As the heat pipe forces hot air through the middle stem in the underside of the cell (See Figure 3.8), there could be an increased Rb vapour density local to the heat pipe. This could cause increased heating in the middle of the cell from higher local Rb laser absorption.

The reason these experiments did not measure a reduction of  $\text{N}_2$  temperature with increasing  ${}^4\text{He}$  as seen in the work by H. Newton et al. could be a result of the higher Rb vapour density within a spread cell. Additionally, the 200 Torr of Xe was double that used in H. Newton et al.'s experiments. This meant the gas mix had a reduced thermal conductivity when using an equivalent  ${}^4\text{He}$  partial pressure. These factors contributed to the reduced effect of the increased thermal conductivity provided by  ${}^4\text{He}$ .  ${}^4\text{He}$  was therefore not able to significantly reduce the internal  $\text{N}_2$  temperature and prevent the onset of Rb runaway at 160 C .

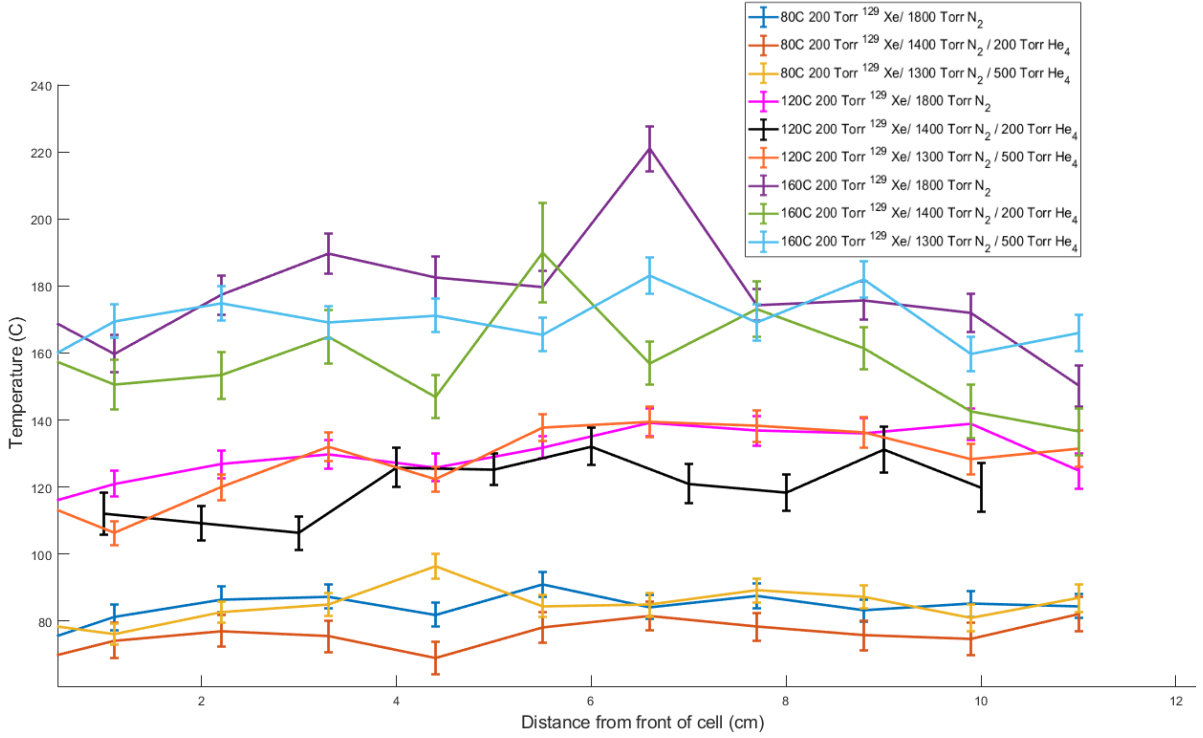


Figure 3.27: 1DTM taken along the length of the cell from front (where the OP laser enters) to the back at different  ${}^4\text{He}$  fractions in the buffer gas mix. 2000 Torr gas mix with 200 Torr Xe at 80 C, 120 C, 160 C oven temperature in a spread cell

After the XeMAT conference, the experiments were repeated with a 30-minute  $P_{\text{Xe}}$  build-up. This was to confirm the results achieved in the initial 11-minute experiments. It also allowed more time for the  $P_{\text{Xe}}$  to build up and for the temperature to stabilise before the 1DTM was taken. The final polarisation after 31 minutes in order of increasing  ${}^4\text{He}$  partial pressure was  $17.4\% \pm 3\%$ ,  $20.4\% \pm 4\%$  and  $15.0\% \pm 3\%$  at 80C. At 160 C, the final  $P_{\text{Xe}}$  was  $19.8\% \pm 4\%$ ,  $17.7\% \pm 4\%$  and  $12.9\% \pm 3\%$  for the same gas mixes. These results agreed with the initial 11-minute build-up experiments, as the increased  ${}^4\text{He}$  fraction in the buffer gas mix did not significantly change the final  $P_{\text{Xe}}$  achieved. (See Figure 3.28).

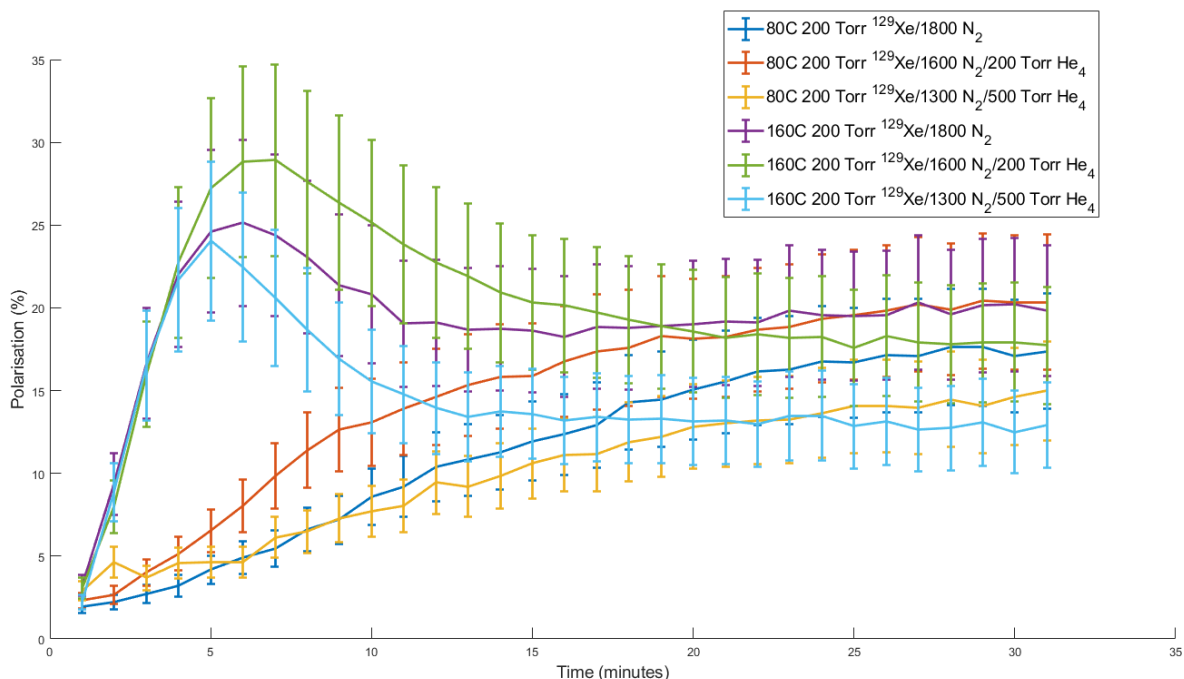


Figure 3.28: Polarisation build-up at different  ${}^4\text{He}$  fractions in the buffer gas mix. 2000 Torr gas mix with 200 Torr Xe at 80 C and 160 C oven temperature in a spread cell with a 31-minute build-up

The 1DTM maps also generally agreed with the previous data in that there was no significant difference in the average  $N_2$  temperature across the cell with increasing  ${}^4\text{He}$  partial pressure. However, the average temperature was higher in the 30-minute experiments as the cell had almost triple the time to absorb energy.

The one exception is that, at 80 C, there is a small significant difference between the average temperature at 80 C with no  ${}^4\text{He}$  and 500 Torr  ${}^4\text{He}$  of  $\approx 5\text{C}$ . At an oven temperature of 80 C, the average temperatures across the 1DTM were  $97\text{C} \pm 5\text{C}$ ,  $105\text{C} \pm 12\text{C}$  and  $81 \pm 7\text{C}$  for gas mixes 200 Torr  ${}^{129}\text{Xe}$  / 1800 Torr  $N_2$ , 200 Torr  ${}^{129}\text{Xe}$  / 1600 Torr  $N_2$  / 200 Torr  ${}^4\text{He}$  and 200 Torr  ${}^{129}\text{Xe}$  / 1300 Torr  $N_2$  / 500 Torr  ${}^4\text{He}$ , respectively. In the same order of gas mixes, the average  $N_2$  temperatures for an 120 C oven temperatures were  $148\text{C} \pm 9\text{C}$ ,  $144\text{C} \pm 10\text{C}$  and  $131\text{C} \pm 12\text{C}$ .

Lastly, the average  $N_2$  temperatures for the 160 C oven temperature were, in order of increasing  ${}^4\text{He}$  partial pressure,  $187\text{C} \pm 22\text{C}$ ,  $179\text{C} \pm 29\text{C}$  and  $152\text{C} \pm 27\text{C}$ . In the longer 30-minute experiment, when a cell enters Rb runaway, it spends more time in the feedback loop. This leads to an increased cell temperature and Rb vapour density compared to the 11-minute experiment. Increased light absorption at the front of the cell occurs due to this higher Rb vapour density, and, as a result, a larger thermal gradient builds across the cell. At 160 C oven temperature, the thermal gradients between the hottest and coolest region of the cell are, in order of ascending  ${}^4\text{He}$  fraction,  $72\text{C} \pm 25\text{C}$ ,  $83\text{C} \pm 13\text{C}$  and  $97\text{C} \pm 18\text{C}$ . These findings confirm the results seen in the 11-minute ex-

periments that, in a spread cell, the increased fraction of  $^4\text{He}$  does not improve the thermal gradients across the cell during runaway. The corresponding 1DTM maps are shown in Figure 3.29.

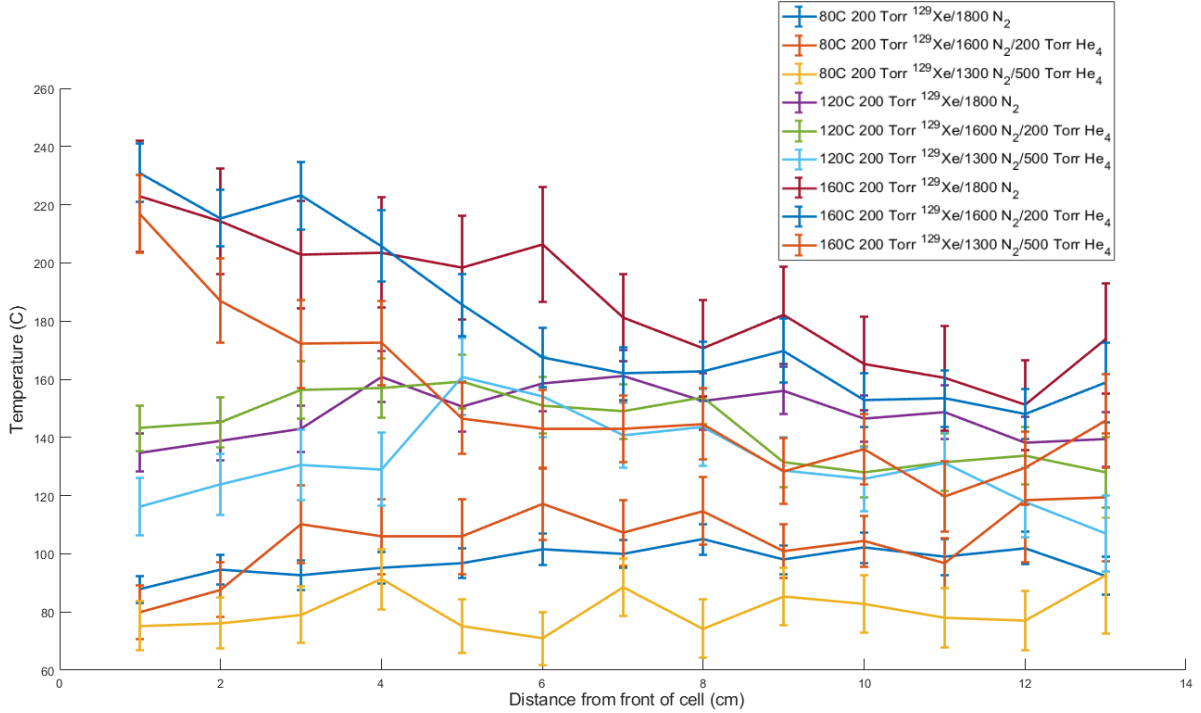


Figure 3.29: 1DTM at different  $^4\text{He}$  fractions in the buffer gas mix. 2000 Torr gas mix with 200 Torr Xe at 80 C, 120 C, 160 C oven temperature in a spread cell after 31-minute build-up

## Discussion

These experiments were undertaken to investigate if, in a spread cell and rich Xe gas mix,  $^4\text{He}$  could reduce the gas temperature gradient within the cell. This, in turn, could have prevented the onset of Rb runaway in a stopped-flow polariser and offered an increased  $P_{\text{Xe}}$  and polarisation build-up rate at higher oven temperatures. The hope was that this could then be applied to current stopped-flow polarisers with rich Xe gas mixes where spread cells are the norm. This could have enabled higher  $P_{\text{Xe}}$ s to be achieved quicker, increasing MRI image quality and HP  $^{129}\text{Xe}$  production speed.

This is in contrast to the conclusion found by J. Birchall et al. when investigating  $^4\text{He}$ 's effect on the polarisation achieved during SEOP in rich Xe gas mixtures in the context of improved patient tolerability [136]. They found a small increase,  $1.13 \pm 0.08$  and  $1.14 \pm 0.04$  in  $P_{\text{Xe}}$  when utilising a buffer gas rich in  $^4\text{He}$  compared to a pure  $\text{N}_2$  buffer gas and was slightly more thermally stable, providing a greater window for SEOP. However, they used a larger  $^4\text{He}$  fraction in the buffer gas mix of 900 Torr (45%) to achieve this and they used a two-inch cell, sub 71 C oven temperatures and 170 W. This is not what the data

indicated with in these experiments.  $^4\text{He}$  at the partial pressures used seemed to offer no benefit to the polarisation achieved at high oven temperatures or improve thermal management in a 1-inch cell. This could be due to the smaller surface area of the 1-inch to allow heat dissipation or due to the smaller  $^4\text{He}$  fractions and thus the small increase in  $P_{\text{Xe}}$  seen by J. Birchall et al. was not observed.

### 3.4.5 Caesium SEOP

The most common alkali metal used in  $^{129}\text{Xe}$  SEOP is Rb. Rb has a large spin exchange cross-section, so it can easily exchange its spin to  $^{129}\text{Xe}$  [137]. Furthermore, Rb only requires a moderate cell temperature to produce a vapour pressure that can facilitate SEOP [138].

Laser technology was perhaps one of the most important factors in Rb's widespread use in SEOP. There are many companies that are producing high-power narrow-band lasers tuned to the Rb  $D_1$  line [139, 140, 141]. Since lasers are one of the biggest expenditures when building a polariser, Rb offered a lower barrier to entry compared to other alkali metals such as Cs or K.

Cs however has several properties that make it more suitable than Rb for  $^{129}\text{Xe}$  SEOP. The binary spin-exchange cross-section between Cs and  $^{129}\text{Xe}$  is between 1-1.90 times the size of the binary cross-section between Rb and  $^{129}\text{Xe}$  [142] increasing with Xe partial pressure. In addition, the spin-destruction cross-section between Cs and  $^{129}\text{Xe}$  is 50% of the Rb and  $^{129}\text{Xe}$ 's spin-destruction cross-section [143]. Therefore the increasing spin destruction from higher  $^{129}\text{Xe}$  partial pressures has less of an effect on Cs polarisation compared to Rb, which becomes more significant in richer mixes. Cs also has a higher vapour density compared to Rb at the same temperature, providing a greater number of Cs nuclei for optical pumping at a given temperature. This could also be thought of as being able to achieve comparable results to the Rb with Cs the requires lower oven temperature, reducing the energy requirement of the system.

Cs is not without its disadvantages; the lack of high-power light sources in the early days of SEOP means it is playing catch-up to Rb. As a result, there are more manufacturers making Rb at 795 nm. This means Cs lasers are still costly compared to their Rb counterparts at a similar power and linewidth. Furthermore, Cs is a harder metal to work with than Rb as it is one of the most reactive metals on the periodic table [144]. When exposed to the oxygen in the air, it can ignite spontaneously, so extra care must be taken when cleaning and loading a cell with Cs. It is also one of only a few metals that is liquid at room temperature. Attention must also be paid to ensure the liquid Cs does not get on the cell windows, as it can easily slide over the SurfaSil<sup>TM</sup> coating to the end of the cell. In a clinical setting, where the HP gas mix is delivered to a patient, the cell must be cooled well below room temperature to prevent the Cs leaving the cell during gas extraction. This is to stop Cs reacting with the moisture in the human body during inhalation, which can cause thermal and chemical burns to the patient. Rb will also react with the moisture, but its reaction is less violent [144, 131, 145]. After the two alkali metals react with the water in the body, they form rubidium hydroxide (RbOH) and caesium hydroxide (CsOH). RbOH and CsOH are severely corrosive to the body tissue and can be destructive to the respiratory tract, which can result in inflammation, chemical pneumonitis and oedema. The subject can then experience symptoms from coughing and

shortness of breath to nausea and vomiting [146, 147]. It is therefore imperative that all alkali metals are separated from the HP  $^{129}\text{Xe}$  gas mix before it is administered to the subject. There is no data for acute lethal doses in humans, however, the median lethal doses ( $LD_{50}$ ) in rats for RbOH and CsOH are 586 mg/kg and 570 mg/kg. It is highly unlikely that a subject will receive a lethal dose of either alkali metal during the inhalation of the HP  $^{129}\text{Xe}$  gas mix, but this does not negate the need to remove the alkali metal to safeguard the subject from the other adverse effects.

### 3.4.6 Comparison between Cs and Rb SEOP in a spread cell

#### Introduction

N. Whiting et al. have compared the polarisation achieved in rich Xe gas mixes when optically pumping on the Cs  $D_1$ , Cs  $D_2$  and Rb  $D_1$  lines. They found Cs to offer a two-fold improvement in polarisation. Another study involving Cs in  $^{129}\text{Xe}$  SEOP looked at using a hybrid of Rb and Cs in the same cell and was undertaken by J. Birchall et al. [148, 115]. They found that, contrary to predictions, Cs suppressed  $P_{Xe}$  from SEOP when introduced to an Rb cell, although it did indicate greater thermal stability and faster build-up time [115]. They also took Raman  $N_2$  measurements of the regime. The resultant  $P_{Xe}$  has been compared when using SEOP with the two alkali metals, and Raman spectroscopy has been used to measure the effect on internal cell  $N_2$  temperature Cs has on a hybrid regime. However, no investigations had been undertaken that compare the in-cell  $N_2$  temperatures between pure Rb and Cs cells during SEOP, and the following experiments aimed to fill that knowledge gap.

#### Methods

The investigation was undertaken using both “lean” (3% Xe) and “rich” (10% Xe) 2000 Torr gas mixes. A lean gas mix was selected as it is the same Xe fraction used in the Polarean 9810 polariser which produces HP  $^{129}\text{Xe}$  for clinical work in the QMC. The rich mix was chosen as it is a similar  $^{129}\text{Xe}$  fraction to the rich regime used in the initial XeNA and XeUS stopped-flow polariser work [25, 24]. This means that the data would have relevance to a range of clinical polarisers, should users be thinking of making the switch to Cs.

Rb and Cs are spread in their respective cells as detailed in Subsection 3.4.2. Two lasers are used: Cs BrightLock and Integra. Each laser performs SEOP on both rich and lean gas mixes. The Cs BrightLock was close to the end of its predicted lifetime, and could not, therefore, exceed 30 W of on-resonance power out of the polarising cube while tuned to the Cs  $D_1$  line. In order to have a like-for-like comparison, the output of the Integra laser from polarising cube also needs to be 30 W. This was achieved by reducing its output power and raising its internal temperature to keep the laser output on the Rb  $D_1$  line. However, it was not possible to reduce the output power to 30 W while keeping the laser within safe operating temperatures. The laser light is not completely linearly polarised when exiting the fibre and after collimation, hence the need for the linear polarising cube. If the cube is rotated about the beam axis, it is possible to increase or decrease the fraction of photons that are transmitted

through the cube. The remaining photons are rejected by the cube and sent to the beam dump. The cube, beam dump and quarter waveplate setup were rotated until the power of the laser light entering the cell was 30 W. By keeping the quarter waveplate in the same orientation relative to the polarising cube, the laser light entering the cell remains circularly polarised.

The cells were run at a range of different oven temperatures to find the optimal oven temperature for each alkali metal. Each experimental run took just over 30 minutes. NMR was taken every 60 seconds and a Raman spectrum every 90 seconds. A 1DTM was also taken at the 30-minute mark. Optimal conditions for each gas mix and alkali are defined as the conditions under which the final  $P_{Xe}$  is highest. Optimal final  $P_{Xe}$  and build up rate ( $\gamma_{SEOP}$ ) are calculated by fitting a Box-Lucas exponential function to a graph of  $P_{Xe}$  against time. The equation for  $\gamma_{SEOP}$  can be seen in Equation (3.18). It is the reciprocal of the build-up time ( $T_B$ ), which is the product of the spin exchange ( $\gamma_{SE}$ ) and spin destruction ( $\gamma_{SD}$ ) rate.

$$\gamma_{SEOP} = \frac{1}{T_B} = \gamma_{SE} + \Gamma_{SD} = \gamma_{SE} + \frac{1}{T_1} \quad (3.18)$$

## Results

The rich  $P_{Xe}$  build-up curves are shown in Figures 3.30 and 3.31 for the Cs and Rb cell, respectively. A greater maximum  $P_{Xe}$  under optimal conditions was achieved in the Cs cell compared to the Rb cell.

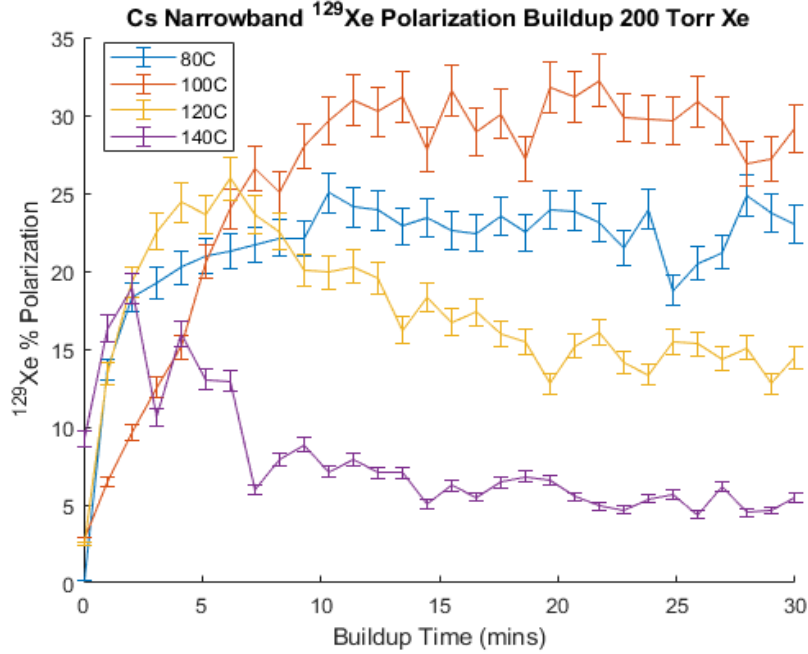


Figure 3.30:  $P_{Xe}$  build-up curves with a 200 Torr Xe and 1800 Torr  $N_2$  gas mix in the Cs cell using a 30 W laser

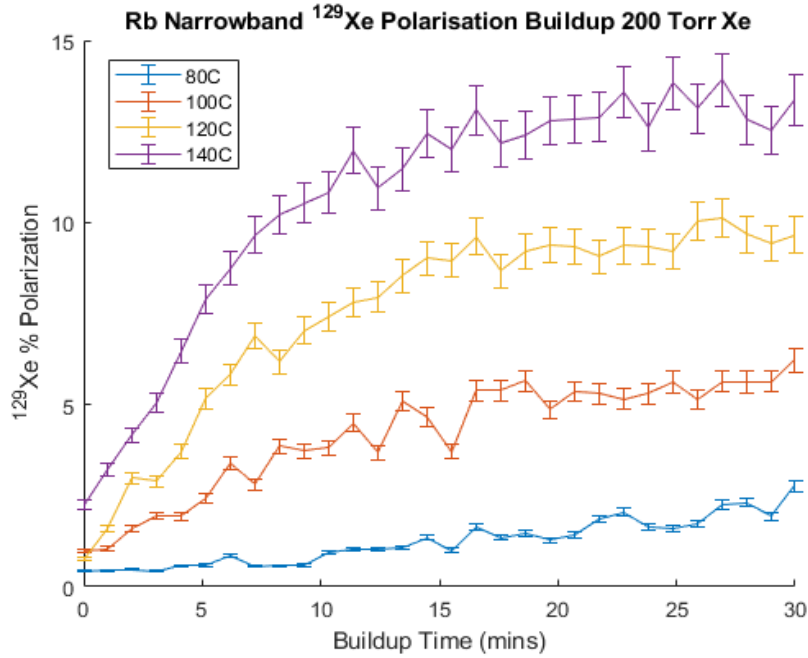


Figure 3.31:  $P_{Xe}$  build-up curves with a 200 Torr Xe and 1800 Torr  $N_2$  gas mix in the Rb cell using a 30 W laser

The Cs cell achieved a maximum  $P_{Xe}$  of  $30.5\% \pm 1.1\%$  and the Rb a maximum  $P_{Xe}$  of  $13.3\% \pm 0.4\%$ . Optimal build-up curves are presented in Figure 3.32.  $\gamma_{SEOP}$  was not significantly different between the two alkali metals, despite the difference in  $P_{max}$ . The data concurs with the results presented by N. Whiting [149], which also showed an approximate two-fold increase in  $P_{Xe}$  when optical pumping on the Cs  $D_1$  line compared to the Rb  $D_1$  line under optimal conditions. Due to the low Xe partial pressure ( $>250$  Torr), the spin-exchange cross-section between Xe and Rb/Cs is not significantly different according to measurements made by N. Whiting et al. [149]. The main contributing factors in the difference in maximum  $P_{Xe}$  between Rb and Cs are thought to be increased Cs vapour density and the lower energy Cs  $D_1$  line, meaning there are more photons per watt of light compared to Rb. The optimum Cs run had an average internal  $N_2$  temperature of  $205C \pm 11C$  compared with  $162C \pm 19C$  of the optimum Rb run. A slight elevation in  $N_2$  temperature was measured in the middle of the cell, attributed to the hot air being forced into the outer cell through the central stem. The average internal  $N_2$  temperature was 100 C above the oven temperature for the Cs cell and only 20 C for the Rb cell at optimal conditions. This is due to the higher partial pressure of Cs compared to Rb [138], resulting in a higher Cs vapour density and therefore increased laser light absorption at lower oven temperatures.



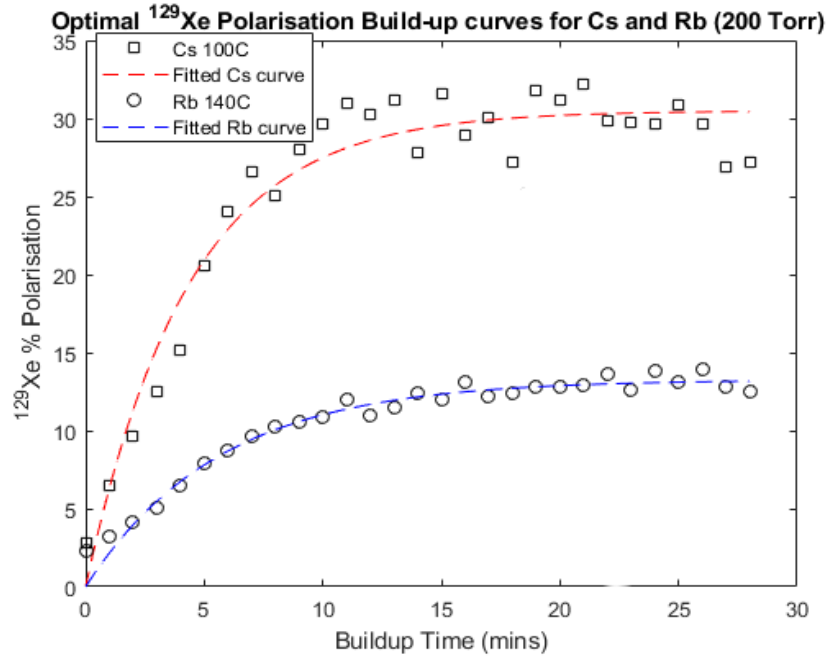


Figure 3.32: Optimal build-up curves using a with 200 Torr Xe and 1800 Torr  $N_2$  gas mix in the Cs and Rb cells

Under optimal oven conditions, the temperature difference between the front and back of both cells was small, at 16.6 C for the Cs cell and 19.9 C for the Rb cell (see Figures 3.33 and 3.34). The lack of a strong thermal gradient between the front and back of the cell and the polarisation build-up curves indicate that neither cell entered runaway. Once the Cs cell's oven temperature was increased to 120 C, the cell entered the runaway regime. This is shown by the front  $N_2$  temperature significantly increasing from  $\approx 179$  C to  $\approx 329$  C at respective oven temperatures of 100 C and 120 C. The runaway feedback loop increased the Cs vapour density at the front of the cell, absorbing more of the pump laser and reducing light transmission to the rear of the cell. As a result of Cs runaway, a significant thermal gradient of 163 C along the cell can be seen in the 1DTM. With increased opacity, the Cs polarisation dropped and increased the proportion of unpolarised Cs, which then absorbed more incoming laser light, adding to the runaway feedback loop. The reduction in Cs polarisation, in turn, reduced the final  $P_{Xe}$  to  $15.9\% \pm 1.1\%$ .

**N<sub>2</sub> Raman 1D Temperature Maps along the cell, Cs Narrowband 200 Torr Xe**

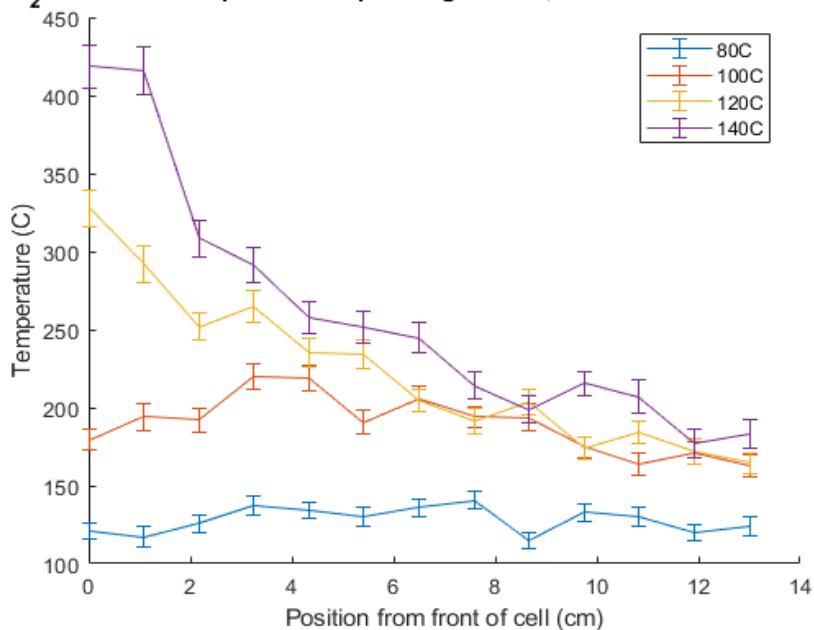


Figure 3.33: 1D temperature maps with 200 Torr Xe and 1800 Torr N<sub>2</sub> gas mix in the Cs cell

**N<sub>2</sub> Raman 1D Temperature Maps along the cell, Rb Narrowband 200 Torr Xe**

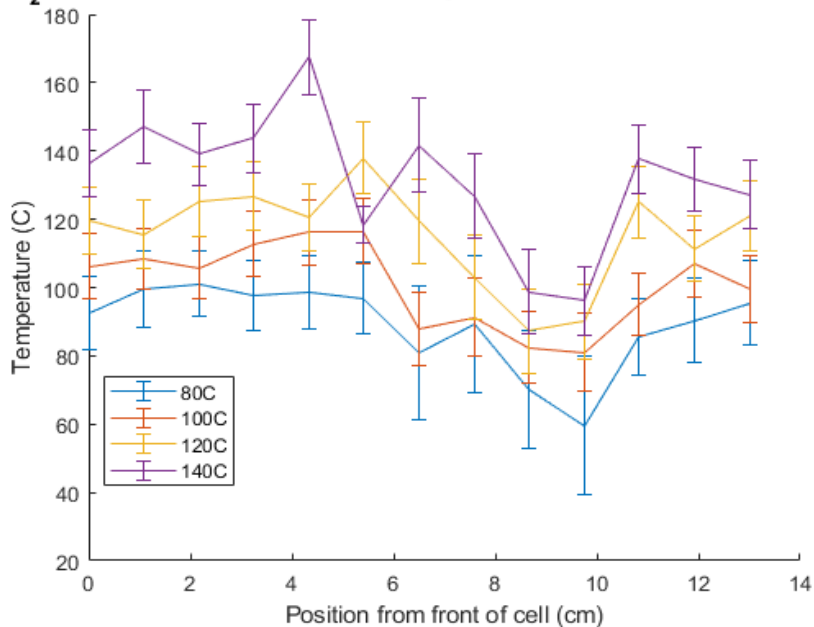


Figure 3.34: 1D temperature maps with 200 Torr Xe and 1800 Torr N<sub>2</sub> gas mix in the Rb cell

Increasing the oven temperature to 140 C exacerbates the effects of runaway and the  $N_2$  temperature therefore rises. At 140 C, the front  $N_2$  temperature was 418 C with a thermal gradient of 236 C along the cell. After peaking, the  $P_{Xe}$  reduced to an even lower steady polarisation of  $5.9\% \pm 0.8\%$  because of the more extreme Cs runaway.

The Rb cell did not enter runaway conditions under any of the oven temperatures investigated. The final Rb polarisation increased with oven temperature, as a result of higher Rb vapour density. The average  $N_2$  temperatures were  $107C \pm 10C$ ,  $126C \pm 15C$ ,  $137C \pm 19C$  and  $162C \pm 19C$  for oven temperatures of 80 C, 100 C, 120 C and 140 C, respectively. These are slightly elevated over the oven temperature due to the laser heating. The temperature gradients along the cell were less than 25 C for all oven temperatures. This shows that the Rb vapour density was low enough that the regions towards the rear of the cell were not shadowed by those at the front.

In the lean gas mix, the lower partial pressure of  $^{129}Xe$  caused the ( $^{129}Xe$  -  $^{129}Xe$ ) and (Rb or Cs -  $^{129}Xe$ ) spin destruction collisions to decrease. This allowed the  $P_{Xe}$  to build up to a higher value, as shown in Figure 3.35 and 3.36. Although the percentage  $P_{Xe}$  is higher in the lean mix compared to the rich mix, the bulk magnetisation is lower. This agrees with the results found by N. Whiting [150] and confirmed in the XeNA and XeUS rich mix stopped-flow clinical polarisers studies [25, 24].

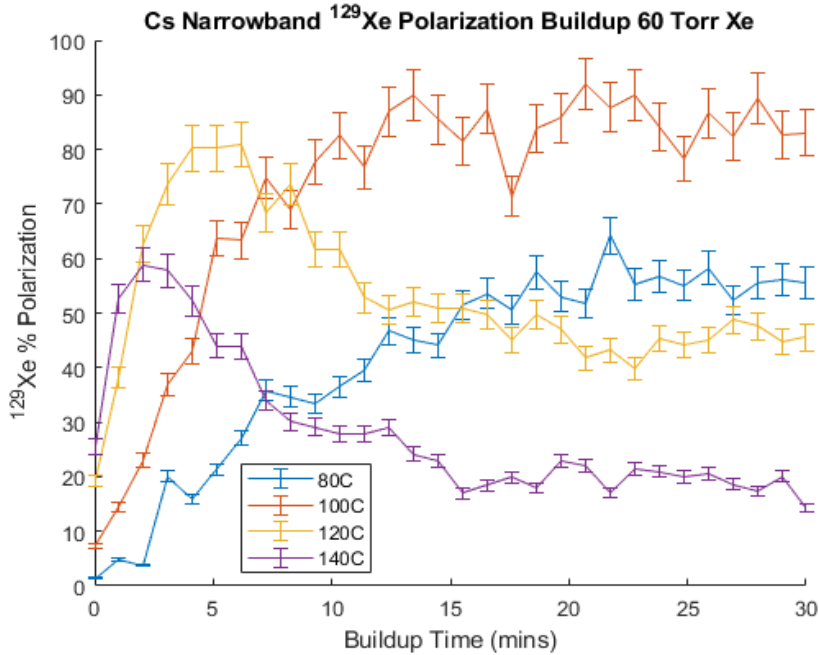


Figure 3.35:  $P_{Xe}$  build-up curves with 60 Torr Xe and 1940 Torr  $N_2$  gas mix in the Cs cell

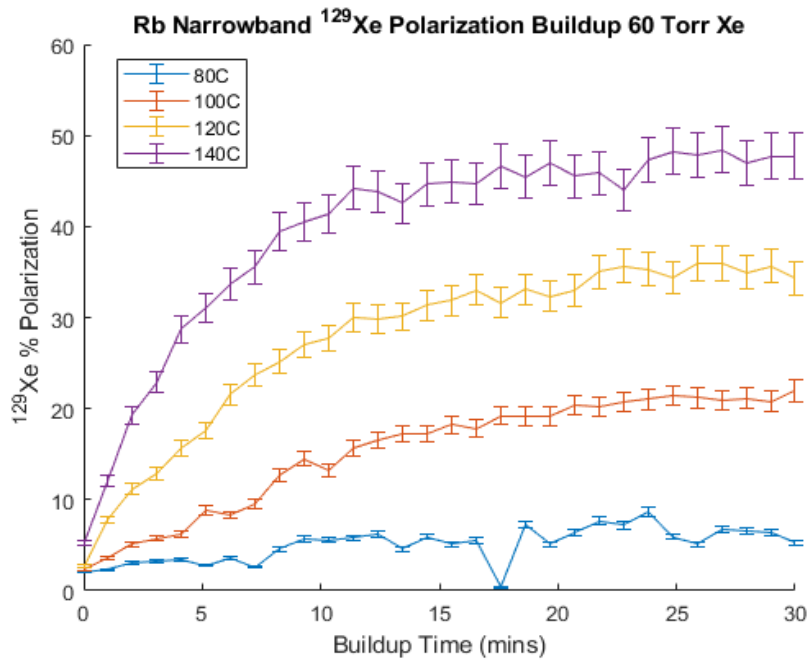


Figure 3.36:  $P_{Xe}$  build-up curves with 60 Torr Xe and 1940 Torr  $N_2$  gas mix in the Rb cell

The optimal oven temperatures for the lean mixes were the same as for the rich mixes, at 100 C for the Cs cell and 140 C for the Rb cell. The optimal polarisation build-up curves are shown in Figure 3.37. A maximum  $P_{Xe}$  of  $87.0\% \pm 3.3\%$  is achieved in the Cs cell and  $46.9 \pm 0.9\%$  for the Rb cell. There was no significant difference in build-up rates between the rich and lean Cs cells. The Rb cell saw a small increase in the optimal build-up rate, attributed to the reduced spin destruction from  $^{129}\text{Xe}$ , which has a more significant effect on Rb polarisation compared to Cs polarisation.

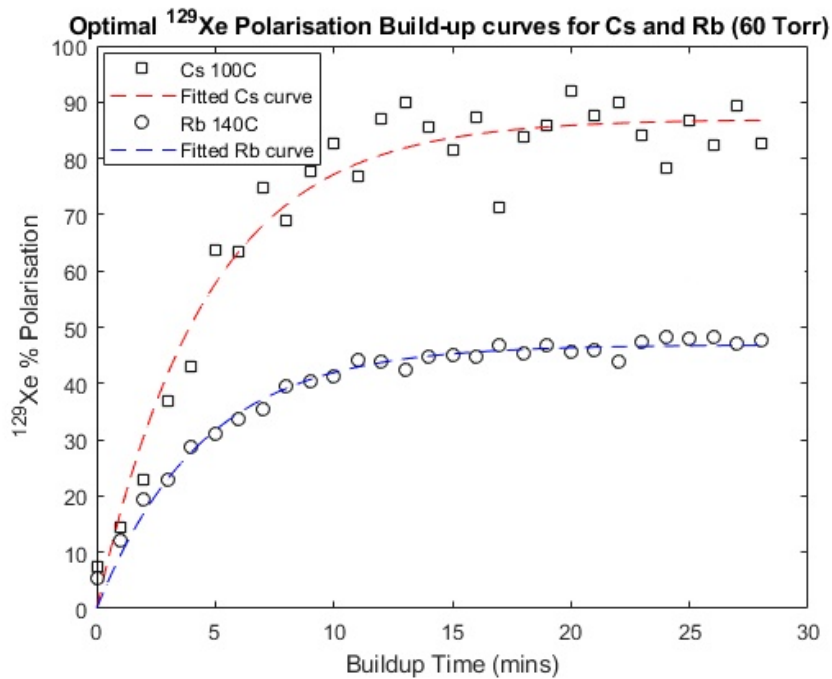


Figure 3.37: Optimal build-up curves with a 60 Torr Xe and 1940 Torr  $N_2$  gas mix in the Cs and Rb cells

The internal  $N_2$  temperature was lower in the lean mix than in the rich mix, as were the thermal gradients across the cell. 1DTMs for the lean mix are shown in Figures 3.38 and 3.39. For the optimal oven temperatures, the temperature gradient from front to back was less than 11 C for both cells. The average cell temperature across the Rb cells was lower in the leaner mix, but the difference was not significant.

In the order of ascending oven temperature, the average  $N_2$  temperature in the Rb cell was calculated to be  $93C \pm 6C$ ,  $117C \pm 9C$ ,  $139C \pm 9C$  and  $160C \pm 13C$ . The increased  $N_2$  partial pressure and the reduced  $^{129}Xe$  partial pressure also contributed to the reduction in the  $N_2$  temperature in the lean gas mix. Energy absorbed by the  $N_2$  in quenching collisions was spread over a larger amount of  $N_2$  molecules. The thermal conductivity of the lean gas mix was also higher because  $N_2$  has a higher thermal conductivity than  $^{129}Xe$  [94]. Therefore, the leaner gas mixes can conduct more heat away to the cell walls.

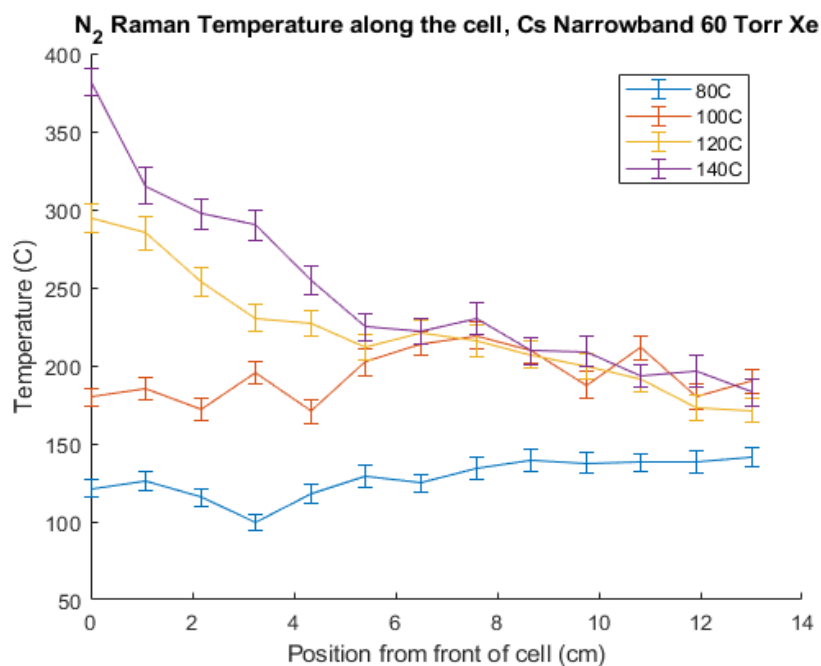


Figure 3.38: 1D temperature maps with 60 Torr Xe and 1940 Torr  $N_2$  gas mix in the Cs cell

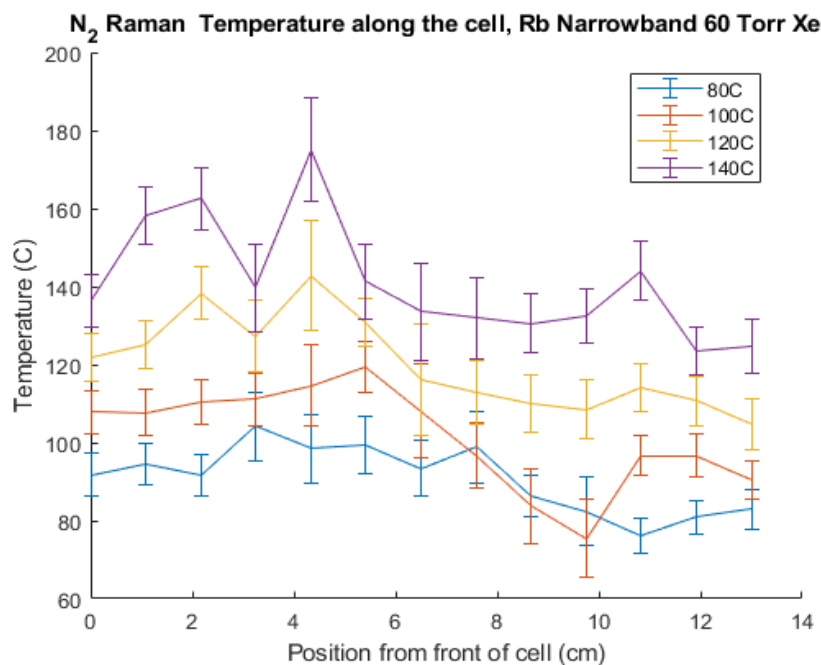


Figure 3.39: 1D temperature maps with 60 Torr Xe and 1940 Torr  $N_2$  gas mix in the Rb cell

## Discussion

The  $P_{Xe}$  data confirms the findings of N. Whiting [149] that, under optimal SEOP conditions and using comparable laser power, Cs offers a two-fold improvement in the  $P_{Xe}$  compared to Rb. Optimal conditions of Cs can be achieved at a significantly lower oven temperature than Rb requiring less energy to achieve a greater final  $P_{Xe}$ .

Measuring the  $N_2$  temperature with Raman spectroscopy showed that, although the Cs can offer a higher  $P_{Xe}$  at lower oven temperatures the system can also be pushed into runaway conditions at lower oven temperatures. During runaway the temperature at the front of the cell can be upwards of 170 C above the oven temperature, which causes a significant reduction in the final polarisation.

The increase in  $^{129}Xe$  partial pressure increases the bulk magnetisation that can be achieved with both Cs and Rb. The internal  $N_2$  temperature does, however, rise as a result. This temperature rise is predicted to be more pronounced in richer gas mixes and when using more powerful lasers. If using Cs for SEOP in a stopped-flow polariser using a high-powered laser (>150 W), like with the XeUS platform discussed in Chapter 4, the thermal management of the cell will only require very low oven temperatures to produce high  $P_{Xe}$  levels. However, the oven temperature will need to be tightly controlled as small temperature fluctuations could cause significant changes in Cs vapour density and push the system into runaway.

Utilising Cs in a clinical setting could open the door to a higher  $P_{Xe}$  in similar production times. Alternatively, if speed, not ultimate polarisation was the goal, Cs could lower the HP  $^{129}Xe$  production time to reach an equivalent  $P_{Xe}$  target compared to Rb. A lower duty cycle time is beneficial as bags can be produced quicker, meaning more images can be taken during a subject's visit or visit times can be shortened, reducing costs.

In future work, it would be beneficial to repeat these experiments using a higher-powered laser (>150 W) so that the data is more representative of the regimes seen in stopped-flow clinical polarisers.

## 3.5 Conclusion

These experiments used Raman spectroscopy to investigate the effect of different starting conditions on the  $N_2$  temperature inside the cell during  $^{129}Xe$  SEOP. This is to inform the operators of stopped-flow clinical polarisers so that they can maximise the  $P_{Xe}$  achieved on their devices.

The first set of experiments found that  $^4He$  does not offer a significant improvement in the thermal management or the final  $P_{Xe}$  in a one-inch spread cell in the  $^4He$  fractions studied. However, in a clinical setting, the addition of  $^4He$  would reduce the density of the gas and, as suggested by J. Birchall, may make the gas more tolerable to patients as it is easier to inhale [136]. This potential increased tolerability would have to be quantified and weighed against the increased costs of  $^4He$  in the gas mix to determine its value in a clinical setting.

The comparison of SEOP between Cs and Rb in a spread cell found that the Cs enters runaway at lower oven temperatures. If a Cs cell can be kept out

of the runaway regime, the  $P_{Xe}$  can be  $\approx$  two times higher than Rb. Thermal management is the key to achieving high  $P_{Xe}$  with Cs. Controlling the cell temperature is even more essential in stopped-flow clinical polarisers with richer  $^{129}\text{Xe}$  gas mixes and higher laser powers [24, 25].

The drawback to these experiments is the low power of the lasers used. It was not possible to investigate the internal  $N_2$  temperatures with high laser powers equivalent to those used in the current stopped-flow clinical polarisers [24, 25].

The range of Xe partial pressures used offered a good starting point for these initial experiments. However, they were too low to take advantage of the difference in Rb-Xe and Cs-Xe spin-exchange cross-sections exhibited at higher Xe partial pressures. Using lower-powered lasers and Xe partial pressures therefore only gives an indication of behaviour expected at higher laser powers and not an exact prediction. Increasing the laser power and the range of Xe partial pressures used is recommended as the next step in this work. Higher laser powers and rich Xe gas mixtures with Rb resulted in higher bulk magnetisation at the optimum temperatures, which is discussed in Section 4.2.2. Using Cs in this regime could result in higher final bulk magnetisation. The high Xe partial pressures should also result in faster build-up times as the Cs-Xe spin-exchange cross-section at the pressure will be above that of Rb-Xe, providing thermal management is robust enough. Taking tandem Raman data in the regime described would give a total picture of the thermal dynamics within the cell when using Cs compared to Rb.

It is important to note that, despite the advantages displayed by Cs in these experiments, Rb is used in all the SEOP polarisers detailed in the following chapters. This is due to the availability of the lasers at both the University of Nottingham and Wayne State University. The cost of procuring equivalent power Cs lasers to replace the Rb lasers already acquired would have been on the order of £10,000 per laser, which was not feasible in the scope of this thesis.



## Chapter 4

# Upgrade and quality assurance of a N-XeUS2 stopped-flow xenon-rich SEOP polariser

### 4.1 Introduction

This chapter details the construction, redesign and testing of the N-XeUS2, a semi-automated stopped-flow clinical polariser. This polariser is an upgrade of the N-XeUS polariser built by J. Skinner [151] and the upgrade involved modification of most of the polariser's sub-systems.

The purpose of the N-XeUS2 is to hyperpolarise  $^{129}\text{Xe}$  via SEOP for clinical research. The end goal is to deliver HP  $^{129}\text{Xe}$  to patients and healthy volunteers in the SPMIC unit in the QMC. The N-XeUS2 will replace a Polarean 9810 continuous-flow polariser [152]. This chapter starts with a comparison of continuous and stopped-flow polarisers and then discusses the operation and construction of the N-XeUS2 as well as its previous design iterations. The chapter concludes with the results of testing the XeUS2 design, including its polarisation build-up rates, maximum polarisation and cell lifetimes, comparing them to the Polarean 9810.

### 4.2 Stopped-flow vs continuous-flow polarisers

#### 4.2.1 Operation

##### Continuous-flow polarisers

By definition, a continuous-flow polariser continually flows the Xe gas mixture through the optical cell during SEOP. The theory of SEOP is described in Section 2.4.7. The HP  $^{129}\text{Xe}$  is collected and separated from the rest of the gas mix using cryo-collection [21]. Cryo-collection works by flowing the HP  $^{129}\text{Xe}$

gas mix through a cold finger submerged in liquid  $N_2$ , which creates a low-temperature surface that causes the cryo-collection of  $^{129}\text{Xe}$  gas. The liquid  $N_2$  does not cause the buffer gases ( $N_2$  and  $^4\text{He}$ ) to solidify, as  $^{129}\text{Xe}$  solidifies at a higher temperature (161 K). It can therefore be separated from the buffer gases and collected in solid form.

The amount of polarisation loss during storage is dictated by the  $T_1$  relaxation of  $^{129}\text{Xe}$ . The cold finger is kept in a high magnetic field to increase the  $T_1$  of the HP  $^{129}\text{Xe}$  [153]. After the desired amount of  $^{129}\text{Xe}$  has been collected, it is then quickly thawed out [153] and delivered to a bag before it is given to the patient.

The Polarean 9810 is the continuous-flow polariser used to produce HP  $^{129}\text{Xe}$  for the work undertaken in Chapters 5, 7 and 8. Which utilises a lean mixture of between 1% and 3% naturally abundant Xe, 10%  $N_2$  and the balance  $^4\text{He}$ . It operates at a cell temperature of 130 C, using a pre-saturator to increase the Rb vapour density with the cell. A full description of its hardware and operation can be found in Chapter 5.

### Stopped-flow polarisers

In a stopped-flow polariser, the optical cell is filled with the required gas mix and then sealed [25]. During SEOP, the cell remains sealed until the  $^{129}\text{Xe}$  has reached the desired polarisation level. The cell is then cooled, causing the alkali metal to condense back into a solid, which separates it from the HP gas mix. Cooling ensures the gas mixture is at a temperature that does not damage its target. The cell is then opened, and the HP gas mix is delivered to its target. For clinical polarisers, the HP gas fills a Tedlar bag for inhalation [25]. Raman experiments in Chapter 3 also use a stopped-flow procedure, although, in those experiments, the gas was not sent to another location after SEOP had taken place.

## 4.2.2 Gas mixes

### Continuous-flow polarisers

In continuous-flow polarisers, the gas mix is resident inside the cell for a short period of time and exploits the fast spin exchange between Rb and  $^{129}\text{Xe}$  to hyperpolarise the  $^{129}\text{Xe}$ . The method was first employed by Driehuys et al. using a laser with a broad linewidth [20]. The gas is run through the cell at high pressure, broadening the Rb  $D_1$  line for efficient absorption of the pump laser photons. At higher pressures, however, the Rb-Xe spin destruction rate is increased (See Equation (2.24), in Chapter 2).

In order to minimise spin destruction, the partial pressure of Xe is kept low, leading to a lean Xe gas mix of typically 1-3% [154]. Cryo-collection is therefore a vital part of a continuous-flow polariser as it enables a sufficient volume of HP  $^{129}\text{Xe}$  to be collected from a lean gas mix. This poses a problem as the  $^{129}\text{Xe}$  slowly depolarises while it is being stored in solid form. A balance needs to be struck when selecting the flow rate of the gas through the cell. A quicker flow rate will mean a shorter collection time for a set volume of Xe gas. A faster flow rate also means there is less time for Rb-Xe spin exchange to occur, reducing the percentage polarisation of gas leaving the cell. A more in-depth explanation

of the theory and exploration of this parameter space is discussed in Section 2.4.7.

The buffer gases used in continuous-flow polarisers are typically  $N_2$  and  $^4He$ , whose function has already been described in Section 2.4.7. The Xe then flows to the target for continuous NMR and MRI measurements.

### Stopped-flow polarisers

Stopped-flow clinical polarisers typically use higher Xe fractions in their gas mixes ( $> 10\%$ ) compared to continuous-flow polarisers. As a result, they do not have to flow gas mixes through the cell and perform cryo-collection to produce an HP gas sample with sufficient volume and bulk magnetisation.

There is an unexpected relationship between the peak polarisation of  $^{129}Xe$  and its partial pressure in the cell [150]: higher Xe gas densities achieved peak polarisation at lower temperatures [150]. This relationship was discovered during stopped-flow Xe studies using volume holographic grating narrowed laser diode arrays (VHG LDAs) [150]. The VHG LDAs could offer a narrower spectral width, reducing the FWHM from 2 nm to 0.3 nm. However, VHG feedback makes tuning the central wavelength of a VHG LDA non-trivial compared to simple thermal tuning ( $\approx 0.3$  nm/C) of in standard LDAs [155]. The increased coupling between the narrowed lasers output and the Rb  $D_1$  line negated the need to pressure broaden the Rb  $D_1$  line with high gas pressures inside the cell. Furthermore, the  $^4He$  is no longer required in the gas mix to further broaden the Rb  $D_1$  line.

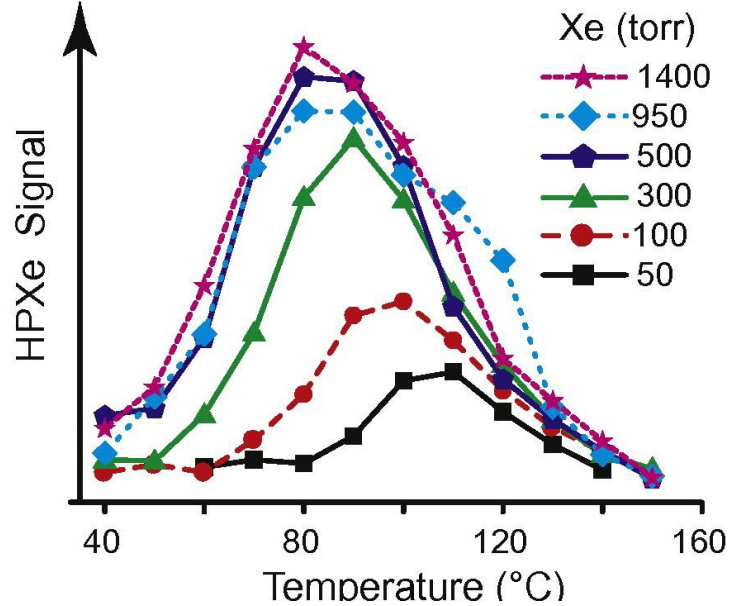


Figure 4.1: HP  $^{129}Xe$  signal for rich Xe gas mixes and oven temperatures reproduced from [150]

When using richer Xe gas mixes with these narrower lasers, the polarisation was higher than expected based on previously reported data [156]. The polarisa-

tion did not fall to zero as the Xe partial pressure increased, but rather reached a non-zero steady-state [157]. Results showed that the optimum temperature for maximum percentage polarisation reduced as the Xe partial pressure increased. However, under optimum conditions, higher Xe partial pressures gave higher bulk magnetisations, despite the percentage polarisation reducing.

The inverse relationship between optimum cell temperature and Xe density is linked to Rb spin destruction. This is related to the spin rotation interaction between Rb and Xe. At higher  $^{129}\text{Xe}$  partial pressure, this interaction causes the Rb vapour to become less transparent, meaning less of the Rb vapour will undergo optical pumping. As less laser light is transmitted through the whole cell, the Rb polarisation and in turn  $P_{Xe}$  are reduced.

In order to counteract the increased Rb vapour opacity, its density must be reduced. By reducing the oven temperature, less Rb is vaporised and pump laser transmission through the cell is increased. Since high-power lasers are being used, there is an excess of photons on the Rb  $D_1$  line. As the  $^{129}\text{Xe}$  fraction increases so does the SEOP rate; Rb density can therefore be reduced for an equivalent laser power to achieve the optimal  $P_{Xe}$ .

### 4.3 XeNA

“XEnon polarisatioN Automated” (XeNA) was the first stopped-flow polariser created by the multi-team consortium between researchers at Vanderbilt University, Southern Illinois University and the University of Nottingham. The consortiums’ goal was to create a cost-effective open-source  $^{129}\text{Xe}$  polariser. The reason behind this design goal was that the polariser could then easily be replicated for a relatively low cost by any other team that needed a  $^{129}\text{Xe}$  polariser for their research. To achieve this, XeNA is composed of mostly stock parts that are easy to procure [158].

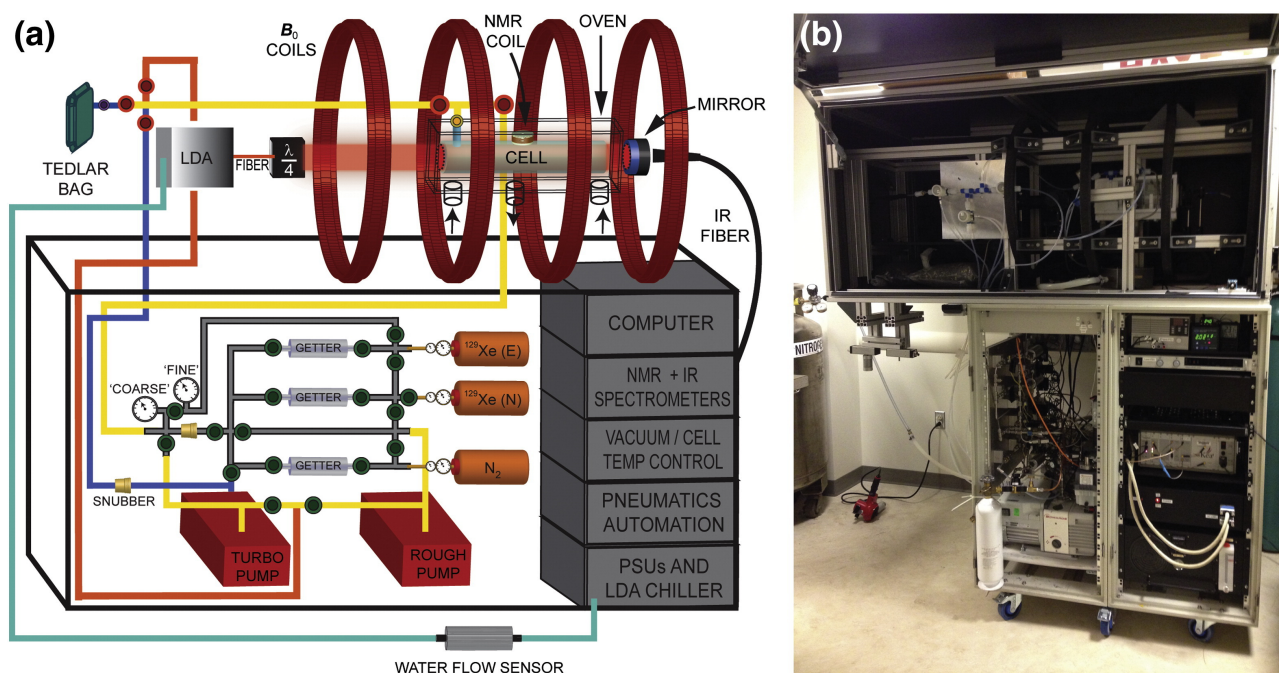


Figure 4.2: Diagram and photo of the XeNA polariser reproduced from [25]

XeNA was the first step towards creating a fully automated polariser and was built around an Arduino Mega 2560 micro-controller. The Arduino controls the gas handling manifold, laser power, and NMR systems. It also monitors the cell temperature and manifold pressure using a bespoke GUI. The GUI was created using a software package called “Processing” [159]. Both Arduino and Processing are free software packages and are open source, in keeping with XeNA’s design ethos [158].

XeNA’s cells were filled with gas mixes with pressures up to 2000 Torr and could produce one litre of HP gas mix per hour. XeNA was able to produce samples with 90%, 57%, 50%, and 30%  $P_{Xe}$  at 300 Torr, 500 Torr, 760 Torr and 1570 Torr partial pressures of  $^{129}Xe$ , respectively [25]. The polariser is currently in use at Brigham Women’s Hospital at the Harvard Medical School, where it produces HP  $^{129}Xe$  for various lung imaging studies [160].

XeNA comprises the following sub-systems: a 200 W frequency-narrowed laser, a gas handling manifold, a vacuum pump system, a magnetic  $B_0$  field created by four 24-inch Helmholtz coils, an automated control system and an oven for the optical cell.

The gas used in the heating and cooling systems comes from a self-pressurising liquid,  $N_2$  Dewar. To produce hot air for the oven, the gas is passed through a pair of 400 W heat pipes mounted inside an aluminium enclosure. Liquid  $N_2$  is used instead of forced air because it means XeNA is not reliant on an external compressed airline to operate, increasing the number of locations it can be used. XeNA can perform cryo-collection if needed, but the high bulk magnetisation produced with the rich mixes negates the need for this step. Full details and specifications of the XeNA are discussed in a paper by P. Nikolaou et al. [158].

## 4.4 XeUS

The lessons learnt from the XeNA polariser enabled the design to be refined and led to the creation of a second-generation polariser, the “Xenon Ultimate Spin-exchange” (XeUS). This polariser is an improvement on the XeNA as it has a simpler design and fully automated operation. The simpler design reduces the build cost and the number of components needed, aligning the XeUS even closer with the low-cost, open-source mission statement set out by the consortium. Refinements to its design automation increased its ease of use, streamlining the training process for new users. This section covers the sub-systems that make up the XeUS and acts a primer for the sections discussing further iterations of the design, i.e. the N-XeUS and N-XeUS2.

### 4.4.1 Gas handling manifold

Compared to the XeNA, the XeUS’s gas handling manifold is simplified by reducing the number of pneumatic valves. Fewer valves mean fewer connections, decreasing the chance of leaks in the manifold. Furthering its simplicity, the XeUS only uses one pre-mixed cylinder of Xe/N<sub>2</sub>. This comes at the expense of flexibility, as the cylinder needs to be swapped out should another gas mix be required. In a clinical setting, however, this is not a large drawback as, once the gas mix is selected, the chance of it being changed is low.

$\frac{1}{8}$ -inch tubing is used where possible to reduce the manifold’s dead volume and therefore reduce the polariser’s gas consumption. This has the added benefit of removing the need for a gas snubber, as the thinner tubing is able to impede the flow rate of the gas, reducing the stress the glass cell experienced while it is filled.

A particle filter was installed on the outlet side of the manifold between the cell and the bag. This removes any residual Rb vapour in the Xe gas mix during gas extraction.

### 4.4.2 Oven and TEC thermal management system

The body of the XeUS oven is 3D printed using a fused deposition modeling (FDM) 3D printer with a polycarbonate filament [161]. Its 3D printed design offers several advantages over traditional manufacturing methods. It allowed for rapid prototyping, so the final design could be reached more efficiently and quicker than with traditional processes where each design iteration has to be sent off to a fabricator. The lid, thermoelectric cooler (TEC), cell mounts, optical window, rotary blower and NMR coil mount all fit flush with the oven body. The resolution of modern 3D printers means that there is no air gap between the oven walls and any of the components [162]. Continuity of the components means the oven is well insulated. Polycarbonate is used to 3D print the oven as it offered the best compromise between structural and thermal properties. The point where polycarbonate becomes soft and deforms (glass transition temperature) [163] is 161 C and the temperature at which it deflects under load (heat deflection temperature) [164] is 138 C [161]. These properties impose a maximum operating temperature of the oven of 100 C. The oven walls are also made as thick as possible to reduce heat loss. Where the oven walls have to be thinner, foam was added to compensate, keeping insulation as consistent

as possible [161]. 3D printing allows cell mounts to be printed integral to the oven. This means that, when aligning the cell with the beam of the laser, the oven and cell act as a single unit. After initial alignment, further adjustments are not needed when cells are swapped over, as they can only be positioned in one orientation.

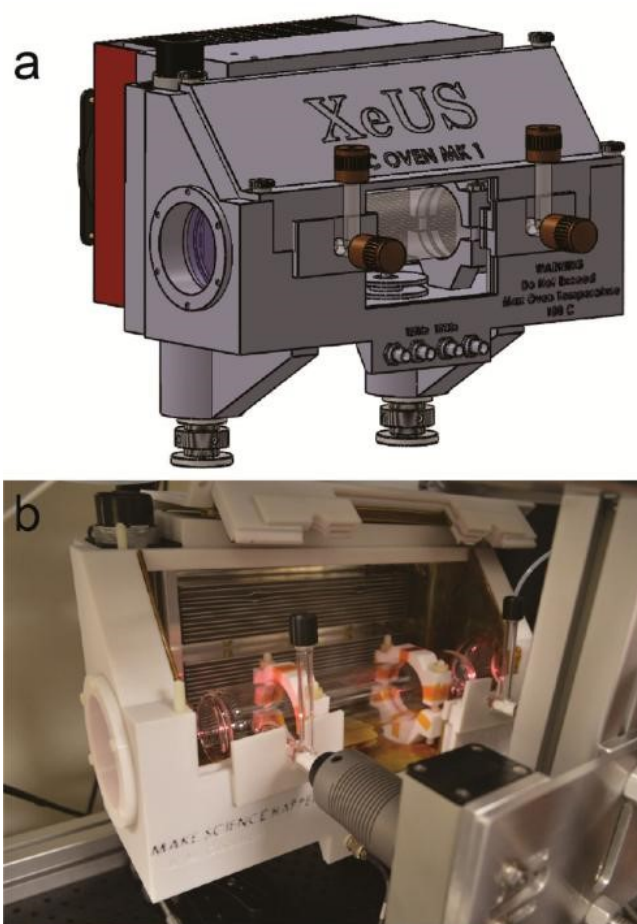


Figure 4.3: a) CAD drawing of the 3D-printed oven with TEC mounted to the rear and cell mounted inside. b) Photo of cell mounted in the oven with lid and insulation removed

The temperature regulation of the oven is controlled by an Oven Industries 5R7-001 Thermoelectric Controller connected to an air-to-air TEC, a Kryotherm Thermoelectric 380-24-AA cooling assembly.

A vertical rotary blower placed in the oven's corner creates forced convection between the TEC elements and the cell. Without this forced convection, the change in temperature would be much slower. An exploded CAD drawing of the oven and TEC sub-system can be seen in Figure 4.4.

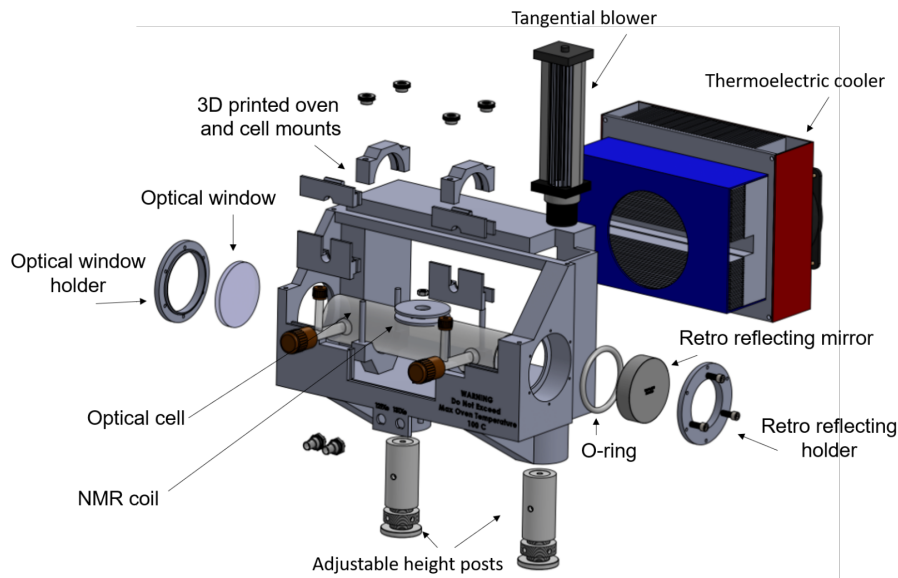


Figure 4.4: Labelled exploded diagram of the oven and TEC sub-system

The TEC is used to ensure the temperature of the cell can reach and maintain a specified set point for optimal SEOP. The TEC relies on the Peltier effect [165], where heating or cooling occurs between two conductors with different electronegativities and work functions at an electrified junction. When a direct current passes through the device, one conductor increases in temperature while the other decreases, and the inverse occurs when the direction of the current is reversed. The TEC can therefore heat and cool the cell. The TEC has a heat sink on either side, radiating heat either into the oven or out to middle polariser section. Fans keep the heat sink of the outer element at room temperature, making it possible for the element on the inside of the oven to go below room temperature when cooling is required. The Oven Industries 5R7-001 thermoelectric controller uses a PID feedback loop, monitoring the temperature with a thermocouple attached to the surface of the cell and continually adjusting the current sent to the TEC. The GUI displays the thermocouple reading and the TEC heating/cooling power, giving real-time feedback. The user can control the oven temperature via the GUI either manually or automatically during a pre-programmed sequence.

#### 4.4.3 Automation system

XeUS’s automation uses the same Arduino micro-controller and GUI software as used in the XeNA, although several improvements have been made. The laser and Helmholtz coil power supplies, the TEC and pneumatic valves on the gas handling manifold are all incorporated into the automation system. This makes XeUS fully automated, with every system controllable via the GUI [24]. Having total control of the system enables “single-button” operation. When instructed, the software will move XeUS through the entire stopped-flow SEOP procedure and can produce a bag of HP  $^{129}\text{Xe}$  with no outside intervention. The XeUS’s



fully automated design improves user experience and ease of use over the XeNA. If manual control is needed, this can be accessed via the GUI, giving greater utility to the system if non-standard operations are required. This manual mode also allows new protocols and sequences to be tested before implementation.

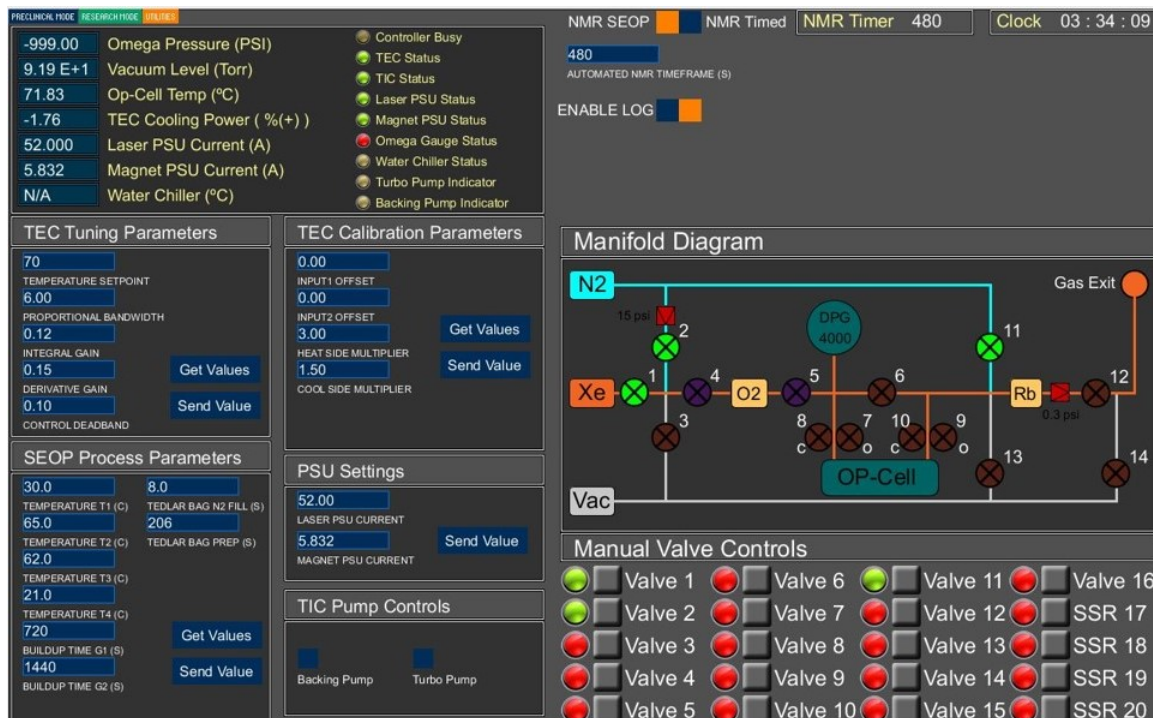


Figure 4.5: Original XeUS GUI

#### 4.4.4 XeUS performance

The XeUS was able to deliver an in-cell  $P_{Xe}$  of 95%, 73%, 60%, 41% and 31% at Xe partial pressures of 275, 515, 1000, 1500 and 2000 Torr, respectively. The full study was published by the consortium in 2014, verified with low field 47.5 mT MRI after the HP  $^{129}\text{Xe}$  gas mix was released to a Tedlar bag [24].

### 4.5 N-XeUS

This section briefly covers the modifications made to the original XeUS design through to its next iteration, the “Nottingham Xenon Ultimate Spin-exchange” (N-XeUS). These modifications were performed by J. Skinner and are fully detailed in his thesis [151].

#### 4.5.1 Gas handling manifold

The gas handling manifold design was altered to accommodate two gas cylinders so that a pure  $N_2$  cylinder could be incorporated in addition to the Xe/ $N_2$  mix. The pure  $N_2$  replaced the Xe/ $N_2$  mix when performing the purge/evacuation

cycles of the manifold. These cycles are required to ensure that the lines are clear of contaminants before cell filling so that the Rb within the cell is not poisoned.

Using pure  $N_2$  reduced the polariser's running costs, as  $N_2$  is far cheaper than  $^{129}\text{Xe}$ . This is significant in a clinical setting with high throughput.  $N_2$  is also easier to vacuum down than a Xe gas mix and more likely to carry any contaminants with it. These purge cycles mean only a rotary pump is needed to remove atmospheric  $O_2$  and other impurities from in the inlet manifold to a level where their effect on the Rb is negligible. This negated the need for a turbo pump backing the rotary pump, increasing the simplicity of the design. The second cylinder also increased the utility of the N-XeUS as  $N_2$  can fill the rest of the cell after the desired  $^{129}\text{Xe}$  partial pressure has been reached. This allows more gas mixes to be used in the polariser as the ratio of Xe to  $N_2$  can be altered. Although this is not essential for a clinical setting, it makes it possible to test different Xe/ $N_2$  ratios without having to swap out cylinders. This is useful when investigating which gas mix offered the optimal  $^{129}\text{Xe}$  bulk magnetisation.

#### 4.5.2 $B_0$ field system

The original XeUS used four magnetic coils to generate a  $B_0$  field required for SEOP [166]. To achieve the best  $P_{Xe}$ , possible  $T_1$  relaxation should be kept to a minimum [31]. In order to maximise SNR for NMR measurements, the  $T_{2^*}$  must be minimised [31], which is achieved by maximising the homogeneity of the magnetic field. The N-XeUS reduced the number of coils in this Barker arrangement from four to three and gave the user more space to work in the polariser. This makes replacing the delicate glass cells far easier. The three coils were repositioned and adjusted to optimise the  $B_0$  field homogeneity [166].

### 4.6 N-XeUS2

This section provides a detailed description of the N-XeUS2, an updated version of the N-XeUS. All the following work undertaken on the N-XeUS2 was carried out within the scope of this thesis. For completeness, the section details all sub-systems of the polariser:

- Chassis
- Gas management system
- $B_0$  field
- Oven and TEC thermal management system
- Pump laser system
- NMR measuring system
- Automation system

Each subsection explains the changes made from the N-XeUS design and the reasoning behind them. Results produced from N-XeUS2 are also discussed and compared with the Polarean 9810. The final stage of the N-XeUS2 work presented is a long-term QA study investigating the cell the lifetime.

#### 4.6.1 Chassis

The chassis is a simple box frame composed of three sections (see Figure 4.6). The middle section contains the optical train, TEC, oven, Helmholtz coils, IR spectrometer, gas cylinders and gas handling manifold. This section is enclosed but can be accessed by two doors on the front of the polariser. Once the doors are closed and locked, the chassis provides an optically enclosed environment. This means that the N-XeUS2 can be operated as a class-1 device and does not require the use of laser goggles, as long as the doors are closed. The doors are both wired to an interlock system, meaning the power to the laser PSU is cut when they are opened. Two banks of fans sit on top of the middle section and provide ventilation. The fans remove the heat generated by the laser and the TEC. This is vital as both the laser and cell's temperatures must be tightly controlled as overheating can cause irreversible damage to the laser or runaway in the cell. Additionally, the fans assist the TEC when it is cooling the cell for gas extraction.

The lower section is unenclosed and contains the micro-controller, compressor, water chiller, vacuum pumps and all the PSUs. This means the user can turn the various sub-systems on and off without having to access the optically enclosed middle section. Cooling fans are mounted to the back of this lower section to keep the devices cool while under operational load to prevent them from overheating.

The frame itself is made of aluminium box sections supplied by Minitec. Aluminium was chosen as it is non-magnetic so does not affect the homogeneity of the  $B_0$  field. Both the walls and roof of the middle section are made of Alupalite sheeting. Alupalite consists of a corrugated plastic core sandwiched between two thin aluminium sheets. This rigid material is both durable and light-tight when mounted into the aluminium frame.

The load-bearing floor of the middle section is made of a single aluminium sheet. The overall dimensions of the polariser are 175.26 cm high by 137.16 cm long by 81.28 cm wide. Its size means it can fit through most building corridors and doors. The polariser sits on a set of four heavy-duty brake caster wheels, making it portable. The chassis was designed at Vanderbilt University using the computer-aided design (CAD) program SolidWorks.

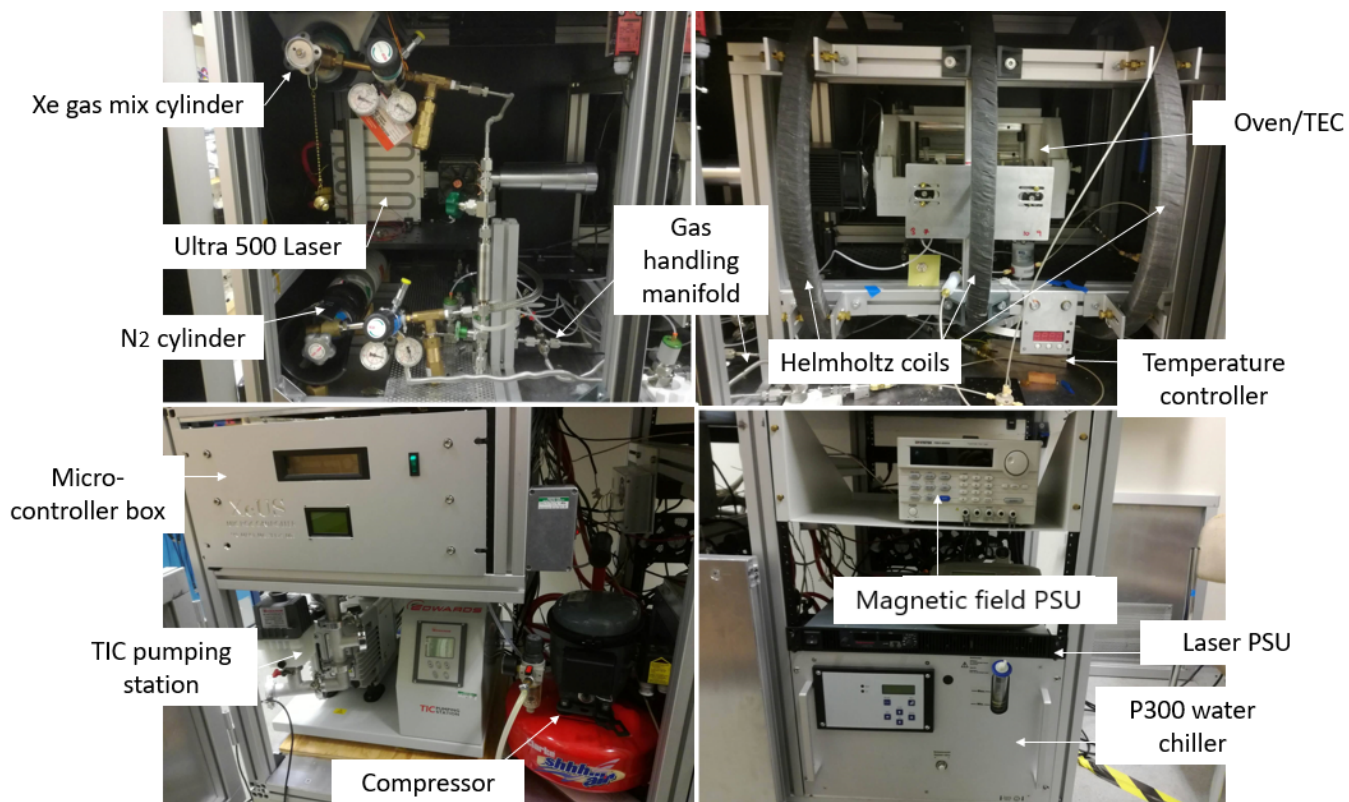


Figure 4.6: Photos showing the N-XeUS2 with all the main components labelled

#### 4.6.2 Gas management system

A complete diagram of the N-XeUS2's gas handling manifold and parts list can be found in Appendix: Figure B3 and Table B4. Pictures of the different manifold sections can be found below in Figure 4.7 and a simple graphic representation of the manifold layout is shown in Figure 4.9.

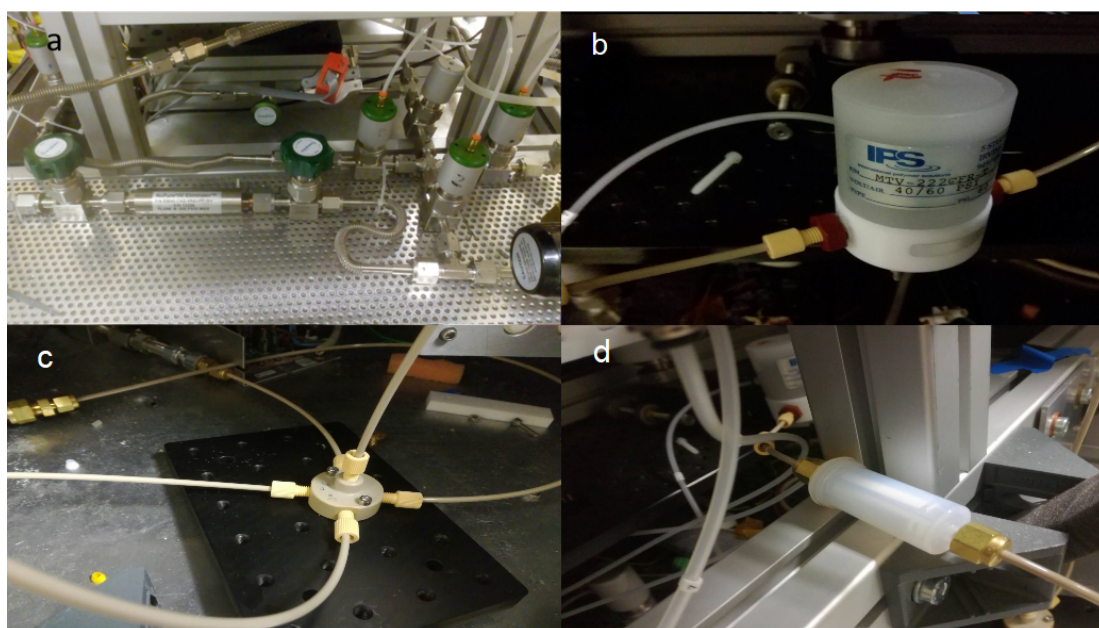


Figure 4.7: a) Section of the VCR fittings and CAG eliminator b) “Valve 12” plastic pneumatic valve c) Section of the outlet side of the manifold showing the PEEK connectors d) Rb filter on the outlet side of the manifold

In the N-XeUS2, the gas management system is composed of gas cylinders, getters, an optical cell, a Tedlar bag and a manifold connecting them all. The manifold was upgraded due to the demand for longer cell lifetimes, which are dictated by the Rb quality in the optical cell. Rb reacts with any impurities entering the cell, such as  $O_2$ , limiting the maximum polarisation that a cell can achieve (see Section 3.4.2). Over time, Rb poisoning increases as it is exposed to more impurities, and the maximum  $P_{Xe}$  decreases until the cell is no longer viable for use. Each cell therefore has a finite lifetime. It is advantageous to maximise this lifetime to enable the polariser to produce the highest  $P_{Xe}$  possible for the largest number of bag fills. Cleaning a cell also comes with incurred costs which, if the cell lifetimes are short, may be significant in a clinical setting where throughput is high.

The gas handling manifold is composed of two sides: the inlet and outlet. The inlet side takes the gas from the cylinders to the cell, while the outlet side delivers the HP gas from the cell to the Tedlar bag.

The N-XeUS used PTFE tubing between valves, which allowed atmospheric impurities to leach into the manifold. Western analytical “Vacutight” plastic nut and ferrule connectors were used to mate the tubing to valves. These connectors were not rated to the vacuum levels required for the purge/evacuation cycles and would also deform the PTFE tubing, which made leaks at the connections more likely. The N-XeUS manifold also used plastic pneumatic valves from International Polymer Solutions (IPS), some of which had a defect which caused them to leak when actuated. A complete rebuild of the manifold was required using new components as the N-XeUS cell’s lifetime was only on the order of 10s of runs.

The manifold was rebuilt with metal components where possible to prevent diffusion of atmospheric gases and to reduce leaks. The valves used on the inlet side of the N-XeUS2 manifold are 316L Stainless Steel High Purity Bellows Sealed Valves from Swagelok. These valves use vacuum coupling radiation (VCR) fittings, which have a negligible leak rate of  $4 \times 10^{-9}$  std cm<sup>3</sup>/s [167]. Most of the connectors on the inlet side of the manifold also use VCR connectors. The other connection types used on the inlet side of the manifold are also rated to hold the vacuum and pressure levels required. The connections are Klein Flange (KF) fittings to connect the manifold to the Edwards rotary vacuum pump and vacuum gauge and National Pipe Taper (NPT) connectors to connect the gas cylinder regulators and the Omega pressure gauge to the rest of the manifold.

A getter is situated on each gas line between the cylinders and the inlet manifold; these remove any impurities from the gas before it enters the manifold and cell. The getters on the N-XeUS2 were upgraded to NuPure CAG Eliminators, which guarantee a purity of <0.5 ppb for H<sub>2</sub>O, O<sub>2</sub>, CO<sub>2</sub>, CO, H<sub>2</sub>, NMHC and CH<sub>2</sub>. Compared to the Entegris air purifiers used in the N-XeUS, the CAG Eliminator offers a two-fold increase in purity for H<sub>2</sub>, CO<sub>2</sub> and CO and an increase of eight orders of magnitude for H<sub>2</sub>O and O<sub>2</sub>, which are the main gases that cause Rb poisoning.

The outlet side of the manifold is constructed from non-ferrous materials to decrease HP <sup>129</sup>Xe depolarisation as it is released to the bag. Polyetheretherketone (PEEK) was found to have properties that made it an ideal material for the outlet manifold. PEEK tubing is employed as a steel replacement in many HPLC systems [168] and is one of the few plastics that can be used in ultra-high vacuum applications. Besides these advantages, it is easy to work with as it is flexible, mechanically stable and easy to cut.

The N-XeUS2 outlet manifold is constructed from  $\frac{1}{8}$ -inch OD PEEK tubing. Valves 6, 9/10, 11, 13 and the Rb filter are connected using the PEEK tubing via a five-port PEEK manifold assembly. A PEEK tee-piece connected the tubing between valve 12, 14 and the bag. The manifold and tee-piece are connected to the PEEK tubing via an Upchurch flangeless nut and ferrule. The PEEK tubing connects to the VCR valves via male VCR to  $\frac{1}{8}$ -inch Swagelok adapters, which are made of steel. Only a small part of the gas will “see” the steel adapters as they are not in the path the gas takes from the cell to the bag so polarisation losses will be minimal.

An Entegris GT Plus in-line gas filter is used to prevent any uncondensed Rb vapour reaching the bag and, by extension, the patient. The filter sits on the path the gas takes from the cell to the bag. The Entegris is attached to the tubing via two  $\frac{1}{8}$ -inch Swagelok brass nuts/ ferrule pairs. The brass components do not come into direct contact with the gas, and since brass is non-ferrous, it does not contribute to <sup>129</sup>Xe depolarisation.

In order to prevent any backflow of gas from the bag to the cell, a one-way PEEK BIO-CHEM 973 263-3001 valve is also connected to the tubing via the Upchurch nuts and ferrules. One pneumatic valve sits on the extraction pathway from the cell to the bag and is listed as “Valve 12” on the manifold diagram. It was not possible to use a steel VCR Swagelok pneumatic valve, so a plastic IPS valve was used instead. The specific valve was tested for leaks and selected as it did not have the leak behaviour exhibited in other IPS valves. Valve 12 is also connected to the PEEK tubing via Upchurch nuts and ferrules. Finally,

the bag was connected to the manifold by a glass chem thread adapter. After the new manifold was constructed, the TIC rotary pump was able to achieve a vacuum on the order of  $10^{-3}$  Torr on the inlet side and  $10^{-2}$  Torr on the outlet side. These are both lower than the minimum vacuum achieved by the Polarean 9810, which has long cell lifetimes and produces HP  $^{129}\text{Xe}$  with long  $T_1$  times in a Tedlar bag. When evacuating the inlet and outlet sides of the manifold, three  $\text{N}_2$  purge/evacuation cycles are completed on each side independently; the inlet side before cell filling and the outlet side before the gas is released to the bag.

### 4.6.3 $B_0$ field

The Barker arrangement used to create the  $B_0$  field have not changed from the three-coil design implemented by J. Skinner. Coils 1, 2 and 3 have the following respective properties: number of turns: 179, 95, 179, inductance (mH): 35, 18, 35, resistance (Ohms): 1.6, 1, 1.7. The coils were positioned by J. Skinner to achieve a homogenous  $B_0$  field and were not changed for the N-XeUS2.

The PSU was changed from a Sorensen XG 80-10.5 to a Kenwood PDS60-12 regulated DC, as the Kenwood has ripple noise 2.5 times lower than the Sorensen [169, 170], ripple noise being the broadband noise of the power supply. [171]. The Kenwood also offers greater current stability, meaning the current supplied to  $B_0$  coils fluctuated less about its set point. This ensures the  $B_0$  field strength remained consistent, critical in obtaining a useable water signal given the long times used for data collection.

### 4.6.4 Oven and TEC thermal management system

The oven design was not changed from that of the original XeUS polariser discussed above, however an issue was found with the current system. When TEC is in operation, it generates a large amount of noise at approx 40.4 kHz that can be picked up by the NMR coil as the current delivered to TEC rapidly fluctuates when it is close to its temperature setpoint (see Figure 4.8 a) ). This is because the Oven Industries 5R7-001 [172] is based on pulse width modulation (PWM) in conjunction with the PID feedback loop. When the TEC is at 100% power, its current is constant, and the noise disappears, as shown in Figures 4.8 c) and d) compared to the spectra obtained with the TEC off (Figure 4.8 b)).

In order to remove the noise peaks from the NMR spectra, the TEC was turned off during NMR acquisitions. However, the cell's temperature was not managed during this time. Due to the high laser power, the internal gas temperature could increase significantly while NMR is being acquired, so Rb runaway could be initiated while the TEC is turned off. As a result, the maximum oven temperature was limited to enable NMR acquisitions, which are essential for QA, to be taken without triggering Rb runaway. In order to remove the noise without turning off the TEC, the Arduino code controlling NMR acquisition was modified. Just before the NMR pulse was triggered, the TEC was set to 10 C below its set point, and the code waited for six seconds. The pause allows time for the TEC to respond to the setpoint change and have 100% of its power dedicated to cooling, allowing for a constant current and no background noise peaks. The spectrometer is then triggered, and, after NMR acquisition, the TEC set point would revert to its original value. As the NMR acquisition time is so short, the TEC does not have enough time to significantly reduce the oven

temperature before the setpoint is reverted. This solution was not discovered until after the work at Wayne State University was completed, where the old NMR protocol was used.

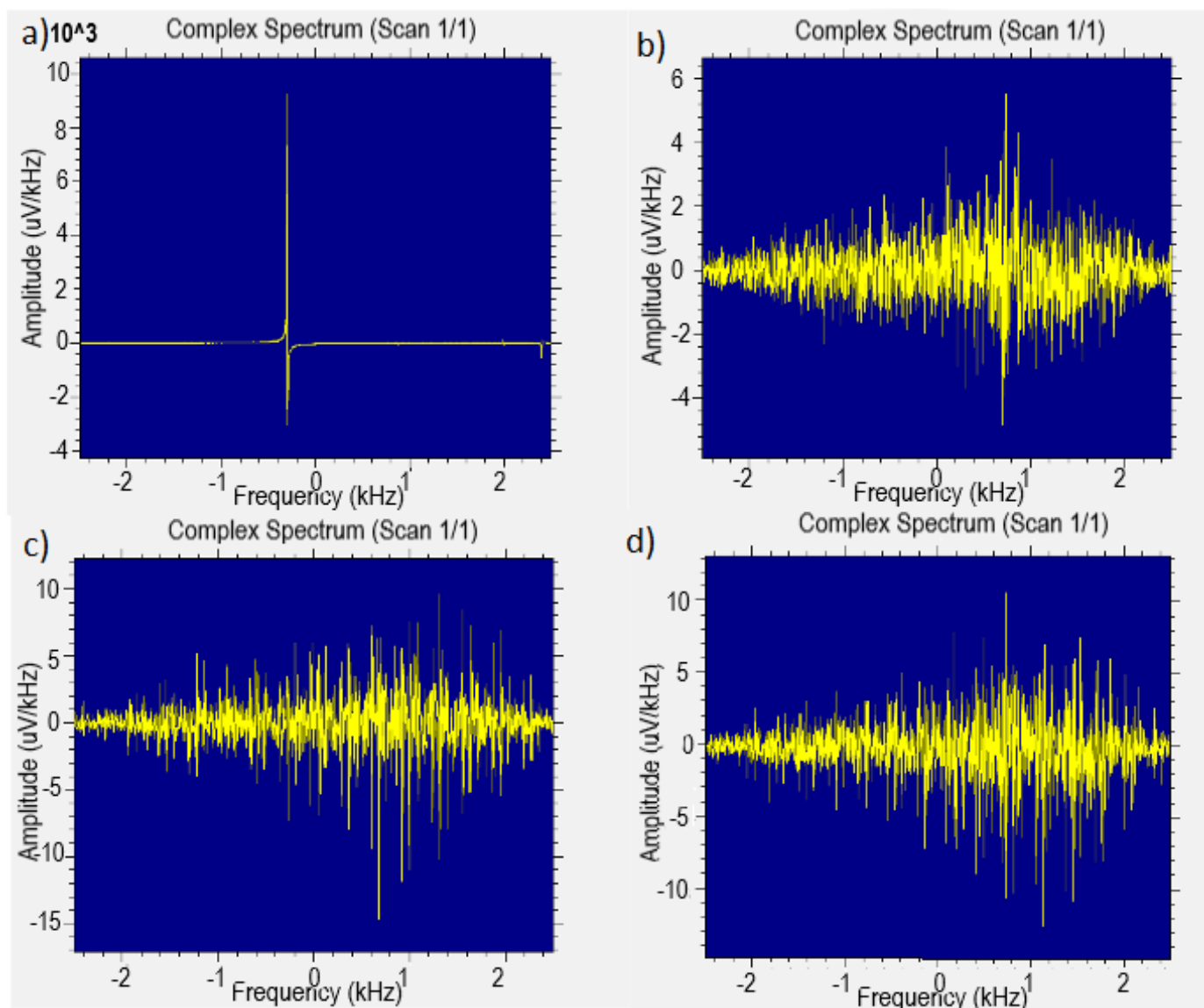


Figure 4.8: Graphs to show the noise that can be detected on the NMR coil when the TEC is a) operating at less than 100%. (Graph y axis scale:  $10^3 \mu\text{V}/\text{kHz}$ ) b) Off (Graph y axis scale:  $\mu\text{V}/\text{kHz}$ ), c) 100% heating (Graph scale y axis:  $\mu\text{V}/\text{kHz}$ ) d) 100% cooling (Graph scale y axis:  $\mu\text{V}/\text{kHz}$ )

#### 4.6.5 Automation system

Like the XeUS, the N-XeUS2's automation system is built around an Arduino Mega 2560 micro-controller. The system is controlled by a GUI based on the



software “Processing”. In the N-XeUS2 upgrade, the Arduino and GUI code were both modified.

The Arduino Mega 2560 is a more advanced version of the Arduino Uno microcontroller and has a larger memory for code (sketch memory) and more random-access memory (RAM). This allows the user to write more input and output (I/O) lines into their code [173], which is essential when automating the N-XeUS2, where the Arduino communicates with many sub-systems and conveys information to and from the GUI. Crucially, the Mega has more hardware and software ports than the Uno, allowing it to communicate with more devices at once.

During testing, the Mega would often lose communication with the GUI, and the polariser would become unresponsive. The GUI would respond to user input, but no commands would be received by the Arduino and no sensor data would be received by the GUI. The only way to regain communication was to restart the Arduino and GUI. Upon restart, the polariser reverted to its initial settings. This would not be acceptable in a clinical environment as software crashes would halt production of  $^{129}\text{Xe}$ , wasting scanner time and the costs associated with a clinical run. Furthermore, losing control of the gas handling manifold and laser could be potentially hazardous if it occurred at the wrong moment. This could result in the laser overheating and becoming damaged or the manifold over-pressuring the cell, which could potentially cause an explosion. Error diagnosis was not easy as, when the Arduino froze, it would not give any error messages. Eventually, the source of the communication loss was found to be a serial communication library.

The Arduino has four hardware ports connected to:

- PC/GUI communication
- TIC controller
- TEC controller
- Omega pressure gauge

These communicate with Arduino via hardware serial communication (HSC). The rest of the sub-systems have to use the Arduino’s software ports via software serial communication (SSC). These are:

- Laser power supply
- Magnet power supply
- LCD screen
- Debug messages

HSC is built into the Arduino hardware and devices using HSC are connected to the Arduino via physical pins specifically dedicated to HSC. HSC is the quickest and most reliable method of communication the Arduino uses. Devices using HSC can also communicate in tandem with other tasks and can transmit and receive data at the same time. Lastly, HSC is built into the Arduino integrated development environment (IDE), so no extra software libraries need to be installed. For this reason, devices that needed to communicate fast-changing

information communicated with the micro-controller via HSC in the N-XeUS2 [174].

On the N-XeUS2 there are more sub-systems than hardware pins, meaning some devices need to be connected via virtual ports. These also connect physically via pins in the same way as those using HSC, but have to communicate using SSC. A software library called “Software Serial” was installed to facilitate SSC. This library makes it possible to use the digital pins on the Arduino for serial communication, increasing its capacity. The drawback is that only one of the digital pins can perform SSC at a time. The loss of communication between the GUI and Arduino was linked to the poor long-term stability of Software Serial.

There were two solutions:

- Use a different software serial communication library
- Eliminate software serial communication

The GUI and Arduino codes are complex and were originally written by A. Coffey, who was no longer available to offer consultation. Software serial libraries vary, so replacing the library would have required the GUI and Arduino code to be rewritten. This would have been time-consuming, and the possibility of introducing new errors was high. The decision was therefore made to eliminate the SSC from the code, as the sub-systems using the SSC do not strictly require automation. The LCD screen displays no information that is not easier to observe through the GUI or the instruments’ own display screens. The magnet power supply will only ever be at two current values, one for  $^{129}\text{Xe}$  NMR and one for water signal acquisition. These will never have to be switched between dynamically. Code debugging can be done through the hardware ports connected to the PC. Lastly, the laser system does not require adjustment once it has been brought up to power and temperature. The laser was also deemed to be safer under manual control; should Arduino lose control of the PSU, the laser could be damaged before the user notices and can regain control of the system.

Once all software communication was removed from the code, its stability was tested. The Arduino was able to communicate with the GUI for over 48 hours without issue. The code was then modified to remove inputs from the old serial software sub-systems so that the code would not stop and wait for variables that no longer existed. The removal of these features in the automation process did not affect the production time of the polariser or increase operational complexity.

An extra feature added to the automation system was the ability to create custom gas mixes via the GUI. The polariser will be in a clinical setting for most of its operational life, so will use a one pre-selected gas mix. However, if the user requires a different gas mix, the usual procedure on the N-XeUS would be to change the gas cylinder. This requires multiple  $^{129}\text{Xe}/\text{N}_2$  gas cylinders, meaning the costs associated with running the polariser will increase. In addition, there will be downtime while the cylinder is changed. This complexity makes changing cylinders less appealing, reducing the flexibility of the device and its ability to test different  $\text{Xe}/\text{N}_2$  ratios.

It was possible to fill the cell with custom  $\text{Xe}/\text{N}_2$  gas mixes using the  $\text{N}_2$  and pre-mixed cylinders and by actuating the manifold valves manually. A small lag between the Arduino receiving the pressure value from the Omega gauge and it

being displayed on the GUI made it almost impossible to fill the cell accurately. This accuracy was further reduced when human reaction time was factored in, leading to poor consistency between identical custom gas fills. A new function was therefore written into the Arduino and GUI code which allowed the cell to be filled with custom gas mixes automatically. Utilising an 80% Xe 20%  $N_2$  gas cylinder, the user can select the percentage of  $^{129}\text{Xe}$  they want in their final gas mix. The polariser will then automatically fill the cell with the pre-mixed Xe/ $N_2$  until the correct Xe partial pressure has been reached; the remainder is then filled with pure  $N_2$ . To prevent selecting a percentage that could overpressure the cell if a value of over 80% is selected, the GUI displays an error message asking for a lower value. Any Xe percentage can be selected from 1% to 80%, offering greater flexibility than swapping between pre-mixed cylinders.

For added safety, an “Abort” button was programmed into the GUI which, when pressed, halts the polariser’s operation and return it to its idle state. The abort button means the user can stop any automation sequence while in progress, bypassing the safety checks that prevent two sequences running at once. Once the polariser is returned to its idle state, the user can then troubleshoot the behaviour that prompted them to hit the “Abort” button. The manifold displayed in the GUI was also altered to match the new getter location (see Figure 4.9). Lastly, a button was created for to start the QA testing automation sequence which is explained in Section 4.8.

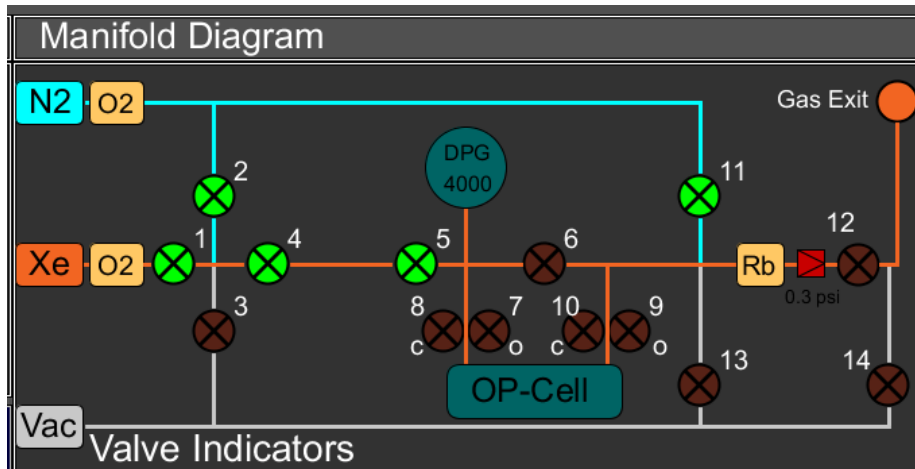


Figure 4.9: N-XeUS2 manifold diagram, displayed in the GUI

The full wiring diagram for the N-XeUS2 automation can be seen in Appendix A Figure B1, and the key for the diagram is shown in Figure B2.

#### 4.6.6 Laser system

The N-XeUS used a 150 W laser at (Ultra 500, QPC, Sylmar California, USA) laser manufactured by QPC. When the N-XeUS2 redesign process started, the laser was replaced because it had been run at a temperature above recommended settings, which led to a drop in its output power. The laser was replaced with a QPC micro-channel cooled (MCC) 170 W laser which utilised the same optical

train as the Ultra 500. The optical train was enclosed within the laser and telescope. This makes the alignment of the optical train easier and more resistant to knocks as parts cannot move independently of one another. The polariser can then be moved to different locations without having to go through a lengthy realignment process each time.

In order to manage the temperature of the MCC laser, chilled water is flown through the micro-channels cut into the cooling plate of the laser. Micro-channels are small tubes with diameters of  $\approx 100\mu m$ . The surface area of the interface between the cooling plate and the coolant in an MCC system is much larger than in a conventional laser cooling system, where the water passes through a single large pipe. This design makes cooling more efficient, so more power can be produced by each diode, as they can be driven at a higher current without overheating [175]. The higher laser power produced by the MCC laser should give improved SEOP and higher  $P_{Xe}$ .

The MMC design does, however, come with drawbacks. The coolant passing through the micro-channels needs to be within specific conductivity and cleanliness parameters. Deionised (DI) water was selected as it has low electrical conductivity, which reduces the chance of a short circuit within the micro-channels. However, if the conductivity is too low, the DI water will electrochemically react with the copper micro-channels, corroding them and thus reducing their cooling efficiency and effectiveness. The size of the micro-channels also makes them vulnerable to blockages from any particulates in the coolant. Blocked channels reduce the localised cooling ability around them, leading to localised failure of the diodes as they overheat [176]. The MCC laser is also very sensitive to humidity, so dry compressed air must flow over the diodes during operation to prevent condensation. Humidity is monitored by a passive sensor on the top of the laser.

The DI coolant meant that the previous K-O Concepts 600 W water chiller had to be replaced with a Termotek P312. The P312 has several features that make it suitable for use with the high-power MCC laser. Firstly, it has a cooling capacity that ranges from 200 W to 3 kW, so more than capable of dissipating the heat load from the MCC laser. The user can tune the conductivity of the coolant via a sensor and DI cartridge filter, which cleans up the DI water to an appropriate level of conductivity. The chiller will also send out an alarm if the coolant is not meeting the temperature, conductivity or flow-rate set by the user. If the alarm were not present, the laser could be exposed to damaging conditions for a prolonged period before the user noticed.

Before connecting the P312 to the MCC laser, the DI water was run through the chiller and connecting pipes in a closed loop. This was performed in order to clean up the water in the lines to the correct conductivity and filter out particulates before connecting it to the laser.

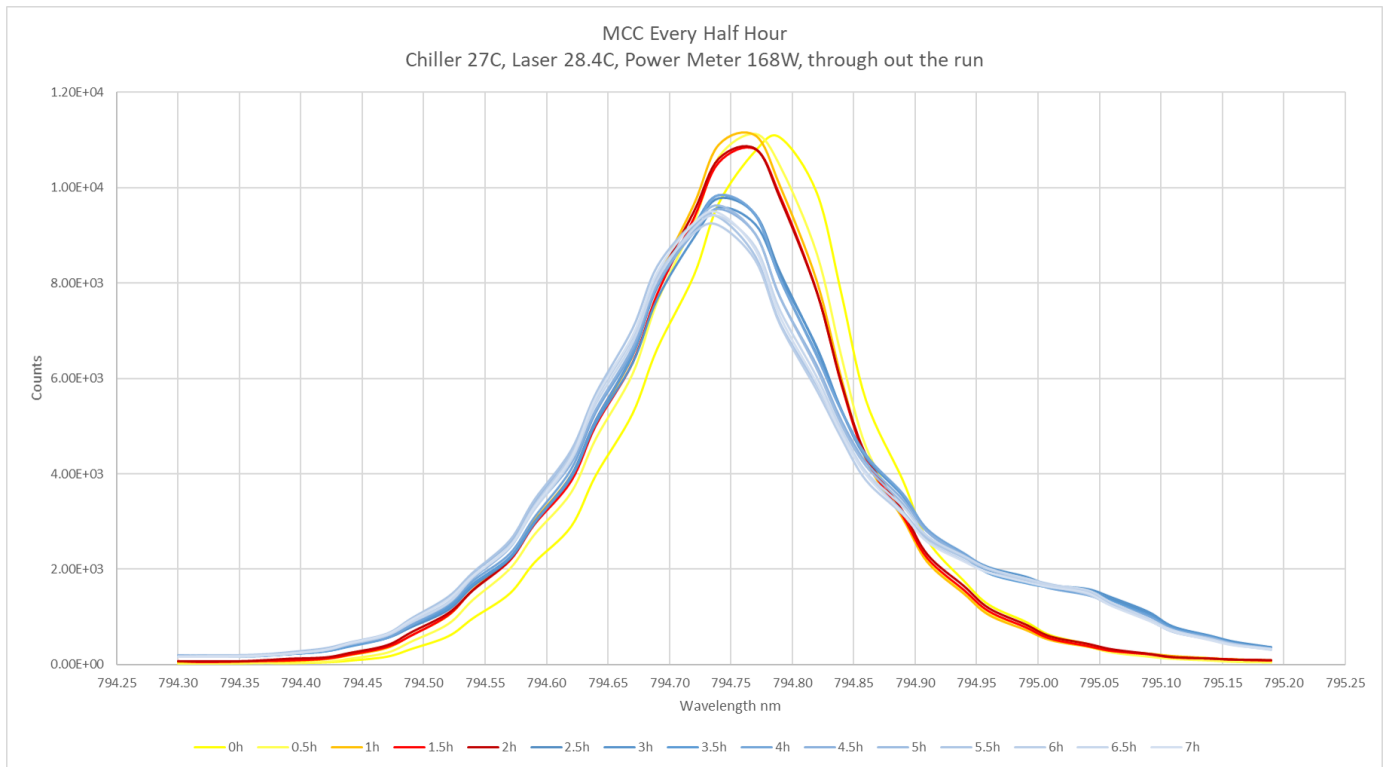


Figure 4.10: Graph showing MCC laser bar unlocking during bench testing

In a benchtop test, the MCC laser produced 168 W out of the telescope. With the chiller set to 27 C, the laser temperature was 28.4 C at a flow rate of 5.3 L/min. The FWHM of the laser output was measured with an Ocean Optics HR4000 high resolution spectrometer (0.025 nm resolution (FWHM) [177]) and was found to be 0.2 nm.

The MCC laser was run for seven hours at these settings with no change in output power or laser temperature. However, two hours and thirty minutes into this test, one of the laser bars unlocked, creating a secondary off-resonance peak. This failure reduced the power of the main peak resonant with the Rb  $D_1$  line (See Figure 4.10). This behaviour was observed in the other MCC lasers requisitioned for the consortium’s XeUS based polarisers, and this test was the first time the failure was observed in real-time.

The MCC laser was sent back to QPC and replaced with an Ultra 500 using the same optical train technology. This Ultra 500 produced 167 W of power with an FWHM of 0.263 nm (see Figure 4.11). The P312’s DI cartridge was bypassed to allow distilled water to be used as the coolant, so as not to damage the conventional water-cooling plate present in the Ultra 500. The chiller was also able to maintain the laser temperature, which varied by less than 0.1 C on the time scale of hours.

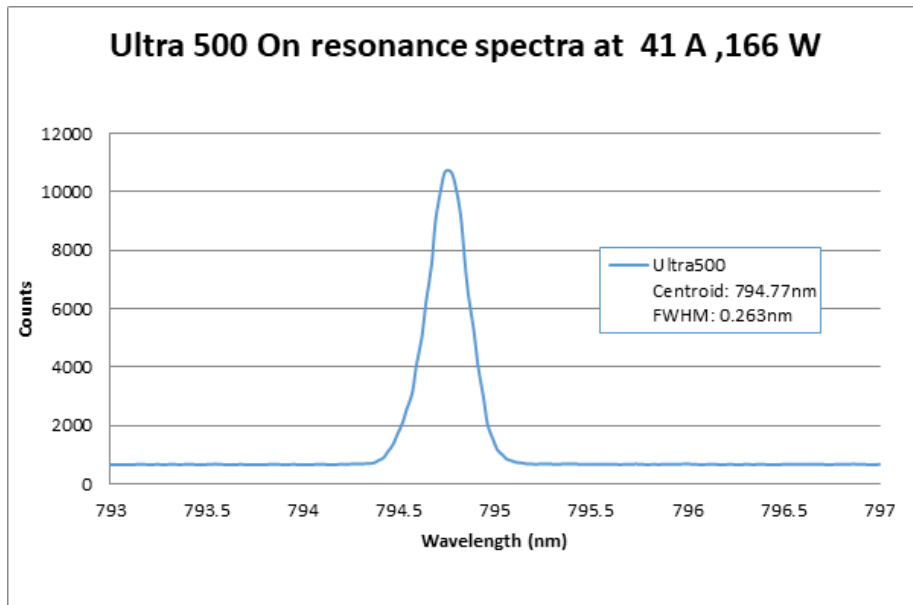


Figure 4.11: Ultra500 bench test spectra

The new Ultra 500 was installed in the N-XeUS2 and aligned with the cell using its internal aiming beam. A fibre optic sensor coupled to the HR4000 was then positioned after the oven, behind the retro-reflector rear window. The spectrometer is connected to the controlling PC via USB, with spectra recorded and displayed in Oceanview software [178].

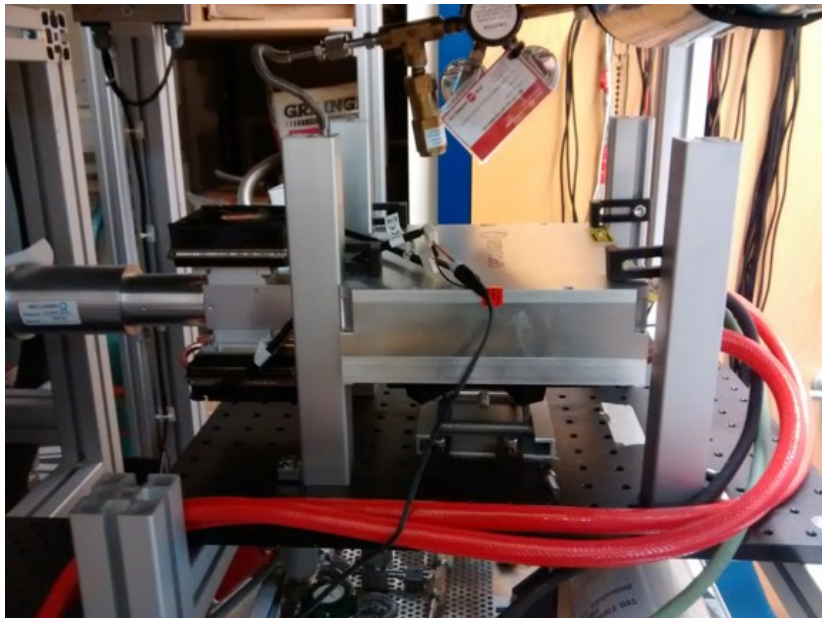


Figure 4.12: Ultra 500 mounted in the N-XeUS2

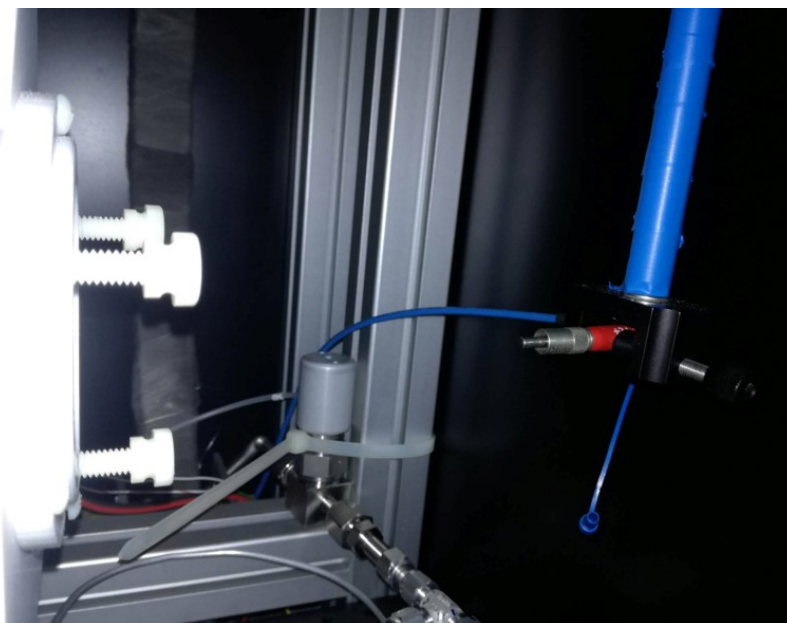


Figure 4.13: Position of fibre optic connected to the HR4000

#### 4.6.7 NMR system

The system used to acquire NMR measurements is similar to that employed in the Raman experiments. It consists of a Magritek Kea2 NMR spectrometer controlled by Prospa and a single NMR search coil. NMR acquisition can either be controlled directly by Prospa or triggered through the GUI. Once the  $^{129}\text{Xe}$  NMR signals have been analysed, the polarisation is calculated using the same method described in Section 3.3.2. A water reference signal for this calculation is also acquired using a cell with similar geometry filled with water that is doped with copper sulphate.

The NMR coil used on the N-XeUS was a simple surface coil with the same specifications as those used to take NMR measurements in Chapter 3. The coil could record an NMR signal from the HP  $^{129}\text{Xe}$  during SEOP with a reasonable SNR. It was not, however, able to record a water signal with a high enough SNR to perform accurate polarisation calculations

The reason it is so hard to get a usable water signal on the N-XeUS2 is because of the homogeneity of the  $B_0$  field and the ultra-low polarisation at this field strength. The homogeneity was maximised when the Barker arrangement were constructed and tuned by J. Skinner. However, there are ferrous materials near or inside the Helmholtz coils, which disturb the  $B_0$  field's homogeneity. The oven sits on two large legs that are adjustable so that the oven can be aligned with the laser. These legs have ferrous components that disturb the homogeneity of the magnetic fields. The inlet manifold is also ferrous, and some components are situated very close to the Helmholtz coils. All efforts were made to minimise the ferrous material inside  $B_0$  field, but, due to limited space, the field homogeneity may still be disrupted by these components.

In order to improve SNR, a new coil was constructed by J. Birchall based on

a design by A. Coffey. The “butterfly coil” consists of two surface coils connected in series. The specifications of the coil can be seen below. The noise detected by the coils is reduced as the coils are wound in opposite directions to each other. This counter winding reduces the detected NMR signal but the noise-cancelling more than offsets this loss in signal resulting in an increased SNR compared to a conventional surface coil.

A diagram of the coil can be seen in Figure 4.14. The coil and mount specifications are as follows:

- AWG30 (0.255 mm diameter) wire
- 90 turns per coil
- Coil diameter of 7.5 mm
- 27000pF tuning capacitor
- 45 mm x 23 mm block, rising to a height of 14.5 mm at either edge and sloping downwards towards the centre at a  $20^\circ$  angle, meeting at the centre of the long edge to a height of 6.5 mm, equating to an angle of  $140^\circ$  between the coils.

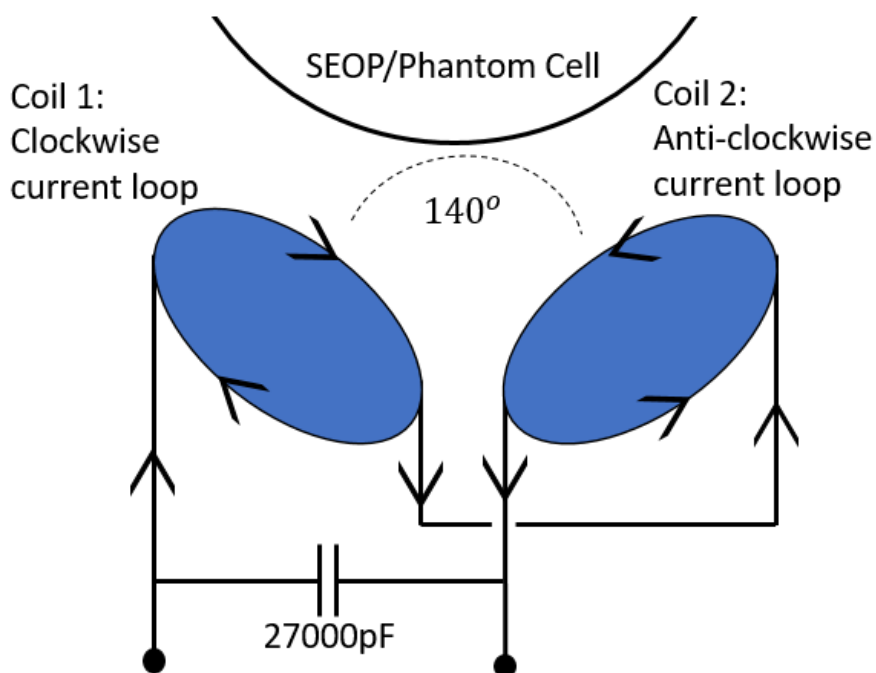


Figure 4.14: Diagram of the butterfly coil used to take NMR data in the N-XeUS2

The butterfly coil was estimated to be tuned to  $\approx 40$  kHz, and this was tested using a signal generator. The set-up involved positioning the butterfly coil a



set distance away from a single loop (SL) coil which is connected to a TTI 40 MHz Arbitrary Waveform Generator (AWG). A single send/receive pulse was sent out by the butterfly coil at the same frequency as the one produced by the signal generator. The butterfly coil then received the signal from the SL coil. This process was repeated at different frequencies throughout the region of interest. Both coarse and fine frequency sweeps were performed to investigate where the butterfly coil is most responsive, as shown in Figure 4.15.

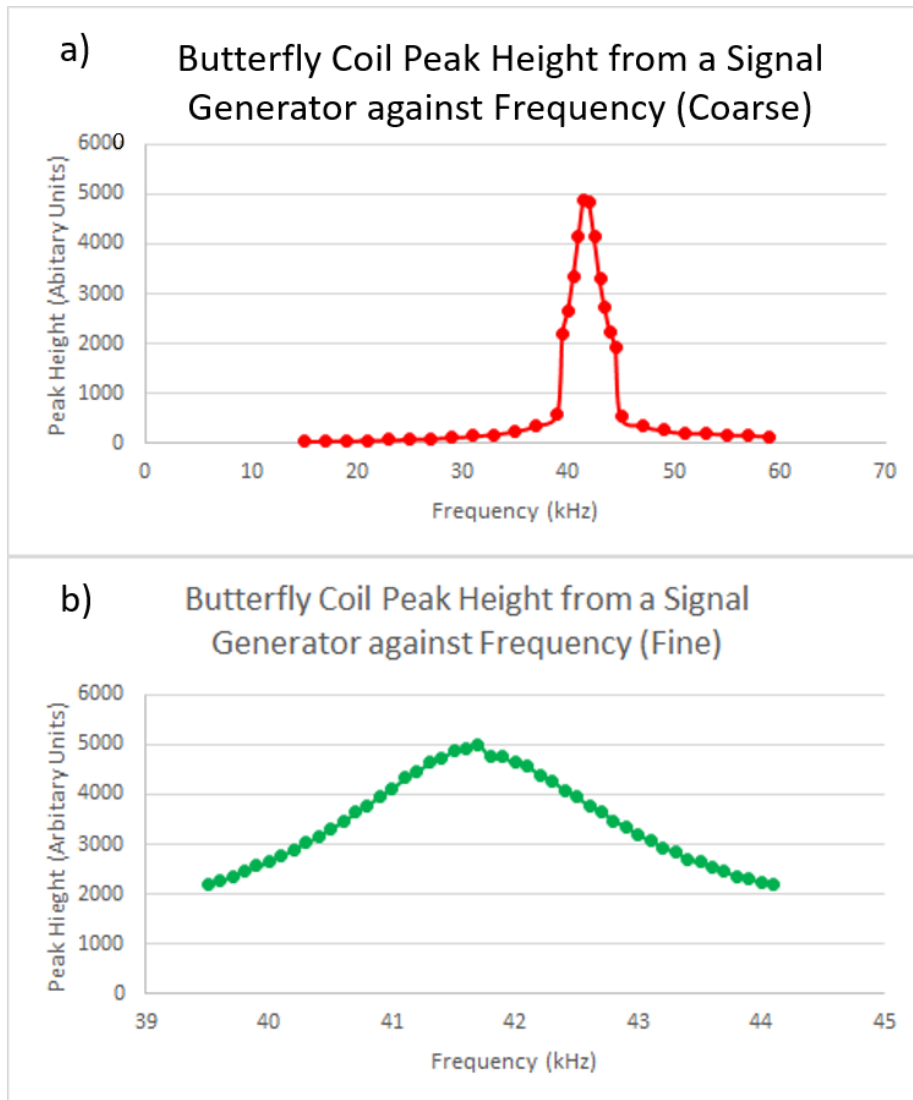


Figure 4.15: Butterfly Coil tuning a) Coarse b) Fine

The investigation found that the butterfly coil was tuned to 41.7 kHz. The coil was, unfortunately, able to detect a transient noise peak that was likely from the MRI scanner in the next room, which was close to 41.7 kHz. 40.8 kHz was therefore selected as the frequency of choice during testing as it would allow

the coil to work near its maximum sensitivity while having the NMR signal discernible from the noise peak.

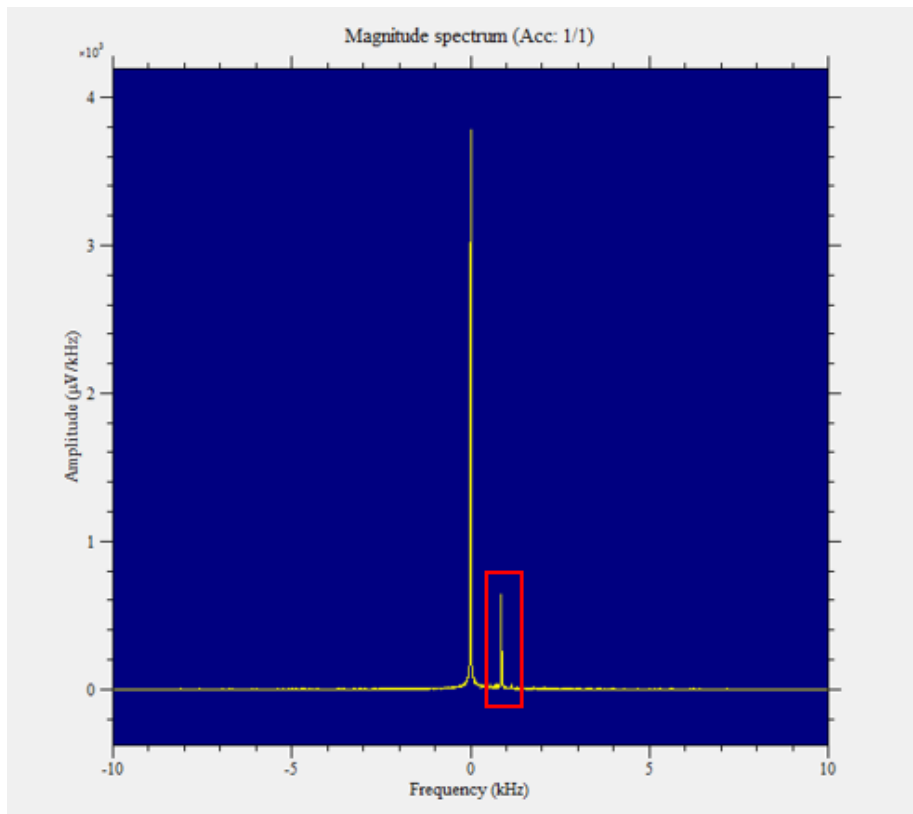


Figure 4.16: Example spectra from the tuning process, noise peak highlighted in red

Using the butterfly coil, the NMR peak appears out of the noise floor after 10,000 scans, producing a much higher SNR than the previous surface coil. A pulse amplitude sweep was performed from -50 to 0 dB, with a pulse length of  $300\mu\text{s}$ . -17 dB gave the highest SNR and, as a result, was selected as the pulse amplitude used to generate the water reference signal. The sweep is shown in Figure 4.17, and the water reference is shown in Figure 4.18. Although the NMR peak could be seen after 10,000 scans the reference water signal was taken over  $10^6$  scans to produce the maximum SNR possible.

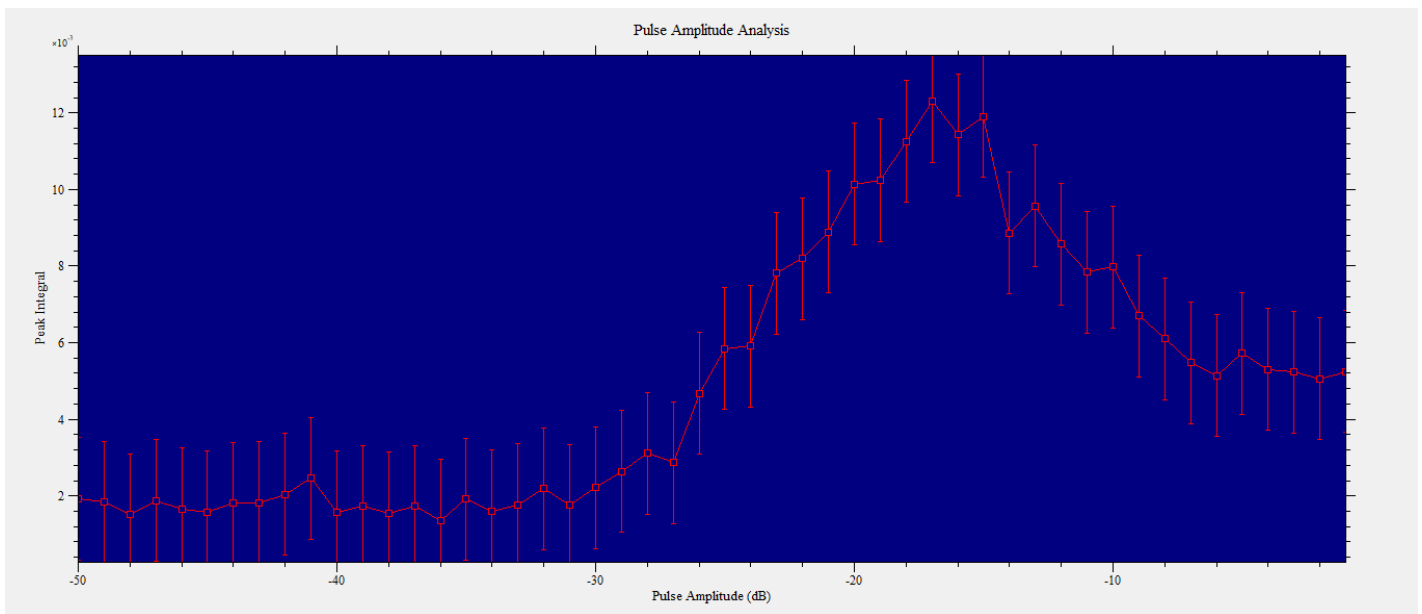


Figure 4.17: Pulse amplitude sweep with a pulse length of  $300 \mu\text{s}$  and pulse acquisition delay of 3 ms

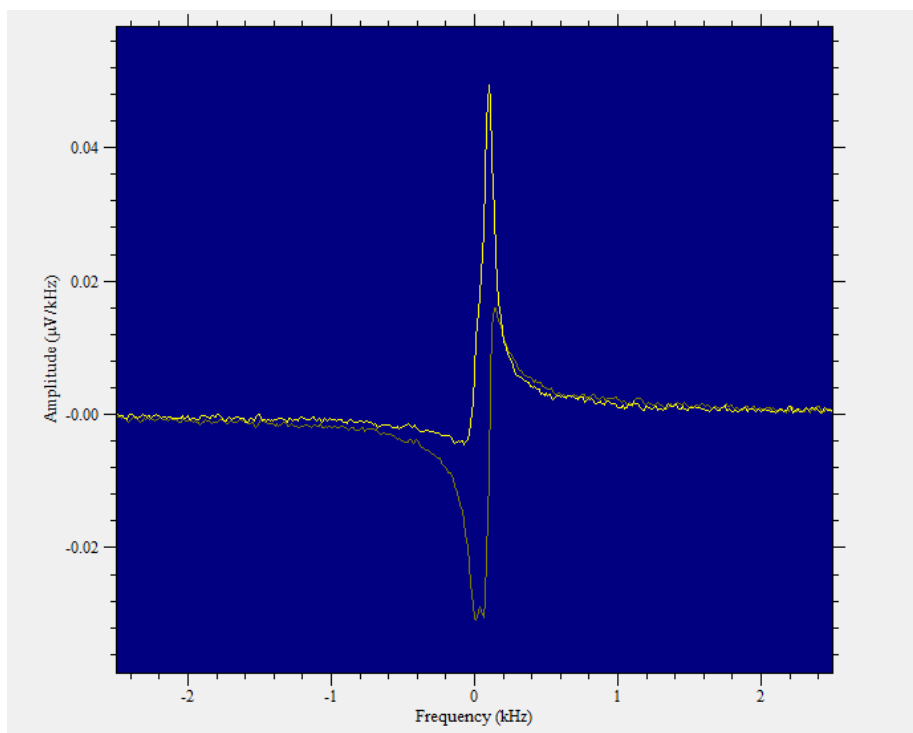


Figure 4.18: Water single reference signal acquired on the N-XeUS2

## 4.7 N-XeUS2 performance

### 4.7.1 Introduction

The Ultra 500 failed shortly after its installation and was sent back to QPC. They reported that the failure was due to flashover of the laser bar insulator pads as a result of poor earthing. This failure was also seen on other replacement Ultra 500s in the consortium and was suspected to be part of a faulty batch of lasers. J. Birchall had newly constructed an identical polariser (W-XeUS2) using the N-XeUS2 as a blueprint at Wayne State University in Detroit. The W-XeUS had a fully operational Ultra 500 laser, so a lab visit was arranged to Wayne State to investigate the performance and reliability of the XeUS2 platform.

The following experiments investigated the performance of the W-XeUS2 at different cell temperatures using several different gas mixes. The aim was to find the optimal oven temperature for each gas mix and determine the highest bulk magnetisation the polariser could produce. Results were then compared to the 9810.

### 4.7.2 Polariser performance for different binary gas mixes

#### Methods

For each gas mix, a cell “map” was produced. The map shows the maximum  $P_{Xe}$ , the polarisation build-up rate ( $\gamma_{SEOP}$ ) and Rb polarisation ( $P_{Rb}$ ) for each oven temperature.

The TEC/NMR protocol described in Section 4.6.5 was not implemented during these experiments; instead, the old protocol, where the TEC is turned off during NMR acquisitions, was used. NMR was therefore taken every six minutes during SEOP, as it allowed the TEC to maintain the oven temperature while still providing good temporal resolution for the  $P_{Xe}$  build-up curve which was created in the same way as the optimal  $P_{Xe}$  build up curves in Section 4.6.5 and an example build up curve can be seen in Figure 4.19.

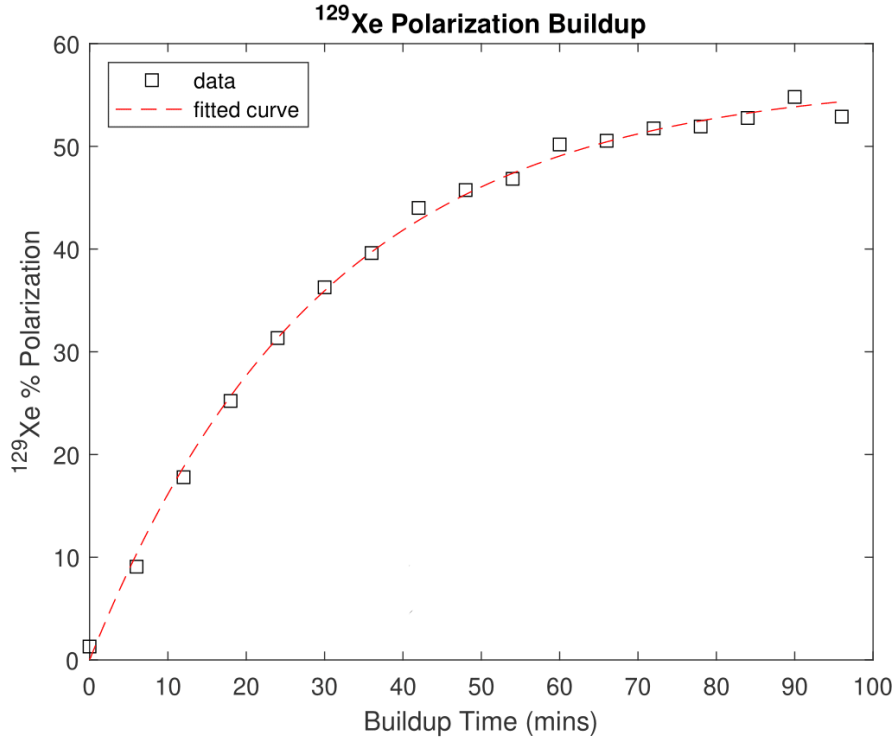


Figure 4.19: Example  $P_{Xe}$  build up curve, for a cell filled with 1350 Torr Xe 1350 Torr N<sub>2</sub> at 65 C on the W-XeUS2

$P_{Rb}$  was calculated by taking five IR spectra from the laser at full power with the cell at room temperature. Then, at the end of each run, five IR spectra were taken with the magnet on and off. Every five-spectra set was averaged, and these average spectra were then used to calculate the  $P_{Rb}$ . This calculation used the Beer-Lambert law [179] and IR bleaching [25]. When the Rb electrons are spin polarised during optical pumping, they are no longer available to absorb further photons until their spin has been transferred to the  $^{129}\text{Xe}$  during spin-exchange. As a result, there is a lower proportion of the Rb absorbing the photons from the pump laser, and a higher number of photons may be transmitted through the entire cell. The absorption ( $A$ ) is calculated by comparing the peak integral of the laser light intensity transmitted through the optical cell at room temperature ( $I_{cold}$ ) to its intensity when the cell is heated for SEOP ( $I_{hot}$ ). This defined in the Equation (4.1).

$$A = -\ln \frac{I_{hot}}{I_{cold}} \quad (4.1)$$

Absorption with the magnet off ( $A_0$ ) is greater because no Rb electrons are spin polarised, so all the Rb is available to absorb the incoming photons. Using these  $A$  and  $A_0$  values,  $P_{Rb}$  can be calculated, as shown in Equation (4.2).

$$P_{Rb} = \frac{A}{A_0} - 1 \quad (4.2)$$

After the last IR spectra were collected for each day, a  $T_1$  relaxation measurement was performed to ensure that the cell had not been poisoned when loading new gas mixes. The laser power was reduced to zero, the cell was cooled to room temperature and the TEC was turned off. NMR was taken every four minutes for four hours, and the  $T_1$  relaxation of  $^{129}\text{Xe}$  was calculated from the resultant exponential decay curve.

## Results and discussion

These experiments were all conducted on the same cell loaded with 0.5 g of Rb. The Rb was artificially spread with a heat gun, and dry ice was used to accelerate plating on the cell walls.

The following gas mixes were investigated: 1350 Torr Xe/1350 Torr  $N_2$ , 2025 Torr Xe/675 Torr  $N_2$ , 1000 Torr Xe/1000 Torr  $N_2$ , 1500 Torr Xe/500 Torr  $N_2$  and 500 Torr Xe/1500 Torr  $N_2$ . These mixes had a total pressure of 2700 Torr or 2000 Torr. 2000 Torr was used as it is the standard working pressure of the XeUS2 platform and allowed for comparison with previous work on the XeNA and XeUS. 2700 Torr gas mixes gave an insight into the extent to which the  $^{129}\text{Xe}$  percentage polarisation is suppressed by an increase in Xe partial pressure. The increased pressure would also compensate for the dead volume in the outlet side of the manifold to ensure no underfills would occur when gas was decanted to a 1L bag.

For all gas mixes, at optimal conditions, the higher the Xe partial pressure, the lower the final  $P_{Xe}$ . The  $P_{Xe}$  in the 2000 Torr cell was  $59.1 \pm 1.5\%$ ,  $76.3 \pm 2.0\%$  and  $97.9 \pm 1.9\%$  for 1500, 1000 and 500 Torr of Xe respectively (see Figure 4.20 a), b) and c)). The W-XeUS2 was able to outperform the XeUS polariser, which achieved  $41 \pm 1\%$ ,  $60 \pm 2\%$  and  $73 \pm 4\%$  at Xe partial pressures of 1500, 1000 and 515 Torr.

The  $P_{Xes}$  attained in the 2700 Torr gas mixes were  $56.0 \pm 1.5\%$  and  $51.8 \pm 1.5\%$  at Xe partial pressures of 1350 and 2025 Torr, respectively (see Figure 4.21). The  $P_{Xe}$  was slightly suppressed compared to the polarisation in the 2000 Torr cell, as the higher pressure within the cell caused more collisions to occur, increasing the spin destruction rate.

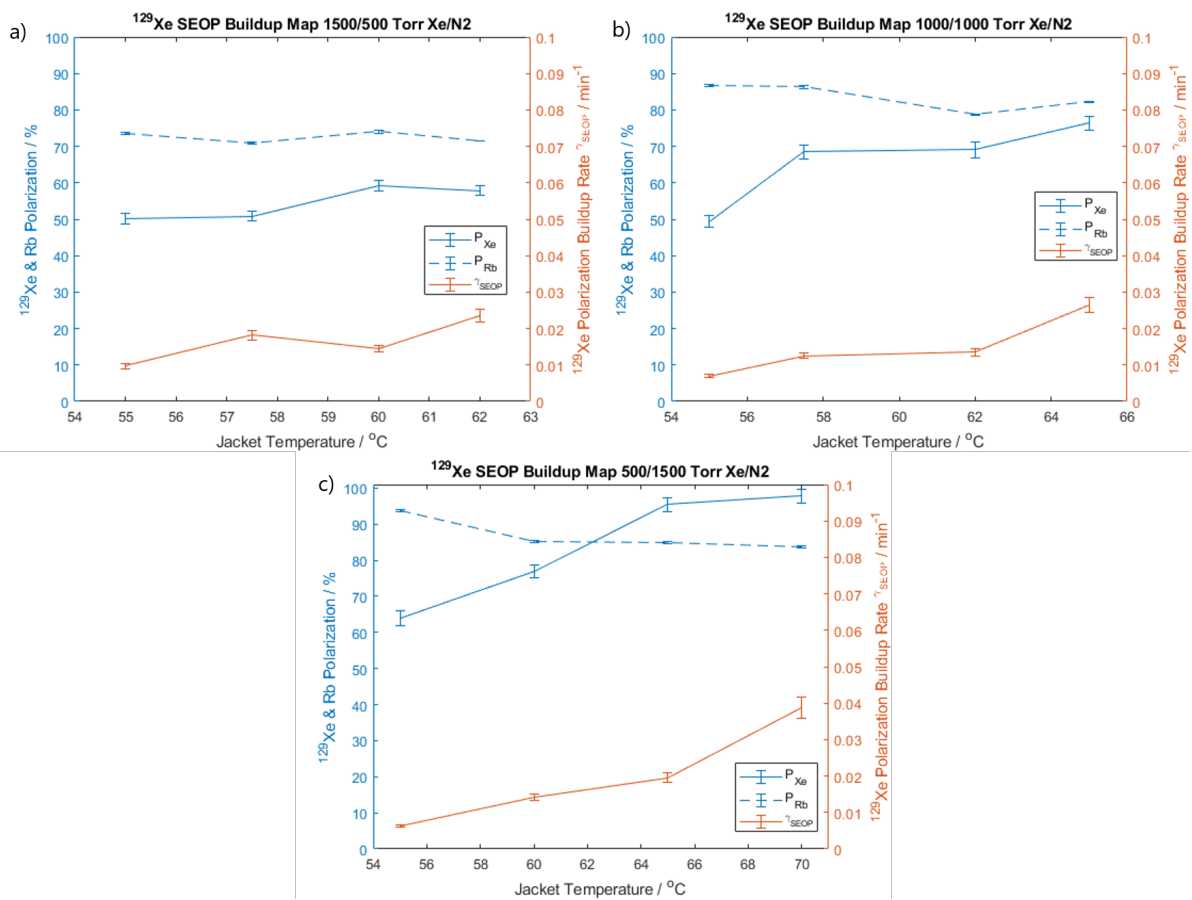


Figure 4.20: Cell maps displaying  $P_{\text{Xe}}$ ,  $P_{\text{Rb}}$  and  $\gamma_{\text{SEOP}}$  different over temperatures filled with the following gas mixes a) 1500 Torr Xe 500 Torr  $\text{N}_2$  b) 1000 Torr Xe 1000 Torr  $\text{N}_2$  c) 500 Torr Xe 1500 Torr  $\text{N}_2$

Gas Mix	Pressure (Torr)	PXe	Volume (L)	$^{129}\text{Xe}$ Fraction	DE (L)	Production time (hr)	DE rate (L/hr)	Error
1500 Xe 500 N <sub>2</sub>	2000	27.0%	0.8	0.20	0.043	0.90	0.048	0.0011
1000 Xe 1000 N <sub>2</sub>	2000	37.7%	0.8	0.13	0.040	0.87	0.046	0.0011
500 Xe 1500 N <sub>2</sub>	2000	57.2%	0.8	0.07	0.030	0.98	0.031	0.0007
1350 Xe 1350 N <sub>2</sub>	2700	32.1%	1	0.13	0.042	0.93	0.045	0.0011
2025 Xe 675 N <sub>2</sub>	2700	24.9%	1	0.20	0.049	0.90	0.055	0.0013
9810	N/A	14.2%	1	0.26	0.037	0.75	0.050	0.0039

Table 4.1: Dose equivalence comparison between the Polarean 9810 and the N-XeUS2 using different gas mixes

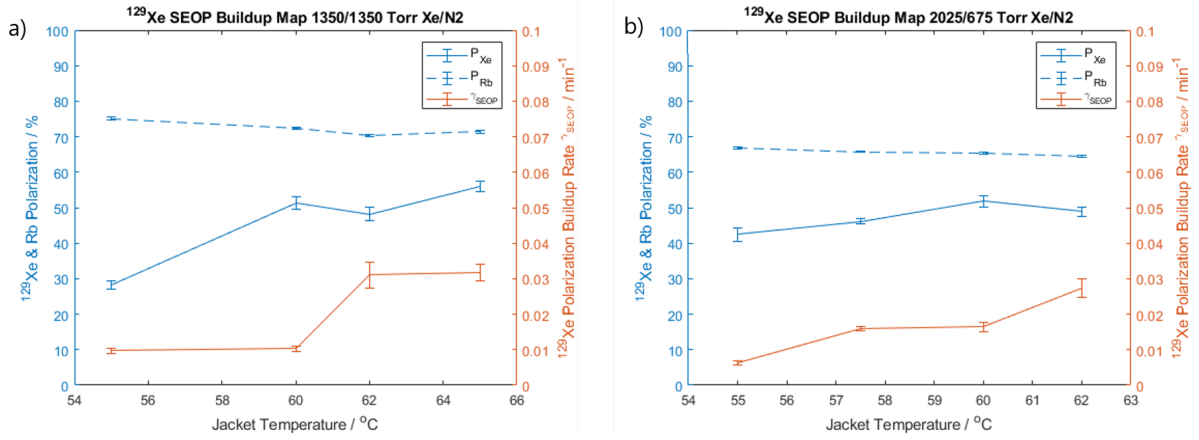


Figure 4.21: Cell maps displaying  $P_{Xe}$ ,  $P_{Rb}$  and  $\gamma_{SEOP}$  different oven temperatures filled with the following gas mixes a) 1350 Torr Xe 1350 Torr N<sub>2</sub> b) 2025 Torr Xe 675 Torr N<sub>2</sub>

The direct comparison between the maximum  $P_{Xe}$  produced by the W-XeUS2 and the Polarean 9810 is not a fair one. This is because Polarean 9810 takes  $\approx 30$  minutes to make a 1 L bag and has a sub-45-minute turnaround time. The Polarean 9810 is currently using a gas mix comprising 3% naturally abundant Xe, 10% N<sub>2</sub> and the balance  $^4\text{He}$ . Utilising this gas mix, the 9810 can produce a  $P_{Xe}$  of  $14.2 \pm 1.1$  in a 1 L under the timescales described above. Comparing maximum polarisations produced by the polarisers does not reflect the  $P_{Xe}$  the N-XeUS2 platform can deliver in a clinical timescale. Therefore, the N-XeUS2 and Polarean 9180 are compared using their dose equivalence (DE) production rate [180]. The DE production rate is the production rate per unit time of 100% hyperpolarised, 100% enriched pure  $^{129}\text{Xe}$  gas per unit time. DE is the product of the isotopic fraction of ( $f_{129}$ ), ( $P_{Xe}$ ) and Xe volume ( $V_{Xe}$ ), as shown in Equation (4.3).

$$DE = f_{129} \times P_{Xe} \times V_{Xe} \quad (4.3)$$

The  $P_{Xe}$  produced by the N-XeUS2 is calculated from the maximum polarisation reached in 30 minutes for each gas mix under optimal conditions, less the polarisation lost during cooldown. This polarisation loss is based on a  $T_1$



decay time of  $187 \pm 1$  minutes. The total production time for the N-XeUS2 polariser is the sum of a 30-minute production time, time to cool the cell to 42 C for extraction and six minutes to refill the cell and bring the cell up to temperature. The cooldown time is calculated based on previous results which state that the TEC can cool the cell from 72 C to 42 C in 24 minutes [181]. The DE rate for each gas mix compared to the Polarean 9810 is shown in Table 4.1. The figure shows that the N-XeUS2 is able to produce a greater DE for all gas mixes except the 500 Xe 1500  $N_2$  gas mix. However, the increased production time of the N-XeUS2 means that there is no significant difference in the DE rate. The DE and the DE rate increase with Xe fraction size. This is due to the higher bulk magnetisation produced when using richer mixes and the fact that they must be run at cooler temperatures to prevent runaway, resulting in a shorter cooldown time and thus a shorter total production time.

This shows that the N-XeUS2 is able to compete with the Polarean 9810 in a clinical setting while providing a much more user-friendly experience. In order for the N-XeUS2 to outperform the DE rate provided by the Polarean 9810, the total production time will need to be reduced.

## 4.8 Long term quality assurance

### 4.8.1 Introduction

The N-XeUS2 will replace the Polarean 9180 in the QMC, which acts as a benchmark not just for polarisation but also for cell lifetime. Over time, impurities enter the Polarean 9180 cell and poison the Rb, and this has a limited impact on performance until a critical point is reached. At this critical point, a change in laser absorption is observed in the IR spectrum, along with a significant drop in  $P_{Xe}$ . When this happens, the cell needs to be changed. Typically, 1000s of litres of gas can be run through the Polarean cell before it reaches this critical point, equating to  $\approx 1.5$  years of normal use.

The XeUS2 platform uses purge/evacuate cycles to remove any contaminants before the cell is filled. An investigation was undertaken to determine if the new manifold resulted in increased cell lifetimes that could compare with the 9810.

This QA study could not be performed using “real world” conditions, i.e. heating the cell, performing SEOP and cooling the cell over the number of refills needed to replicate 1-2 years of typical use. Firstly, it would translate into 1000s of man hours running the polariser, which was not practical. Secondly, the cost associated with running a Xe mix through the cell hundreds of times would be considerable. Finally, the pump laser has a lifetime on the order of  $10^4$  hours, so a significant amount of the laser’s lifetime would be expended for QA. A protocol was therefore devised to simulate 1-2 years of use by repeatedly filling the cell with pure  $N_2$ . A bespoke automation sequence was coded for the micro-controller and GUI, enabling a lower cost, more time-efficient QA to be undertaken.

The study does not replicate the heating and cooling that the Rb would be subject to during typical use. The lack of heating may cause a slower degradation of Rb in the QA study compared to real-world conditions. However, as a QA study replicating real-world conditions was not practical, this simulation was deemed to be an acceptable alternative. This study performed in collabo-

ration with J. Birchall and was published in the Journal of magnetic resonance (JMR) [182].

#### 4.8.2 Methods

The QA code was created for this thesis, however, due to limited time at Wayne State University, a portion of the QA data was recorded in partnership with J. Birchall. A simplified version of the QA protocol is described in the steps below:

1. Purge and evacuate the inlet manifold with  $N_2$
2. Repeat step one three times
3. Leave manifold under positive  $N_2$  pressure
4. Open the cell
5. Evacuate out the current gas mix
6. Fill cell with  $N_2$
7. Wait 1 minute
8. Go back to step 4 for the required number of repeats
9. Final fill with Xe gas mix
10. Polarise gas mix

A flow chart describing the whole automated QA refill sequence is shown below in Figure 4.22.

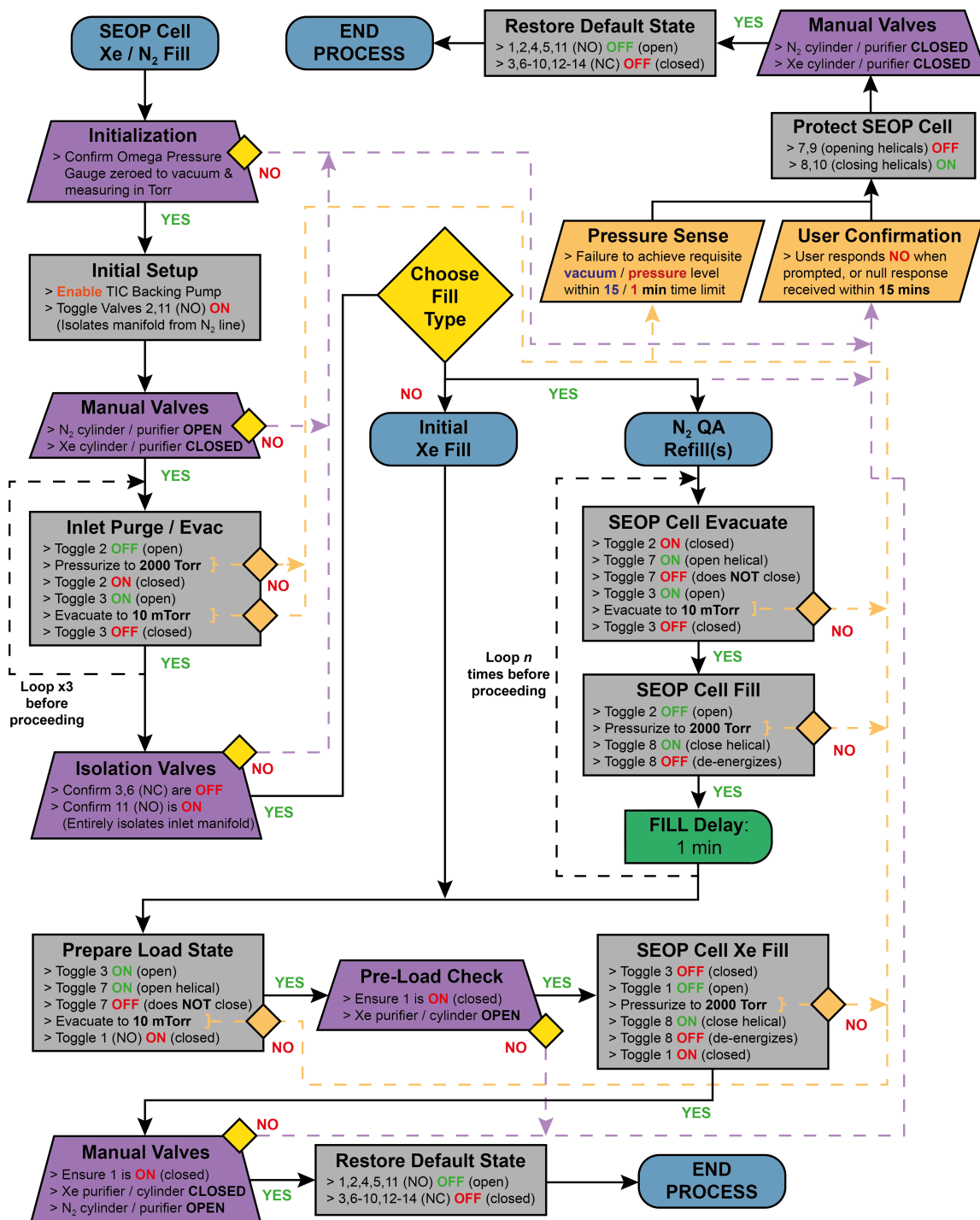


Figure 4.22: QA cell refill sequence as coded for the Arduino; diagram produced by J. Birchall reproduced here with permission

The time taken for each  $N_2$  cell refill is on the order of minutes, compared

to a full polarisation run that can take several hours. This enabled the study to be completed over the course of a few weeks.

The cell was loaded with a 1000 Torr Xe/ 900 Torr  $N_2$ / 100 Torr  $^4He$  gas mix. The QA study used a new cell with a fresh Rb load. Following this, a cell map was created using the same protocol detailed in Section 4.7.2. The optimal oven temperature for the cell was found to be 70 C (Figure 4.23). Increasing the oven temperature above 70 C resulted in a decrease in  $P_{Xe}$ , and TEC could not maintain the oven temperature above 71.5 C as the cell entered Rb runaway.

After each batch of  $N_2$  refills, the cell would be filled with the same gas mix as the initial fill. The  $P_{Xe}$  build-up curve, was created, followed by a  $T_1$  measurement to track the degradation of the Rb and SEOP performance. After the initial Xe gas mix fill, the following number of  $N_2$  refills were performed between polarisation runs: 15, 51, 111, 256 and 256. Taking account of the 6 Xe gas mix fills, the cell was filled a total of 694 times.

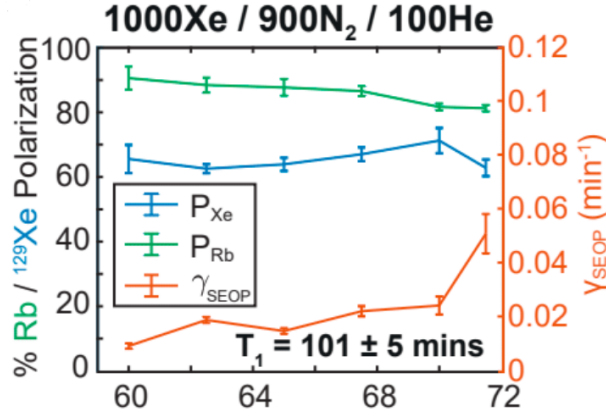


Figure 4.23: Initial map of the QA cell [182]

### 4.8.3 Results

The initial cell fill achieved a  $P_{Xe}$  of  $73.6 \pm 4.6\%$ , and no significant change in  $P_{Xe}$  was observed after 180 cell fills. The  $P_{Xe}$  on the 180<sup>th</sup> fill (4<sup>th</sup> polarisation run) produced a  $P_{Xe}$  of  $72.3 \pm 2.3\%$ . The 5<sup>th</sup> Xe gas mix fill was taken after the number of  $N_2$  fills had more than doubled, and it was the 437<sup>th</sup> fill in total. This run saw a significant drop in  $P_{Xe}$  to  $60.0 \pm 1.8\%$ . This showed that, between the 180<sup>th</sup> and 437<sup>th</sup> fill, the Rb purity had decreased to the point where the SEOP performance was negatively affected. The  $P_{Xe}$  continued to decrease as the number of fills increased and, after another 256  $N_2$  fills, the 6<sup>th</sup> Xe gas mix fill could only achieve a  $P_{Xe}$  of  $42.4 \pm 1.1\%$ .

The polarisation build-up timescale  $T_b$  were also investigated during the experiment, and, initially, there was a small but not significant increase in its value. Between the 1<sup>st</sup> and 2<sup>nd</sup> Xe (17<sup>th</sup> total) gas mix fills, the  $T_b$  increased from  $43 \pm 7$  minutes to  $57 \pm 8$  minutes. The high  $T_1$  values of both runs, in combination with the  $P_{Xe}$ , indicated that the increase in  $T_b$  was not from Rb degradation. The 3<sup>rd</sup> and 4<sup>th</sup>  $^{129}Xe$  fills seemed to support this, with the  $T_b$

value remaining consistent at  $56 \pm 9$  minutes and  $59 \pm 5$  minutes, respectively. By the 5<sup>th</sup>  $^{129}\text{Xe}$  gas mix fill, the  $T_b$  had begun to decrease, achieving a value of  $48 \pm 4$  minutes.  $P_{Xe}$  had also reduced, which was attributed to an increased spin-destruction rate. The  $T_b$  value continued to drop, reducing significantly to  $18 \pm 2$  minutes in the final polarisation run and dropping below the initial  $T_b$ , where the spin-destruction was assumed to be the lowest as the Rb had not been poisoned. This showed that the increase in spin destruction was a result of Rb poisoning. Although in isolation having a smaller  $T_b$  may seem advantageous, as it decreases the total production time. However, the ultimate  $P_{Xe}$  being reached is reducing, which is why it takes less time to reach.

$T_1$  relaxation increased with an increasing number of cell refills. It went from an initial value of  $102 \pm 5$  minutes in the 1<sup>st</sup> Xe gas mix fill to  $78.1 \pm 1.5\%$  in the 4<sup>th</sup> Xe gas mix fill. This was attributed to an increasing number of impurities accumulating in the cell throughout the 180 cell fills. The  $T_1$  did however rise again on the 5<sup>th</sup> Xe gas mix fill to  $99.2 \pm 3.5\%$ . This  $T_1$  measurement appears to contradict the  $P_{Xe}$  and  $T_b$  observed during this fill which follow the expected trend of reduced SEOP performance. Although this rise could be explained by Rb metal regeneration due to repeated heating and cooling cycles, explained in Section 3.4.2, this may have resulted in a temporary improvement in  $T_1$ . The increased  $\gamma_{SEOP}$  ( $0.011 \pm 0.002$  minutes<sup>-1</sup>) was over double the previously measured value and seemed to corroborate this theory. The 6<sup>th</sup> SEOP fill saw a continuation of the initially observed trend with a significant drop in  $T_1$  to  $25 \pm 4$  minutes. Combined with the drop in  $P_{Xe}$  and  $T_b$ , this shows how the SEOP performance has been reduced by increasing spin-destruction from Rb poisoning.

The build-up curves and  $T_1$  relaxation curves for all 6 Xe gas mix fills can be found in Figure 4.24. A map was also created which showed how the  $P_{Xe}$ ,  $T_b$ ,  $P_{Rb}$  and  $T_1$  changed with increasing number of cell refills (see Figure 4.25). A full cell map was taken after the 694<sup>th</sup> to see how its performance at different temperatures had changed (see Figure 4.26).

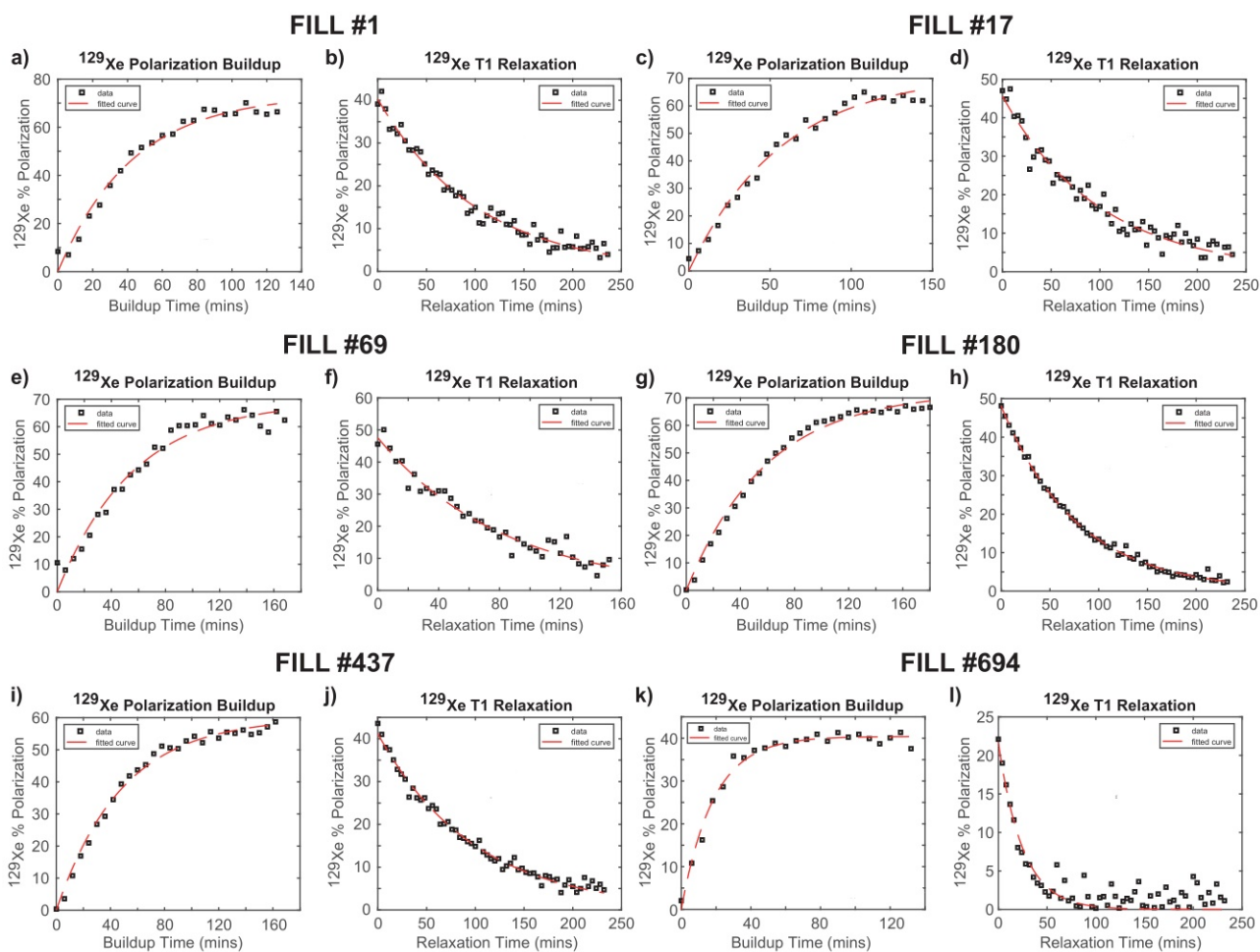


Figure 4.24: Polarisation build-up and  $T_1$  curves for Fill 1 ( a) and b) ), Fill 17 ( c) and d) ), Fill 69 ( e) and f) ), Fill 180 ( g) and h) ), Fill 437 ( i) and j) ) and Fill 694 ( k) and l) ) [182]

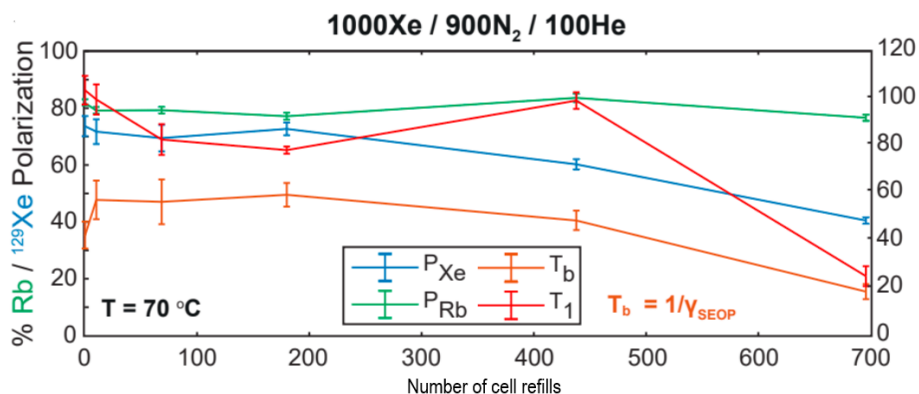


Figure 4.25: Map showing the progression of final  $^{129}\text{Xe}$  polarisation ( $P_{Xe}$ ), rubidium polarisation ( $P_{Rb}$ ), build-up time ( $T_b$ ) and  $T_1$  relaxation time ( $T_1$ ) with number of cell refills.

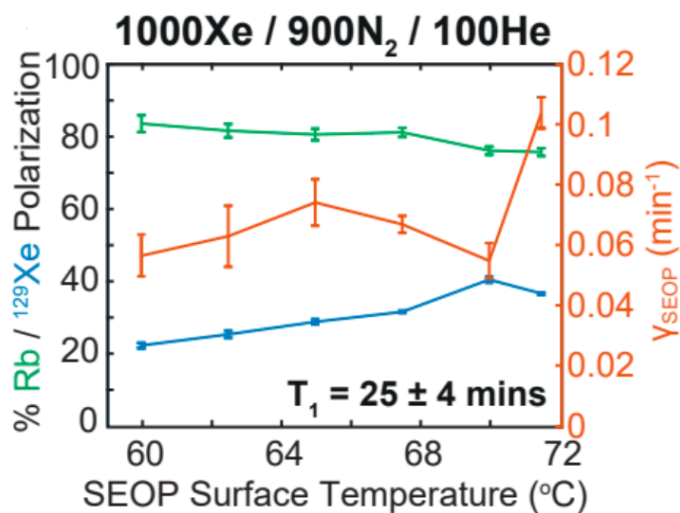


Figure 4.26: Map of the QA cell after 694 refills [182]

The optimal cell temperature (70 C) and maximum operating temperature (71.5 C) remained unchanged, showing that all  $P_{Xe}$  gas mix fills were run under optimal conditions and were thus comparable.

An additional smaller-scale QA study was carried out at the University of Nottingham before the failure of the QPC Ultra 500 in the N-XeUS2. It used a gas mix of 1000 Torr Xe / 1000 Torr  $N_2$ . As this study was a quick investigation, no  $N_2$  fills took place between Xe gas mixes fills, and SEOP only occurred for 30 minutes. SEOP occurred at an oven temperature of 60 C, and the  $P_{Xe}$  did not reach a steady state.

The results of the investigation can be seen in Figure 4.27. They show that the NMR peak integral attained after 30 minutes exhibited a degree of variation between successive cell refills. This was attributed to the polarisation

not reaching steady-state conditions, so was in a greater state of flux compared to when it was at a steady state. A linear fit and its 95% confidence bounds applied to the data showed a small downward trend, which predicted that the integral peak would reduce to half of its initial 65.3 a.u value after 109-452 cell refills. The reason for the large estimated range is the fact the downward linear trend, although present is not statistically significant, with a  $R^2$  value of 0.11 [183]. The reduction in performance from the Rb poisoning was concluded to be minimal. Furthermore, the shortest useable cell lifetime predicted would still be on the order of  $10^2$  runs.

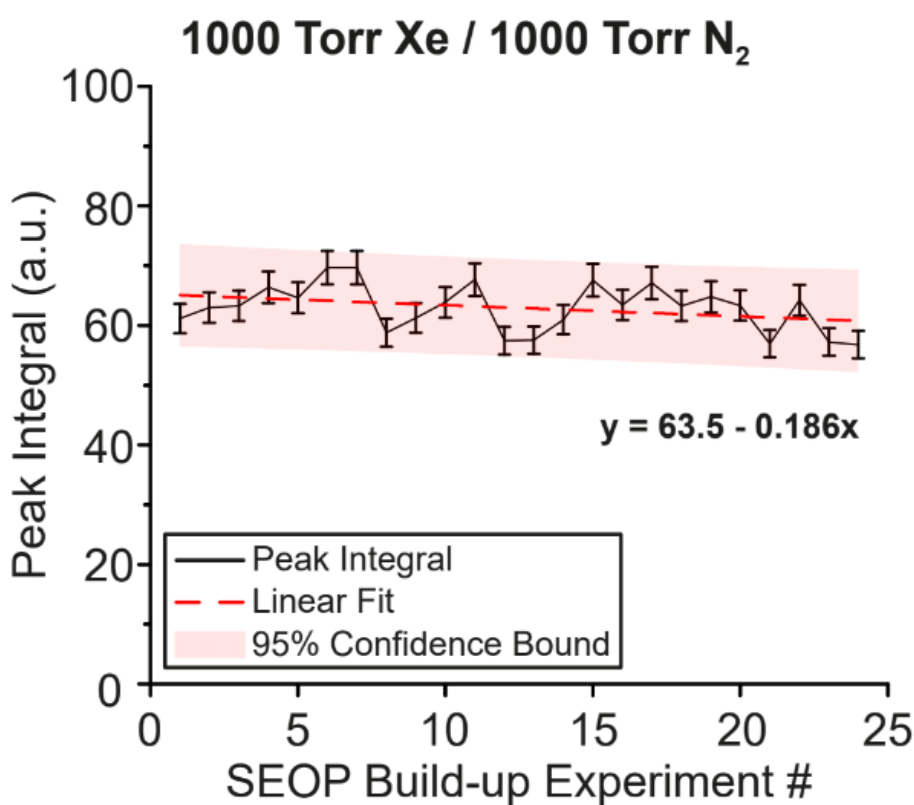


Figure 4.27: Graph showing the peak integral of the  $^{129}\text{Xe}$  NMR peak against the number of SEOP runs [182]

The prediction was less than the  $\approx 700$  refills predicted in the W-XeUS2 QA study. There are several factors that could account for this discrepancy. Firstly, the increased temperature cycling experienced by the Rb in the N-XeUS2 polariser could have provided a harsher environment and therefore greater poisoning. There was also a slightly different cell filling and spreading protocol between the two polarisers, as well as a different amount of Rb loaded into the cells ( $\approx 0.25\text{g}$  in the University of Nottingham and  $\approx 0.5\text{g}$  at Wayne State).



#### 4.8.4 Discussion

Current ethics (detailed in Section C) dictate that the maximum number of Xe doses a patient can be given during a visit is four. Under these ethics, the N-XeUS2 is predicted to have no significant drop in polarisation after  $\approx 45$  subjects. A further 45 subjects would only lead to a drop in performance of  $\approx 15\%$ , which would still provide sufficient polarisation for MRI imaging.

Clinical studies using  $^{129}\text{Xe}$  MRI typically have a small cohort of between 5-30 subjects (healthy volunteers and patients) [184, 185, 186], equating to a maximum of  $\approx 120$  bags of HP  $^{129}\text{Xe}$ . The N-XeUS could provide bags of a consistent polarisation throughout the lifetime of one or more clinical studies, depending on their size. If the user wanted to keep the polarisation levels at their maximum for each study or if the polarisation had significantly dropped, the cell can be easily replaced. Replacing a cell takes around five minutes, providing a replacement cell is prepared in advance, which would not cause any hold up to a clinical program. The cell can then be cleaned, tested for integrity, surfacled and refilled with Rb for future use, cells can be reused in this way unlimited times provided they incur no damage. Cells are custom made by professional glassblowers and cost on the order of £100. Currently, there are five cells in stock at the University of Nottingham. With the Polarean 9180, on the other hand, swapping out takes two people and a much longer amount of time, and can put stress on several delicate components. If the cell is not prepared in advance, it would require a three-day turnaround time to prepare a new cell which if the program was running at full capacity of 10 patients a week could significantly impact a clinical program as subjects would have to be rescheduled. However, this would have the same impact should a cell need to be prepared for the 9810. These QA tests show that the N-XeUS2 has predicted cell lifetimes capable of delivering the throughput needed for a clinical study without a significant drop in performance.

### 4.9 New oven design

#### 4.9.1 Motivation

The major shortcoming of the current N-XeUS2 design is its inability to maintain oven temperatures at the set point close to runaway conditions. This is because of how heat is transmitted between the cell and the TEC.

The TEC is an air-to-air Kryotherm Thermoelectric cooling assembly 380-24-AA based on a Peltier cooler. In order to remove heat from the cell, energy is transferred via convection through oven air to the TEC heat sink. The Peltier device then pumps the heat from the internal heatsink to the external heatsink, where the energy is radiated into air space in the polariser's upper chassis. Fans on the upper chassis then ventilate the hot air out of the polariser. The main limiting factor of heat transfer is the low thermal conductivity of air [187]. The air in the oven is the principal contributor to the thermal capacity of the system and slows the temperature change at the cell [188].

When not illuminated by the laser, the cell takes between 20-60 minutes (with and without insulation) to reach 70 C [151]. If the rotary blower is turned off, convection is reduced, and the TEC cannot heat the cell above 50 C [151]. With the laser illuminating the cell and being absorbed by Rb vapour, the cell

can be brought up to temperature within a few minutes. The same issue is experienced during cool down as described in Section 4.8.3 and results in a slower total production time leading to a smaller DE rate.

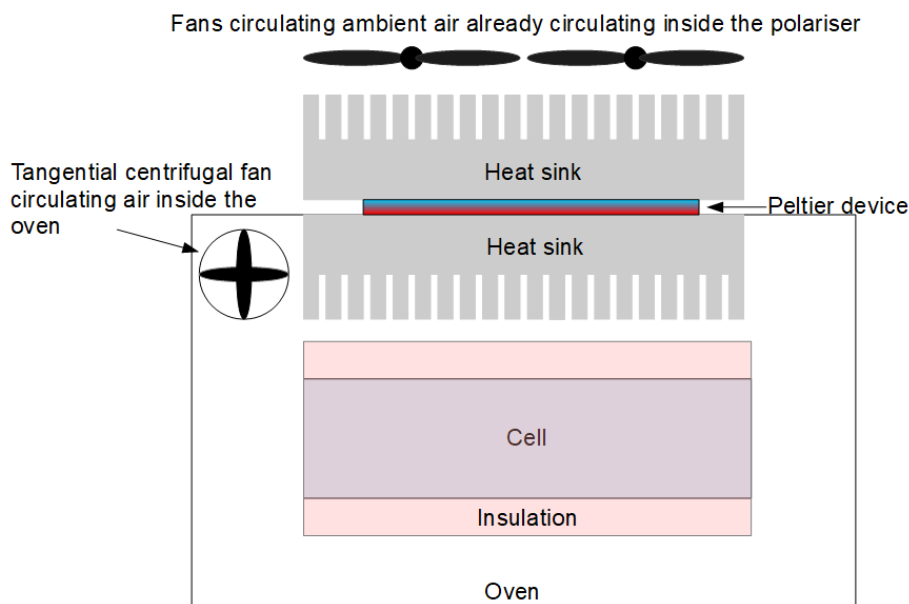


Figure 4.28: Diagram of the TEC/oven

At a certain Rb vapour density, the energy absorbed from the laser will be greater than the maximum amount of heat energy the TEC can remove from the system. When this occurs, thermal control is lost, and the cell rises above its setpoint and quickly enters runaway. In all experiments, the highest oven temperature for each W-XeUS2 experiment was limited by the TEC's ability to maintain the oven temperature.

The third generation of the stopped-flow clinical polarisers (GEN-3) made by XeUS Technologies sought to improve thermal management of the cell with a new oven design [189]. The oven design is based around an aluminium jacket, which is in direct thermal contact with the cell. Heating is provided by four, 50 W cartridge heaters and the heat is then dissipated via three CPU heatsinks mounted directly to the jacket. Aluminium offers greater thermal conductivity than air [190], so heat energy can be transferred to and away from the cell much more efficiently. This design can heat a similar-sized cell from room temperature to 70 C in four minutes and can cool the cell to extraction temperatures in the same amount of time. In a paper by J. Birchall et al., the jacket could maintain an oven temperature of 85 C while performing SEOP on a 1000 Torr Xe / 1000 Torr  $N_2$  gas mix using an identical QPC Ultra 500 laser [189]. This is 20 C higher than that achieved with a similar gas mix on the W-XeUS2. Therefore, a higher Rb vapour density can be achieved without the cell entering runaway, increasing the SEOP rate and shortening  $T_b$ . However, a significant  $P_{Xe}$  drop was seen in the GEN-3 compared to the N-XeUS2 which is still being investigated [189].

## 4.9.2 Design and fabrication

The new aluminium jacket design is based on the one found in the GEN-3 polariser. A labelled CAD drawing of the N-XeUS2 jacket is shown in Figure 4.29.

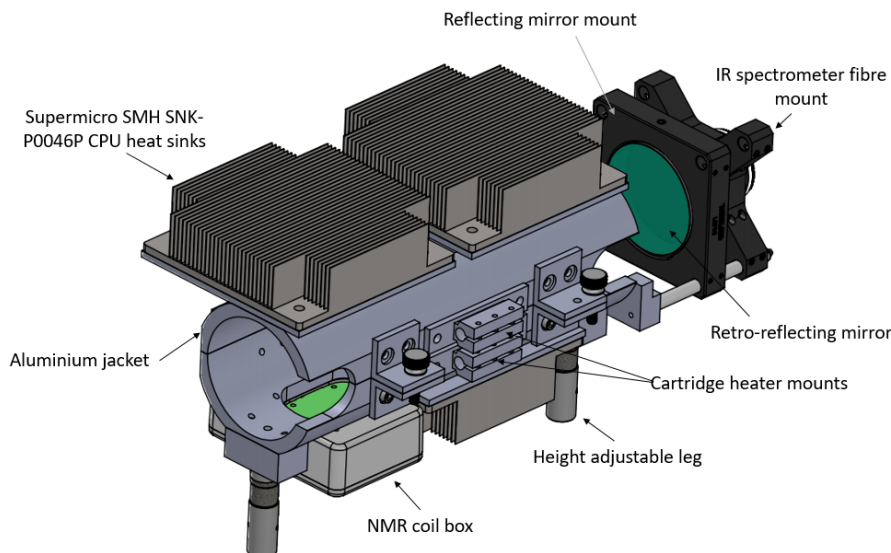


Figure 4.29: Labelled CAD drawing of the N-XeUS2 jacket

Two cartridge heaters are mounted on either side of the cell, with one of each pair mounted on the top and bottom halves of the jacket. Because of the high conductivity of the aluminium, the heat is distributed uniformly throughout the jacket [189]. To allow heat from the jacket to be uniformly transferred to the cell, a layer of Arctic Alumina thermal paste was used between the two to ensure good thermal contact.

In the Gen-3, the 50 W heaters were driven at 230 V, and this would mean that the N-XeUS's temperature controller, which had a maximum voltage of 36 V, was not compatible. To enable compatibility, four 12 V, 50 W cartridge heaters, designed for use in 3D printer nozzles, were acquired. The four heaters were divided into two pairs, which were connected in parallel. The two pairs were then connected in series. The 5R7-001 can control purely resistive heating up to loads of 900 W, which would allow the heaters to be driven by the 5R7-100. This meant temperature control of the aluminium jacket could be automated with the existing software with only minimal modifications to the Arduino and GUI code.

Cooling comes from the fans in the upper chassis of the N-XeUS2, passing cool air over three Supermicro SMH SNK-P0046P CPU heat sinks. The heat sinks provide a large surface area for air cooling to take place.

A two-inch retro-reflecting mirror is mounted in a holder at the rear of the jacket. In the Gen-3 a single NMR surface coil is mounted inside a die-cast aluminium box on the underside of the jacket to shield the coil from outside noise, improving SNR. The jacket has a cut out for the NMR coil that allows close contact between the coil and cell.

Several modifications had to be made to the design before the N-XeUS2 jacket could be fabricated. The GEN-3 cell has a slightly thinner maximum diameter compared to the N-XeUS2, and a had different stem design, as shown in Figure 4.30.

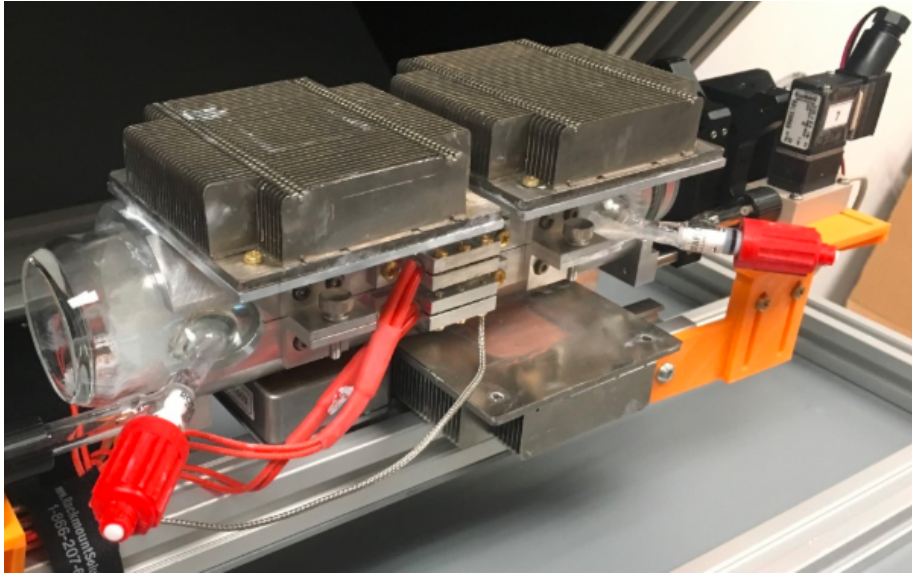


Figure 4.30: Picture of the GEN-3 cell sitting inside the aluminium jacket on the GEN-3 polariser

The diameter of the aluminium jacket was increased, and the stem location was taken into account so that the cell could fit. The jacket was fabricated in the SPMIC workshop and is shown in Figure 4.31 and 4.32.

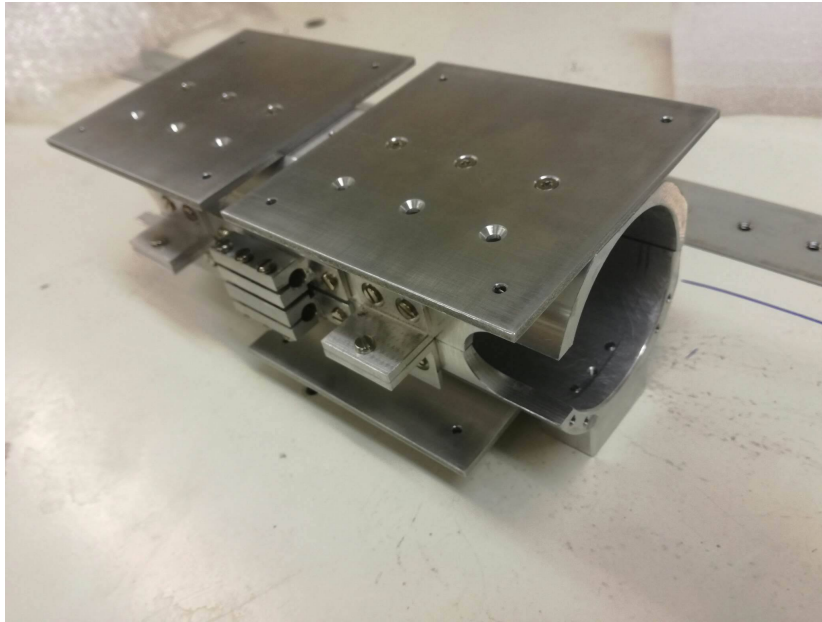


Figure 4.31: N-XeUS2 aluminium jacket

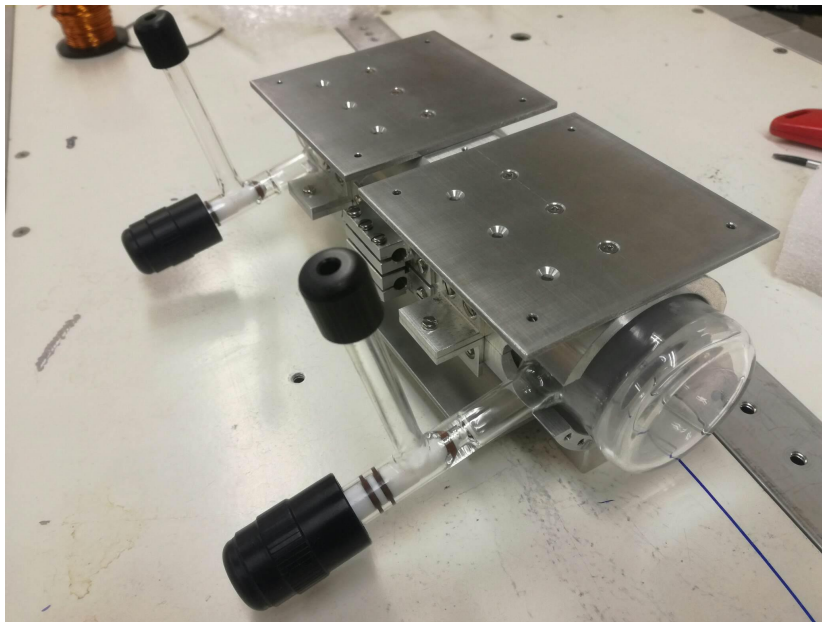


Figure 4.32: N-XeUS2 aluminium jacket with a cell inside

### 4.9.3 Installation and testing

The jacket has not yet been installed and tested as the COVID-19 pandemic caused work to cease [191]. The next steps are to: replace the current oven/TEC

with the aluminium jacket design, test 5R7-001 and the jacket in resistive heating mode while being controlled directly with the Oven Industries software. The 5R7-001 then will be re-integrated into the automation system, and the required changes to the Arduino and GUI code will be made. The system will then be tested to ensure it can heat and cool the cell to the desired setpoint when controlled via the GUI. Once the system is working correctly, an investigation will be undertaken to see if it can be used to improve the N-XeUS2's SEOP performance and duty cycle speed.

## 4.10 Future work

### 4.10.1 Introduction

Performance and QA testing of the N-XeUS2 and W-XeUS2 have shown that the XeUS2 platform is suitable for use in a clinical setting. This testing has brought to light an additional improvement that can be made to N-XeUS2, which will increase its performance and reliability, namely the design of the pump laser used. This section covers the plans for the new laser design and also what is required to allow N-XeUS2 to produce HP  $^{129}\text{Xe}$  contrast agent in a clinical setting.

### 4.10.2 New laser design

The QPC Ultra 500 laser was returned to the University of Nottingham unrepaired due to the associated costs. The poor reliability of the QPC Ultra 500 is common with not just the laser in the University of Nottingham but also with lasers at Southern Illinois University Carbondale (SUIC) and Wayne State University. Therefore, the creation of a new laser platform was proposed that would not only be more economical but modular and user-serviceable.

The proposed laser design will combine the power of several 50 W laser bars with a low antireflection (AR) coating provided by Coherent, achieving a narrow spectral width using volume Bragg gratings (VBGs) from Spectra-Physics [192]. VBGs are holographic media that have a grating present throughout their volume. VBGs are transmissive gratings, so they are non-dispersive and act like a filter that is highly spatially and spectrally selective. This is because only the illumination incident on the VBGs that satisfy the Bragg condition is filtered efficiently according to the relation in Equation (4.4).

$$\lambda = 2n\Delta\cos(\theta) \tag{4.4}$$

The variables given in Equation (4.4) are:

- $\lambda$  : wavelength of the incident light
- $n$ : bulk refractive index of the medium the grating occupies
- $\Delta$  : grating spacing
- $\theta$  : angle of incidence

When the Bragg condition is satisfied, the efficiency of the filtering is maximised.

Work by A. Petersen et al. has shown that it is possible for a single laser bar, with its output controlled by a VBG, to produce 54 W of power with the majority concentrated over just a 0.1 nm range [193]. These gratings can also be temperature tuned, offering 0.4 nm of adjustability. However, with a thermal tuning coefficient of  $\approx 0.01$  nm/C, they require a wide range of temperatures to exploit the full range of adjustability. The laser in question was tuned to the Rb  $D_2$ , showing that VBGs can be used at wavelengths relevant to  $^{129}\text{Xe}$  SEOP. VBG work at Rb wavelengths has also been performed by A. Gourevitch et al. in 2008 [194] and P. Nikolaou et al. [155] in 2009.

If this proposed laser design can replace the Ultra 500, the highest cost component of the N-XeUS2 will have a much lower risk associated with it, as it will have lower estimated upfront and repair costs. Additionally, it will be a laser that can be fabricated and serviced by the user, furthering the open-source nature of this polariser.

### 4.10.3 Clinical work

Under the MHRA, it does not matter which device is producing HP  $^{129}\text{Xe}$ , so a new device does not need to be inspected. However, a new protocol will need to be designed for the N-XeUS2. Before the N-XeUS2 can replace the Polarean 9810, a process called “change control” must be implemented [195].

Change control is a formal procedure for changing a process in a controlled way; the process in question is HP  $^{129}\text{Xe}$  production for in-vivo MRI imaging. Any changes in protocol between the two polarisers have to be identified, planned and then introduced. During change control, a request must be submitted to the relevant parties detailing the change. This request is then evaluated for safety to public health and impact on other processes. Any issues that came to light in the review should be resolved before approval is granted. Once the changes have been approved, they will be implemented, with any unforeseen issues resulting in further risk assessment of the change. When the N-XeUS2 has been running in the QMC for an appropriate amount of time, its effectiveness is reviewed.

The N-XeUS2 is a safer piece of equipment compared to the 9810 and is much easier to use. Therefore, no issues with change control are predicted. Strict adherence to the change control process will be observed, following which the N-XeUS2 can finally be used to support the clinical program.

## Chapter 5

# Hyperpolarised $^{129}\text{Xe}$ production for in-vivo clinical imaging using a continuous-flow polariser

### 5.1 Polarean 9810

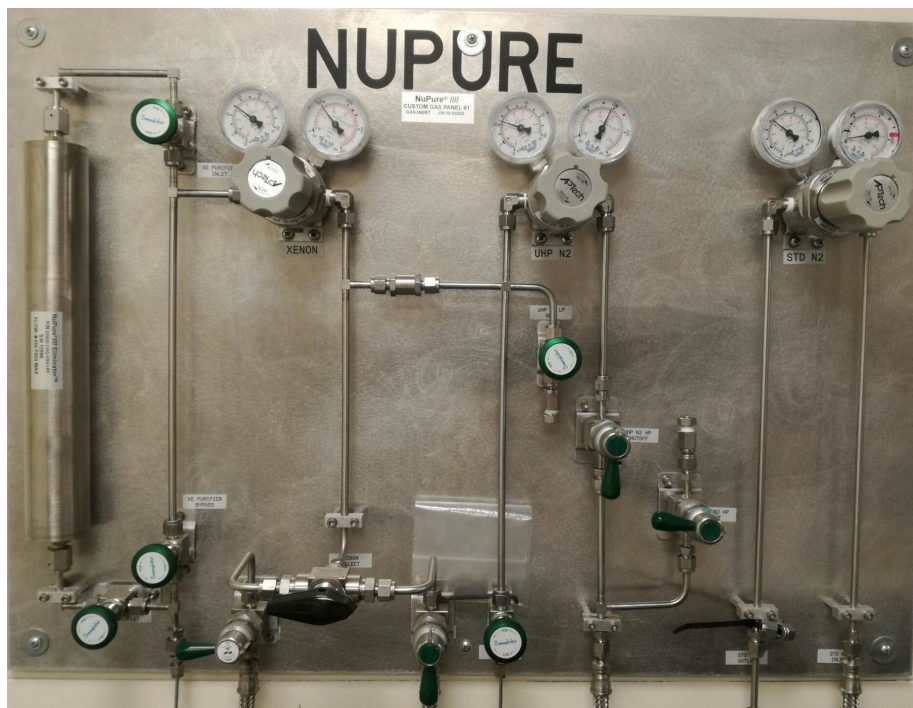
The Polarean 9810 (9180) is a continuous-flow  $^{129}\text{Xe}$  polariser. Unlike the N-XeUS2, which is stopped-flow [24], the gas mix is constantly flowing through the cell during SEOP. The polariser comprises of several subsystems that work together to produce a bag of HP  $^{129}\text{Xe}$ . The 9810 in the QMC has been recently upgraded with a 3777 upgrade kit [196], which was designed to improve the polarisation level produced. As discussed in Chapter 4, the 9810 will eventually be replaced by the N-XeUS2, however the 9810 currently supports all clinical  $^{129}\text{Xe}$  MRI work undertaken in the QMC. This section is an overview of the 9810 hardware and the 3777 upgrade.

#### 5.1.1 Gas management system

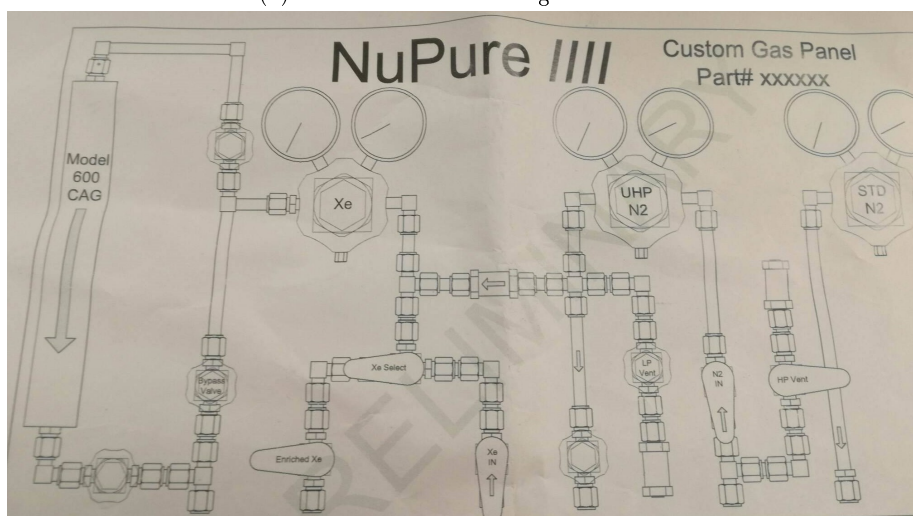
The gas management system of the 9810 has two main sections: a wall-mounted steel manifold custom made by NuPure (Figure 5.1), and an outlet manifold composed primarily of aluminium components (Figure 5.2) and including a glass cold finger within the Polarean 9810 polariser. The sections of the outlet manifold are isolated from one other by manual valves. These have to be manually actuated in a specific order to allow gas to reach its desired location at the correct time, for example during evacuation and purge cycles.

The 9810 requires three different gas cylinders to operate. The first is a lean Xe gas mix, which contains between 1% and 3% naturally abundant Xe, 10%  $\text{N}_2$  and  $^4\text{He}$  making up the remainder. After leaving the gas cylinder and regulator, the Xe gas mix passes through a NuPure Model 600 CAG getter [197] to purge it of any impurities before it flows through the optical cell, where the  $^{129}\text{Xe}$  is hyperpolarised using SEOP. Once it has left the optical cell, the





(a) Custom NuPure inlet gas manifold

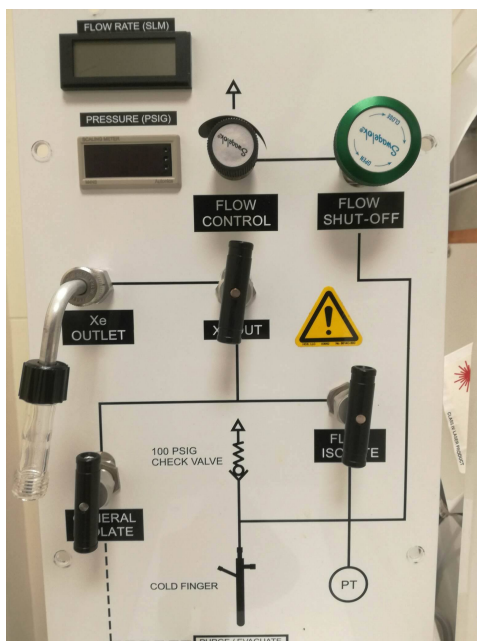


(b) Custom NuPure inlet gas manifold diagram

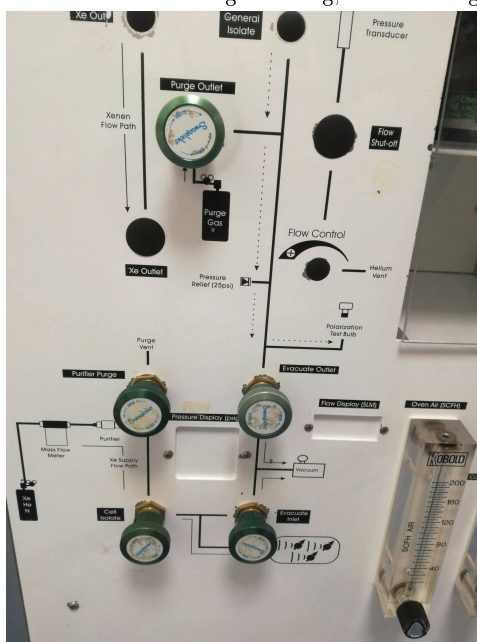
Figure 5.1: Custom NuPure manifold

gas mix flows through the liquid  $N_2$  cold finger where the Xe frozen out and collected, separating it from the other components of the mix. This frozen Xe is released into the bag when it is thawed. The flow rate of the gas mix through the system is indicated by a flow rate meter and controlled via a needle valve that vents to the atmosphere. Controlling the flow rate is essential as it dictates

how long the gas mix is resident inside the optical as well as how quickly the desired volume of Xe can be collected.



(a) Outlet manifold from cold finger to bag, outlet and general isolate



(b) Outlet manifold from general isolate to purge outlet and vacuum

Figure 5.2: 9810 Outlet manifold

The second gas cylinder contains ultra-high purity (UHP)  $N_2$ , which is used

for flushing any atmospheric impurities from the manifold before the Xe gas mix is allowed to flow through to the cell, which protects the Rb within the cell from poisoning. As the structure of getters on the inlet manifold could be damaged by evacuation, this flushing of the inlet manifold is achieved by flowing the UHP  $N_2$  through the entire manifold for 30 minutes. Following this, the inlet manifold and cell are isolated from the outlet manifold and left under constant positive pressure until SEOP begins. This prevents the ingress of impurities as any leaks are outward to the atmosphere.

Impurities in the outlet manifold are flushed before every new bag using three purge/evacuation cycles of  $N_2$ , as performed on the N-XeUS2.  $N_2$  enters the outlet manifold via the purge outlet valve. If the outlet manifold is not purged and evacuated, there is a small chance that impurities could back-flow into the cell and poison the Rb. After these cycles are completed, the Xe gas mix is allowed to flow through the cold finger from the cell out to the atmosphere. Three purge/evacuation cycles are also performed on the Tedlar bag to ensure its structural integrity and to remove any atmospheric  $O_2$  which may depolarise the HP  $^{129}\text{Xe}$ .

### 5.1.2 SEOP cell and oven

The most distinctive feature of the optical cell used in the Polarean 9810 (Figure 5.3) is the pre-saturator, a small bulb on the inlet path of the cell. The Rb is loaded into the cell, so that it resides in the pre-saturator. The bulb is heated to a higher temperature than the primary cell chamber, where SEOP takes place. The Rb vapour diffuses from the pre-saturator into the main cell chamber. The higher temperature in the pre-saturator allows for a higher Rb vapour density while keeping the main chamber's temperature relatively low. The ratio between the SEOP rate and the spin destruction rate is therefore increased. This allows  $P_{Xe}$  to build up more quickly [22], which is critical for a continuous-flow polariser where the residence time of the  $^{129}\text{Xe}$  in the cell is short  $\approx 30$  s. Furthermore, situating the bulk of the Rb outside of the main cell chamber means it cannot contribute to the feedback loop characteristic of Rb runaway, preventing the latter from occurring even with high Rb vapour densities.

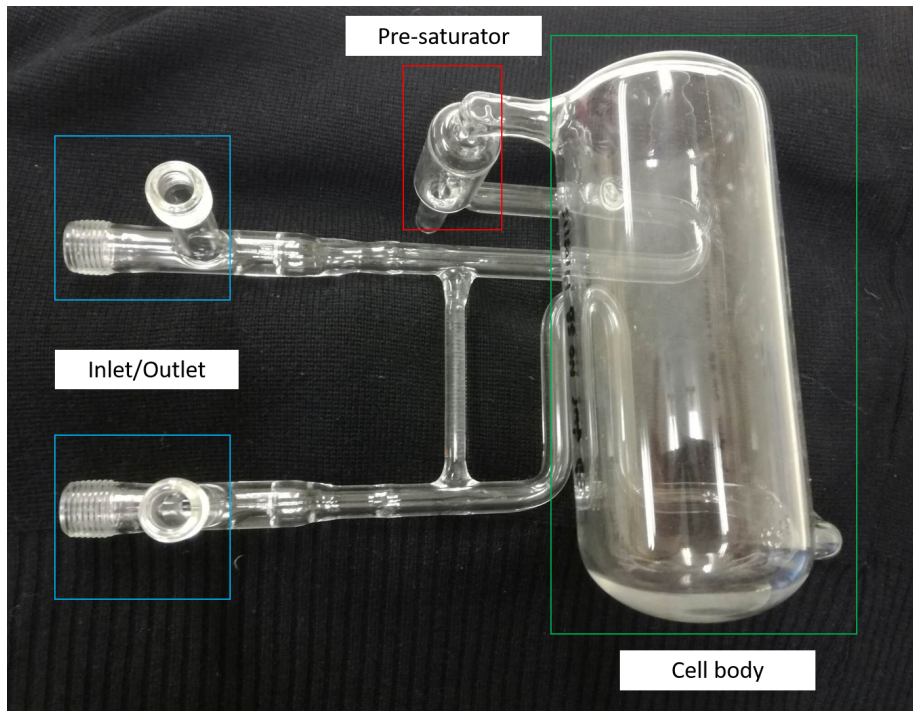


Figure 5.3: 9810 optical cell, pre-saturator (silicon heating tape wrapping the pre-saturator not pictured)

The inlet and outlet pipes are shaped to improve gas flow into and out of the cell. Xe gas mix is allowed to flow more freely from the cell to the cold finger[196]. Therefore, the time the HP gas spends between the Helmholtz coils and storage magnet is reduced. The HP  $^{129}\text{Xe}$  therefore spends less time in earth's field where the  $T_1$  relaxation is faster [198]. The gas also spends less time in the complex field region between the Helmholtz coils and the high-strength storage magnet around the cold finger which, this region contains zero-field regions and regions where the magnetic field rapidly changes directions, both of which are cause an increase the HP  $^{129}\text{Xe}$  relaxation rate [199]. The increased speed through these regions reduces polarisation losses from relaxation and increases the final in-bag  $P_{\text{Xe}}$  level.

A forced-air oven heats the cell by flowing compressed air from an external compressor over a heating element into an insulated oven. The temperature is monitored via a PT100 temperature sensor and is controlled by a Fuji PXR4 PID temperature controller [200] using a tuned feedback loop with the PT100 to ensure the cell reaches its temperature set-point with minimal overshoot.

The pre-saturator is wrapped in a silica heating tape, which can heat the pre-saturator to temperatures above that of the oven. Another PXR4 is used to control the pre-saturator temperature, and this sits just below the oven controller on the front panel of the polariser (see Figure 5.4).



Figure 5.4: 9180 front panel

### 5.1.3 Hyperpolarised $^{129}\text{Xe}$ cryo-collection and storage

The polariser uses a lean gas mix, which, in its current form, would not have sufficient bulk magnetisation to produce the signals required for clinical MRI imaging. The HP  $^{129}\text{Xe}$  therefore needs to be separated from the carrier gases within the mix, and a sufficient volume of it needs to be collected to fill a Tedlar bag for subject administration. This is achieved using cryo-collection. Xe has a much higher freezing point ( $-111.7\text{ C}$ ) compared to  $^4\text{He}$  ( $-272.05\text{ C}$ ) and  $\text{N}_2$  ( $-209.86\text{ C}$ ) [201]. This difference is exploited when the gas mix flows through the cold finger that is submerged in liquid nitrogen. The temperature within the cold finger is such that the Xe freezes to the walls while the rest of the mix remains in a gaseous state and flows out to atmosphere.

As part of the 3777 upgrade, the cold finger's straight shape, similar to that of a test tube, was replaced by the new "puzzler" design. Now with more turns to it, the finger's surface-area-to-volume ratio is increased, meaning the Xe is frozen and thawed out more efficiently [196]. The  $^{129}\text{Xe}$  therefore spends less time near the phase transition point where the  $T_1$  is on the order of seconds [202], reducing polarisation losses. The cold finger features a second gas path that allows room-temperature  $\text{N}_2$  to flow over the cold-finger outlet. The outlet is the narrowest point of the cold finger's body and is therefore at most risk of being blocked by frozen  $^{129}\text{Xe}$ . The room temperature  $\text{N}_2$  therefore keeps this section above the Xe freezing point. If a blockage were to occur, a dangerous amount of pressure would build behind it, which could damage the glassware and even cause an explosion. Although there is an integral blow-off valve in the cold finger, the glass could be compromised before the pressure is high enough

to trigger its opening.

During cryo-collection, polarisation losses are mitigated due to the magnet storage field [153]. The magnetic storage field is created around the cold finger by a set of permanent neodymium magnets producing a field strength of 2000 G (see Figure 5.5). This strong magnetic field increases the  $T_1$  relaxation time of the HP  $^{129}\text{Xe}$  [199]. The fact that the Xe is frozen also reduces polarisation losses as solid form HP  $^{129}\text{Xe}$  relaxation times are on the order of hours [202].

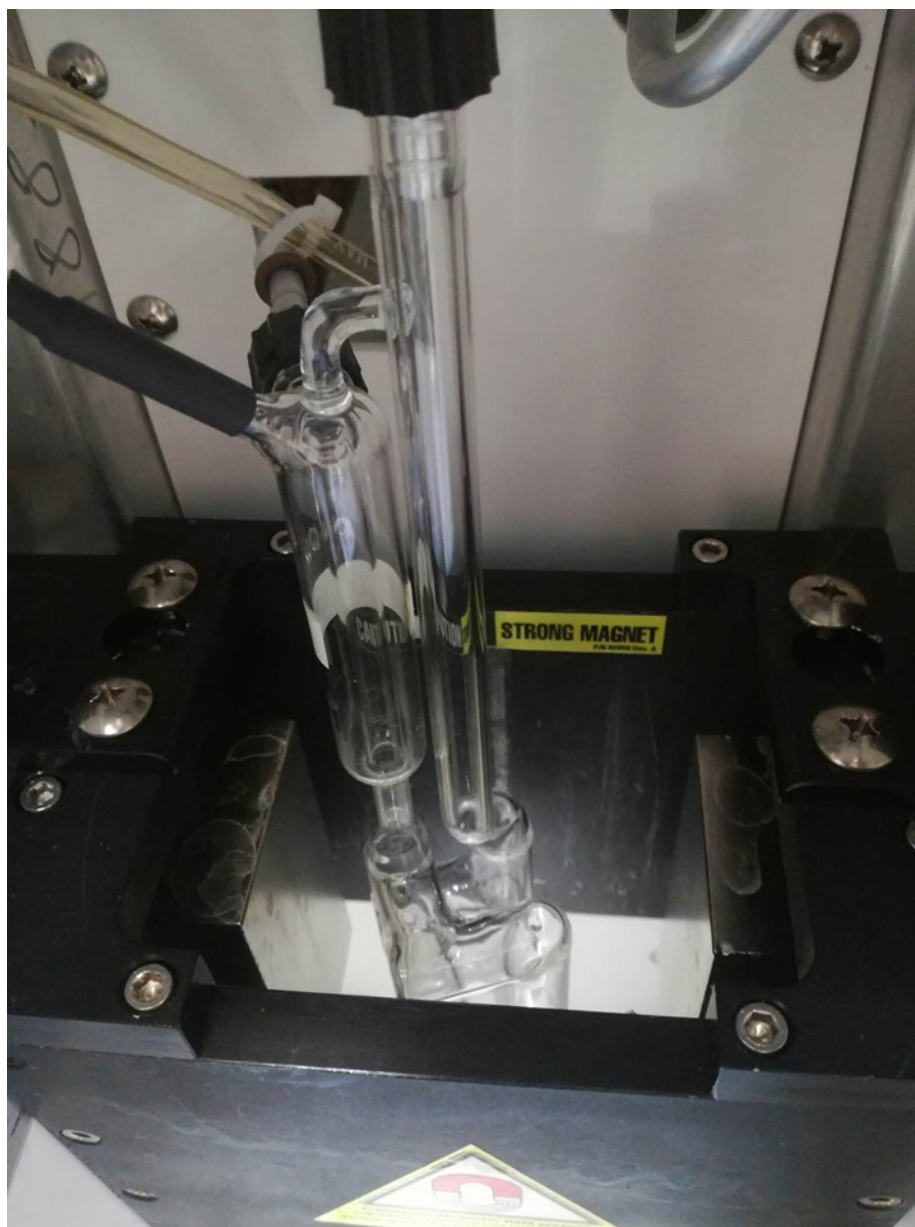


Figure 5.5: Cold finger sitting within the permanent magnetic field

To submerge the cold finger in liquid  $N_2$ , a Chemglass dewar is raised into position so the cold finger is sitting inside it. When the Xe gas mix and room temperature  $N_2$  are flowing through the two paths of the cold finger at the correct flow rate, liquid  $N_2$  is poured through a funnel and into the dewar via a flexible hose. The liquid  $N_2$  is poured into the dewar until the body of the cold finger is completely submerged to maximise the cold surface area for cryo-collection.

#### 5.1.4 $B_0$ Field

The  $B_0$  field in which the SEOP cell sits is created by two Helmholtz coils connected to a TDK-Lambda PSU. A 3 A current through the coils provides a field strength of 20 G.



Figure 5.6: Helmholtz coils providing the  $B_0$  field with the cell sitting inside a light-tight enclosure

#### 5.1.5 Laser system

The 9810 polariser uses a QPC Ultra 200 laser based on the same laser technology as the Ultra 500 laser used on the N-XeUS2 in Chapter 4. As stated in Section 4.6.6 of this chapter, the laser uses the same beam-expanding telescope as the Ultra 500. The laser is powered by a compact Xantrex XTR power supply, and its temperature is managed via water-cooling with a Melcor M600 chiller.

The entire optical train is fully enclosed, as seen in Figure 5.7. The polariser is designed to be a class-1 device, meaning it can be operated safely without laser goggles.

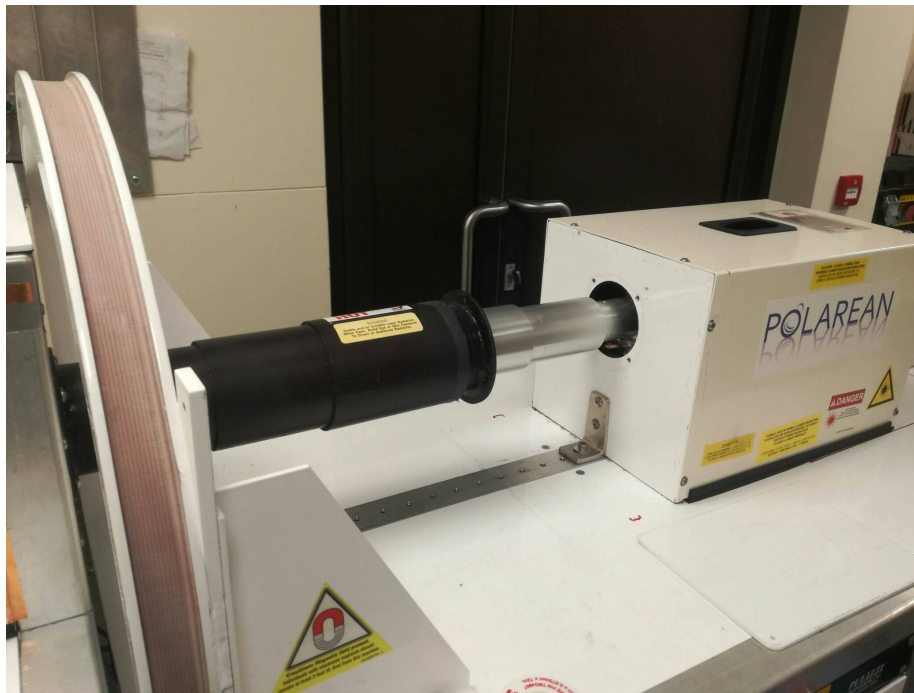


Figure 5.7: Fully enclosed optical train with laser, beam-expanding telescope and beam tube

There are two sensors situated at the rear end of the optical cell to monitor laser output and absorption within the SEOP cell. The first is a fibre-optic sensor connected to an Ocean Optics HR2000 IR spectrometer, and the second is a photodiode, as shown in Figure 5.8. The HR2000 functions in the same way as it does in the N-XeUS2. The spectrometer's output can be monitored using SpectraSuite. This allows the user to see the laser's output spectrum and then fine-tune the laser's power and temperature to bring its output onto resonance with the Rb  $D_1$  line. During SEOP it can also be used to observe the laser light absorption by the Rb in the cell. The photodiode measures the fraction of the laser light able to pass through the cell. A percentage transmission value is calculated by dividing the power incident on the photodiode when the cell is hot during SEOP by the power when the cell is at room temperature (zero absorption assumed). During clinical runs, the value is recorded for QA purposes but can also be used in tandem with the IR spectrometer to observe how Rb vapour density inside the cell changes with different polariser settings.





Figure 5.8: Fibre-optic cable coming out to the spectrometer (blue) and cable exiting the photodiode (black)

### 5.1.6 Polarean 2881 polarisation measurement station

Because the Polarean 9810 does not have its own dedicated NMR system,  $P_{Xe}$  has to be measured on a separate measuring station after the Xe has been decanted into the Tedlar bag. The Polarean 2881 polarisation measurement station (2881) is pre-calibrated using an STS source from Polarean, and this is itself calibrated against a water signal as described in Chapter 3 Section 3.3.2. The

pre-calibration allows accurate measurement of the  $P_{Xe}$ . The polarisation calculation is performed using the software Polarimetry 4.3 on a laptop connected to the measurement station [203].



Figure 5.9: NMR surface coil on the 2881 measurement station

To generate a  $B_0$  field for polarisation measurement, the 2881 has two 24-inch Helmholtz coils powered by an ultra-low noise, high stability Kenwood PDS120-6 DC power supply to improve SNR and hence accuracy of the recorded polarisation. This generates a magnetic field for HP  $^{129}\text{Xe}$  nuclei to precess about to enable NMR measurements to be taken. The NMR measurements are performed using a surface coil. This operates at 25 kHz and is connected to an NMR circuit powered by its own PSU [203].



Figure 5.10: 2881 measurement station

It is essential to have an accurate measurement of the  $^{129}\text{Xe}$  in a clinical setting.  $^{129}\text{Xe}$  is classed as an investigational drug by the Medicines and Healthcare products Regulatory Agency (MHRA). Its manufacture and delivery are therefore subject to international Good Manufacturing Practice (GMP) standards enforced by the MHRA for an investigational drug.

Despite its safety, there is a lower polarisation limit for ethics approval by the National Research Ethics Service (NRES). Below this limit (3%), the image quality would be compromised to such a level that it would be of minimal diag-

nistic use. Accurate measurement on a correctly calibrated measuring device is essential for QA as well as ensuring that any bags delivered to a human subject are above the 3% limit.

### 5.1.7 Optimal operating conditions

#### Continuous-flow SEOP with a 3% Xe gas mix

In all previous clinical work in the QMC, the 9810 was run with a 2% Xe, 10%  $N_2$  and 88%  $^4He$  gas mix. To reduce collection times with minimal polarisation losses, the gas mix was switched to a 3% Xe, 10%  $N_2$  and 87%  $^4He$  gas mix. This richer mix was installed before the upright and 1.5 T studies detailed in Chapters 7 and 8 were performed. This marked the first time a 3% mix had been used on the 9810 after its upgrade. Work on the original Polarean 9800 using 1%, 2%, 3% and 5% gas mixes suggest that a 3% mix would still provide a useable polarisation following the upgrade. Moving to a richer Xe gas mix would cause higher spin-destruction rate, negatively impacting on the final  $P_{Xe}$ . However, a richer mix allows for a shorter cryo-collection times, compensating for the increased spin destruction with reduced depolarisation time while the Xe is being stored in solid form.

The effect of the final  $P_{Xe}$  using a 3% mix was investigated by measuring the in-bag polarisation from a 0.6 L bag at different flow rates. As with the 2% gas mix, the temperatures of the oven and pre-saturator were 130 C and 210 C, respectively, allowing a fair comparison to be made between the two gas mixes. As expected, the slower the flow rate, the higher the polarisation, with 0.67 SLM giving the highest final polarisation of  $22.3\% \pm 0.3\%$ , and 1.33 SLM producing the lowest polarisation of  $16.7\% \pm 0.1\%$  (see Figure 5.11). Fitting an exponential trend line to this graph gives a polarisation of 16.65% for a flow rate of 1.25 SLM. Using the same flow rate and bag volume, a  $P_{Xe}$  of  $\approx 18\%$  was achieved with the 2% mix. Although there was a drop in  $P_{Xe}$  between the 2% and 3% mix for the same flow rate (1.5%), this was within the run-to-run variability of the polariser. This meant the reduced cryo-collection time had prevented a significant drop in  $P_{Xe}$  when using the richer 3% mix.

Final  $^{129}\text{Xe}$  polarisation in 0.6 L bag from the Polarean 9810 at different Xe gas mix flow rates

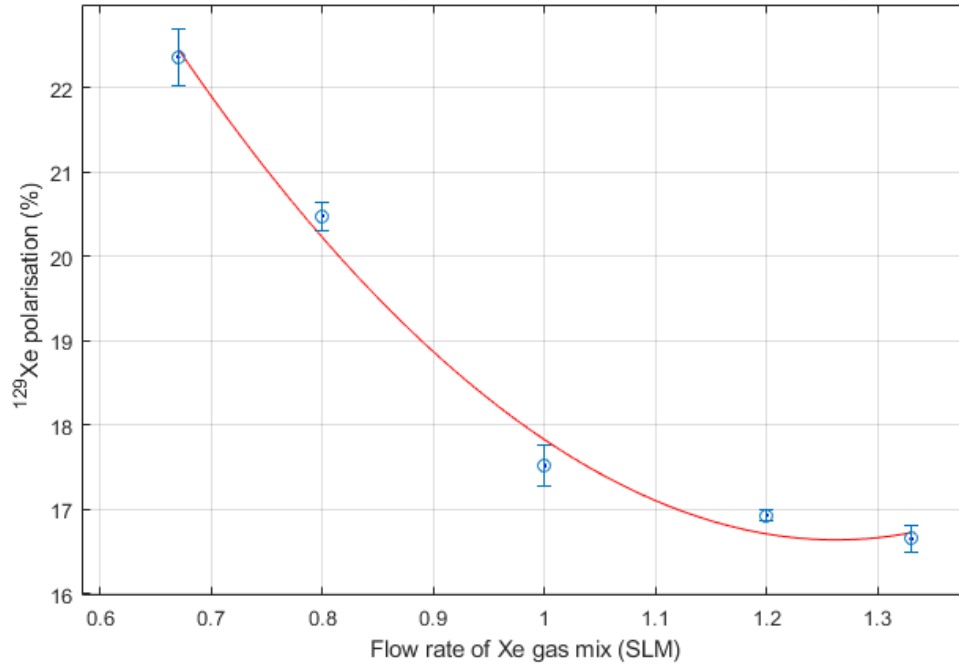


Figure 5.11: Graph to show how  $P_{Xe}$  is affected by flow rate through the Polarean 9810 optical cell

For the 3% mix, a flow rate of 1.25 SLM was selected as a 1 L sample can be produced with an acceptable level of polarisation after 28 minutes of cryo-collection. After the sample has been produced, it needs to undergo QA and be delivered to the scanner. When combined with time needed to perform the requisite purge/evacuation cycles on the outlet manifold, the minimum time between bags is 35-40 minutes. The minimum time between HP  $^{129}\text{Xe}$  scans dictated by the study's ethics is 30 minutes. In practice, the minimum time is closer to 40 minutes, as the subject needs to be removed from the scanner and have their vital signs monitored before they are returned. Therefore, the turnaround time of the polariser is equal to or less than that of the subject scanning time. This means that the production of HP  $^{129}\text{Xe}$  is no longer the rate-limiting step during a clinical visit, which increases subject throughput and reduces pressure on the polariser operator.

Before the upgrade, the 9810 could produce a 1 L bag in 40 minutes with a  $P_{Xe}$  of 5-8%. In its current configuration, the polariser can 1 L produce samples with a the  $P_{Xe}$  of  $14.2\% \pm 1.1\%$  without increasing the overall turnaround time and is therefore well suited to supporting clinical work in the QMC.

A full description of the HP  $^{129}\text{Xe}$  drug production protocol is detailed in Appendix section C.

## 5.2 Conclusion

The switch from a 2% to a 3% Xe gas on the Polarean 9810 polariser resulted in a reduction in production time by 12 minutes without a significant loss in polarisation. Using this gas mix, a 1.25 SLM flow rate was able to produce 1L of HP  $^{129}\text{Xe}$  in 28 minutes, lowering bag-to-bag production time to below that of the scanner turnaround time.

This chapter discussed the SOP used to ensure HP  $^{129}\text{Xe}$  can be given to a subject safely with the MHRA guidelines. For this process, a special IMP licence is needed which allows the QP to sign off on a batch release based on the QC checks of the first bag. This enables rapid delivery of the bag to patient after production, which in turn reduces polarisation losses and maximises the signal available for imaging. Four people are required for the clinical production of HP  $^{129}\text{Xe}$ , ensuring rigorous QC for subject safety and high traceability should an adverse subject response occur.

## Chapter 6

# Clinical HP $^{129}\text{Xe}$ MRI and NMR - lung, brain and kidney disease states

### 6.1 Introduction

This chapter gives a brief overview of the key diseases being investigated with HP gas in the lungs, brain and kidneys, providing further detail into the motivation behind research in this field and highlighting relevant HP  $^{129}\text{Xe}$  imaging studies relating to each disease state. The earliest HP gas MRI performed in the lungs was undertaken using HP  $^3\text{He}$  before the field began to move towards using HP  $^{129}\text{Xe}$ . The reasons for the switch and details of comparison studies between HP  $^{129}\text{Xe}$  and HP  $^3\text{He}$  MRI in the lungs are therefore discussed at the start of the lung diseases section.

### 6.2 Lung diseases

Although the lungs are one of the most vital organs in the human body, they are also one of the most vulnerable, at risk from airborne infection and damage from particulates in the atmosphere. According to a report from the World Health Organisation (WHO), respiratory diseases cause the highest number of deaths and cases of disability globally [1]. Four million people suffer a premature death annually as the result of chronic respiratory diseases, and the number exposed to toxic or polluted air is in the billions [1]. The WHO advises that preventing, controlling and curing respiratory diseases should be the number one priority when making decisions in the healthcare sector [1].

When inhaled, Xe takes the same pathway as oxygen, dissolving into the blood from the lungs. This behaviour enables functional information about the lungs to be obtained, complementing the structural information provided by an HP noble gas. The high chemical shift of  $^{129}\text{Xe}$  also means it is sensitive to its environment, making it possible to identify where the HP  $^{129}\text{Xe}$  is within different domains of the body, i.e. the airways of the lung, lung parenchyma or blood, and how it transfers between them. It therefore makes sense that

HP  $^{129}\text{Xe}$  MRI could be used as a key technique in understand mechanisms underlying chronic respiratory diseases and hence contribute to the global effort against respiratory diseases. The most common lung diseases that HP  $^{129}\text{Xe}$  has been used to investigate are described in brief below.

### 6.2.1 HP $^3\text{He}$ vs HP $^{129}\text{Xe}$ MRI Imaging

Initially, HP  $^3\text{He}$  was used for HP gas MRI imaging in the lungs and the high repeatability of such studies has been well-documented [204]. However, due increasing costs of  $^3\text{He}$  described in Section 2.5.4, the focus has switched to the more affordable  $^{129}\text{Xe}$ . There were concerns that the anaesthetic properties of  $^{129}\text{Xe}$  would pose a safety risk and reduce tolerability in patients; however, studies have shown that it is well-tolerated in healthy adults and those with impaired lung function [205] [206]. A study by L. Walkup et al. was carried out in 2016 to observe the tolerability of HP  $^{129}\text{Xe}$  when inhaled by paediatric patients with CF. The study showed that no minor, serious or severe adverse events were reported that related to the inhalation of  $^{129}\text{Xe}$ . [207]

$^{129}\text{Xe}$  also possesses a lower gyromagnetic ratio of a third of  $^3\text{He}$  and lower enrichment, which makes MRI imaging more challenging. Comparison investigations have been undertaken using both  $^3\text{He}$  and  $^{129}\text{Xe}$  in patients with COPD and cystic fibrosis (CF) in 2012 and 2016, respectively. These investigations have shown that there is a significant correlation between HP  $^{129}\text{Xe}$  and HP  $^3\text{He}$  MRI when quantifying lung ventilation at 3 T [208] [209].  $^{129}\text{Xe}$  and  $^3\text{He}$  both had correlations between the FEV1 and ventilation defect percentage (VDP), showing that the sensitivity of both gases when measuring lung function is comparable [208] [209]. Both studies found that, in patients CF and COPD, HP  $^{129}\text{Xe}$  measured a higher VDP value than  $^3\text{He}$ . This may be due to its lower diffusion coefficient, which leads to high sensitivity to regional ventilation [208] [209]. The CF comparison study performed also reported a correlation between repeated HP  $^{129}\text{Xe}$  images taken in the same patient, which indicated that HP  $^{129}\text{Xe}$  MRI images also have a high reproducibility [209]. A study in 2018 by N. Stewart et al. compared HP  $^3\text{He}$  and HP  $^{129}\text{Xe}$  MRI's ability to evaluate the microstructure and ventilation of the lungs at 1.5 T in healthy volunteers and patients with COPD. The reason for this change in field strength is due to magnetic susceptibility differences between 1.5 T and 3 T affecting the lung ventilation and diffusion-weighted microstructural MRI for both  $^{129}\text{Xe}$  and  $^3\text{He}$  [210] [97]. The study concluded that, at 1.5 T, HP  $^{129}\text{Xe}$  is able to provide almost the equivalent quantitative lung ventilation information and microstructural MRI to HP  $^3\text{He}$  [211]. This demonstrates that HP  $^{129}\text{Xe}$  MRI is becoming a clinically viable replacement to HP  $^3\text{He}$  MRI when measuring the ventilation and microstructure of the lungs.

### 6.2.2 Cystic fibrosis

CF is a disease that can affect many parts of the body. However, due to the majority of symptoms manifesting in the respiratory system, it is frequently thought of as a lung disease [212]. CF occurs because the sufferer cannot properly regulate the movement of water and salt between the body's cells due to a faulty gene. As a result, thick and sticky mucus can build up inside the lungs and digestive system [212]. People with the condition have pulmonary



symptoms that include a persistent cough, wheezing and a higher risk of lung infection as the mucus creates an environment conducive to the growth of harmful bacteria. CF also reduces lung function as the walls of the airways thicken, become damaged and are obstructed by the mucus [212].

CF is a genetic disorder, requiring the individual to have inherited two defective CF genes, one from each parent [213]. CF prevalence varies globally, with 1 in 2000-3000 new-borns being diagnosed with CF in the European Union, and the number standing at 1 in 3500 in the US [213]. CF also vastly reduces life expectancy, with the median survival age of sufferers in the UK currently estimated to be 46 years for males and 41 years for females [214].

Although CT is currently the benchmark for investigating lung structure in CF patients, exposure to ionising radiation means its use is limited in long-term studies and paediatrics. Extensive efforts have gone into investigating HP gas MRI's use as a tool for monitoring the progression of CF and the CF patient's response to treatment.

Initial HP MRI studies were performed on patients with CF using HP  $^3\text{He}$ , investigating regional defects in lung ventilation [215], [216]. HP  $^3\text{He}$  is also able to observe long-term changes in the lung ventilation of CF patients [217]. The focus of HP gas MRI has shifted from  $^3\text{He}$  to  $^{129}\text{Xe}$  in recent years, and investigations have shown that HP  $^{129}\text{Xe}$  can image ventilation defects in CF patients, including children with mild symptoms [218]. Work has also been undertaken that showed HP  $^{129}\text{Xe}$  MRI to be effective in monitoring CF patients' response to treatment [219].

### 6.2.3 Chronic obstructive pulmonary disease

The defining marker of COPD is airflow limitation in the lungs. The functional consequences of COPD varies from patient to patient depending on the severity of their airflow obstruction, their environment and lifestyle. The severity of the symptoms increases over time, linked to an inflammatory response of the lung tissue to toxic agents (e.g. from smoking) or particulates in the air. The damage COPD does to the lungs cannot be reversed [220]. COPD puts an immense burden on the healthcare system. Its prevalence and morbidity vary from country to country because of different environmental factors. These factors include air pollution levels, smoking rates and quality of healthcare. In the US, before the COVID-19 pandemic COPD was the fourth-largest cause of death, with an estimated cost of 14 billion dollars to the US economy [220]. As of the date of this thesis, COPD has no cure, and its treatment is palliative.

Multiple studies have imaged patients with COPD using HP  $^{129}\text{Xe}$  MRI. Work by Kaushik et al. showed that it was possible to use HP  $^{129}\text{Xe}$  to create ADC maps that could distinguish between aged-matched subjects with COPD and healthy volunteers [221]. They concluded that  $^{129}\text{Xe}$  ADC mapping could detect early lung changes due to COPD, which would enable earlier intervention and thus generate better patient outcomes. HP  $^{129}\text{Xe}$  could also be used to non-invasively phenotype COPD sufferers and monitor their treatment [221]. In 2019, a study by Myc et al. showed that HP  $^{129}\text{Xe}$  functional pulmonary MRI could in fact differentiate between COPD phenotypes such as chronic bronchitis, emphysema and intermediate phenotypes [222]. There is growing evidence indicating that HP  $^{129}\text{Xe}$  MRI can help clinicians identify and treat patients with COPD. This utility is growing as new ways of exploiting  $^{129}\text{Xe}$  are found,

and new polariser technology is producing HP  $^{129}\text{Xe}$  with higher bulk magnetisation.

#### 6.2.4 Asthma

Asthma is a chronic lung condition, characterised by symptoms such as shortness of breath, wheezing and a tight chest. These symptoms arise from inflammation of the lungs. The walls of the airways become thicker, restricting the airflow. In contrast to COPD, the degree of airflow obstruction seen in asthma varies over time and can usually be reversed. However, asthma can be fatal in extreme cases when the airways can become blocked by excreted mucus and cells [223]. Asthma affects 300 million people around the globe. This will rise as urban populations grow which may, in turn, increase exposure to high air pollution levels [224]. A greater understanding is needed to know what causes asthma. New methods of treatment are needed to reduce its pervasiveness.

In 2016, a study by M. He et al. used HP  $^{129}\text{Xe}$  MRI to quantify the ventilation distribution within the lungs, using older and younger control groups to compare against asthmatics of a similar age. They found it was possible to see the heterogeneity of ventilation within the lungs. The MRI scans showed how low ventilation regions of the lungs increased, and high ventilation regions were significantly reduced in asthmatics compared to the control group. HP  $^{129}\text{Xe}$  was able to image and quantify ventilation distribution in asthmatics and even show impairment in lung function that cannot be detected by spirometry [225]. This study also investigated the responses of two patients to albuterol, a bronchodilator, affected lung ventilation. HP  $^{129}\text{Xe}$  MRI showed that, even though the FEV1 from spirometry showed no change, the low ventilation regions of the lungs unexpectedly increased in one of the patients [225]. HP  $^{129}\text{Xe}$  has also been used to see the effect of treatments other than bronchodilators, such as Bronchial thermoplasty. Bronchial thermoplasty is a heat treatment performed on the inside walls of the airways to lower the amount of thickened small muscle tissue. A recent study used HP  $^{129}\text{Xe}$  to guide the treatment of bronchial thermoplasty, using HP  $^{129}\text{Xe}$  MRI images to treat the most affected areas and comparing the effectiveness compared to unguided treatment. It found that a single guided bronchial thermoplasty session achieved improvements similar to three unguided visits [226]. As the treatment is specific to affected tissue when guided, this increases the safety and reduces stress to the patient's lungs. HP  $^{129}\text{Xe}$  can therefore detect the progression of asthma, assess treatment strategies and guide certain treatments to make them more effective.

#### 6.2.5 Idiopathic pulmonary fibrosis

The progression of IPF is not fully understood. Recent evidence points towards inflammation being caused by the anomalous activation of alveolar epithelial cells. This activation leads to fibrosis of the lungs as the activated cells cause fibroblast and myofibroblast foci to be created. They both excrete substances that damage and scar the lung tissue. This reduces lung elasticity and its ability to perform gas exchange. These effects have a massive negative impact on a patient's quality of life. Although IPF is an age-related condition, the connection between age and alveolar epithelial cell activation is not known [227]. The exact prevalence of IPF is also unclear and differs from country to country.

[228]. The estimates for prevalence vary because of differences in methodological practices and limited data. However, a study by Raghu et al. estimated that, in the US, 89,900 patients were suffering from IPF in 2000 [229].

HP  $^{129}\text{Xe}$  has been used to measure the diffusion limitation within the lungs of subjects with IPF compared to healthy volunteers. Using NMR and the chemical shift of  $^{129}\text{Xe}$ , it is possible to see how gas diffuses from the gas phase to the pulmonary tissue and into the red blood cells (RBCs). They found that the ratio between the HP  $^{129}\text{Xe}$  signal from red blood cells and pulmonary was 3.3 times lower for IPF subjects compared to healthy volunteers [230], showing that diffusion was limited through pulmonary tissue to the RBCs. The signal ratio of HP  $^{129}\text{Xe}$  in the gas phase to in the RBCs can also be compared [231]. The unique properties of HP  $^{129}\text{Xe}$  can assist in assessing lung function and monitoring the response of potential therapies of those suffering from IPF.

## 6.3 Brain diseases

According to a report from Public Health England, 366,728 people over the age of 20 who died between 2001 and 2014 had neurological conditions mentioned on their death certificate [232]. In this time, the number of deaths per annum increased by 39% from 23,051 deaths to 31,925 [232]. At the end of this period, this accounted for 7% of yearly deaths in England. This impact does not factor in that some diseases are degenerative and can considerably reduce the quality of life of the sufferer and increase the cost of healthcare cover.

$^{129}\text{Xe}$  takes the same pathway as oxygen, from the lungs into the blood and into the brain. The chemical shift of HP  $^{129}\text{Xe}$  makes it possible to image the brain vasculature and parenchyma [233], meaning HP  $^{129}\text{Xe}$  MRI can be used to image a wide range of neurological diseases. Conventional proton MRI currently produces a greater signal than HP  $^{129}\text{Xe}$  within the brain. However, this does not mean that HP  $^{129}\text{Xe}$  cannot be used to gain clinically useful information or even as an alternative to blood oxygen level-dependent (BOLD) functional MRI [234]. This alternative is becoming more and more common with new polariser technology producing ever-higher  $P_{\text{Xe}}$  levels.

### 6.3.1 Stroke

A stroke is caused when a reduction in blood flow in the brain causes the cells in a localised area to die from a lack of oxygen. Cell death causes a drop in brain function in the areas affected [235]. Symptoms are varied, ranging from being unable to move certain limbs or sides of the body to not being able to understand speech. The effects of the stroke can be transient or permanent [236]. A report from the American Heart Association in 2016 stated that, although stroke mortality has decreased in recent years, it is still a major risk to public health. It remains the fifth-largest cause of death in the US and affects 795,000 people a year nationwide [237].

In 2011, HP  $^{129}\text{Xe}$  was used to image a stroke in a rat's brain as a cerebral blood-flow tracer. This study proved that HP  $^{129}\text{Xe}$  could detect the ischemic core area of a stroke [238], as shown in Figure 6.1. It also demonstrated that HP  $^{129}\text{Xe}$  can be used alongside proton MRI to study reduced blood flow in the brain. An investigation imaging a human stroke victim's brain with HP  $^{129}\text{Xe}$

showed that signal from the damaged areas of the brain was 60% less than that from unaffected areas [239]. This study proved the feasibility of using HP  $^{129}\text{Xe}$  to image a stroke in-vivo, and that  $^{129}\text{Xe}$  can be administered to a subject with cerebral pathology. Scan times are also reduced compared to proton imaging, so the scanning itself is more tolerable to those with cerebral pathologies.

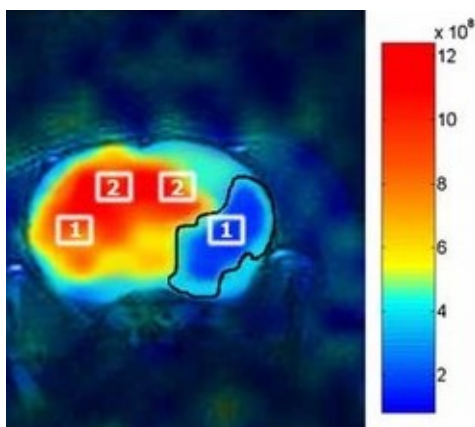


Figure 6.1: HP  $^{129}\text{Xe}$  chemical shift image (CSI) of a rat brain that has suffered a stroke, with the ischemic core highlighted with a black border [238]

### 6.3.2 Alzheimer's disease

Alzheimer's is a degenerative disease that affects neurons in the brain. The key pathologies include the build-up of plaques on the exterior of the neurons. The interior of the neuron, partly driven through the protein tau, becomes damaged. These changes lead to neuron dysfunction, ultimately resulting in the death of the neuron [240]. Symptoms can escalate from poor short- to long-term memory in the early stages. Later-stage symptoms can comprise behaviour changes or an inability to perform simple tasks such as walking or swallowing [240]. This is a very distressing experience which extends to people beyond the sufferer themselves. In the US, an estimated 5.4 million people are living with the disease, with 700,000 people over the age of 65 dying from Alzheimer's in 2016 [240]. Due to an ageing population, this number is set to more than double by the middle of the century, further increasing pressure on the healthcare system.

Biomarkers are objective indicators of a patient's medical state that can be observed from outside the patient [241]. If biomarkers can be measured accurately and reproducibly, they can be used as diagnostic tools. The use of biomarkers with Alzheimer's is limited due to the fact that most of them overlap with those seen in healthy individuals. A recent study found that HP  $^{129}\text{Xe}$  may offer some novel biomarkers without this overlap, namely the sixty-second  $^{129}\text{Xe}$  retention time and the  $^{129}\text{Xe}$  washout parameter in the white and grey matter of the brain [242]. They found that patients with Alzheimer's retained significantly more  $^{129}\text{Xe}$  compared to the healthy controls, and the  $^{129}\text{Xe}$  washout rate was much slower [242]. Although further validation is needed in the form of larger clinical trials, this shows the potential of HP  $^{129}\text{Xe}$ 's use in diagnosing Alzheimer's disease.

## 6.4 Kidney disease

Chronic kidney disease is the gradual loss of kidney function, impeding its ability to filter waste and excess fluids in the blood and causing them to build up to dangerous levels in the body [243]. Symptoms of kidney disease range from nausea to high blood pressure. The disease is progressive and, since the kidneys can compensate for the reduced function, symptoms may not appear until after irreversible damage has been caused [243]. Since kidney disease can have secondary effects on nearly every part of the human body, the complications of it may be extensive. These can include anaemia, damage to the nervous system and cardiovascular diseases. When irreversible damage occurs, known as end-stage kidney disease, dialysis or transplant will be needed for the patient's survival [243].

Kidney disease has many complex causes, including as a comorbidity of diabetes and hypertension. It was estimated that, in 2015, that kidney failure caused 1.2 million people to lose their lives [244], a 32% increase on the numbers in 2005. When combined the number of kidney disease sufferers who died without dialysis [245] and those who died from acute kidney injury [246] is combined, the global annual death toll from kidney disease is estimated to be between five and ten million people.

Kidney disease poses a substantial economic burden, with higher income countries having to spend 2-3% of their yearly health-care budget on the treatment of end-stage kidney disease [245]. In the case of the US, Medicare expenditures to treat chronic and end-stage kidney diseases were above 64 and 34 billion dollars, respectively [247]. The number of people on dialysis worldwide is predicted to rise to 5.24 million by 2030, doubling the number in 2010 [245], with the associated costs rising in step.

The kidney is one of the most perfused organs in the body, receiving a 5<sup>th</sup> of cardiac output. The circulatory transit time from the lungs is approximately a few seconds. HP  $^{129}\text{Xe}$  has a  $T_1$  of  $\approx 8$  seconds in blood [248] so can reach the kidneys with sufficient polarisation for in-vivo detection. Work by J. Chacon-Caldera et al. assessed the feasibility of dissolved HP  $^{129}\text{Xe}$  MRI in human kidneys [14]. Using a bespoke coil, they were able to detect HP  $^{129}\text{Xe}$  dissolved in the kidneys in both NMR spectroscopy and MRI experiments at a  $B_0$  field of 3 T. These experiments showed that measuring parenchymal tissue perfusion in the kidneys was possible. They also predicted that it might be possible to use HP  $^{129}\text{Xe}$  to measure early filtration in the kidney. Based on these results, they advised that pilot clinical studies to assess kidney physiology with HP  $^{129}\text{Xe}$  could now be considered.

## 6.5 Conclusion

As outlined in the previous sections, even a small handful of lung, brain and kidney diseases has a wide-reaching impact on society. These debilitating and often fatal diseases not only have a human cost, but, due to the sheer number of cases, has a significant economic toll. Developing imaging techniques to observe lung, brain and kidney function is therefore of utmost importance. HP  $^{129}\text{Xe}$  MRI is being used in clinical studies, and its feasibility in helping clinicians identify and monitor the treatment of various diseases is being demonstrated.

Before it can be routinely used as a clinical tool, it requires more focused research effort, reduced costs and improved manufacturing techniques. Nevertheless, HP  $^{129}\text{Xe}$  MRI and NMR could potentially have a real impact when translated into a clinical setting.

## Chapter 7

# HP $^{129}\text{Xe}$ imaging results with a 0.5 T upright MRI scanner

### 7.1 Introduction

This chapter focuses on the preliminary work undertaken on the 0.5 T MROpen Upright Paramed Medical Systems (Upright) scanner using HP  $^{129}\text{Xe}$ . It starts with a discussion of the scanner and coil hardware, before moving onto the NMR and MRI work undertaken. Finally, the chapter covers the future work planned, including acquiring a new chest coil and getting the coils approved for in-vivo human use.

### 7.2 Imaging hardware

#### 7.2.1 0.5 T Paramed upright MRI scanner

The 0.5 T Upright scanner's design is different from a conventional flatbed MRI scanner. The differences begin with the main magnet, which in a conventional flatbed scanner is a super-conducting coil, and the subject is laid down inside the magnet's bore. The Upright scanner's field of view (FOV) is located between the two poles of a 0.5T magnesium diboride  $MgB_2$  cryogen-free horseshoe magnet. The scanner's magnetic field direction can be seen in Figure 7.1. As the magnet is a high-temperature superconductor, it does not need to be cooled with liquid He. Should the Upright scanner need to be shut down for maintenance, inspections or in case of emergency, the magnet's current can be ramped down quickly and ramped back up again on the time scale of hours. This contrasts to the costly quenching procedure that must occur to shut down a conventional flatbed scanner.

This magnet design gives the Upright both its key advantage and its main drawback. The perpendicular field means the homogenous region of the scanner is smaller than that of a conventional flatbed scanner, resulting in a smaller FOV. However, it should be large enough to contain the whole volume of the

lungs. The advantages is that it allows the subject to be imaged in a wide range of positions. The bed can be removed, and the floor can be lowered or raised, allowing the subject to be imaged standing up, with the region of interest (ROI) (from the head to feet) residing the scanner's FOV.



Figure 7.1: 0.5T Paramed upright MRI scanner with  $B_0$  field direction labelled

This allows for a comparison of images taken of a subject in different positions. Another advantage is that an ROI can be imaged when it is experiencing load-bearing stresses; for example, an ankle can be imaged while the subject is standing. Positional freedom is beneficial for HP  $^{129}\text{Xe}$  lung imaging, as lung function and oxygen levels can change with body position [249]. The majority of people spend most of their lives upright, either standing or sitting; therefore, the Upright scanner is able to produce images that provide more clinically relevant data. Additionally, reduced lung function in patients with conditions such as COPD may mean they cannot lie down for prolonged periods [250], which is where the Upright scanner demonstrates a key advantage. It is normally hard to recruit patients with lung diseases that have progressed to more advanced stages, as the patient's tolerability to being scanned while supine decreases. The Upright is, therefore, far more tolerable for such patients. Another factor increasing tolerability is that the scanner is not enclosed, eliminating the feeling



of claustrophobia that is common with flatbed scanners [251]. This also opens up the possibility of scanning younger children without the need for sedation as the lack of enclosure provides for a less stressful experience. Very young children can even be scanned while on their parent's lap if needed. Children as young as three years' old, for example, have been scanned on the Upright scanner in the University of Nottingham without any sedation.

The Upright scanner's magnet produces a field strength of 0.5 T, which is a third of that provided by even the lowest-strength clinical flatbed scanner in the SPMIC-QMC. Higher field strengths provide better SNR for proton images, which in turn allows for faster imaging and for thinner slices to be taken while still providing an acceptable SNR. Thinner slices increase the spatial resolution the scanner can achieve [252]. Unlike with protons, the polarisation of the HP  $^{129}\text{Xe}$  does not depend on the field strength of the scanner. At lower field strengths, the relaxation due to  $T_{2^*}$  is also reduced. J. Parra-Robles et al. found that the SNR of HP  $^{129}\text{Xe}$  MRI peaked close to 0.5 T [253], indicating that the lower field strength of the Upright scanner should be able to provide high-quality  $^{129}\text{Xe}$  MRI images.

The Upright scanner is the only multi-nuclear scanner of its type in the world. The Redstone spectrometer connected to the scanner has two separate RF amplifiers: one to image protons and one for  $^{129}\text{Xe}$ . There are also eight receive lines on the spectrometer, with four for proton and four for  $^{129}\text{Xe}$  MRI.

The scanner is controlled via the NGR clinical interface. This software is like those found on other clinical scanners and enables basic control over sequences that have been approved for clinical use. The clinical interface uses sequences that have been developed in the program TechMag Inc NMR (TNMR). TNMR can also control the scanner directly when it is not being used clinically, giving the user more flexibility and finer control. TMNR allows the user to build sequences via a user-friendly GUI, increasing the ease of sequence development. Sequence development for GE scanners is more complex, requiring the user to learn GE's Environment for Pulse Programming (EPIC) language and requiring a research agreement with GE for the user to access and use the code. The sequence development on TNMR for the Upright used in the following experiments was performed by J. Harkin, who was also responsible for the scanner's operation.

## 7.2.2 0.5 T Paramed upright receive coil

### $^{129}\text{Xe}$ surface coil

The initial testing of the multi-nuclear capabilities of the Upright scanner was undertaken using a single-channel, 10 cm-squared surface coil supplied by Clinical MR Solutions (CMRS). The coil operates as a T/R NMR coil, tuned to the Larmor frequency of  $^{129}\text{Xe}$  in the 0.5T field. A picture of the coil can be seen in Figure 7.2.

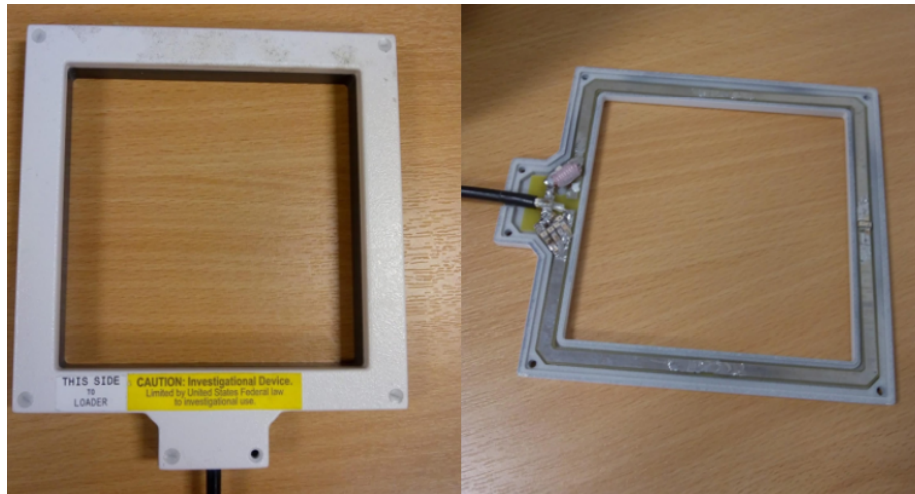


Figure 7.2: Surface coil with the covers on and off

The exact resonance frequency of the coil had to be determined before any other experiments could be conducted. The coil was loaded with two bags full of Hartmann's solution (HS) [254] to replicate the loading the coil would experience when placed on a subject's chest. The interaction between the load and the coil shifts the coil's resonant frequency and dampens its peak response [255]. If not loaded correctly, its peak resonance will be shifted away from the  $^{129}\text{Xe}$ 's Larmor frequency, resulting in a lower SNR. A simulated load must be used as the coil is not currently approved for use with humans.

Two 0.5 L HS bags were used for loading and were placed on top of the coil. The coil was connected to an Agilent Technologies E5061A 300 kHz-1.5 GHz ENA Series Network Analyser. The coil's resonance frequency was found to be 5.890 MHz with a peak response of 28.016 dB and FWHM of 43 kHz (see Figure 7.3).



Figure 7.3: Surface coil loaded with HS bags and Tedlar bag with  $^{129}\text{Xe}$  sitting in the coil

The coil was tested on a 1 L bag of HP  $^{129}\text{Xe}$  with an initial polarisation of 9%. A simple pulse/acquire sequence was used with a TE of 30 ms, a 70 dB Tx attenuation and a small flip angle RF pulse of 3 ms. No gradient fields were applied during this sequence, meaning the  $B_0$  magnetic field was homogeneous. The  $^{129}\text{Xe}$  signal was found and confirmed by changing the pulse length of the RF pulse, which altered the size of the  $^{129}\text{Xe}$  signal. After multiple pulses interrogating the  $^{129}\text{Xe}$ , polarisation was measured using the 2881 measuring station and had dropped by  $< 1\%$ . The minimal change in polarisation showed that the flip angle of the RF pulse was indeed small. During this test, the Larmor frequency of the  $^{129}\text{Xe}$  was found to be 5.841 MHz

J. Harkin re-tuned the coil to bring its peak response closer to 5.841 MHz. A 33pF 3kV capacitor was added in parallel to alter the peak frequency of the surface coil. The peak response shifted to 5.842MHz and improved, giving a response of 33.039 dB with a 27 kHz FWHM. The  $^{129}\text{Xe}$  Larmor frequency is now within the FWHM of the coil's peak response. Using the same pulse sequence on a 1 L bag with 12.25% polarisation gave a peak height of 27623. Before the coil was re-tuned, a bag with 5.73 % polarisation gave a peak height of 8222 arbitrary units. When compensating for the difference in polarisation between the two bags, the re-tuning resulted in  $\approx 57\%$  increase in performance at the peak response frequency.

### 7.3 Upright $^{129}\text{Xe}$ NMR spectroscopy

The sequence development work on the Upright scanner was undertaken by J. Harkin and can be found in his thesis [256]. The work presented instead focuses

on the NMR spectra and MRI images of HP  $^{129}\text{Xe}$  achieved on the Upright and the relevance to future clinical work.

### 7.3.1 $^{129}\text{Xe}$ dissolved phase NMR spectroscopy

As discussed in Section 2.5.4, one of the unique features of HP  $^{129}\text{Xe}$  is its high chemical-shift sensitivity. These experiments investigate the ability of the surface coil to detect the chemical shift of  $^{129}\text{Xe}$  in the dissolved phase with NMR spectroscopy.

The advantage of surface coils is their high sensitivity. RF sensitivity is given by the magnitude of  $B_1$  magnetic field strength by a unit current (i) through the coil  $\frac{B_1}{i}$ , which allows them to produce a higher SNR compared to a volume coil [257]. Relative sensitivity of the coil is inversely proportional to its diameter, which increases the SNR that can be achieved in smaller coils [257]. The issue with a smaller coil is that its sensitivity drops off quickly with distance. With its small size, the CMRS surface coil should therefore be suitable for dissolved-phase NMR, where high sensitivity is needed due to the low fraction of  $^{129}\text{Xe}$  in the dissolved phase compared to the gas phase. The useable  $^{129}\text{Xe}$  signal in the dissolved phase measurements will also reduce quickly because the  $\text{O}_2$  introduced into the syringe during  $^{129}\text{Xe}$  gas loading will result in short  $T_1$  and  $T_2^*$ .

#### Methods

To measure its chemical shift,  $^{129}\text{Xe}$  was dissolved in four different liquids: water, olive oil, tert-butanol and ethanol. This was performed on the surface coil using NMR spectroscopy.

The HP  $^{129}\text{Xe}$  was introduced to these liquids using the following protocol. The liquid was sucked into a syringe, filling half of its volume. As  $\text{O}_2$  would increase the depolarisation of the  $^{129}\text{Xe}$ , it was important to ensure no air bubbles entered the syringe during this process. The syringe was then attached to the tube of the Tedlar bag, the bag was then unclipped and the  $^{129}\text{Xe}$  was sucked into the syringe until full. The bag was then clipped, and blue tac was used to cover the end of the syringe to limit the exposure of the HP  $^{129}\text{Xe}$  to atmospheric  $\text{O}_2$ . The syringe was then vigorously shaken by hand to mix the liquid and HP  $^{129}\text{Xe}$ . This increased the surface area between the two, meaning more  $^{129}\text{Xe}$  dissolved into the liquid. Finally, before the scan was performed, the syringe was placed inside the loaded surface coil.

The NMR signals were acquired with a 3ms RF pulse with a 30 dB attenuation, producing a  $\approx 30^\circ$  flip angle. This flip angle was chosen as it ensured no  $^{129}\text{Xe}$  nuclei were completely depolarised in the coil's non-uniform  $B_1$  field. A short TE (2.2 ms) was also used in order to maximise the signal collected in the acquisition window.

#### Results

On the day of the experiments, the  $^{129}\text{Xe}$  gas-phase peak was found to be 5.84035 MHz. The dissolved phase peak in water was found at 5.84146 MHz, equivalent to a chemical shift in water of 190.0 ppm. When dissolved in ethanol,  $^{129}\text{Xe}$  had a chemical shift of 160.5 ppm. The chemical shifts observed are

similar to the results found by K. W. Miller et al. [258], although their results were slightly higher, with a chemical shift of 198 ppm and 165 ppm for water and ethanol respectively. K. W. Miller et al.'s experiments were undertaken at 760 Torr of pressure, which are the same values as the Upright experiments. [258, 259]. The difference between the published values and the experimental values may be in part due to differences in temperature between the two. Although both were taken at "ambient" temperature, what is considered ambient can vary and cause a change in  $^{129}\text{Xe}$  chemical shift up to 0.25 ppm/C for lipids [260] and  $\approx 0.08$  ppm/C for water [261]. This is a result of decreasing local liquid density with temperature, increasing collision energetics between  $^{129}\text{Xe}$  and the liquid [261]. K. W. Miller also carried out their work at 2.1 T, and, although it has been recently reported that field strengths can affect the size of chemical shift, [262], the impact is only significant at higher fields [262].

The dissolved phase  $^{129}\text{Xe}$  signal olive oil produced a twin peak, and the centre between these two peaks was chosen as the chemical shift value (192.2 ppm) (see Figure 7.4).

As with the previous two liquids, this shift was lower than the published value of 198 ppm [258]. In addition to the temperature and systematic errors mentioned above, the non-standardised method of production between olive oils [263] could also be a factor. Work presented in E. Woolley's thesis measured a chemical shift of 190 ppm when  $^{129}\text{Xe}$  was dissolved in olive oil [264]. E. Woolley also measured the chemical shift of  $^{129}\text{Xe}$  dissolved in toluene, the results of which matched those published (190 ppm) [264, 258]. The fact that the set-up was able to measure only one of the peaks correctly supports the theory that not all olive oils are created equal so do not induce the same  $^{129}\text{Xe}$  chemical shift. The olive oil composition could therefore be a factor behind the double peak. Even pure olive oil has many different components and, as a result, NMR has been used to fingerprint olive oils to determine their purity and source [265]. Olive oil is composed of mainly triglycerides which differ in length, degree and the type of unsaturation of the acyl groups [266]. This gives rise to multiple chemical shifts [267], [268]. However, the NMR signals of the smaller olive oil components, such as mono- and di-glycerides, sterols, tocopherols, aliphatic alcohols, hydrocarbons, fatty acids, pigments and phenolic compounds, have their own peaks with their own chemical shifts. These can also be measured when they are present in sufficient quantities so not overwhelmed by triglyceride peaks [269]. These multiple components could contribute to the double peak from  $^{129}\text{Xe}$  in the olive oil, which was a supermarket's own-brand product, normally a composite of olive oils from several sources [270]. This mean there is a slight variation of chemical composition throughout the olive oil. The variation in chemical composition could result in slightly different chemical shifts, hence the double peak. The last experiment dissolved HP  $^{129}\text{Xe}$  in tert-butanol and exhibited a chemical shift of 176 ppm.

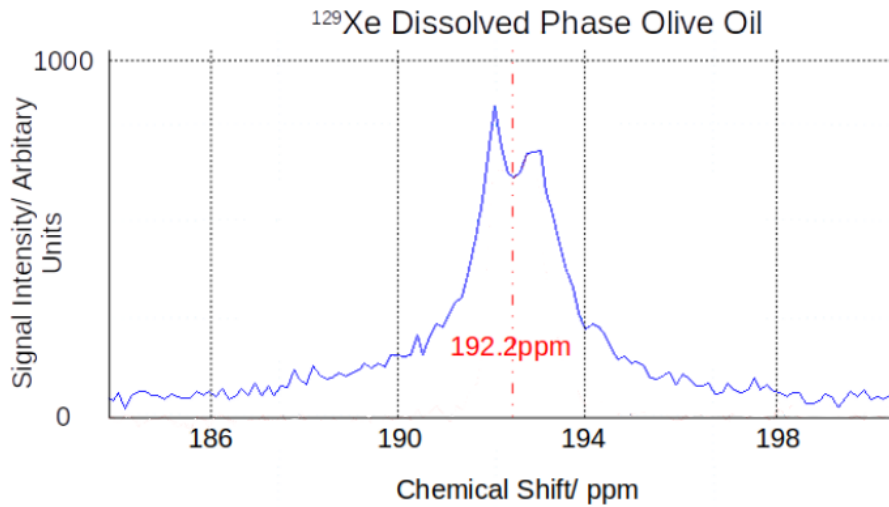


Figure 7.4: NMR spectra showing the shifted double peak produced by HP <sup>129</sup>Xe in olive oil

These tests have shown that the surface coil can observe the chemical shift of <sup>129</sup>Xe with NMR spectroscopy. Once the coil is approved for human use, it can be used for preliminary in-vivo dissolved-phase NMR and MRI imaging on the Upright in readiness for future work on a Pulseteq <sup>129</sup>Xe/<sup>1</sup>H chest coil.

## 7.4 Upright <sup>129</sup>Xe MRI imaging

### 7.4.1 Introduction

This section covers the first <sup>129</sup>Xe images obtained on the Upright scanner, looking at the sequence used and the coil and scanner's ability to image more complex structures.

### 7.4.2 Methods

#### Sequence selection

Several sequences had been developed and tested for <sup>1</sup>H imaging on the Upright scanner. To reduce development time, an existing 3D-spoiled GRE <sup>1</sup>H sequence was therefore modified for <sup>129</sup>Xe imaging.

When spoiling occurs in a GRE sequence, it acts to disrupt the transverse coherence that might remain between cycles [271]. It ensures that no transverse component to the magnetisation is present before each RF pulse. If the TR of the sequence is much higher than  $T_{2^*}$ , the transverse magnetisation has time to decay to zero before the next RF pulse. A long TR is not always practical for several reasons. Firstly, it increases scan time, which is not acceptable for <sup>129</sup>Xe MRI lung imaging where images have to be taken in a single breath-hold. Furthermore, a longer TR time in a GRE sequence weights the contrast more

towards  $T_2^*$  [272]. Depending on the aim of the scan, another contrast may be more useful.

There are two spoiling methods, which occur between the signal acquisition and the next RF pulse. The first is RF phase-cycling, known as “RF-spoiling”, a method many MRI scanner companies use in their pre-installed sequences. It works by changing the RF pulse phase using a recursive formula [273]. The benefits of this method are that it does not generate eddy currents, and it is spatially invariant. Therefore, if there is a uniform transmit, the spoiling will also be uniform.

The second method is “gradient spoiling”, which works by applying multiple slice-select gradients. The strengths of these spoiler gradients are varied either linearly or randomly. Unlike RF-spoiling, gradient spoiling is non-uniform [274], which can lead to artefacts in the final MRI image. The 3D-spoiled GRE sequence employed in the following experiments uses a mixture of the two to ensure the transverse magnetisation retained between TR’s is minimised.

### 7.4.3 Sequence testing

#### $^{129}\text{Xe}$ phantom loading

The sequence testing was performed in a simple phantom constructed from a Compactor Aspifresh rectangle vacuum food storage container (Tupperware). The Tupperware has a simple rubber valve that is used to evacuate air out of the container in order to keep food fresh. The valve was removed and replaced with the inlet found on the Tedlar bags, after which a  $\frac{1}{4}$ -inch plastic tube could then be connected to the inlet. The tube enables the Tupperware to be attached to the manifold of the Polarean 9810 polariser. Atmospheric impurities were removed from the phantom using the same protocol as that for a Tedlar bag (see Section 5.1.1). The Tupperware was then evacuated, and the tube was clipped to seal the phantom in preparation for  $^{129}\text{Xe}$  loading. The Tupperware phantom set-up can be seen in Figure 7.5.



Figure 7.5: Image showing the Tupperware phantom used in the first  $^{129}\text{Xe}$  images on the Upright, there are depressions in the phantom as it has been evacuated in preparation for HP  $^{129}\text{Xe}$  loading.

The 9810 polariser then produces 1 L of HP  $^{129}\text{Xe}$ , which is decanted into a Tedlar bag. In the scanner, the Tupperware is placed atop the HS bags and surface coil. A Chemglass adapter connects the bag and Tupperware. The bag is unclipped, followed by the evacuated Tupperware, and the pressure differential causes the HP  $^{129}\text{Xe}$  to be sucked into the Tupperware. To aid in gas transfer, the bag is squeezed at the same time. The Tupperware is then clipped, and the 8-slice 3D spoiled GRE MRI sequence is initialised.

#### 7.4.4 Flip angle optimisation

To be able to determine the optimal FA, the FA for given attenuations must be known. To achieve this in a FA calibration, the non-recoverable nature  $^{129}\text{Xe}$  must be taken into account. When using a constant FA, the HP signal of the  $k^{\text{th}}$  pulse ( $S_k$ ) is given by equation 7.1.

$$S_k = S_1(\cos(\theta)\exp(\frac{-TR}{T_1}))^{k-1} \quad (7.1)$$

- HP signal of the  $k^{\text{th}}$  pulse:  $S_k$
- HP signal of the  $1^{\text{st}}$  pulse:  $S_1$



- Repetition time:  $TR$
- Longitudinal relaxation time of  $^{129}\text{Xe}$ :  $T_1$
- Flip angle:  $\theta$
- Total number of excitations:  $N$
- Excitation number  $0,1,2, \dots, N$ :  $k$

The transmit gain (TG) of the pulse is measured in dB for a given angle ( $\theta$ ), shown in Equation 7.2. This allows FA to be determined for a variety of attenuations.

$$TG_{\theta} = TG_{90} + \lambda \log\left(\frac{90}{\theta}\right) \quad (7.2)$$

- TG in dB for a given angle ( $\theta$ ):  $TG_{\theta}$
- TG in dB for a  $90^\circ$  pulse:  $TG_{90}$
- A factor approximately equal to 20, dependent on the RF pulse shape:  $\lambda$

By measuring the  $S_k$  after a sufficient number of repeated pulses with equal attenuation, the measurements can be fitted to Equation 7.1 to determine the FA. In the Tedlar bags in the Upright scanner  $T1 \gg TR$ , so Equation 7.1 can be reduced to Equation 7.3.

$$S_k = S_1 (\cos(\theta))^{k-1} \quad (7.3)$$

In the lungs, however, the presence of  $O_2$  will significantly reduce the  $T_1$  of  $^{129}\text{Xe}$  in comparison with the  $^{129}\text{Xe}$  in the Tedlar bag. This affects the  $T_1$  as given by Equation 7.4.

$$\frac{1}{T_1} = \frac{pO_2}{\xi} \quad (7.4)$$

- Partial pressure of  $O_2$ :  $pO_2$
- Oxygen enhancement factor (temperature dependent):  $\xi$

FA can be accurately determined, provided that  $N$  is sufficiently large. J. Zhong et al. found that FA measured at  $N = 8$  is approximately the same as when using  $N = 112$  [275]. This shortened  $T_1$  means that, for the FA to be calibrated within the lungs, the  $T_1$  also needs to be measured. Typically this was achieved in two separate breath holds. As  $pO_2$  cannot be kept exactly the same breath hold to breath hold this was not ideal.

Therefore, the calibration undertaken by J. Harkin used a method designed by J. Zhong et al. where both FA calibration and  $T_1$  can be measured within a single breath hold (less than 4 seconds) [275]. A simple explanation of the method will be described here. For full details of the calibration, see J. Harkin's thesis [256]

. A number of FAs ( $m$ ) can be obtained by  $8 \times m$  excitations and  $m$  different transmitter gains. It is important to note that there is a limit to the FA used as  $^{129}\text{Xe}$  is non-recoverable so the FA needs to be small to preserve polarisation during the FA calibration scan. The surface coil's  $B_1$  strength differs depending on its loading and distance the Tedlar bag is from the coil. Therefore, the FA calibration was measured at two positions:

- Position 1: Tedlar bag inside the coil loaded with two bags of Hartman solution. Initial test.
- Position 2: Tedlar bag on top of the two bags of Hartman solution loading the coil. This is to mimic the loading and distance the lungs would be from the surface coil.

The results of the FA calibration of position 2, the position used for the imaging experiments in this chapter, can be seen in Figure 7.6 and Table 7.1. The different clusters of 8 points in Figure 7.6 are from each FA calibration for a given TG.

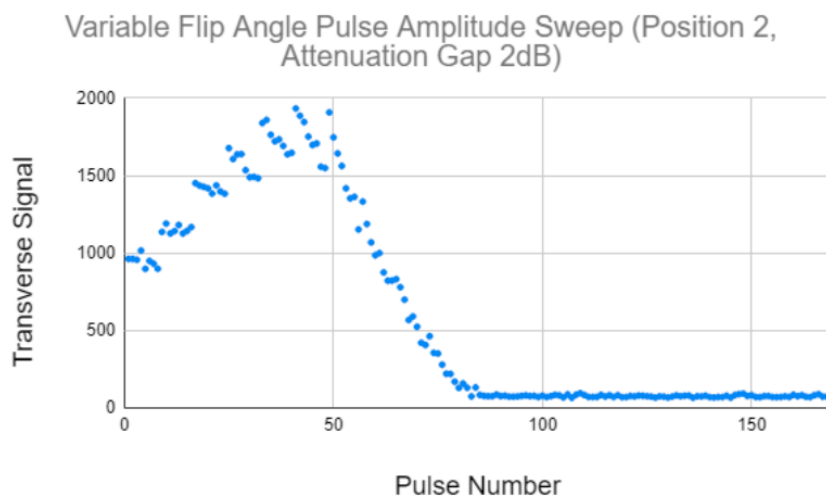


Figure 7.6: Flip angle calibration using a pulse amplitude sweep. Attenuation is decreased every 8th slice by 2 dB with the first pulse at 42 dB.

For simplicity, a constant  $6^\circ$  flip angle was chosen as a starting point. If using a variable flip angle [276] sequence where the flip angle is altered throughout the scan to maximise signal a lower flip angle of  $2.5^\circ$  for the middle RF pulse would be used. However, when the flip angle is constant, it needs to be higher, so there is enough excitation in the whole volume of interest and the edges of the bag can be adequately depolarised. This is because the strength of the RF pulse experienced by the  $^{129}\text{Xe}$  nuclei reduces with distance from the surface coil, so the edges of the coil's FOV experience a lower flip angle than those towards the centre. A  $6^\circ$  flip angle required a 40 dB attenuation; the resultant images are shown in Figure 7.7. To make the most of the polarised  $^{129}\text{Xe}$ , two more sequences were run on the phantom with RF attenuations of 35 dB and 30 dB, equating to flip angles of  $11^\circ$  and  $18^\circ$ , respectively. The resultant images can be seen in Figures 7.8 and 7.9.

Transmit Gain (dB)	Fitted Theta (Radians)	R2
-42	0.1138 (0.05246, 0.1752)	0.27
-40	4.77E-07 (-1.07E+04, 1.07E+04)	-0.44
-38	0.1137 (0.09268, 0.1347)	0.57
-36	0.1944 (0.1733, 0.2155)	0.84
-34	0.1846 (0.1684, 0.2009)	0.9
-32	0.2487 (0.2343, 0.2631)	0.96
-30	0.3637 (0.3465, 0.3809)	0.97
-28	0.3959 (0.37, 0.4218)	0.93
-26	0.422 (0.4162, 0.4679)	0.96
-24	0.5663 (0.5354, 0.5973)	0.97
-22	0.5073 (0.408, 0.6067)	0.6

Table 7.1: Table showing the fitted flip angle related to attenuation with the 95% confidence bounds shown in brackets.

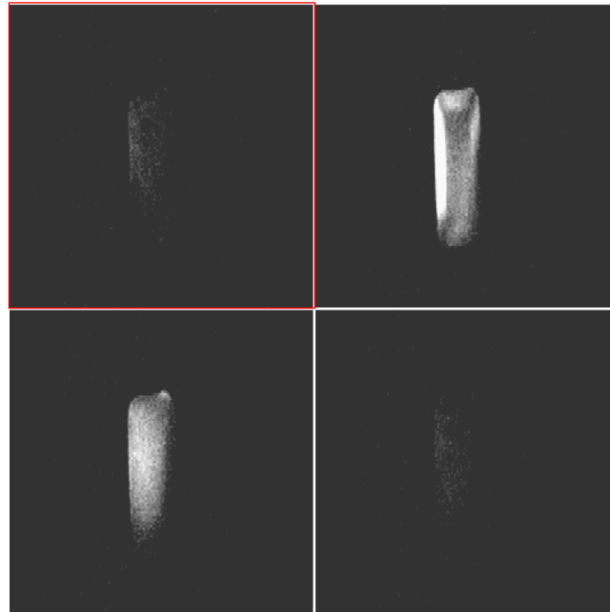


Figure 7.7: Slices 3, 4, 5 and 6 from an eight-slice 3D spoiled GRE sequence with 40 dB attenuation

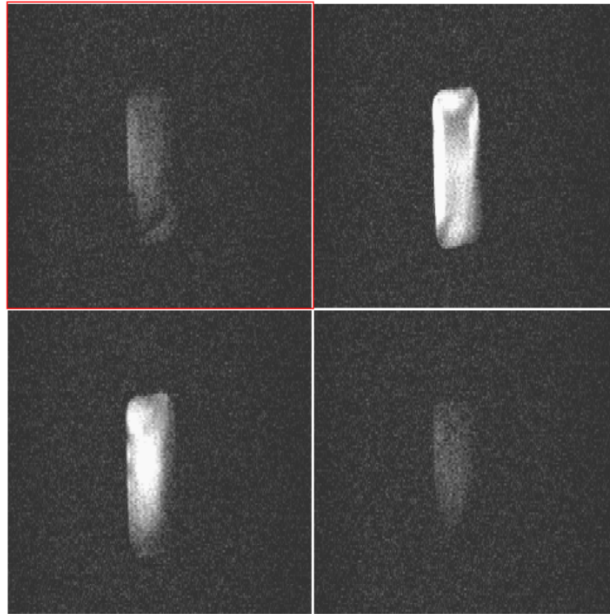


Figure 7.8: Slices 3, 4, 5 and 6 from an eight-slice 3D spoiled GRE sequence with 35 dB attenuation



Figure 7.9: Slices 3, 4, 5 and 6 from an eight-slice 3D spoiled GRE sequence with 30 dB attenuation

It was predicted that the resultant  $P_{Xe}$  after the 1024 RF pulses in the sequence with 40 dB attenuation would be minimal ( $< 1\%$ ). However, there

was enough  $P_{Xe}$  remaining to take two more images with lower attenuation sequences. This indicates that the flip angle dropped off significantly in regions where the box was further away from the coil. The fact the 35 dB images exhibited the highest SNR despite being the second scan supports this. The 30 dB sequence had a lower SNR, but it is unclear if this is due to the flip angle being too high or the  $^{129}\text{Xe}$  in the Tupperware being significantly depolarised.  $^{129}\text{Xe}$  can freely move within the volume of the Tupperware so, even if the slice closest to the coil had been depolarised, polarised  $^{129}\text{Xe}$  from further away slices will be able to diffuse into it between scans.

As shown in Figure 7.5, the Tupperware is not a uniform shape, the bottom having a slightly raised central portion with an indentation around the outside. This feature can be seen on the fifth slice of each scan. The indentation is brighter due to the relatively heavy  $^{129}\text{Xe}$  nuclei settling at the lowest regions. This feature is on the order of 1cm, and there is a well-defined line between the indentation and raised region. Another interesting feature in the 30 dB scan is a region of signal outside the Tupperware at the images' top and bottom, thought to be from the Tedlar bag which still contains a small amount of HP  $^{129}\text{Xe}$ . The bag signal is wrapped around the top and bottom of the image due to aliasing. The 30 dB sequence is strong enough to depolarise the bag sitting 15 cm away from the coil.

40 dB was selected for work going forward with the surface coil. Although the SNR is not maximal, it is sufficient for imaging, and it will not wholly depolarise the  $^{129}\text{Xe}$  closest to the coil before the sequence is completed. Finally, even with 40 dB attenuation, there is still enough signal to resolve the finer detail of the image (see Figure 7.7).

### 7.4.5 Fine structure capabilities

HP  $^{129}\text{Xe}$  MRI in a clinical setting can offer a much higher utility if fine structures, such as ventilation defects, can be resolved. The coil's ability to resolve fine structures was therefore investigated. One test examined how well the coil could detect voids within the phantom, and the other tested its ability to resolve small areas of signal on the scale of millimetres.

The void test involved placing a glue stick and sealed glass vial inside the Tupperware shown in Figure 7.10 before it underwent the  $N_2$  purge/evacuation cycles. The Tupperware was then filled with  $^{129}\text{Xe}$  as per the protocol in Section 5.1.1. The image in Figure 7.11 shows that both voids can be resolved. For the most part, these voids are featureless tubes. However, at the bottom of the glue stick, there is a knurled knob for adjusting its height. This knurling is on the order of millimetres and can be seen in Figure 7.10 b), which demonstrates that the coil can resolve finer structures as well as larger voids.



Figure 7.10: Image showing the Tupperware phantom with glue stick and glass voids

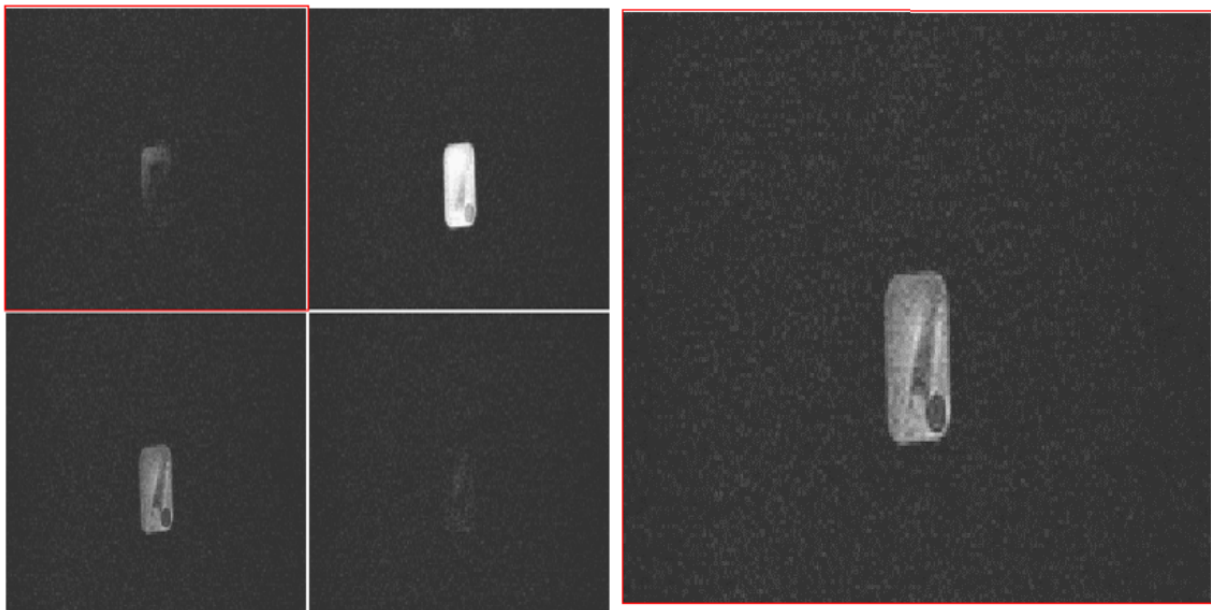


Figure 7.11: a) Slices 3, 4, 5 and 6 from an eight-slice 3D spoiled GRE sequence with 40 dB attenuation performed on the Tupperware phantom with voids b) An enlargement of slice 6 clearly showing the glass vial and glue stick

A 3mm internal diameter tube was used as a phantom and tested the ability

of the coil to resolve fine structure. A bag of HP  $^{129}\text{Xe}$  with a 14% polarisation was produced and attached to the tubing. The Xe was then pushed through the tubing by squeezing the bag. The tube was then clipped at both ends, coiled and placed on top of the loaded coil. The 40 dB sequence was then performed, the final images of which are shown in Figure 7.12. The images show that the sequence and surface coil not only detect the signal inside the tube but were also able to discern between the signal in different loops of the tube. This indicates that the sequence and coil will be able to image fine structures in the lungs when the coil is approved for human use.



Figure 7.12: Slices 3, 4, 5 and 6 from an eight-slice 3D spoiled GRE sequence with 40 dB attenuation performed on the tube phantom

## 7.5 Discussion

These tests have demonstrated that this 3D-spoiled GRE sequence and surface coil can produce  $^{129}\text{Xe}$  MRI images with high SNR in a range of different phantoms and that it is also able to resolve fine structure on the order of millimetres. The images shown are the first HP  $^{129}\text{Xe}$  images acquired on a scanner of this type. The HS bags in between the coil and phantoms simulate the distance the lungs would be from the coil when on a subject's chest. The FOV of the coil would also be able to image a significant portion of the lungs given the size of the Tupperware phantom used (23.2 x 15.2 x 7.3 cm).

## 7.6 Future work - Pulseteq chest coil

A bespoke chest coil with a similar vest form factor to that of the CMRS coil discussed in Chapter 8 was procured from Pulseteq Ltd. It is a  $^{129}\text{Xe} / ^1\text{H}$  array coil, composed of two identical sections: one in the front of the vest and one in the back. The Xe array has four element coils, two in each section. Using smaller surface coils in an array allows there to be a higher sensitivity and SNR, while the array configuration increases the FOV so the whole lungs can be imaged [277]. Adjacent coils are  $90^\circ$  out of phase and opposite coil pairs are  $180^\circ$  out of phase. These coil pairs can couple with each other to create a more uniform field through the subject compared to a lone surface coil, working under similar principles to a Helmholtz pair [278]. The two fields between the coil pairs (coils 1/coil 3 and coil 2/coil 4) are perpendicular, so can be driven in quadrature. Quadrature imaging [279] means the signal from  $^{129}\text{Xe}$  can be detected at multiple orthogonal directions and then combined after an appropriate phase shift. This increases the SNR, as the same signal is acquired multiple times. The surface coils also allow the design to be flexible, which is much better tolerated over a wider variety of body shapes compared to a rigid chest coil. The flexibility also increases the filling factor of the coil as it can be fitted tight to the subject's chest, unlike a rigid coil. The coils operate in T/R mode, each with their own T/R switch. The transmit signal is split and fed into each element using a four-way power splitter. The two elements in each section overlap each other to give a total size of 32 cm x 40 cm [280].

The proton array is intended to perform  $^1\text{H}$  imaging on the same target tissue, enabling easier co-registration of  $^{129}\text{Xe}$  and proton images. It is of two element coils, one in each section. These elements are integrated into the same sections as the Xe elements and centred within them. The  $^1\text{H}$  elements operate only in receive mode and can be detuned so that they do not interfere with the transmit pulses. The size of each element is 32 x 22 cm [280] and a diagram of the coil can be seen in Figure 7.13.



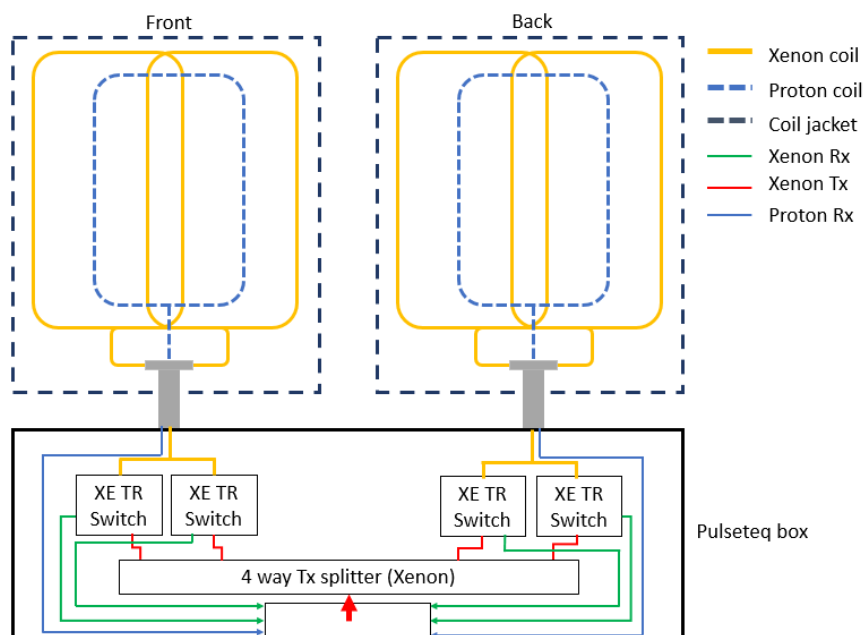


Figure 7.13: Pluseteq chest coil diagram

The Pulseteq coil has an FOV that covers the entire volume of the lungs. It should therefore be able to produce a uniform  $B_1$  field in the whole region of interest, enabling more accurate flip angle calibration. The above features make it significantly more suited to HP  $^{129}\text{Xe}$  imaging than the surface coil. Using the Pulseteq coil, the 3D-spoiled GRE sequence can also be further optimised using a variable flip angle [276] rather than keeping the value constant throughout the sequences.

## 7.7 Conclusion

The experiments demonstrated that surface coil should be able to perform in-vivo dissolved-phase NMR and  $^{129}\text{Xe}$  lung imaging with the 3D-spoiled GRE sequence on the Upright scanner.

Before any human imaging can begin, the coil must first be approved for human use by SPMIC. This process requires the amount of RF power delivered to the subject, otherwise known as the Specific Absorption Rate (SAR), to be quantified. This is unlikely to be above unsafe levels, as the SAR values for similar sequences and target on the 1.5 T GE flatbed scanner have posed no safety issues and are approved for human use. SAR scales with  $B_0^2$ , among other variables, so should be within safe limits at 0.5 T [281]. However, too much RF power concentrated in one area could cause localised heating, which may pose a risk of burns to subjects and exceed EU SAR guidelines. For approval to be granted, a monitoring system also needs to be built to take the SAR measurements in tandem with computer simulations.

This initial in-vivo work on the surface coil will pave the way for the work undertaken with the Pulseteq coil, subject to its approval.

## Chapter 8

# HP $^{129}\text{Xe}$ imaging results with a 1.5 T flatbed MRI scanner

### 8.1 Introduction

This chapter focuses on the work undertaken on a conventional 1.5 T flatbed scanner using a coil developed by CMRS. The chapter starts with a brief description of previous work undertaken on an older rigid coil. It then continues with a discussion of the tests conducted on the CMRS coil. The work investigated the ability of the CMRS' coil to image HP  $^{129}\text{Xe}$  in both phantoms and healthy volunteers. From this work, it was possible to determine if the coil is fit for use on patients with compromised lung function.

### 8.2 Imaging hardware

The QMC division of the SPMIC has access to a 1.5 T HDxt MRI scanner made by General Electric (GE 1.5 T) [282]. This scanner is based on the GE Signa series of 1.5 T MRI scanners and has undergone an upgrade to enable multinuclear spectroscopy (MNS) so it can be used to image  $^{129}\text{Xe}$  as well as protons. The GE 1.5 T's design is that of a conventional horizontal flatbed scanner. The  $B_0$  field is produced by a superconducting coil which takes the form of a solenoid. The coil needs to be kept at Liquid helium temperature to maintain its superconducting state where it can produce a  $B_0$  field of 1.5 T. The FOV is  $48\text{cm}^3$ , which allows it to image the entire volume of the lungs.

The GE 1.5 T is controlled via GE's proprietary scanner software, meaning sequences can only be coded in GE's EPIC language. EPIC poses its own unique set of challenges for sequence development, as described in Section 7.2.1, in addition to the existing safety tests required by SPMIC for every new sequence intended for humans use. The sequences used in the following experiments were developed by S. Hardy [283] in 2015 based on a fast gradient-echo (FGE).

## 8.2.1 GE 1.5 T receive coils

### Rapid biomedical coil

Previous  $^{129}\text{Xe}$  in-vivo MRI work on the GE 1.5 T scanner at the University of Nottingham was undertaken by J. Thorpe [284] and S. Safavi [285] using the Rapid Biomedical coil (Rapid coil) [286], and is presented in their theses. The Rapid coil is briefly described to give context to why the switch was made to the CMRS coil.

The Rapid coil is a birdcage coil supported by a rigid outer shell. A birdcage coil is constructed from an even number of straight wires pointing parallel to the  $B_0$  field. These wires are connected to two conductive loops at either end [287]. Depending on the position of the capacitors the coils can be either in high or low pass mode. For high pass coils, the capacitors are placed between the rungs on the end loops. For low pass, coils the capacitors are placed on each leg. A low pass mode birdcage coil is shown in Figure 8.1. A birdcage coil can create a very homogenous  $B_1$  field within its volume. The Rapid coil is a two-part design, which clips together once the is subject inside (see Figure 8.2). Please note that the subject pictured in this chapter is the author of this thesis, who gives full consent to his images being used. There are receive arrays in the bottom of the solid shell connected to a flexible receive array placed on top of the subject before the top shell is connected (see Figure 8.3. The flexible array ensures that there is no dead space between the top arrays and the  $^{129}\text{Xe}$  inside the lungs. If the receive arrays were instead in the top half of the coil, there may be some distance between the top arrays and the chest of thinner subjects. The coil being rigid ensures that the geometry of the coil remains unchanged between subjects, which keeps the  $B_1$  transmit field uniform.

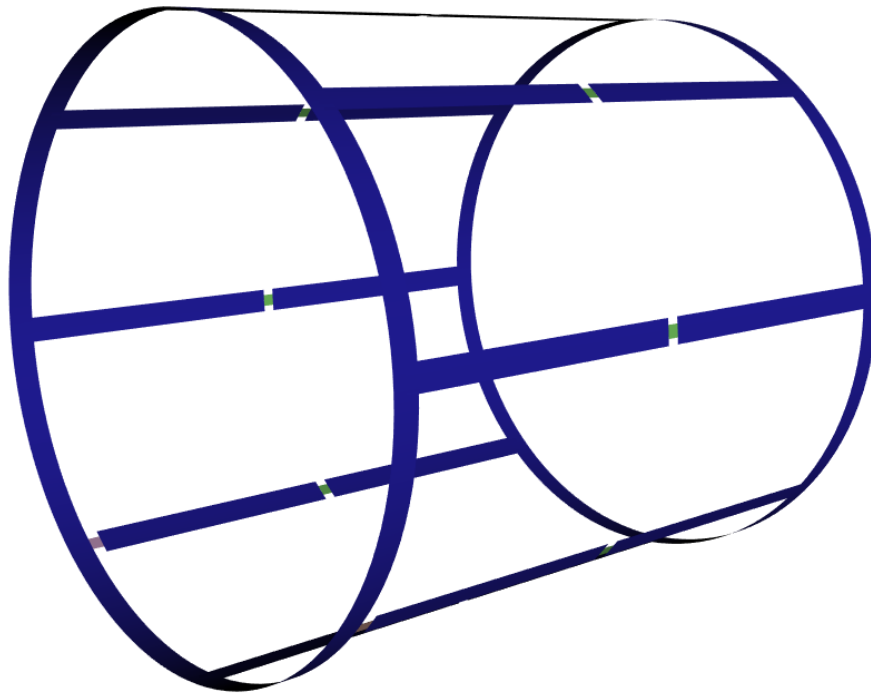


Figure 8.1: Simple diagram of a birdcage coil with end rings and rungs (blue) and capacitors (green). This figure was created with OpenEMS [288] and Matlab.

The coil's rigid design puts a limit on the maximum body dimensions of the subject. The flexible receive arrays further reduce the space inside the coil. In addition to this, the subject's arms must be placed by their sides as subjects cannot tolerate having their arms above their head during scanning. The coil also adds to any feelings of claustrophobia within the scanner, placing greater psychological pressures on the subjects. The cohort of subjects that can tolerate this coil is therefore small, reducing its utility.



Figure 8.2: Image showing how a subject is positioned inside the Rapid coil

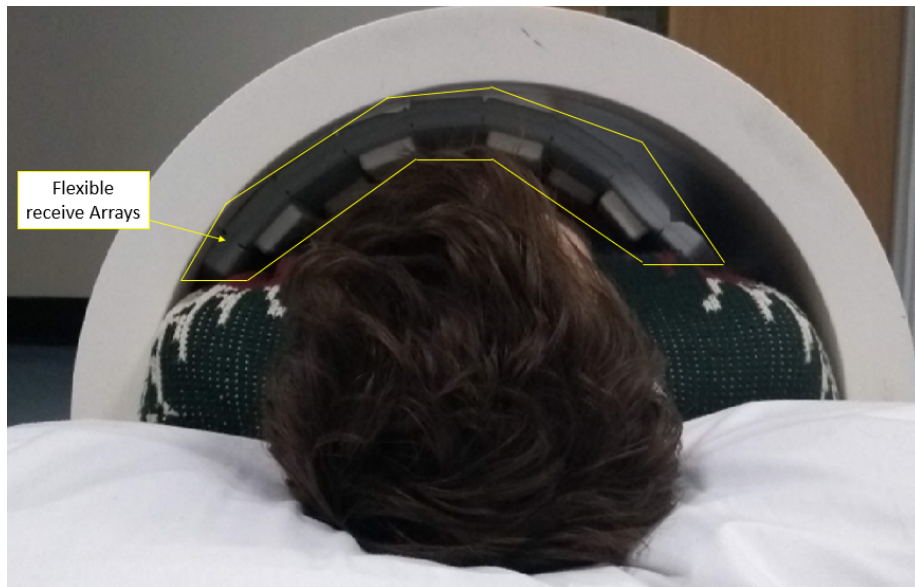


Figure 8.3: Image showing the position of the flexible arrays on top of the subject within the Rapid coil

#### **Clinical MR Solutions coil**

As the cohort of subjects that could tolerate being scanned was restricted by the Rapid coil's geometry, a replacement was needed. This came in the form of a coil made by CMRS (CMRS coil). The coil is constructed from a hard-wearing fabric and is worn like a bullet-proof vest. Adjustment to the fit can be made with several Velcro straps, allowing for a more diverse range of body types to be scanned than with the Rapid coil. Moreover, the CMRS coil does not confine the subject's arms when worn, further increasing comfort and therefore acceptability. The CMRS coil has a similar design to the coil used by J. Roos et al. [105], although it is not restricted to a single operational mode.



Figure 8.4: Image showing how the subject is positioned inside the CMRS coil

The coil can be run in two different modes: quadrature transmit array receive (QTAR) and quadrature transmit / quadrature receive (Quad T/R). Both modes used the coils housed in the vest to transmit the RF excitation pulse to the  $^{129}\text{Xe}$ . There are eight element coils which make four two-coil arrays. These two-coil arrays form pairs with opposing arrays in the same way that the coil pairs couple in the Pulseteq coil. They also operate in a similar way as described in Section 7.6 and should confer the same benefits to the final image. The main

difference between the two coil designs is that, instead of four coils, there are four two-coil arrays, allowing the individual coils to be smaller. The CMRS coil therefore benefits from higher sensitivity and SNR provided by using smaller surface coils [277].

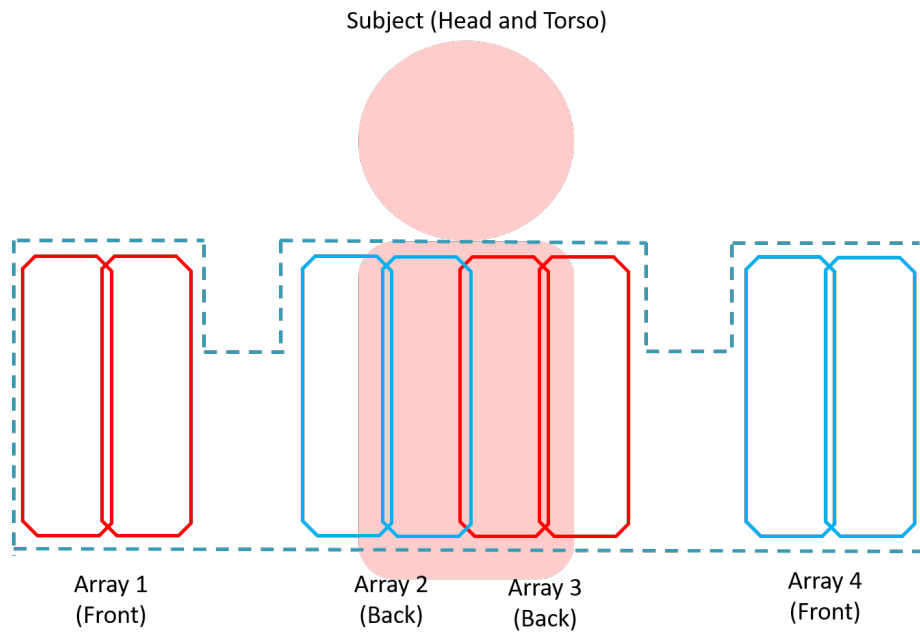


Figure 8.5: Representation of the four two-coil arrays inside the vest used during QUAD T/R mode



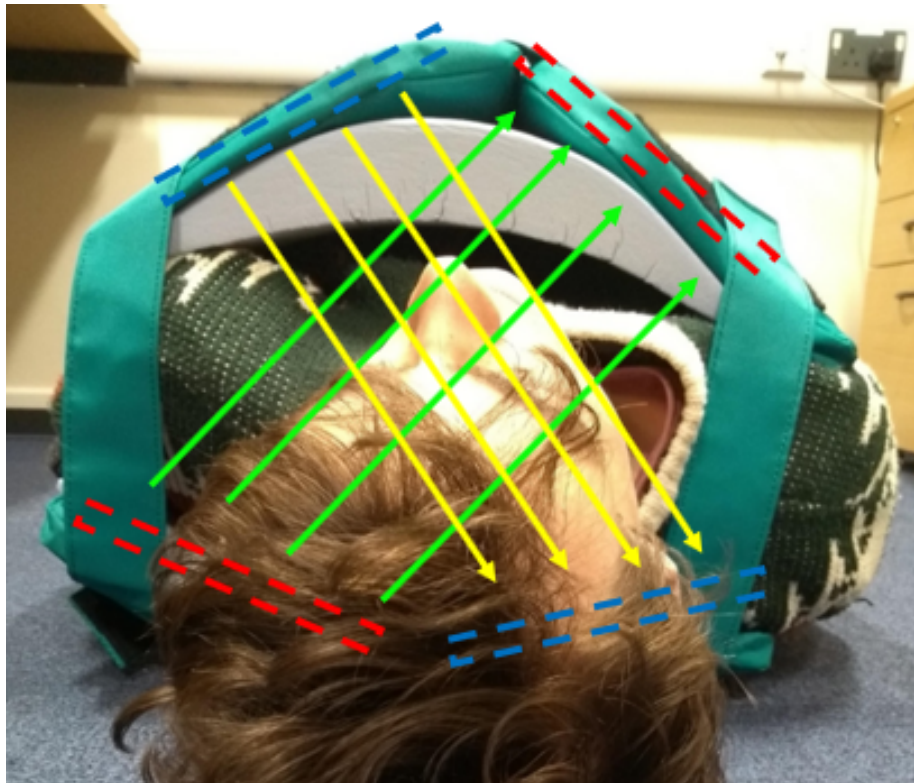


Figure 8.6: Picture showing the 4 coil array locations in the vest (blue and red) and the magnetic field lines (green and yellow)

Both pairs of arrays induce diagonal magnetic fields at  $90^\circ$  to each other, which pass through the subject's chest and are orientated in the x-y plane (see Figure 8.6). The uniformity of the resultant  $B_1$  is dependent on how well the coils in a pair couple with each other. As the CMRS coil has a flexible design; its shape can be easily deformed, significantly impacting the uniformity achieved. The top of the vest must be rounded so that the coils are pointing in the correct direction for optimum coupling. The more subjects fill out the vest, the closer the coils is to its optimum shape. This is harder to achieve in smaller subjects, which leave more space for the coil to deform (see Figure 8.7a). To mitigate deformation of the vest when worn by smaller subjects and foam pad is inserted (see Figure 8.7b).



(a) Picture showing the vest deformation in a smaller subject with no pad



(b) Picture showing the vest with foam padding to reduce deformation, increasing uniformity between patients of different sizes

The method of  $^{129}\text{Xe}$  signal detection depends on the mode in which the coil is operating. QTAR mode requires eight additional receive arrays to be placed between the subject and the vest, four at the top and four at the bottom. These arrays act as independent receive surface coils operating in quadrature. The receive arrays can therefore detect the maximal NMR signal from the  $^{129}\text{Xe}$  as they are acquiring signals  $90^\circ$  out of phase [279]. Furthermore, as the arrays are in different locations, combining their signal offers an increased sensitivity across the entire volume of the lungs [279]. They are also closer to the region of interest compared to the transmit coils in the vest, further increasing the SNR of the final image. In some subjects, they also negate the need for a foam pad as they fill out the coil and maintain its shape. QUAD T/R does not require any additional arrays and uses the coils in the vest for both Tx and Rx. QTAR mode should offer an improved SNR over QUAD T/R. QTAR mode is, however, more complex, requiring switching to ensure the receive arrays do not interfere with the transmitted RF.



Figure 8.8: Duplexer which connects the coil and the scanner with an inbuilt GE coil ID chip

The cabling and box are shown in Figure 8.8; they connect the CMRS coil to the GE 1.5 T so that the coil can be controlled by the scanner operator. In addition to the connectors, the black box also contains an ID chip. This ID chip is recognised by the GE 1.5 T scanner and allows the operator to run the pulse sequences they wish to use. Without an ID chip, the GE software blocks the operator from initialising any sequences with the CMRS coil.

## 8.3 Imaging with the Clinical MR Solutions coil in QTAR mode

### 8.3.1 Introduction

This section covers the testing and imaging undertaken with the CMRS coil in QTAR mode. The sequences used, sequence optimisation, images taken and issues encountered are all discussed. The HP  $^{129}\text{Xe}$  for these experiments was manufactured using the SOP laid out in Section C. When  $^{129}\text{Xe}$  was made to be inhaled by subjects, the pre-approved checks were undertaken as described in Section C. All volunteers provided informed consent after a screening with our clinician; following this, they read through and signed the relevant safety documentation. The National Research Ethics service reference number for these imaging studies is 13/EM/0401.

### 8.3.2 Methods

#### Sequence selection

The sequence used for  $^{129}\text{Xe}$  imaging on the CMRS coil was based on a 2D fast GRE (FGRE) supplied by GE. This sequence was converted from the Larmor frequency of  $^1\text{H}$  in the GE 1.5 T  $B_0$  field to that of  $^{129}\text{Xe}$  by S. Hardy and was previously used with the Rapid coil.

Although the sequence has been modified for use with  $^{129}\text{Xe}$ , the central frequency may have shifted due to the slight tuning differences between the Rapid and CMRS coil. The correct central frequency must be determined so that the RF pulses produced by the coil are resonant with the  $^{129}\text{Xe}$ , maximising the SNR of the final images. The central frequency is found by using a Free Induction Decay Chemical Shift Imaging (FID-CSI) sequence, with a 3 s TR and 48 cm FOV. As  $P_{\text{Xe}}$  is non-recoverable, the FID-CSI excitation is minimised so the polarisation can be preserved for imaging. To minimise excitation, the transmit gain is set to zero and the Tedlar bag is placed on top of the coil. The HP nature of  $^{129}\text{Xe}$  means high SNR spectra can be acquired to find the correct central frequency with negligible depolarisation of  $^{129}\text{Xe}$ .

The FID-CSI showed that the central frequency only shifted by  $\approx 10$  Hz between scans, even when the volunteer got into and out of the scanner. Based on these findings, the inter-scan shift is small enough that the spectro pre-scan only needs to be taken at the start of a new day of scanning.

#### Sequence optimisation

The initial 2D FGRE sequence parameters used a slice thickness of 10 mm and a matrix size of 128 frequency-encoding and phase-encoding steps. This small matrix size kept the scan time to within the duration of a single breath-hold ( $\approx 20$  seconds).

The next issue to account for when setting up a  $^{129}\text{Xe}$  scan is how to maximise the signal collected throughout the region of interest. The  $^{129}\text{Xe}$  is exhaled by the volunteer after their breath-hold, so there is no need to preserve any polarisation for future scans. A balance, however, needs to be struck between providing the highest SNR and not completely depolarising the  $^{129}\text{Xe}$

before the scan ends so there is uniform signal throughout the lungs. In the regime where TR is much smaller than  $T_1$ , and the flip angle is constant, the magnetisation ( $M_x$ ) after x pulses is shown in Equation (8.1).

$$M_x = M_0(\cos\alpha)^{x-1} \quad (8.1)$$

If each slice is excited separately, assuming no diffusion,  $x=128$ . The fact that polarisation does not need to be preserved for the next scan does not necessarily mean that completely depolarising the  $^{129}\text{Xe}$  yields the best image quality. The drop in polarisation from the initial to the final phase-encoding step in each slice must be taken into account. Otherwise, the phase-encoding steps towards the end of the slice may have a significant reduction in signal. The aim was to lose half of the polarisation during each scan. For an x of 128, this equates to a flip angle of  $6^\circ$ . Equation (8.1) assumes no diffusion, which is not a perfect assumption for the Tedlar bag as it allows free diffusion. It is, however, a reasonable assumption for the lungs whose microstructure greatly restricts diffusion. There are two other assumptions made when calculating the flip angle. The first is that the slice selection is perfect, so no  $^{129}\text{Xe}$  is depolarised in the adjacent slices. This will not necessarily hold for this coil but can be mitigated by increasing the spacing between slices. Secondly, it is assumed the flip angle is consistent throughout the region of interest. This will not hold if there are any inhomogeneities in the  $B_1$  field as the RF power transmitted will result in different flip angles throughout the lungs' volume. This will make achieving the optimum flip angle challenging as it may be too high in some regions and too low in others. The  $B_1$  will also change depending on how the coil is loaded, in turn altering the flip angle. Despite these drawbacks, it is still worth performing a flip angle calibration, even if imperfect, to get as close to the optimal flip angle as possible.

RF Attenuation (dB)	Bag $P_{Xe}$ Before (%)	Bag $P_{Xe}$ After (%)	Approx FA (degrees)
10	7.5	6.5	2.7
6	6.5	4.85	3.9
2	4.85	2.5	5.9
0	16.9	7.5	6.5
2	18.3	7.4	6.9
-4	7.4	2.2	8

Table 8.1: Approximate flip angle calibration using a range of RF attenuations using a 2D FGRE sequence 10mm slices on the CMRS coil loaded with saline bags

Flip angle calibration used the 2D FGRE sequence with the following parameters: 10 mm slice thickness, 128x128 matrix size and  $48\text{cm}^2$  FOV. Saline bags were used to load the coil, simulating the load of a volunteer. A Tedlar bag of HP  $^{129}\text{Xe}$  was placed inside the coil in the approximate location of the lungs. After each scan, the Tedlar bag was returned to the 2881 measurement station and its polarisation was measured. The bag was then returned to same position within the coil. The RF pulse attenuation was altered for each scan, ranging from 10 dB to 4 dB, in steps of 4 dB. The results can be found in Table 8.1. The attenuation that produced the highest SNR (34.1) was -2 dB, equating

to an approximate flip angle of  $6^\circ$ . Images acquired during the -2 dB scan are displayed in Figure 8.9.



Figure 8.9: Example slices produced with the 2D FGRE sequence with a  $48\text{cm}^2$  FOV and 10 mm slice thickness and -2 dB RF attenuation, SNR of slice 1 = 34.1

### Initial volunteer lung imaging

After the sequence parameters had been chosen and optimised using a Tedlar bag as a phantom, the coil's performance in QTAR mode when imaging  $^{129}\text{Xe}$  in healthy volunteers was assessed. Alongside the clinical screening and  $^{129}\text{Xe}$  tolerability tests, the volunteers were trained in how to inhale the HP  $^{129}\text{Xe}$  properly. This ensured that the  $^{129}\text{Xe}$  was inhaled in such a way that the  $\text{O}_2$  content of the lungs was minimised and the  $^{129}\text{Xe}$  was maximised to achieve the best SNR. Furthermore, this breathing protocol was verbally dictated by the clinician during each scan to improve consistency. A standard protocol enables a better comparison of multiple images of an individual and between individuals. The protocol is detailed below:

- Breathe out
- Breathe in
- Big breath out (exhaling the gas in the lungs)
- Inhale  $^{129}\text{Xe}$  from the Tedlar bag
- Hold breath for the length of the scan
- Breathe out
- Breathe normally

A 2D FGRE sequence with a  $48\text{cm}^2$  FOV, 10 mm slice thickness and a -2dB RF attenuation was used. The volunteer inhaled 1 L of HP  $^{129}\text{Xe}$  with a polarisation of 15%. The resultant images produced can be seen in Figure 8.10. The SNR of these images was lower than predicted, with the lungs barely visible. Even with the difference in the initial  $P_{\text{Xe}}$  taken into account, this is a major shortfall compared to the SNR seen when imaging a Tedlar bag. Also compared to the rapid coil despite the  $P_{\text{Xe}}$  produced by the 9810 being higher.

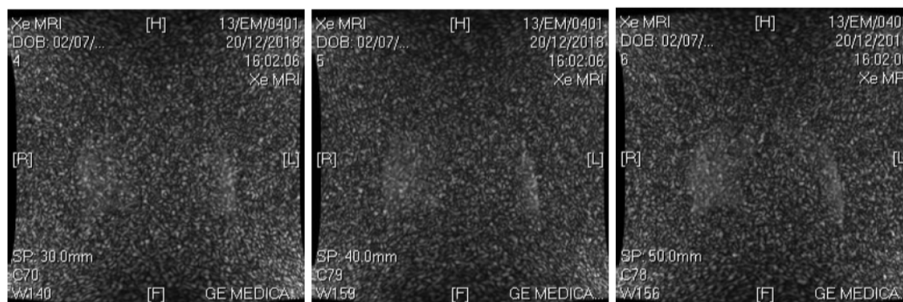


Figure 8.10: Initial attempt at lung imaging using the CMRS coil in QTAR mode, 1L bag of HP  $^{129}\text{Xe}$  15% polarisation

It was theorised that the reduction in signal could be due to the difference in coil loading with a human compared to saline bags. This difference in loading could result in a different flip angle from the RF pulse. As the coil is designed for human loading, it may be more sensitive when loaded with a human. The same RF power could therefore produce an increased flip angle that is further away from the optimal value when calibrated using saline bags.

To test this theory, the  $^{129}\text{Xe}$  Tedlar bag was placed on the chest of a volunteer inside the CMRS coil. Another flip angle calibration was performed, using attenuations from 20 dB to 0 db in steps of 2 dB. The flip angles were higher when the coil was loaded with a human compared to with saline bags at an equivalent RF attenuation. Four different bags of HP  $^{129}\text{Xe}$  were used with polarisations of 13.1%, 16%, 16.6% and 17%. The bag, coil and volunteer arrangement were kept as consistent as possible between scans given the volunteer was removed from the scanner while waiting for the next bag of HP  $^{129}\text{Xe}$  to be produced. The bag is also removed to measure its polarisation between scans. If moving the patient affects the loading in a significant way, then the coil may not be fit for use as it is tough to optimise the flip angle based on a variable that cannot be controlled. The resultant flip angle calibration can be found in Table 8.2.

RF Attenuation (dB)	Bag $P_{Xe}$ Before (%)	Bag $P_{Xe}$ After (%)	Approx FA (degrees)
20	13.1	11.8	2.3
18	11.8	10.5	2.5
16	10.5	8.95	2.9
14	8.95	7.3	3.3
14	16	13.1	3.2
12	7.3	5.7	3.6
10	5.7	3.6	4.9
8	3.6	2.1	5.3
8	16.6	9.8	5.3
6	2.1	1	6.2
6	9.8	4.4	6.5
4	4.4	1.7	7.1
4	17	7.1	6.8
2	7.1	2.4	7.5
0	2.4	0.6	8.5

Table 8.2: Approximate flip angle calibration using a range of RF attenuations using a 2D FGRE sequence 10mm slices on the CMRS coil loaded with a human volunteer with bag inside the coil on the volunteer’s chest

The images taken with an RF attenuation of 14 dB, 8 dB and 4 dB are shown in Figures 8.11, 8.12 and 8.13, respectively. The 7<sup>th</sup> slice in each scan is used to calculate the SNR of each image. Due to the inhomogeneity in Figure 8.13, the signal value was averaged from the 25 voxels about two different locations (red and yellow cross), and the noise value was calculated from 25 voxels about the green cross. SNR values can be found in Table 8.3. The SNR of the 8 dB was higher than 14 dB and 4 dB. 8 dB RF attenuation resulted in a flip angle closest to optimal. It had more than double the SNR compared to using an RF attenuation of 14 dB, despite only having 1.04 times the polarisation. The 4 dB RF attenuation image had a higher initial polarisation, and depolarised more of the HP  $^{129}\text{Xe}$  compared to the 8 dB scan, yet still had a lower SNR. This shows that the resultant flip angle was above optimal and depolarised too much of  $^{129}\text{Xe}$  before the scan was complete.

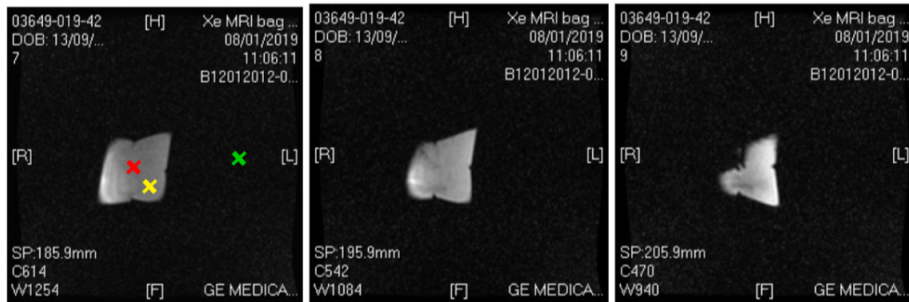


Figure 8.11: 2D FGRE sequence with a  $48\text{cm}^2$  FOV and 10 mm slice thickness and 14 dB RF attenuation, 16%  $^{129}\text{Xe}$  polarisation, coil loaded with a human volunteer with bag inside the coil on the volunteer’s chest



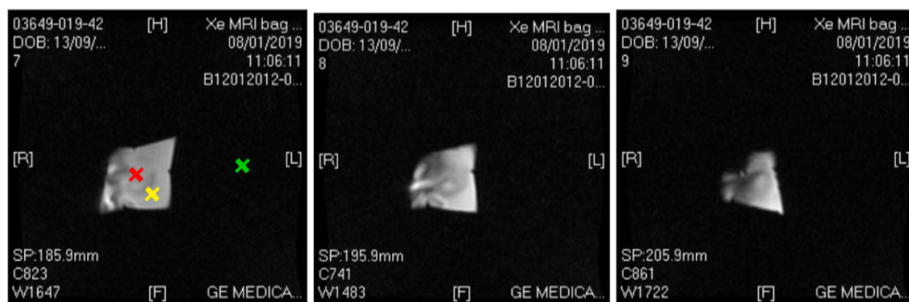


Figure 8.12: 2D FGRE sequence with a  $48\text{cm}^2$  FOV and 10 mm slice thickness and 8 dB RF attenuation, 16.6%  $^{129}\text{Xe}$  polarisation, coil loaded with a human volunteer with bag inside the coil on the volunteer's chest



Figure 8.13: 2D FGRE sequence with a  $48\text{cm}^2$  FOV and 10 mm slice thickness and 4 dB RF attenuation, 17%  $^{129}\text{Xe}$  polarisation, coil loaded with a human volunteer with bag inside the coil on the volunteer's chest

RF Attenuation (dB)	$P_{Xe}$ before imaging (%)	SNR Red Cross	SNR Yellow Cross
14	16	27.9	30.6
8	16.6	56.3	62.1
4	17	29.3	50.5

Table 8.3: SNR calculations for the 7<sup>th</sup> slice in Figures 8.11, 8.12 and 8.13

### Coil loading

An Agilent Technologies network analyser was connected to the CMRS coil to investigate the coil's response to different loading strategies. The Agilent displays the coil response, allowing the peak amplitude, its frequency and the amplitude at  $^{129}\text{Xe}$ 's resonant frequency inside GE 1.5 T (17.663 MHz).

The response of the coil was investigated under a variety of different loading conditions using both saline bags and human volunteers. Four different volunteers were placed inside the coil to test how the coil's response varied between body types and weights. Volunteers 1, 2, 3 and 4 (V1, V2, V3, V4) weighed

approximately 65 kg, 70 kg, 70 kg and 85 kg, respectively. Variations linked to the volunteers' arm position (tight versus loose) were also investigated, as volunteers' arms are restricted by the bore of the scanner to be tight to the vest. To see how the response could have been affected during the previous flip angle calibration, the response was compared with and without a Tedlar bag on the volunteer's chest.

The peak amplitude (dB), the frequency of the peak (MHz) and the amplitude at 17.663 MHz (dB) for each loading strategy can be found in Table 8.4. The results showed that loading could influence both the coil's peak amplitude and its frequency. The peak amplitude, and thus the coil response, was higher with all volunteers compared to with saline bags. Peak amplitude was also higher when volunteers had their arms tight, both with and without the Tedlar bag. This is because the vest is made more cylindrical, improving coupling between the coil pairs. A more optimal coil shape could also be a factor in explaining why heavier volunteers loaded the coil better than the lighter ones. Heavier volunteers also had less space between their chest and the top of the coil, increasing the filling factor and providing a better peak amplitude. V2 and V3 had similar weights but different coil responses, showing weight is not an exact predictor of coil response. Other aspects of body shape and composition also play a role in coil loading. Loading was worse in all volunteers when a bag was placed on their chest, which reduced the filling factor as it moved the coil away from the volunteer's chest. These tests showed that the coil was very sensitive to different loading strategies, making an accurate flip angle calibration hard to achieve.

Loading Strategy	Peak Amplitude (dB)	Peak Frequency (MHz)	Amplitude at 17.663MHz (dB)
Saline Bags	11.5	17.4227	3.4
V1 arms loose	19.7	17.46	5.2
V1 arms tight	21	17.505	6.4
V1 arms loose bag on chest	16.4	17.471	5
V1 arms tight bag on chest	17.7	17.501	6.3
V2 arms loose	20.9	17.485	5.9
V2 arms tight	21.9	17.543	8.56
V2 arms loose bag on chest	17.5	17.511	6.3
V2 arms tight bag on chest	18.6	17.541	8.1
V3 arms loose	17.4	17.467	4.9
V3 arms tight	19	17.487	5.9
V3 arms loose bag on chest	15.2	17.491	5.5
V3 arms tight bag on chest	17	17.517	6.6
V4 arms loose	20.2	17.513	6.9
V4 arms tight	21	17.586	11.8
V4 arms loose bag on chest	18.5	17.497	6
V4 arms tight bag on chest	21.6	17.555	9.5

Table 8.4: CMRS coil response in QTAR mode with different loading strategies outside of the scanner

Tests were performed with volunteers V2 and V3 to see if the coil’s response to loading within the scanner is more consistent where body position is restricted. The effect of the central frequency inside the scanner was also monitored. The results from the above test are shown in Table 8.5. All loading strategies resulted in a smaller peak response inside the scanner compared to outside, and, as before, the coil loaded with saline bags had a weaker response compared to with volunteers. Although the peak height reduced, the amplitude at the resonance frequency was higher by 7 dB and 4.3 dB for volunteers V2 and V3, respectively. If the coil were to be loaded with a volunteer instead of saline bags, the resultant flip angles would be higher for a given RF attenuation. The increased response at the resonant frequency would explain why the image quality was lower than expected, as the flip angle was calibrated using saline bags. The variation between the two volunteers is significant, measuring 4.2 dB at  $^{129}\text{Xe}$ ’s resonant frequency. Calibration for each subject may, therefore, be required to achieve the best image quality. This is not ideal as recruitment becomes harder with increased visit times. More extended visits also come with increased costs, associated scanner and staff time.

Loading Strategy	Peak Amplitude (dB)	Peak Frequency (MHz)	Amplitude at 17.663MHz (dB)
Saline Bags	10.3	17.603	9.1
V2 Arms tight bag on chest	15.5	17.64	15.1
V3 Arms tight bag on chest	14.3	17.755	10.9

Table 8.5: CMRS coil response in at  $^{129}\text{Xe}$  in QTAR mode with different loading strategies inside the scanner

### Volunteer imaging signal variation within the lungs

Two new healthy volunteers (V5 and V6) were recruited to observe the signal variation inside the lungs. They were imaged using the same protocol and under the same ethics as the experiments in the previous section. The  $^{129}\text{Xe}$  was also produced as per the protocol detailed in Chapter 5.

The imaging performed on volunteer V5 was undertaken to see how both the SNR and signal variation in the lungs changed with different flip angles. Four 2D FGRE scans were run with four different RF attenuations: 12 dB, 8 dB, 4dB and 0 dB. The FOV and slice thickness remained unchanged from the scans in the previous section. The second slice of the lungs in each scan was used for the SNR calculations. This slice was chosen because the first slice with signal may not be fully inside the lungs. The 12 dB, 8 dB, 4 dB and 0 dB scans produced images with SNRs of 2.92, 6.60, 10.7 and 21.7, respectively. These images can be seen in Figures 8.14, 8.15, 8.16 and 8.17. The SNR increased with reducing RF attenuation, which shows that the optimal flip angle had not been achieved and that the flip angle inside the lungs was considerably lower than in the bag on top of the volunteer’s chests.

The signal from slices in the lungs drops from anterior to posterior, and there are several reasons which may explain this behaviour. Firstly, the flip angle variation from anterior to posterior could be so significant that the coil is exciting  $^{129}\text{Xe}$  less towards the posterior. Another reason could be that the

receive arrays are not as sensitive to the signal in the posterior slices. Lastly, the  $^{129}\text{Xe}$  could be depolarising so fast that, by the time the posterior slices are imaged, there is not enough HP  $^{129}\text{Xe}$  left with which to image.

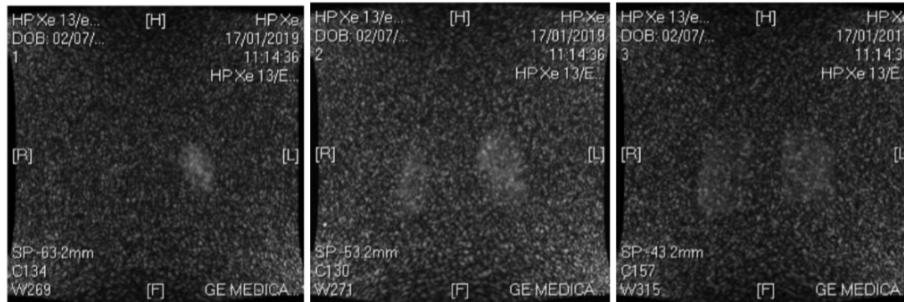


Figure 8.14: 2D FGRE sequence with a  $48\text{cm}^2$  FOV and 10 mm slice thickness and 12 dB RF attenuation, inside healthy volunteer V5's lungs. This figure shows the first three slices anterior to posterior

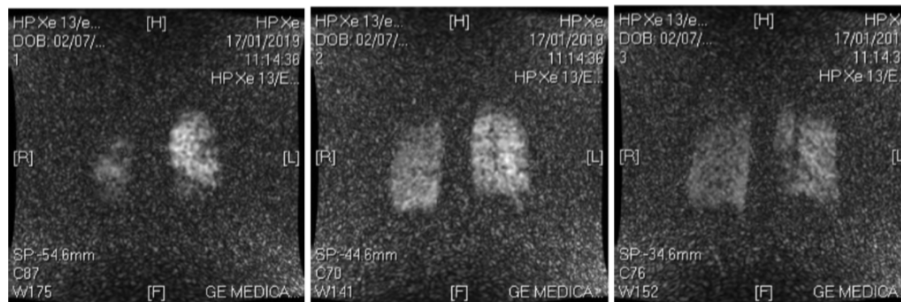


Figure 8.15: 2D FGRE sequence with a  $48\text{cm}^2$  FOV and 10mm slice thickness and 8dB RF attenuation, inside volunteer V5's lungs. This figure shows the first three slices anterior to posterior

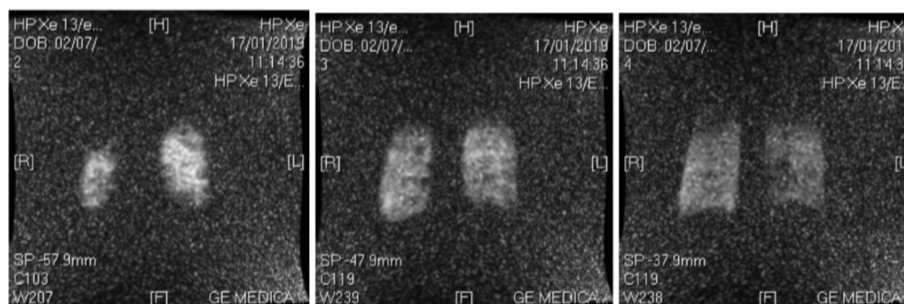


Figure 8.16: 2D FGRE sequence with a  $48\text{cm}^2$  FOV and 10mm slice thickness and 4dB RF attenuation, inside volunteer V5's lungs. This figure shows the first three slices anterior to posterior

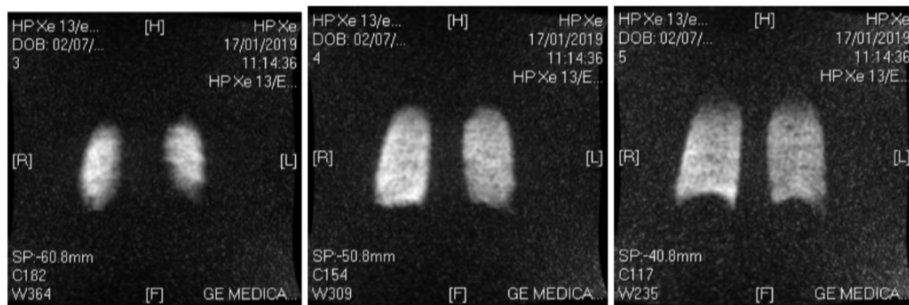


Figure 8.17: 2D FGRE sequence with a  $48\text{cm}^2$  FOV and 10mm slice thickness and 0dB RF attenuation, inside volunteer V5's lungs. This figure shows the first three slices anterior to posterior

An imaging investigation was performed on volunteer V6 in several vest configurations and sequence parameters to try to account for the signal variation. The first set of scans was performed with the same 2D FGRE sequence with 0 dB RF attenuation and slices taken anterior to posterior. The vest configurations were normal, receive arrays swapped, and vest / array configuration reversed (see Figure 8.18). These images show that the reduction in signal from anterior to posterior is still present. The coil orientation is therefore not responsible for the drop in signal.

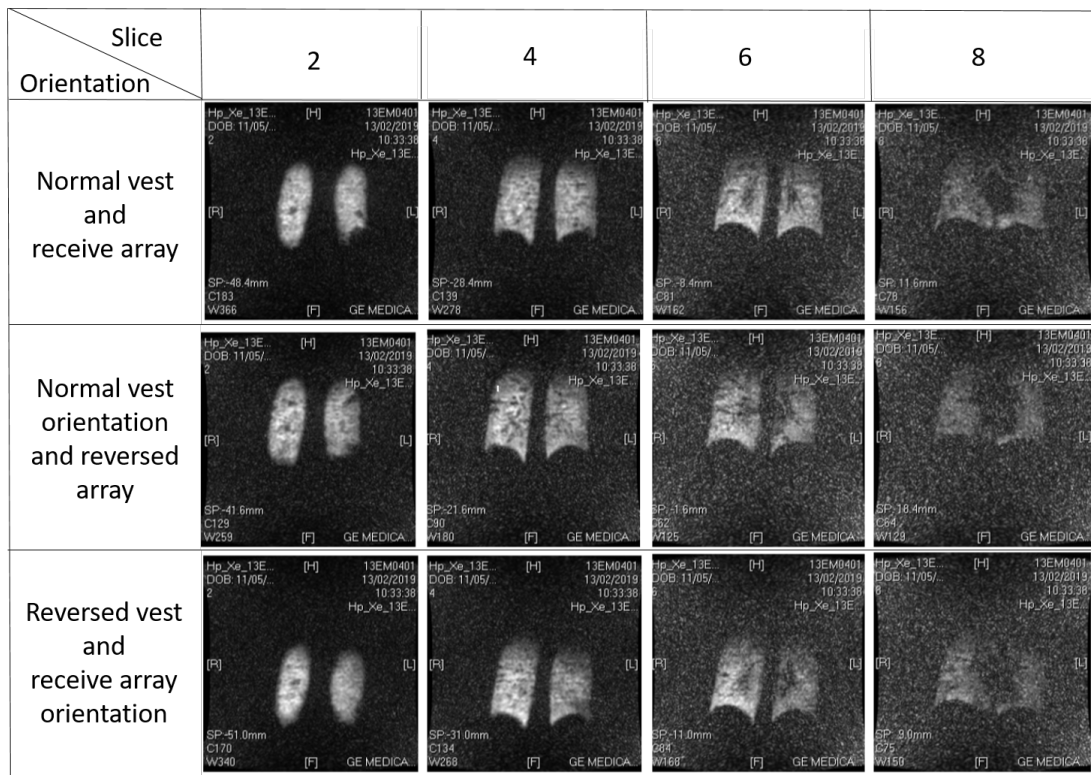


Figure 8.18: 2D FGRE sequence with a  $48\text{cm}^2$  FOV and 10mm slice thickness and 0 dB RF attenuation, inside volunteer V6's lungs with different vest and array configurations

In the subsequent investigation, images were acquired axially, which offers a top-down view of the lungs, unlike the coronal view displayed in all previous images. In the axial sequence, slices were acquired the bottom up, moving from the base of the lungs to the top. Another scan was also performed with the slice order reversed. The images from the two scans can be seen in Figure 8.19 and Figure 8.20. The anterior to posterior signal drop can still be seen in the axial slices. This shows that the drop is not due to  $T_1$  relaxation, as the scan proceeds, but in fact is present regardless of  $^{129}\text{Xe}$  polarisation, suggesting a hardware issue. However, the  $T_1$  relaxation will have exacerbated the signal drop observed in previous scans as the SNR now reduces in later slices of the axial scans.

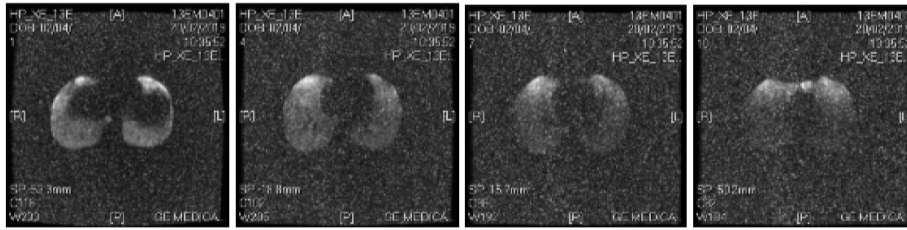


Figure 8.19: Axial 2D FGRE sequence with a  $48\text{cm}^2$  FOV and 10 mm slice thickness and 0 dB RF attenuation, inside volunteer V5's lungs. This figure shows the slices 1, 4, 7, 10 from the bottom of the lungs to the top

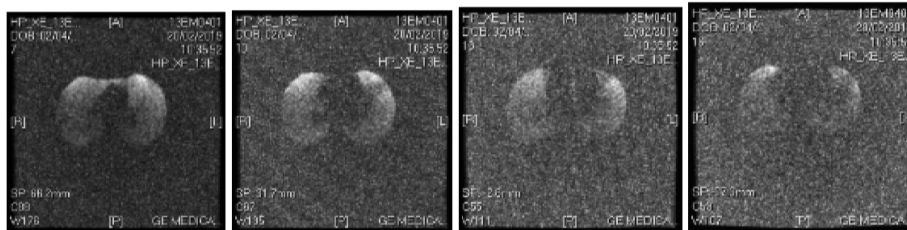


Figure 8.20: Axial 2D FGRE sequence with a  $48\text{cm}^2$  FOV and 10 mm slice thickness and 0 dB RF attenuation, inside volunteer V5's lungs. This figure shows the slices 1, 4, 7, 10 from the top of the lungs to the bottom

## Discussion

These experiments have shown that the CMRS coil is not currently suitable for clinical  $^{129}\text{Xe}$  imaging in QTAR mode. The coil is very sensitive to loading, where even subjects of the same weight can change both the frequency and amplitude of the coil's peak response. Therefore, if not taken into account, the resultant flip angle from the same RF attenuation differs between subjects, affecting the SNR in the final images. The variation in signal means it is not possible to discern the outline of the lungs throughout its volume, let alone the fine structure.

The ability of  $^{129}\text{Xe}$  MRI to find localised ventilation defects sets it apart from current spirometry, but the coil is not able to currently achieve this in QTAR mode. As a result, there is no compelling reason to use the CMRS coil on patients with impaired lung function in this mode.

The receive arrays may be interfering with the transmission coil, or the coil may simply be faulty. Other teams operate the coil in QUAD T/R mode and have encountered no problems. In order to determine if the CMRS coil has a fault or if receive arrays are the issue, it will need to be tested in QUAD T/R mode.

## 8.4 Imaging with the Clinical MR Solutions coil in QUAD T/R mode

### 8.4.1 Introduction

This section covers the testing and imaging of the CMRS coil in QUAD T/R mode. Many other teams operate their CMRS coils in QUAD T/R mode, giving a benchmark of what can be achieved. If the CMRS coil at the University of Nottingham can reach that benchmark, it indicates the coil is working as intended. Examples of the images produced by other CMRS coils can be seen in work by Driehuys et al. [206], Cleveland et al. [289] and Chen et al. [290].

### 8.4.2 Methods

#### Phantom imaging

As the CMRS coil may have had a possible fault, the initial imaging investigations were undertaken using a phantom. The coil was loaded with saline bags instead of recruiting a new healthy volunteer. Another Tupperware phantom was built using the same method as the phantom in Section 7.4.3. The purge/evacuation and  $^{129}\text{Xe}$  filling procedure was also identical to previous phantom work.

The Tupperware phantom used for these experiments had a larger volume than the one used in Chapter 7. Its volume was 1.4 L, the longest side having an internal length of 195 mm, which is longer than the distance between the back and sternum. With Tupperware placed inside the coil with its longest side perpendicular to the bed, it was possible to observe if an anterior to posterior signal drop still occurred in QUAD T/R mode. A Tupperware filled with HP  $^{129}\text{Xe}$  was scanned with the same 2D FGRE coronal sequence as used in QTAR mode. Slices 3, 4, 13 of the scan can be seen in the first row of Figure 8.21 and slices 21, 22, 23 in the second row. The signal is consistent throughout the volume of the phantom. Slices 3 and 23 are discounted, as they are the first and last slices with signal. The Tupperware may therefore not occupy the full diameter of these slices. The consistent signal shows that the anterior to posterior signal drop is not present in QTAR mode.

An additional observation from these images is the small nub of signal that can be seen about half-way down the Tupperware on the left-hand side of the image in slice 13. The signal comes from the HP  $^{129}\text{Xe}$  inlet tube of the Tupperware. The tube has a 6 mm internal diameter, showing the coil's capability of imaging fine structure in QUAD T/R mode.



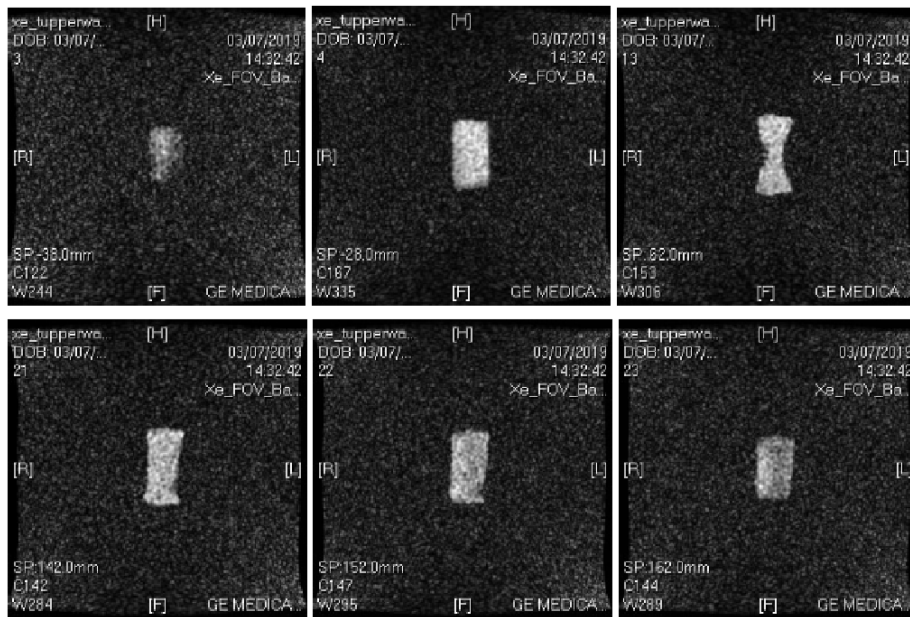


Figure 8.21: 2D FGRE sequence with a  $48\text{cm}^2$  FOV and 10 mm slice thickness and 8 dB RF attenuation, inside a Tupperware phantom using QUAD T/R mode. This figure shows the slices 3, 4, 10 on the top row (left to right) and 21, 22 and 23 on the bottom row (left to right)

### Sequence optimisation

During sequence optimisation, 0.6 L Tedlar bags were used as phantoms. The aim was to produce the best SNR while maintaining an acceptable scan time. For all scans with a similar attenuation, the flip angle was estimated to be comparable as saline bags were used to load the coil, and their position did not change between scans. It is not possible to produce bags with the exact same polarisation on the Polarean 9810. For that reason, the SNR is scaled with the in-bag polarisation to allow for a fair comparison (see Table 8.6).

Scan No.	Orientation	Matrix Size (Freq. enc. x Phase enc.)	Slice Thickness (mm)	RF Attenuation (dB)	Starting $P_{Xe}$ (%)	Ending $P_{Xe}$ (%)	Approx FA (degrees)	Highest Slice SNR	$\frac{SNR}{P_{Xe}}$
1	Coronal	128x128	10	20	17.6	14.68	3.1	11.3	0.65
2	Coronal	256x128	10	20	14.68	12.4	2.9	6.9	0.47
3	Coronal	128x128	5	20	12.4	10.67	2.8	4.6	0.36
4	Coronal	78x128	5	20	10.67	9.46	3.2	3	0.28
5	Axial	128x128	10	10	9.46	4.09	6.6	15.5	1.6
6	Axial	128x128	10	10	3.6	1.4	7	7	1.9

Table 8.6: 2D FGRE sequences performed on a 0.6 L bag of HP  $^{129}\text{Xe}$  using the CMRS coil in QUAD T/R mode

Four coronal 2D FGRE scans were undertaken with an RF attenuation of 20

dB. The number of frequency encoding steps and the slice thickness were varied, but the phase encoding steps remained consistent between the four scans. Scan 1 was the control, using the same sequence parameters as the QTAR CMRS coil tests. This scan had a 17-second duration. Doubling the acquisition window, doubles the number of frequency encoding steps and only increases the scan duration by 2 s. If the number of phase encoding steps is doubled, the scan time also doubles. The scan time also doubles if the slice thickness is halved and the FOV is kept constant. By doubling the frequency encoding points, the voxel size is halved, so each voxel has less HP  $^{129}\text{Xe}$ , therefore reducing SNR (see Scan 2). The same reduction in voxel size occurs when the slice thickness is halved, shown in the SNR reduction between Scan 3 and Scan 1. The smaller voxels do, however, allow for an increase in the image resolution so that finer details can be resolved. Scan 4 acted to preserve the resolution increase using 5 mm slices but had a reduced number of frequency encoding steps to keep the scan time to a single breath-hold. Scan 4 had the lowest scaled SNR, so using its parameters would only be recommended if there was sufficient  $P_{Xe}$  to take advantage of the increased resolution. Two axial identical scans were also taken but the RF attenuation was set to 10 dB they showed that a 10 dB attenuation provided a scaled SNR that was over 2.4 times higher. The parameters used in scan 5 and 6 were used as the starting point of volunteer imaging.

### **Volunteer lung imaging**

Volunteer V6 was imaged with a 2D FGRE sequence using the same parameters as Scan 5/6 in the previous set of tests but using a coronal view. These parameters were chosen as a starting point because they offered the best SNR in the Tedlar bag. However, as seen before, the optimal flip angle is likely to change when the coil is loaded with a human instead of saline bags.

Slices were taken posterior to anterior and a significant drop off in signal over the first few was observed. This drop off between slice 2 and 3 can be seen in Figure 8.22. By the 10<sup>th</sup> slice, the outline of the lungs was no longer visible. This indicated that 10 dB RF attenuation had not resulted in a flip angle close to optimal.

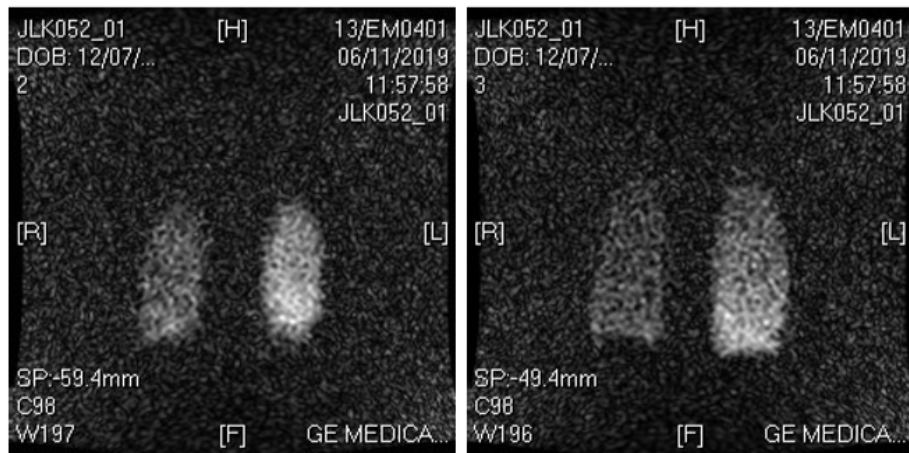


Figure 8.22: 2D FGRE sequence with a  $48\text{cm}^2$  FOV and 10 mm slice thickness and 10 dB RF attenuation, inside V6's lungs, using the CMRS coil in QUAD T/R mode. Slice 2, SNR = 10.5 (left). Slice 3, SNR = 7.9 (right)

In the following scan, the attenuation was reduced to 0 dB and the slices were taken from anterior to posterior. The signal could be seen in all slices within the lungs; however, it was significantly reduced in the central slices (see Figure 8.23). This reduction in signal from the central slices could be explained by their distance away from the coil, as the flip angle could be much larger in the outer regions of the lung. The coil could also be more sensitive to the  $^{129}\text{Xe}$  signal when it is closer to the coil, further compounding the signal variation between central and outer regions of the lungs. Volunteer V6 also had a slim build, which resulted in the coil tenting and moving away from the volunteer's chest, as shown in Figure 8.7a. The back of the volunteer was still flush with the bottom of the vest, which could explain why the signal was higher towards the posterior.

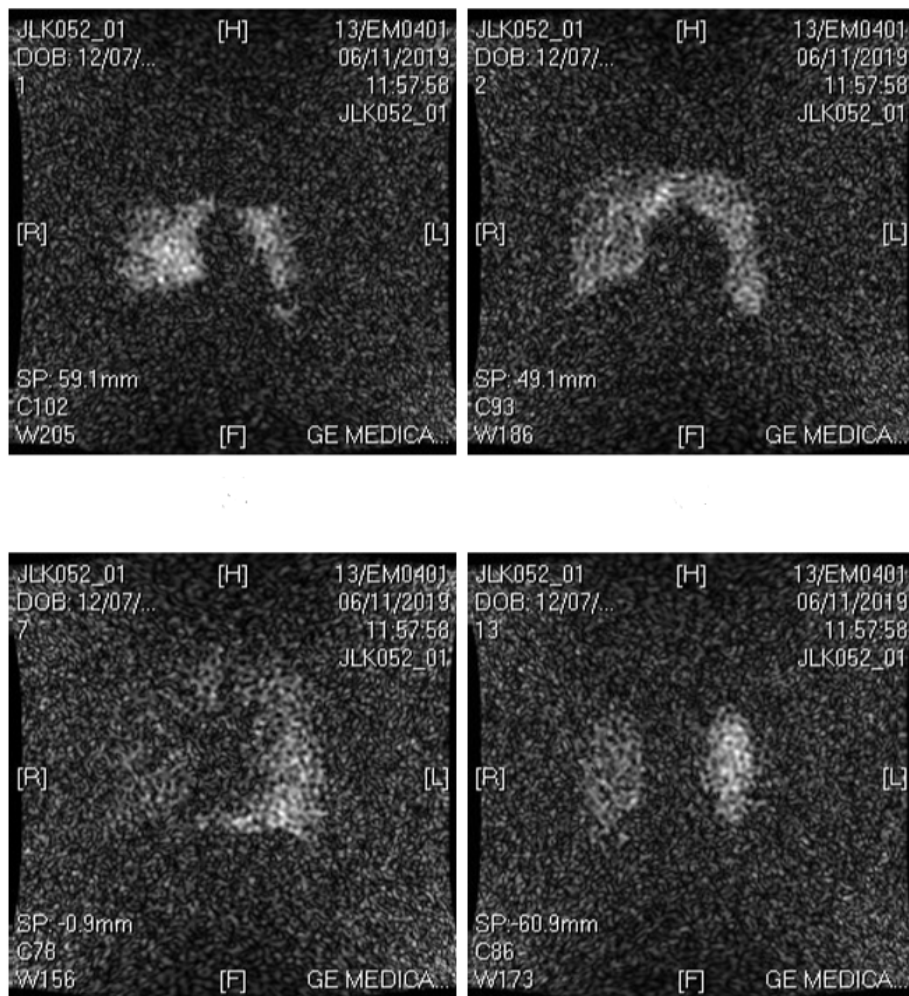


Figure 8.23: 2D FGRE sequence with a  $48\text{cm}^2$  FOV and 10 mm slice thickness and 0 dB RF attenuation, inside volunteer V6's lungs, using the CMRS coil in QUAD T/R mode. Slice 1, SNR=6.7 (top left). Slice 2, SNR=6.8 (top right). Slice 7, SNR=4.8 (bottom left). Slice 13, SNR=7.1 (bottom right).

In order to prevent the coil from tenting, foam pads were inserted between the chest of V6 and the vest (see Figure 8.7b). The scan was then repeated; however it was cancelled by the scanner as it encountered an error. The GUI displayed the following message: “Peak power exceeded on MNS broadband amplifier. Peak power 26 W”. “Peak power 26 W” is believed to refer to the maximum average power that can be transmitted during a scan. To determine the cause of the error, V6 was replaced with saline bags, following which the scan completed without error. V6 was then placed back inside the coil, and the scan was repeated a 3<sup>rd</sup> time. The 3<sup>rd</sup> scan was halted by the same error. Using these specific scanning parameters, loading the coil with a human volunteer appears to increase the power transmitted outside the range deemed safe by the GE 1.5 T scanner.

To diagnose the error, V5 was scanned six times, the results of which can be seen in Table 8.7. They were instructed to either breathe normally or to hold their breath after inhalation. The inhalation caused their chest to expand and simulated a subject inhaling  $^{129}\text{Xe}$  in a clinical run. This change in chest size would affect the loading of the sensitive CMRS coil and may cause the scan to fail. The attenuation was also altered, with two scans performed at 10 dB. The sequence failed with the same error message in half of the scans. The error only occurred when the attenuation was at 0 dB, which is unsurprising as power transmitted is higher. The cause of the error did not appear to be a direct result of RF attenuation, rather the error appeared to be intermittent. This is shown in Scans 1 and 6, where, although identical, one failed and the other succeeded.

Volunteer	Coil Configuration	Response Amplitude at 17.67MHz (dB)
V1	Pads in	16
V1	Pads out arms loose	17.3
V1	Pads out arms tight	18.6
V1	Pads out leaning right	24.5
V1	Pads out leaning left	28.6
V3	Pads in	16.1
V3	Pads out arms loose	16.6
V3	Pads out arms tight	17.6
V3	Pads out leaning right	17.3
V3	Pads out leaning left	17.8

Table 8.7: Table showing the attenuation, breathing pattern and whether the scan run successfully for six 2D FGRE scans using the QUAD T/R coil

To determine if the CMRS coil was the source of the error, it was replaced with an RF terminator acting as a purely resistive load. With this set-up, the scan could be run consistently with 0 dB RF attenuation but would fail if the transmit gain was increased above 0 dB. This indicated that the coil was not responsible for the error. Finally, to rule out the CMRS connector between the scanner and RF terminator, it was replaced with an MNS bridge made by GE. The error persisted despite the change in load and connectors. This indicates that the error was caused by the scanner's MNS train. GE was contacted, and their engineer found an issue with the MNS amplifier and observed higher than expected background noise. These issues may be causing the error message and scan failures.

### 8.4.3 Discussion

Running the QUAD T/R mode can remove the signal drop from anterior to posterior observed in QTAR mode, providing a more consistent signal across the lungs. There is, however, still a variation in signal between the two lungs (see Figures 8.22 and 8.23) and the signal that can be seen is lower than that observed in QTAR mode. This is because the flip angle is below optimal, as the RF power produced is limited by an error with the GE 1.5 T's MNS amplifier.

There is also variation in the flip angle due to the proximity effects in QUAD T/R mode, which cause signal variation between the inner and outer regions of the lungs. This variation is not present in work by other teams. The team at Duke uses custom padding inside the vest to help it maintain its shape and produce a more homogeneous  $B_1$  field (see Figure 8.24).

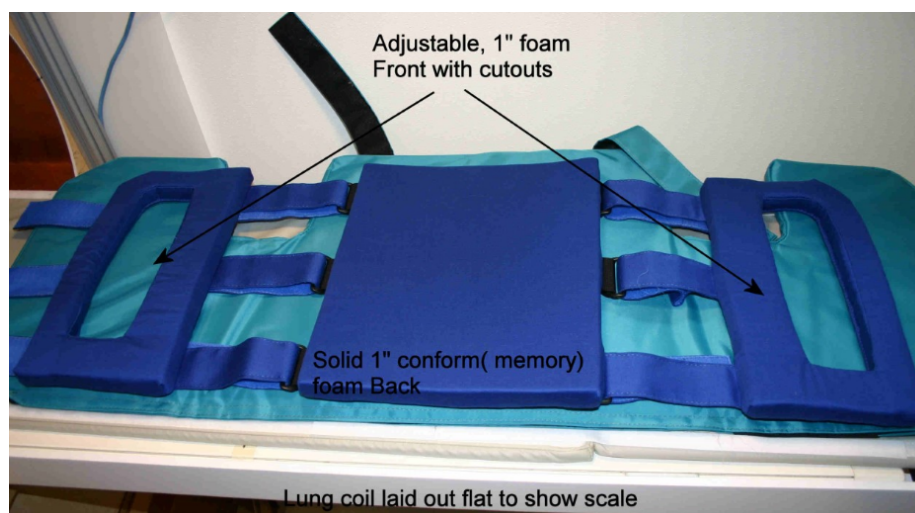


Figure 8.24: Coil padding used inside a CMRS coil at Duke University

In order to make the CMRS coil in QUAD T/R mode suitable for clinical work on the GE 1.5 T scanner, the MNS amplifier needs to be replaced, and a custom padding solution needs to be created for the coil in Nottingham.

## 8.5 Conclusion

The work discussed in the chapter, unfortunately, shows that, because of possible mechanical faults, the CMRS coil in the University of Nottingham is not currently fit for in-vivo  $^{129}\text{Xe}$  MRI imaging in patients. The coil and MNS train fault conditions need to be rectified before human imaging can commence.

The coil was also modified to work in QUAD T/R mode, a mode with which many other teams have been able to achieve high-quality images [206, 289, 290]. The University of Nottingham coil was not able to achieve the benchmark set by other CMRS coils working in this mode even with a comparable  $^{129}\text{Xe}$  bulk magnetisation [289]. Despite eliminating the signal drop found in QTAR mode, it suffered from signal variation due to proximity effects and an undiagnosed signal discrepancy between the left and right lungs. Besides the above issues, the scanner prevented the coil in QUAD T/R from producing a high enough RF power to achieve an optimal flip angle without causing the scanner to flag up an error and cancel the scan. This error was caused by faults with the MNS amplifier and RF connector in the feedthrough panel. Padding may improve the coil's signal inhomogeneity, but it is currently unfit to perform clinical work in QUAD T/R mode.

The plan going forward is to see if the repair on the GE 1.5 T scanner can

fix the intermittent error while the coil is working in QUAD T/R mode. The sequence can only be optimised and other errors properly diagnosed when this intermittent error is fixed. If the CMRS coil in the University of Nottingham still cannot reach the image quality produced by other teams, there are talks in progress with the team in Oxford with regards to borrowing their coil to aid in error diagnosis.

## Chapter 9

# Conclusion

This thesis aimed to contribute to the progression of HP  $^{129}\text{Xe}$  MRI with a focus on imaging the human lungs. The work presented sets out to achieve this goal in several different ways, investigating each stage of the HP  $^{129}\text{Xe}$  imaging pipeline. It began with investigating the thermal dynamics of the gases inside the optical cell during SEOP under different conditions. The goal of these investigations was to inform stopped-flow polariser users on how to achieve the highest  $^{129}\text{Xe}$  bulk magnetisation under various SEOP conditions. The next section discussed the upgrade, redesign and testing of a stopped-flow clinical polariser, the N-XeUS2, with aim of developing a reliable, open-source, user-friendly polariser that can compete with current continuous flow polarisers in a clinical setting. The final contribution to the overall aim were the investigations looking at HP  $^{129}\text{Xe}$  in a clinical setting. This started with optimising the flowrate of the Polarean 9810 continuous-flow polariser to achieve the highest  $P_{\text{Xe}}$  in a clinical setting. The HP  $^{129}\text{Xe}$  produced by the Polarean 9810 was then used in the initial MRI imaging and dissolved phase NMR on a unique 0.5 T upright scanner developed by Paramed. The HP  $^{129}\text{Xe}$  was also used to test a new flexible chest coil made by CMRS on the GE 1.5 T flatbed scanner. These imaging studies aimed to push the boundaries of clinical HP  $^{129}\text{Xe}$  MRI at the University of Nottingham and, in the case of the Upright work, test the capabilities of a unique scanner whose open/upright design will increase the cohort of patients that can undergo MRI imaging. The conclusions of each chapter are outlined below, followed by an overall summary and statement of priorities for work going forward.

### 9.1 Improving stopped-flow $^{129}\text{Xe}$ SEOP with Raman spectroscopy

Chapter 3 detailed the work undertaken to investigate the kinetics of stopped-flow  $^{129}\text{Xe}$  SEOP. Examining the original experimental set-up showed that consistency between experimental runs had to be improved; this was achieved by spreading the alkali metals on the walls of the optical cell. Raman temperature measurements of the  $\text{N}_2$  within the cell showed that, once the alkali metal vapour density hits a critical point and enters thermal runaway, the internal cell temperature becomes significantly elevated above the cell wall and oven set



temperature. Runaway also causes a temperature gradient to form along the length of the cell. This is where the temperature at the front of the cell is the highest, and it reduces towards the back as laser transmission reduces due to the high alkali metal vapour density. A cell entering runaway also has a severe negative impact on the  $P_{Xe}$ , thereby setting an upper limit to useable oven temperature and the  $\gamma_{SEOP}$  that can be achieved. This shows that good thermal management is essential to achieve the highest  $P_{Xe}$  possible.

As previously reported [150] and as observed, the  $P_{Xe}$  decreased with increasing  $^{129}Xe$  partial pressure and the total  $^{129}Xe$  bulk magnetisation was higher in richer mixes. However, increased Xe leads to a greater SE, resulting in a higher optical absorption, so a higher heat load which the  $N_2$  may not be able to dissipate which can result in Rb runaway.  $^4He$  when it replaced  $N_2$  in the gas mix had no significant effect on managing the thermal gradient across a spread cell nor on the final  $P_{Xe}$  achieved in a 1-inch cell. This is contrary to the results presented in by J.Birchall et al. using a 2-inch cell who saw small improvements in  $P_{Xe}$  and build-up rates when using  $^4He$  fractions of 45% [136]. Comparing  $^{129}Xe$  SEOP between Cs and Rb confirmed that using Cs showed an approximate two-fold improvement  $P_{Xe}$  over Rb. The first comparison between the  $N_2$  temperature between Cs and Rb using Raman spectroscopy data showed that due to Cs's higher vapour pressure and larger spin-exchange cross-section with  $^{129}Xe$ , it was subject to runaway at significantly lower oven temperatures than Rb. This means that should Cs be used in a clinical stopped-flow polariser with high power lasers, thermal management is key to preventing runaway. Cs's potential to increase polarisation and reduce build-up times could be a huge benefit in a clinical setting.

## 9.2 Upgrade and quality assurance of a N-XeUS2 stopped-flow xenon-rich SEOP polariser

Chapter 4 first described the upgrade and redesign of the N-XeUS polariser to the N-XeUS2. This involved upgrading the hardware and software. The N-XeUS2 design was then replicated at Wayne State University in Detroit, dubbed the W-XeUS2. Due to a series of laser failures at the University of Nottingham, which have been the cause of most issues within the consortium, a lab visit was undertaken to measure the  $P_{Xe}$  that the XeUS2 design could achieve at different  $^{129}Xe/N_2$  gas mixes. In a 2000 Torr cell, the polariser was able to achieve a  $P_{Xe}$  of  $59.1 \pm 1.5\%$ ,  $76.3 \pm 2.0\%$  and  $97.9 \pm 1.9\%$  for 1500, 1000 and 500 Torr respectively. The  $P_{Xe}$  produced by the N-XeUS2 was higher than the original XeUS polariser [24] for all gas mixes and at 500 Torr the N-XeUS2 achieved the highest  $P_{Xe}$  produced by a polariser of this type. The performance of the W-XeUS using a 2700 Torr pressure produced lower but still high levels of polarisation, generating a  $P_{Xe}$  of  $56.0 \pm 1.5\%$  and  $51.8 \pm 1.5\%$  for 1350 and 2025 Torr, respectively. The full data set has been submitted for publication to the journal of magnetic resonance JMR with a subset of the data already published in the same journal [136]. XeUS2 design, however, exhibited slow build-up rates, sometimes taking up to three hours to reach a steady-state polarisation. This would not be acceptable for a clinical setting where the time between scans is typically 40-45 minutes. A comparison was made between the DE rate achieved

by the W-XeUS2 in 30 minutes and that achieved by the Polarean 9810 in a clinical time scale. It found that aside from the 500 Torr Xe and 1500 Torr  $N_2$  gas mix found there was no significant difference in DE rate, showing that the XeUS2 performance is sufficient for a clinical setting.

The first long term QA study of this polariser design was undertaken by on the W-XeUS2 and was published in JMR [182]. It showed that the new manifold construction enabled a simulated cell lifetime that could produce enough bags for  $\approx 90$  clinical visits while still producing a polarisation level that would yield an adequate SNR for MRI imaging. This would be equivalent to one to two years of regular use, demonstrating that the XeUS2's cell lifetime is suitable for a clinical setting. The N-XeUS2 is a safer, more user-friendly and higher-performance polariser compared to the Polarean 9810. To fully utilise the high  $P_{Xe}$ , future work is planned to employ an aluminium oven design to better thermally manage the cell at high oven temperatures.

### 9.3 Production of hyperpolarised $^{129}\text{Xe}$ for in-vivo imaging using a continuous-flow polariser

Chapter 5 began by discussing the theory and methods behind operating a recently upgraded Polarean 9810 continuous-flow polariser. The investigation in the chapter explored the  $P_{Xe}$  produced when using a 3% Xe gas mix at different flow rates. A 3% gas mix could produce a bag in 1.5 times less time than a 2% gas mix without a significant loss in polarisation and can deliver a 1 L bag of HP  $^{129}\text{Xe}$  with a  $P_{Xe}$  of between 13 – 19% after 28 minutes of cryo-collection. This quicker cryo-collection time meant that the Polarean 9810 was no longer the rate-limiting step during a clinical imaging visit, reducing the pressure on the polariser operator and the scanner time needed for a subject visit.

### 9.4 Hyperpolarised $^{129}\text{Xe}$ work on a Paramed 0.5 T upright scanner

The investigations in Chapter 7 resulted in the first HP  $^{129}\text{Xe}$  NMR spectra recorded, and MRI images taken on a Paramed 0.5 T Multinuclear upright scanner. They showed that using the existing 3D-spoiled GRE sequence in conjunction with a CMRS surface coil could produce  $^{129}\text{Xe}$  MRI images of phantoms with high SNR and resolutions. The other investigation in the chapter assessed the ability of the coil to perform dissolve-phase NMR of  $^{129}\text{Xe}$  on the Upright scanner. It was able to resolve NMR signals from  $^{129}\text{Xe}$  dissolved in water, olive oil, ethanol and tert-butanol. This indicated that, once approved for human use, the coil would be able to perform in-vivo dissolved-phase NMR and gas-phase MRI in the lungs. With the construction of a bespoke chest coil by Pulseteq, the scope of  $^{129}\text{Xe}$  imaging on the Upright scanner is set to increase.

## 9.5 Hyperpolarised $^{129}\text{Xe}$ MRI imaging on a General Electric 1.5 T flatbed scanner

Chapter 8 investigated  $^{129}\text{Xe}$  MRI imaging on the GE 1.5 T scanner using a flexible chest coil made by CMRS. The coil's vest-like design is more comfortable and has higher patient tolerability compared to the rigid chest coil made by Rapid Biomedical. However, it was found that the CMRS coil is not currently fit for clinical imaging in QTAR mode due to a loss in signal from anterior to posterior. When the coil was converted to work in QUAD T/R mode, the issue presented in QTAR mode disappeared. Nevertheless, the Nottingham CMRS coil failed to match the results from other teams with the same coil working in the same mode. This is believed to be due to proximity effects. Due to a scanner error detecting an unsafe amount of RF power being delivered to the subject, it was not possible to achieve an optimal flip angle in-vivo in QUAD T/R mode. The results with QUAD T/R mode looked more promising than those in QTAR mode; however, the coil is still not suitable for clinical work in this mode at this time. No clinical  $^{129}\text{Xe}$  imaging can occur on the GE 1.5 T scanner until the issues with the CMRS coil and scanner have been resolved. The end goal is to move all clinical work onto the Upright scanner with a new chest coil from Pulseteq and then compare those results with images taken by the GE 1.5 T scanner and CMRS coil once they are fully operational.

## 9.6 Overview

The work set out in this thesis broadly achieved the goal it set out to achieve, namely contributing to the progression of clinical  $^{129}\text{Xe}$  MRI imaging. The major challenge, which can be seen throughout the thesis, however, is the reliability of the equipment used to both produce and image the HP  $^{129}\text{Xe}$ . The entire pipeline only functions if all components are functioning correctly. With so many components, reliability may now be one of the greatest hurdles to  $^{129}\text{Xe}$  MRI becoming a routine clinical procedure.

HP  $^{129}\text{Xe}$  MRI is starting to reach the performance of HP  $^3\text{He}$  in clinical lung imaging.  $^{129}\text{Xe}$ 's vastly reduced cost, combined with its large chemical shift and ability to dissolve into the blood to be transported to other organs, makes it more practical and applicable to a wider range of diseases than  $^3\text{He}$ . The field of HP  $^{129}\text{Xe}$  MRI is maturing and the knowledge of production/imaging and associated technology is constantly improving to yield higher  $P_{\text{Xe}}$  and better exploit the available  $P_{\text{Xe}}$  to improve MRI image quality. The advent of upright  $^{129}\text{Xe}$  MRI allows for a whole new cohort of patients who previously could not tolerate a conventional flatbed scanner and enables patients to be imaged in new positions. Clinical HP  $^{129}\text{Xe}$  MRI imaging is currently in an exciting position as it becomes better able to aid clinicians in diagnosing and treating a wide range of diseases, which, if implemented correctly, could have a large positive impact on global health.

## 9.7 Priorities for future work

As discussed in the above section, one of the main priorities for HP  $^{129}\text{Xe}$  MRI imaging is the reliability of production and imaging. The first step would involve pursuing the work set out in Section 4.10.2 to build and install the new laser design within the N-XeUS2 before it is integrated into the QMC. This laser would be user-serviceable and more economical than the current Ultra500, the most unreliable and expensive component of the N-XeUS2.

The next avenue of future work is to begin in-vivo HP  $^{129}\text{Xe}$  imaging on the Upright scanner. This requires the Pulseteq coil to be approved for human use by SPMIC; however, the coil can still be tested on phantoms pending approval. Following this, initial imaging studies with human volunteers can be undertaken before imaging patients with impaired lung function.

Further sequence development may be required on the Upright scanner as patients with impaired lung function may not be able to hold their breath for the amount of time required to complete the current 3D-spoiled GRE sequence. This is especially relevant as the Upright scanner can image those patients who cannot be scanned in a flatbed scanner and who may have even more constraints on their maximum breath-hold time. Reducing scan time could involve investigating techniques such as compressed sensing (CS) and gated MRI imaging. CS is a method of generating images from undersampled data using image reconstruction techniques [291] [292]. Studies have shown that CS is able to accelerate HP MRI imaging with both  $^3\text{He}$  and  $^{129}\text{Xe}$  while still maintaining an acceptable image quality [293] [294]. J. Harkin has developed a CS 3D GRE proton sequence on the Upright scanner which, using 3-fold undersampling, was able to produce a lung image with a matrix size of 256x200x22 in 22.7 s. The resultant image was of a higher resolution than a previous fully sampled SE sequence (duration 21 s), which had a matrix size of 160x128x7. The CS sequence did however produce images with a slightly higher noise [256]. When the matrix size was altered to 256x160x10, imaging could still be performed with an undersampling factor of 4.82, which reduced the scan time even more and could enable imaging to be undertaken on patients with impaired lung function [256]. The next step will be to convert these new CS sequences to use for HP  $^{129}\text{Xe}$  imaging and optimise them to bring scan times to a minimum while still producing clinically useful images. Gated MRI involves starting the MRI sequence once a specific physiologic event has occurred. A simple example of respiratory gating would be using a sensor to detect chest expansion to trigger the MRI sequence at a specific point in the breath cycle [295]. This would make it possible to take multiple  $^{129}\text{Xe}$  MRI images of the lungs and combine them to improve the SNR of the final image. This technique has been used with  $^{129}\text{Xe}$  MRI imaging in mice, where gated images were taken over multiple breath-holds to improve the SNR of the final image [296]. If applied to humans, images could be taken with multiple shorter breath holds instead of a longer single one. The high SNR in the gated mouse images required the mice to be anaesthetised and ventilated with a constant-volume mechanical ventilator [109]. This protocol would not be tolerated by human subjects. Another issue is that the current production capacity of HP  $^{129}\text{Xe}$  in the QMC is 1 L per 45 minutes, and, under current ethics, at least 30 minutes needs to be allowed between  $^{129}\text{Xe}$  MRI scans. This time would allow the patient to move between image acquisitions,

making it difficult to produce an accurate final image. Both techniques pose an interesting avenue for the development of HP  $^{129}\text{Xe}$  imaging on the Upright scanner.

# Bibliography

- [1] Forum of International Respiratory Societies. The global impact of respiratory disease – second edition. *Sheffield, European Respiratory Society*, 2017.
- [2] AD. Lopez CJL. Murray. evidence-based health policy: lessons from the global burden of disease study. *Science*, 274:740-743, 1996.
- [3] F. Martinez et al. Idiopathic pulmonary fibrosis. *Nature Reviews Disease Primers*, 3(1):1–19, 2017.
- [4] NHS. <http://www.nhs.uk/conditions/spirometry/pages/introduction.aspx>. 2015.
- [5] J. Ruckdeschel et al. Therapeutic options for the treatment of small cell and non-small cell lung cancer. *Current opinion in oncology*, 5(2):323–334, 1993.
- [6] N. Memon et al. Segmentation of lungs from ct scan images for early diagnosis of lung cancer. In *Proceedings of world academy of science, engineering and technology*, volume 14, 2006.
- [7] P. Herzog et al. Ct perfusion imaging of the lung in pulmonary embolism. *Academic radiology*, 10(10):1132–1146, 2003.
- [8] S. Gilbert. Ionising radiation and cancer risks: what have we learned from epidemiology? *International journal of radiation biology*, 85(6):467–482, 2009.
- [9] J. Mayo et al. Radiation exposure at chest ct: a statement of the fleischner society. *Radiology*, 228(1):15–21, 2003.
- [10] H. Kauczo et al. Mri using hyperpolarized noble gases. *European radiology*, 8(5):820–827, 1998.
- [11] Robin K et al. Harris. Nmr nomenclature. nuclear spin properties and conventions for chemical shifts (iupac recommendations 2001). *Pure and Applied Chemistry*, 73(11):1795–1818, 2001.
- [12] M. Narazak et al. Analysis of hyperpolarized  $^{129}\text{Xe}$  dynamics in mouse lungs under spontaneous respiration for separate determination of lung functional parameters and relaxation time. *Magnetic Resonance in Medical Sciences*, 5(3):119–128, 2006.

- [13] M. Rao et al. Imaging human brain perfusion with inhaled hyperpolarized  $^{129}\text{Xe}$  mr imaging. *Radiology*, 286(2):659–665, 2018.
- [14] J. Chacon-Caldera et al. Dissolved hyperpolarized xenon-129 mri in human kidneys. *Magnetic resonance in medicine*, 83(1):262–270, 2020.
- [15] A. Kastler. Some suggestions regarding the optical output and the optical detection of a population of unequal levels of spatial quantization atoms: Application to the stern and gerlach experiment and magnetic resonance. *Phys. Radium*, 11:255 - 265, 1950.
- [16] P. Tipler. Modern physics. *pages 34 - 37*, 1978.
- [17] PubChem. Xenon-129. *National Center for Biotechnology Information. PubChem Database*, 2020.
- [18] D. J. Bell et al. Gyromagnetic ratio. <https://radiopaedia.org/articles/gyromagnetic-ratio?lang=gb>.
- [19] M. Albert et al. Biological magnetic resonance imaging using laser-polarized  $^{129}\text{Xe}$ . *Nature*, 370(6486):199–201, 1994.
- [20] B. Driehuys et al. High-volume production of laser-polarized  $^{129}\text{Xe}$ . *Applied Physics Letters*, 69(12):1668–1670, 1996.
- [21] I. Ruset et al. Optical pumping system design for large production of hyperpolarized  $^{129}\text{Xe}$ . *Physical review letters*, 96(5):053002, 2006.
- [22] G. Norquay et al. Optimized production of hyperpolarized  $^{129}\text{Xe}$  at 2 bars for in vivo lung magnetic resonance imaging. *Journal of Applied Physics*, 113(4):044908, 2013.
- [23] G. Schran et al. Characterization of a low-pressure high-capacity  $^{129}\text{Xe}$  flow-through polarizer. *Physical Review A*, 80(6):063424, 2009.
- [24] P. Nikolaou et al. Multidimensional mapping of spin-exchange optical pumping in clinical-scale batch-mode  $^{129}\text{Xe}$  hyperpolarizers. *The Journal of Physical Chemistry B*, 118(18):4809–4816, 2014.
- [25] P. Nikolaou et al. Near-unity nuclear polarization with an open-source  $^{129}\text{Xe}$  hyperpolarizer for nmr and mri. *Proceedings of the National Academy of Sciences*, 2013.
- [26] C. Lederer et al. Table of isotopes. *John Wiley & Sons Inc., New York*, 17:19, 1978.
- [27] Wolfgang Pauli. Pauli exclusion principle. *Naturwiss*, 12:741, 1924.
- [28] R. Nave. Eigenvalues and eigenfunctions. *Hyperphysics*.
- [29] D. Kaseman. Nmr: Theory. [https://chem.libretexts.org/Bookshelves/Physical\\_and\\_Theoretical\\_Chemistry\\_Textbook\\_Maps/Supplemental\\_Modules\\_\(Physical\\_and\\_Theoretical\\_Chemistry\)/Spectroscopy/Magnetic\\_Resonance\\_Spectroscopies/Nuclear\\_Magnetic\\_Resonance/NMR3A\\_Theory](https://chem.libretexts.org/Bookshelves/Physical_and_Theoretical_Chemistry_Textbook_Maps/Supplemental_Modules_(Physical_and_Theoretical_Chemistry)/Spectroscopy/Magnetic_Resonance_Spectroscopies/Nuclear_Magnetic_Resonance/NMR3A_Theory), 2019.

- [30] L. Hanson. Is quantum mechanics necessary for understanding magnetic resonance? *Concepts in Magnetic Resonance Part A: An Educational Journal*, 32(5):329–340, 2008.
- [31] M. H. Levitt et al. Spin dynamics: Basics of nuclear magnetic resonance, second edition. *ISBN 978-0-470-51118-3*, 2008.
- [32] N. Bloembergen et al. Relaxation effects in nuclear magnetic resonance absorption. *Physical review*, 73(7):679, 1948.
- [33] P. C. Lauterbur. Image formation by induced local interactions: examples employing nuclear magnetic resonance. *nature*, 242(5394):190–191, 1973.
- [34] J. M. Dawson. *Paul Lauterbur and the Invention of MRI*. MIT Press, 2013.
- [35] P. Mansfield. Multi-planar image formation using nmr spin echoes. *Journal of Physics C: Solid State Physics*, 10(3):L55, 1977.
- [36] R. V. Damadian et al. Nmr in cancer: Xvi. fonar image of the live human body. *Physiol. Chem. Phys*, 9:97 - 100,, 1977.
- [37] E. J. Blink. Basic mri physics. *9:1-64*, 2004.
- [38] V. D. Schepkin et al. In vivo magnetic resonance imaging of sodium and diffusion in rat glioma at 21.1 t. *Magnetic resonance in medicine*, 67(4):1159–1166, 2012.
- [39] ASG Superconductors. Asg superconductors paramed mri unit. 2019.
- [40] P. Keller. Technologies for precision field mapping. *MetroLab Instruments, Geneva*, 2006.
- [41] J. C. Lindon et al. *Encyclopedia of spectroscopy and spectrometry*. Academic Press, 2016.
- [42] mriquestions. Slice selection. <http://mriquestions.com/slice-selective-excitation.html>.
- [43] C. M. Collins. Fundamentals of mri fields and basic pulse sequences. In *Electromagnetics in Magnetic Resonance Imaging*. Morgan & Claypool Publishers, 2016.
- [44] M. Hammer. Mri physics: Spatial localization. <http://xrayphysics.com/spatial.html#phase>, 2013.
- [45] L Wald et al. Mr image encoding.
- [46] R. B. Buxton et al. Contrast in rapid mr imaging: T1- and t2-weighted imaging. *Journal of computer assisted tomography*, 11(1):7–16, 1987.
- [47] E. M. Delfaut et al. Fat suppression in mr imaging: techniques and pitfalls. *Radiographics*, 19(2):373–382, 1999.
- [48] R Kieret al. Value of lipid-and water-suppression mr images in distinguishing between blood and lipid within ovarian masses. *AJR. American journal of roentgenology*, 158(2):321–325, 1992.



- [49] R. Bammer. Basic principles of diffusion-weighted imaging. *European journal of radiology*, 45(3):169–184, 2003.
- [50] M. Takeuchi et al. Diffusion-weighted magnetic resonance imaging of ovarian tumors: differentiation of benign and malignant solid components of ovarian masses. *Journal of computer assisted tomography*, 34(2):173–176, 2010.
- [51] S. Warach et al. Fast magnetic resonance diffusion-weighted imaging of acute human stroke. *Neurology*, 42(9):1717–1717, 1992.
- [52] H. Carr et al. Effects of diffusion on free precession in nuclear magnetic resonance experiments. *Physical review*, 94(3):630, 1954.
- [53] B. A. Jung et al. Spin echo magnetic resonance imaging. *Journal of Magnetic Resonance Imaging*, 37(4):805–817, 2013.
- [54] mriquestions. Predicting nuclear spin (i). <http://mriquestions.com/predict-nuclear-spin-i.html>.
- [55] Magnetic resonance - technology information portal. *Member of SoftWays' Medical Imaging Group*, 2016.
- [56] F. Fazekas et al. Histopathologic analysis of foci of signal loss on gradient-echo t2\*-weighted mr images in patients with spontaneous intracerebral hemorrhage: evidence of microangiopathy-related microbleeds. *American Journal of Neuroradiology*, 20(4):637–642, 1999.
- [57] L. Østergaard et al. High resolution measurement of cerebral blood flow using intravascular tracer bolus passages. part i: Mathematical approach and statistical analysis. *Magnetic resonance in medicine*, 36(5):715–725, 1996.
- [58] M. R. Prince. Gadolinium-enhanced mr aortography. *Radiology*, 191(1):155–164, 1994.
- [59] Hyperphysics. Nuclear spin polarization.
- [60] J. Rauschenberg et al. Multicenter study of subjective acceptance during magnetic resonance imaging at 7 and 9.4 t. *Investigative radiology*, 49(5):249–259, 2014.
- [61] M. Hirsch et al. Brute-force hyperpolarization for nmr and mri. *Journal of the American Chemical Society*, 137(26):8428–8434, 2015.
- [62] P. Nikolaou et al. Nmr hyperpolarization techniques for biomedicine. *Chemistry—A European Journal*, 21(8):3156–3166, 2015.
- [63] R. Green et al. The theory and practice of hyperpolarization in magnetic resonance using parahydrogen. *Progress in nuclear magnetic resonance spectroscopy*, (67):1–48, 2012.
- [64] S. Duckett et al. Parahydrogen-enhanced nmr spectroscopic methods: A chemical perspective. *eMagRes*, 2007.

- [65] T. Gentile et al. Comparison of metastability-exchange optical pumping sources. *JOSA B*, 20(10):2068–2074, 2003.
- [66] T. Gentile et al. Demonstration of a compact compressor for application of metastability-exchange optical pumping of  $^3\text{He}$  to human lung imaging. *Magnetic Resonance in Medicine: An Official Journal of the International Society for Magnetic Resonance in Medicine*, 43(2):290–294, 2000.
- [67] M. L. Hirsch et al. Brute-force hyperpolarization for nmr and mri. *Journal of the American Chemical Society*, 137(26):8428–8434, 2015.
- [68] S. J. Nelson et al. Metabolic imaging of patients with prostate cancer using hyperpolarized  $[1-^{13}\text{C}]$  pyruvate. *Science Translational Medicine*, 5(198):108, 2013.
- [69] A. W. Overhauser et al. Polarization of nuclei in metals. *Phys. Rev.*, 92(411), 1953.
- [70] U. L. Gunther et al. Dynamic nuclear hyperpolarization in liquids. *Top Curr Chem*, 335:23–70, 2011.
- [71] S. Kozerke. Dissolution dnp. <https://ssnmr.ethz.ch/research/DNP.html>, 2019.
- [72] S. B. Duckett et al. Application of parahydrogen induced polarization techniques in nmr spectroscopy and imaging. *Accounts of Chemical Research*, 45(8):1247–1257, 2012.
- [73] B. Goodson et al. The physics of hyperpolarized gas mri. *Hyperpolarized and Inert Gas MRI*, pages 23–46, 2017.
- [74] C. R. Bowers et al. Parahydrogen and synthesis allow dramatically enhanced nuclear alignment. *Journal of the American Chemical Society*, 109(18):5541–5542, 1987.
- [75] D Barskiy. Parahydrogen. <https://danilabarskiy.com/2018/01/21/parahydrogen/>, 2018.
- [76] Parahydrogen Induced Polarization Studies Using a Continuous-Flow Homogeneous Hydrogenation Reactor. D. schulman et al. 2014.
- [77] S. Kadlecik et al. A simple and low-cost device for generating hyperpolarized contrast agents using parahydrogen. *NMR in Biomedicine*, 24(8):933–942, 2011.
- [78] R. A. Green et al. The theory and practice of hyperpolarization in magnetic resonance using parahydrogen. *Prog Nucl Magn Reson Spectrosc.*, 67:1–48, 2012.
- [79] R. W. Adams et al. Reversible interactions with para-hydrogen enhance nmr sensitivity by polarization transfer. *Science*, 323(5922):1708–1711, 2009.
- [80] P. J. Rayner et al. Signal amplification by reversible exchange (sabre) from discovery to diagnosis. *From Discovery to Diagnosis. Angewandte Chemie International Edition*, pages 6742–6753, 2018.

- [81] Anand et al Manoharan. Achieving biocompatible sabre: an in vitro cytotoxicity study. *ChemMedChem*, 13(4):352–359, 2018.
- [82] B. Kidd et al. Facile removal of homogeneous sabre catalysts for purifying hyperpolarized metronidazole, a potential hypoxia sensor. *J. Phys. Chem.*, 122(29):16848–16852, 2018.
- [83] M. Leduc et al. Étude par pompage optique de l'échange de métastabilité dans le néon. *Journal de Physique*, 38(6):609–622, 1977.
- [84] T. Dohnalik et al. Spectroscopic issues in optical polarization of  $^3\text{He}$  gas for magnetic resonance imaging of human lungs. *The European Physical Journal Special Topics*, 222(9):2103–2118, 2013.
- [85] T. R. Gentil et al. Polarized  $^3\text{He}$  spin filters in neutron scattering. *Physica B: Condensed Matter*, 356(1-4):96–102, 2005.
- [86] D. Steck. Rubidium 87 d line data, 2001.
- [87] I. C. Ruset. Hyperpolarized  $^{129}\text{Xe}$  production and applications. *PhD Thesis, University of New Hampshire*, 1999.
- [88] N. Whiting et al. Interdependence of in-cell xenon density and temperature during  $\text{Rb}/\text{Xe}$ - $^{129}\text{Xe}$  spin-exchange optical pumping using vhg-narrowed laser diode arrays. *Journal of Magnetic Resonance*, vol. 208, pp. 298–304, 2011.
- [89] K. Kluttz et al. Pressure broadening and frequency shift of the d 1 and d 2 lines of  $\text{Rb}$  and  $\text{K}$  in the presence of  $^3\text{He}$  and  $\text{n}^2$ . *Physical Review A*, 87(3):032516, 2013.
- [90] M.S. Freeman. *The Efficiency Limits of Spin Exchange Optical Pumping Methods of  $^{129}\text{Xe}$  Hyperpolarization: Implications for in vivo MRI Applications*. PhD thesis, Duke University, 2015.
- [91] Engineering ToolBox. Stp standard temperature and pressure & ntp normal temperature and pressure. [https://www.engineeringtoolbox.com/stp-standard-ntp-normal-air-d\\_772.html](https://www.engineeringtoolbox.com/stp-standard-ntp-normal-air-d_772.html), 2004.
- [92] Polarean. Polarean 9800 xenon polarizer performance optimization. [http://www.polarean.com/pdf/9800\\_Xenon\\_Polarizer\\_Advanced\\_Training.pdf](http://www.polarean.com/pdf/9800_Xenon_Polarizer_Advanced_Training.pdf), 2019.
- [93] H. Hartmann. Notes on the theory of sublimation. *The psychoanalytic study of the child*, 10(1):9–29, 1955.
- [94] D. Lide. *Crc handbook of chemistry and physics*. volume 85. CRC press, 2004.
- [95] Hyperfine structure of rubidium. *Brown University*, Phys 1560 & 2010, 2010.
- [96] Hiroto et al Hatabu.  $T_2^*$  and proton density measurement of normal human lung parenchyma using submillisecond echo time gradient echo magnetic resonance imaging. *European journal of radiology*, 29(3):245–252, 1999.

- [97] CJ et al Bergin. Lung parenchyma: magnetic susceptibility in mr imaging. *Radiology*, 180(3):845–848, 1991.
- [98] MS et al Albert. Biological magnetic resonance imaging using laser-polarized 129xe. *Nature*, 370(6486):199, 1994.
- [99] John P et al Mugler III. Mr imaging and spectroscopy using hyperpolarized 129xe gas: preliminary human results. *Magnetic resonance in medicine*, 37(6):809–815, 1997.
- [100] J. P. Mugler et al. Mr imaging and spectroscopy using hyperpolarized 129xe gas: preliminary human results. *Magnetic resonance in medicine*, 37(6):809–815, 1997.
- [101] RR et al Kennedy. Anaesthesia and the ‘inert’gases with special reference to xenon. *Anaesthesia and intensive care*, 20(1):66–70, 1992.
- [102] G. A. Johnson et al. Dynamics of magnetization in hyperpolarized gas mri of the lung. *Magnetic resonance in medicine*, 38(1):66–71, 1997.
- [103] Sally Adee. Physics projects deflate for lack of helium-3. *IEEE Spectrum*, 47(9):16–17, 2010.
- [104] Lilburn et al. Perspectives of hyperpolarized noble gas mri beyond 3he. *Journal of magnetic resonance*, 229:173–186, 2013.
- [105] J. E. Roos et al. Hyperpolarized gas mr imaging: technique and applications. *Magnetic Resonance Imaging Clinics*, 23(2):217–229, 2015.
- [106] Institute of Chemistry of the Hebrew University. Chemical shift referencing. 2013.
- [107] Sarah et al. Svenningsen. Hyperpolarized 3he and 129xe mri: differences in asthma before bronchodilation. *Journal of Magnetic Resonance Imaging*, 38(6):1521–1530, 2013.
- [108] D. Ozkan. Hyperpolarized 129xe magnetic resonance imaging of radiation-induced lung injury. 2015.
- [109] Polarean. Image acquisition. [http://www.polarean.com/image\\_acquisition.html](http://www.polarean.com/image_acquisition.html).
- [110] John P et al Mugler. Image-based measurement of  $t_2^*$  for dissolved-phase xe129 in the human lung. In *Proc Int Soc Magn Reson Med*, 2012.
- [111] S. Kruge et al. Functional imaging of the lungs with gas agents. *Journal of Magnetic Resonance Imaging*, 43(2):295–315, 2016.
- [112] Rayleigh Lord. On the light from the sky, its polarization and colour. *Phil Mag*, 41:274, 1871.
- [113] C. V. Raman. A new radiation. *J. Phys*, 2:387-398, 1928.
- [114] Nano Photon. What is raman spectrometry? <http://www.nanophoton.net/raman/raman-spectroscopy.html>, 2016.

- [115] J. Birchall et al. Using raman spectroscopy to improve hyperpolarized noble gas production for clinical lung imaging techniques. *Book: Raman Spectroscopy and Applications*, 2017.
- [116] A. Compaan et al. Rotational raman scattering in the instructional laboratory. *American Journal of Physics*, 62(7):639–645, 1994.
- [117] R. S. Hickman. Rotational temperature measurement in nitrogen using raman spectroscopy. *Review of Scientific Instruments*, 43:769, 1972.
- [118] D. Walter et al. Energy transport in high-density spin-exchange optical pumping cells. *Physical review letters*, 86(15):3264, 2001.
- [119] M. S. Rosen et al. Polarized  $^{129}\text{Xe}$  optical pumping/spin exchange and delivery system for magnetic resonance spectroscopy and imaging studies. *Review of Scientific Instruments*, 70:1546–1552, 1999.
- [120] Wavelength electronics. Optimizing thermoelectric temperature control systems. [http://hexagon.physics.wisc.edu/research/technical/%20info/wavelength\\_tecguide.pdf](http://hexagon.physics.wisc.edu/research/technical/%20info/wavelength_tecguide.pdf), 1995.
- [121] H. L. Newton. Hyperpolarised xenon production via rb and cs optical pumping applied to functional lung mri. [http://eprints.nottingham.ac.uk/14339/1/HNewton\\_PhD\\_2014\\_Final.pdf](http://eprints.nottingham.ac.uk/14339/1/HNewton_PhD_2014_Final.pdf), 2014.
- [122] H. Newton et al. Comparative study of in situ  $n = 2$  rotational raman spectroscopy methods for probing energy thermalisation processes during spin-exchange optical pumping. *Applied Physics B*, 115(2):167–172, 2014.
- [123] K. Hamada et al. Raman microscopy for dynamic molecular imaging of living cells. *Journal of biomedical optics*, 13(4):044027, 2008.
- [124] G. Placzek. *The rayleigh and raman scattering*, volume 526. Lawrence Radiation Laboratory, 1959.
- [125] W. Hardiman et al. An automated nmr acquisition system for measuring the polarisation of  $^{129}\text{Xe}$  during spin-exchange optical-pumping. *University of Nottingham, School of Physics and Astronomy*, 2018.
- [126] R. R. Price et al. Quality assurance methods and phantoms for magnetic resonance imaging: report of aapm nuclear magnetic resonance task group no. 1. *Medical physics*, 17(2):287–295, 1990.
- [127] Mark Winter. Rubidium: reactions of elements. <https://www.webelements.com/rubidium/chemistry.html>.
- [128] Rubidium oxide. <https://www.americanelements.com/rubidium-oxide-18088-11-4>, 2020.
- [129] D. Kennedy et al. An optimized microfabricated platform for the optical generation and detection of hyperpolarized  $^{129}\text{Xe}$ . *Scientific reports*, 7:43994, 2017.
- [130] Welz et al B. *Atomic absorption spectrometry*. John Wiley & Sons, 2008.

- [131] ESPI Metals. Rubidium. <https://www.espimetals.com/index.php/msds/236-Rubidium>, 2015.
- [132] M. Antonacc et al. Depolarization of nuclear spin polarized  $^{129}\text{Xe}$  gas by dark rubidium during spin-exchange optical pumping. *Journal of Magnetic Resonance*, 279:60–67, 2017.
- [133] I. Anderson. Vapour pressure and boiling. *Anaesthesia*, 69(4):396–398, 2014.
- [134] Ch. Paganelli et al. Diffusion in the gas phase: the effects of ambient pressure and gas composition. *Respiration physiology*, 25(3):247–258, 1975.
- [135] H. L Newton et al. Effects of gascomposition on optical pumping and energy transport for hyperpolarized  $^{129}\text{Xe}$  usingin situ raman spectroscopy and nmr. *Poster session presented at: Exotica, 54th Experimental Nuclear Magnetic Resonance Conference*, 2013.
- [136] J. Birchall et al. Helium-rich mixtures for improved batch-mode clinical-scale spin-exchange optical pumping of xenon-129. *Analytical Chemistry*, 2020.
- [137] Y. Jau et al. High-field measurement of the  $^{129}\text{Xe}$  spin-exchange rate due to binary collisions. *Physical review A*, 66(5):052710, 2002.
- [138] J. Singh et al. Alkali metal vapor pressures & number densities for hybrid spin exchange optical pumping. *University of Virginia*, 2008.
- [139] QPC. 795nm,  $\delta\lambda < 0.25\text{nm}$ , 180w diode laser with circularly polarized 2" diameter uniform beam. <https://www.qpclasers.com/product/795nm-spectrally-narrowed-180w-1000um-fiber-coupled-module/>, 2020.
- [140] Dilas. 794.7nm, 400 $\mu\text{m}$ , conduction-cooled, narrow linewidth, fiber-coupled, multi-bar module. [https://www.laserdiodesource.com/files/pdfs/laserdiodesource\\_com/product-1089/795nm\\_80W\\_fiber\\_coupled\\_module\\_DILAS-1416533435.pdf](https://www.laserdiodesource.com/files/pdfs/laserdiodesource_com/product-1089/795nm_80W_fiber_coupled_module_DILAS-1416533435.pdf), 2020.
- [141] QPC. 795nm (0.25nm fwhm) 75w 1000um fiber coupled module. <https://www.qpclasers.com/product/795nm-0-25nm-fwhm-75w-1000um-fiber-coupled-module/>, 2020.
- [142] Y. Jau et al. Measurement of  $^{129}\text{Xe}$ - $^{133}\text{Cs}$  binary spin-exchange rate coefficient. *Physical Review A*, 69(6):061401, 2004.
- [143] A. H. Couture et al. Pressure shifts and broadening of the  $^{133}\text{Cs}$   $d_1$  and  $d_2$  lines by  $^4\text{He}$ ,  $^3\text{He}$ , and  $^{129}\text{Xe}$  at densities used for optical pumping and spin exchange polarization. *Journal of Applied Physics*, 104(9):094912, 2008.
- [144] K. L. Harris. *Cesium*. Department of the Interior, Bureau of Mines, 1979.
- [145] ESPI Metals. Cesium. <https://www.espimetals.com/index.php/msds/122-Cesium>, 2015.

- [146] ESPI Metals. Material safety data sheet rubidium hydroxide, 99.9%, 50 wt% solution in water. <https://fscimage.fishersci.com/msds/80625.htm>, 2008.
- [147] ESPI Metals. Cesium hydroxide. <https://espimetals.com/index.php/msds/515-Cesium>, 2015.
- [148] J. Birchall. Characterisation of rb and cs spin-exchange optical pumping for application to hyperpolarised 129xe functional lung mri. *PhD Thesis, University of Nottingham*, 2017.
- [149] N. Whiting et al. Xe 129-cs ( $d_1$ ,  $d_2$ ) versus xe 129-rb ( $d_1$ ) spin-exchange optical pumping at high xenon densities using high-power laser diode arrays. *Physical review A*, 83(5):053428, 2011.
- [150] N. Whiting et al. Interdependence of in-cell xenon density and temperature during rb/129xe spin-exchange optical pumping using vhg-narrowed laser diode arrays. *Journal of Magnetic Resonance*, 208(2):298–304, 2011.
- [151] J. Skinner. Optimisation of xenon-rich stopped flow spin-exchange optical pumping for functional lung imaging. phd thesis, university of nottingham. *Nottingham ePrints service*, 2017.
- [152] Polarean. Polarean 9800 129xe hyperpolarizer. [http://www.polarean.com/129Xe\\_hyperpolarizer.html](http://www.polarean.com/129Xe_hyperpolarizer.html), 2020.
- [153] N. Kuzma et al. Fast nuclear spin relaxation in hyperpolarized solid 129 xe. *Physical review letters*, 88(14):147602, 2002.
- [154] G. Norquay et al. Optimized production of hyperpolarized xe-129 at 2 bars for in vivo lung magnetic resonance imaging. *Journal of Applied Physics*, vol. 113, no. 4, p. 044908, 2013.
- [155] P. Nikolaou et al. Generation of laser-polarized xenon using fiber-coupled laser-diode arrays narrowed with integrated volume holographic gratings. *Journal of Magnetic Resonance*, 197(2):249–254, 2009.
- [156] M.S Freeman et al. Characterizing and modeling the efficiency limits in large-scale production of hyperpolarized xe 129. *Physical Review A*, 90(2):023406, 2014.
- [157] N. Whiting et al. Using frequency-narrowed tunable laser diode arrays with integrated volume holographic gratings for spin-exchange optical pumping at high resonant fluxes and xenon densities. *Applied Physics B, Volume 106, Issue 4, pp 775–788*, 2012.
- [158] P. Nikolaou et al. Xena: An automated ‘open-source’ 129xe hyperpolarizer for clinical use. *Magn Reson Imaging. Jun; 32(5): 541–550.*, 2014.
- [159] B. Fry et al. Processing. <https://processing.org/>, 2020.
- [160] Patz et al. S. Xenon septal uptake. In *Hyperpolarized Xenon-129 Magnetic Resonance*, pages 336–364. 2015.

- [161] P. Nikolaou et al. A 3d-printed high power nuclear spin polarizer. *Journal of the American Chemical Society*, vol. 136, no. 4, pp. 1636–1642, 2014.
- [162] F. W. Baumann et al. Geometrical fidelity of consumer grade 3d printers. *Proceedings of CAD*, pages 127–130, 2016.
- [163] A. J. Kovacs et al. La contraction isotherme du volume des polymères amorphes. *Journal of Polymer Science - Volume 30, Issue 121 - July*, 1958.
- [164] MatWeb. Deflection temperature testing of plastics. <http://www.matweb.com/reference/deflection-temperature.aspx>.
- [165] Y. Ohnuma et al. Theory of the spin peltier effect. *Physical Review B*, 96(13):134412, 2017.
- [166] J. R. Barker. An improved three-coil system for producing a uniform magnetic field. *Journal of Scientific Instruments*, 27(7):197, 1950.
- [167] Swagelok. Vcr fittings metal gasket face seal fittings. <https://www.swagelok.com/downloads/webcatalogs/en/MS-01-24.pdf>, 2017.
- [168] Separation Science HPLC Solutions. Peek tubing – benefits and liabilities. <https://blog.sepscience.com/liquidchromatography/hplc-solutions-9-peek-tubing-benefits-and-liabilities>.
- [169] Kenwood. Regulated dc powersupplies:pds series. <https://testequipmentconnection.com/specs/KENWOODPDS60-12.PDF>.
- [170] Sorensen. Xg and xtr family programmable dc power supply operating manual. <http://www.sorensen.com/products/XTR/downloads/XG/2017001500850/20User/20Manual/20M370430-01/20Rev/20A.pdf>.
- [171] J. Lisser et al. High-speed high-precision programmable magnet power supply for a wide range of magnet time constant. *IEEE Trans. Nucl. Sci.*, vol. NS-28, no. 3, pp. 2859-2861, June, 1981.
- [172] Oven industries electronic control solutions. 5r7-001 thermoelectric controller. <https://www.ovenind.com/pdf/datasheets/DS-5R7-001.pdf>.
- [173] Arduino. Arduino mega 2560. <http://www.mantech.co.za/datasheets/products/A000047.pdf>, 2010.
- [174] Arduino.cc. Serial communication. <https://www.arduino.cc/reference/en/language/functions/communication/serial/>, 2019.
- [175] E. Stephens. Microchannel cooling ups power capacity for laser-diode bars. <https://www.laserfocusworld.com/lasers-sources/article/16546753/microchannel-cooling-ups-power-capacity-for-laserdiode-bars>, 2006.
- [176] M. Goetz. Thermal management of laser diodes. <https://www.aerodefensetech.com/component/content/article/adt/features/articles/25247>, 2016.



- [177] Ocean Optics. Hr4000 and hr4000cg-uv-nir series high-resolution fiber optic spectrometers hr4000 / hr4000cg-uv-nir: Installation and operation manual document number 210-00000-000-02-1006. [https://www.usna.edu/Users/physics/vanhoy/\\_files/SP425/LabDocs/Ocean\%20Optics\%202000/SpectraSuite/070131\\_1347\%20R/documentation/Spectrometers\%20and\%20Software/hr4000.pdf](https://www.usna.edu/Users/physics/vanhoy/_files/SP425/LabDocs/Ocean\%20Optics\%202000/SpectraSuite/070131_1347\%20R/documentation/Spectrometers\%20and\%20Software/hr4000.pdf), 2006.
- [178] OceanOptics. Oceanview 1.6.7. <https://oceanoptics.com/product/oceanview/>, 2019.
- [179] D. F. Swinehart et al. The beer-lambert law. *Journal of chemical education*, 39(7):333, 1962.
- [180] M. He et al. Dose and pulse sequence considerations for hyperpolarized  $^{129}\text{Xe}$  ventilation mri. *Magnetic resonance imaging*, 33(7):877–885, 2015.
- [181] P. Nikolaou et al. Temperature-ramped  $^{129}\text{Xe}$  spin-exchange optical pumping. *Analytical chemistry*, 86(16):8206–8212, 2014.
- [182] J. Birchall et al. Pilot multi-site quality assurance study of batch-mode clinical-scale automated xenon- $^{129}$  hyperpolarizers. *Journal of Magnetic Resonance*, page 106755, 2020.
- [183] A Colin Cameron and Frank AG Windmeijer. An r-squared measure of goodness of fit for some common nonlinear regression models. *Journal of econometrics*, 77(2):329–342, 1997.
- [184] M. J. Couch et al. A two-center analysis of hyperpolarized  $^{129}\text{Xe}$  lung mri in stable pediatric cystic fibrosis: potential as a biomarker for multi-site trials. *Journal of Cystic Fibrosis*, 18(5):728–733, 2019.
- [185] R. P. Thomen et al. Regional structure-function in cystic fibrosis lung disease using hyperpolarized  $^{129}\text{Xe}$  and ultrashort echo magnetic resonance imaging. *American Journal of Respiratory and Critical Care Medicine*, (ja), 2020.
- [186] L. Smith et al.  $^1\text{H}$  and  $^{129}\text{Xe}$  mri to detect functional and structural lung disease in sub-clinical cystic fibrosis, 2019.
- [187] K. Kadoya et al. Viscosity and thermal conductivity of dry air in the gaseous phase. *Journal of physical and chemical reference data*, 14(4):947–970, 1985.
- [188] Nicolae Lobontiu. *System dynamics for engineering students: Concepts and applications*. Academic Press, 2017.
- [189] J. R. Birchall et al. Batch-mode clinical-scale optical hyperpolarization of xenon- $^{129}$  using an aluminum jacket with rapid temperature ramping. *Analytical Chemistry*, 92(6):4309–4316, 2020.
- [190] H. D. Young et al. *University physics*, volume 9. Addison-Wesley Reading, MA, 1996.

- [191] L. O. Gostin et al. Governmental public health powers during the covid-19 pandemic: Stay-at-home orders, business closures, and travel restrictions. *JAMA*, 2020.
- [192] H. Li et al. Next-generation high-power, high-efficiency diode lasers at spectra-physics. In *Semiconductor Lasers and Applications III*, volume 6824, page 68240S. International Society for Optics and Photonics, 2008.
- [193] A. Petersen et al. Tunable, high power, narrow band emission from a volume grating-controlled diode bar. In *Advanced Solid-State Photonics*, page MD2. Optical Society of America, 2008.
- [194] A. Gourevitch et al. Continuous wave, 30 w laser-diode bar with 10 ghz linewidth for rb laser pumping. *Optics letters*, 33(7):702–704, 2008.
- [195] K. O’Donnell et al. A risk management solution designed to facilitate risk-based qualification, validation, and change control activities within gmp and pharmaceutical regulatory compliance environments in the eu, part i: fundamental principles, design criteria, outline of process. *Journal of GXP Compliance*, 10(4):12–26, 2006.
- [196] Polarean. Polarean 3777 129xe hyperpolarizer upgrade module. [http://www.polarean.com/pdf/3777\\_Xenon\\_Upgrade\\_Kit.pdf](http://www.polarean.com/pdf/3777_Xenon_Upgrade_Kit.pdf), 2019.
- [197] NuPure. The eliminator cag. <https://www.nupure.com/Pages/eliminatorCAG.htm>, 2010.
- [198] T. Meersmann et al. *Hyperpolarized xenon-129 magnetic resonance: concepts, production, techniques and applications*. Number 4. Royal Society of Chemistry, 2015.
- [199] A. Burant et al. Diffusion-mediated 129xe gas depolarization in magnetic field gradients during continuous-flow optical pumping. *Journal of Magnetic Resonance*, 273:124–129, 2016.
- [200] Fuji Electric. Instruction manual micro-controller x model: Pxr4. <https://www.coulton.com/res/IMPXRa.pdf>, 2019.
- [201] angstromsciences. Melting points of elements reference. <https://www.angstromsciences.com/melting-points-of-elements-reference>, 2019.
- [202] M. Gatzke et al. Extraordinarily slow nuclear spin relaxation in frozen laser-polarized xe 129. *Physical review letters*, 70(5):690, 1993.
- [203] Polarean. Polarean 2881 polarization measurement station. [http://www.polarean.com/pdf/2881\\_Polarization\\_Measurement\\_Station.pdf](http://www.polarean.com/pdf/2881_Polarization_Measurement_Station.pdf), 2019.
- [204] B. O’Sullivan et al. Assessment of repeatability of hyperpolarized gas mr ventilation functional imaging in cystic fibrosis. *Academic radiology*, 21(12):1524–1529, 2014.

- [205] Y. Shukla et al. Hyperpolarized  $^{129}\text{Xe}$  magnetic resonance imaging: tolerability in healthy volunteers and subjects with pulmonary disease. *Academic radiology*, 19(8):941–951, 2012.
- [206] B. Driehuys et al. Chronic obstructive pulmonary disease: safety and tolerability of hyperpolarized  $^{129}\text{Xe}$  mr imaging in healthy volunteers and patients. *Radiology*, 262(1):279–289, 2012.
- [207] L. Walkup et al. Feasibility, tolerability and safety of pediatric hyperpolarized  $^{129}\text{Xe}$  magnetic resonance imaging in healthy volunteers and children with cystic fibrosis. *Pediatric radiology*, 46(12):1651–1662, 2016.
- [208] M. Kirby et al. Hyperpolarized  $^3\text{He}$  and  $^{129}\text{Xe}$  mr imaging in healthy volunteers and patients with chronic obstructive pulmonary disease. *Radiology*, 265(2):600–610, 2012.
- [209] M. Koch et al. Comparison of hyperpolarized  $^3\text{He}$  and  $^{129}\text{Xe}$  mr imaging in patients with cystic fibrosis. In *A108. PATHOPHYSIOLOGY IN DIFFUSE PARENCHYMAL LUNG DISEASES*, pages A2567–A2567. American Thoracic Society, 2019.
- [210] M. Deppe et al. Susceptibility effects in hyperpolarized  $^3\text{He}$  lung mri at 1.5 t and 3t. *Journal of Magnetic Resonance Imaging: An Official Journal of the International Society for Magnetic Resonance in Medicine*, 30(2):418–423, 2009.
- [211] N. Stewart et al. Comparison of  $^3\text{He}$  and  $^{129}\text{Xe}$  mri for evaluation of lung microstructure and ventilation at 1.5 t. *Journal of magnetic resonance imaging*, 48(3):632–642, 2018.
- [212] NHS. Overview- cystic fibrosis. <https://www.nhs.uk/conditions/cystic-fibrosis/>, 2018.
- [213] World Health Organization. Genes and human diseases. <https://www.who.int/genomics/public/geneticdiseases/en/index2.html>CF, 2020.
- [214] R. Keogh et al. Up-to-date and projected estimates of survival for people with cystic fibrosis using baseline characteristics: A longitudinal study using uk patient registry data. *Journal of Cystic Fibrosis*, 17(2):218–227, 2018.
- [215] P. Koumellis et al. Quantitative analysis of regional airways obstruction using dynamic hyperpolarized  $^3\text{He}$  mri—preliminary results in children with cystic fibrosis. *Journal of Magnetic Resonance Imaging: An Official Journal of the International Society for Magnetic Resonance in Medicine*, 22(3):420–426, 2005.
- [216] C. McMahon et al. Hyperpolarized  $^3\text{He}$  helium magnetic resonance ventilation imaging of the lung in cystic fibrosis: comparison with high resolution ct and spirometry. *European radiology*, 16(11):2483–2490, 2006.
- [217] G. Paulin et al. Differences in hyperpolarized  $^3\text{He}$  ventilation imaging after 4 years in adults with cystic fibrosis. *Journal of Magnetic Resonance Imaging*, 41(6):1701–1707, 2015.

- [218] R. Thomen et al. Hyperpolarized  $^{129}\text{Xe}$  for investigation of mild cystic fibrosis lung disease in pediatric patients. *Journal of Cystic Fibrosis*, 16(2):275–282, 2017.
- [219] J. Rayment et al. Hyperpolarised  $^{129}\text{Xe}$  magnetic resonance imaging to monitor treatment response in children with cystic fibrosis. *European Respiratory Journal*, 53(5), 2019.
- [220] S. Hurd et al. Global strategy for the diagnosis, management, and prevention of chronic obstructive pulmonary disease gold executive summary. *AMERICAN JOURNAL OF RESPIRATORY AND CRITICAL CARE MEDICINE*, 176:532 - 555, 2016.
- [221] S. S. Kaushik et al. Diffusion-weighted hyperpolarized  $^{129}\text{Xe}$  mri in healthy volunteers and subjects with chronic obstructive pulmonary disease. *Magnetic resonance in medicine*, 65(4):1154–1165, 2011.
- [222] L. A. Myc et al. Beyond chronic bronchitis and emphysema: Characterization of a transcriptomically unique copd phenotype with hyperpolarized  $^{129}\text{Xe}$  mri. In *A98. PHENOTYPING COPD AND PREDICTING THE DISEASE PROGRESSION*, pages A2407–A2407. American Thoracic Society, 2019.
- [223] PK. Jeffery. Pathology of asthma. *British Medical Bulletin*, 48:23-39, 1992.
- [224] M. Masoli et al. The global burden of asthma: executive summary of the gina dissemination committee report. *Allergy*, 59:469-478, 2004.
- [225] M. He et al. Using hyperpolarized  $^{129}\text{Xe}$  mri to quantify the pulmonary ventilation distribution. *Academic radiology*, 23(12):1521–1531, 2016.
- [226] C. Hall et al. Bronchial thermoplasty effect on ventilation guided by hyperpolarized  $^{129}\text{Xe}$  mri in severe asthma, 2019.
- [227] TE. King Jr et al. Idiopathic pulmonary fibrosis. *Allergy*, 378:1949-1961, 2011.
- [228] B. Ley et al. Epidemiology of idiopathic pulmonary fibrosis. *Clin Epidemiol*, 5:483-492, 2013.
- [229] G. Raghu et al. Incidence and prevalence of idiopathic pulmonary fibrosis. *Respir Crit Care Med.*, 174:810 - 816, 2006.
- [230] S. S. Kaushik et al. Measuring diffusion limitation with a perfusion-limited gas—hyperpolarized  $^{129}\text{Xe}$  gas-transfer spectroscopy in patients with idiopathic pulmonary fibrosis. *Journal of applied physiology*, 117(6):577–585, 2014.
- [231] E. A. Bier et al. A protocol for quantifying cardiogenic oscillations in dynamic  $^{129}\text{Xe}$  gas exchange spectroscopy: The effects of idiopathic pulmonary fibrosis. *NMR in Biomedicine*, 32(1):e4029, 2019.
- [232] Public Health England. Deaths associated with neurological conditions in england: 2001 to 2014. 2018.

- [233] S. Chaha et al. Brain imaging using hyperpolarized  $^{129}\text{Xe}$  magnetic resonance imaging. In *Methods in enzymology*, volume 603, pages 305–320. Elsevier, 2018.
- [234] S.C. Feldman et al. The blood oxygen level–dependent functional mr imaging signal can be used to identify brain tumors and distinguish them from normal tissue. *American journal of neuroradiology*, 30(2):389–395, 2009.
- [235] www.nhlbi.nih.gov/. What is a stroke. *National Heart,Lung and Blood Institue*, 2014.
- [236] GA. Donnan et al. What is a stroke. *Stroke. Lancet*, 371:1612 - 1623, 2008.
- [237] D. Mozaffarian et al. Heart disease and stroke statistics 2016 update. *Circulation*, 133:447 - 454, 2016.
- [238] X. Zhou et al. Mri of stroke using hyperpolarized  $^{129}\text{Xe}$ . *NMR in Biomedicine*, 24(2):170–175, 2011.
- [239] M. R. Rao et al. Assessment of brain perfusion using hyperpolarized  $^{129}\text{Xe}$  mri in a subject with established stroke. *Journal of Magnetic Resonance Imaging*, 50(3):1002–1004, 2019.
- [240] Alzheimer’s Association. 2016 alzheimer’s disease facts and figures. *Alzheimer’s and Dementia*, 12:459 - 509,, 2016.
- [241] B. C. Dickerson et al. Alzheimer-signature mri biomarker predicts ad dementia in cognitively normal adults. *Neurology*, 76(16):1395–1402, 2011.
- [242] F. T. Hane et al. Inhaled xenon washout as a biomarker of alzheimer’s disease. *Diagnostics*, 8(2):41, 2018.
- [243] Mayo clinic staff. Chronic kidney disease. <https://www.mayoclinic.org/diseases-conditions/chronic-kidney-disease/symptoms-causes/syc-20354521>.
- [244] H. Wang et al. Global, regional, and national life expectancy, all-cause mortality, and cause-specific mortality for 249 causes of death, 1980–2015: a systematic analysis for the global burden of disease study 2015. *The lancet*, 388(10053):1459–1544, 2016.
- [245] W. Couseret al. The contribution of chronic kidney disease to the global burden of major noncommunicable diseases. *Kidney international*, 80(12):1258–1270, 2011.
- [246] J. Cerda et al. International society of nephrology’s 0by25 initiative for acute kidney injury (zero preventable deaths by 2025): a human rights case for nephrology. *Lancet*, 385(9987):2616–43, 2015.
- [247] T. Liyanage et al. Worldwide access to treatment for end-stage kidney disease: a systematic review. *The Lancet*, 385(9981):1975–1982, 2015.

- [248] G. Norquay et al. Relaxation and exchange dynamics of hyperpolarized  $^{129}\text{Xe}$  in human blood. *74*(2):303–311, 2015.
- [249] D. Elizabeth. Effect of body position on pulmonary function. *Physical Therapy*, 65(5):613–618, 1985.
- [250] DAVID W Hudgel, RICHARD J Martin, MELVIN Capehart, BARBARA Johnson, and PATRICIA Hill. Contribution of hypoventilation to sleep oxygen desaturation in chronic obstructive pulmonary disease. *Journal of Applied Physiology*, 55(3):669–677, 1983.
- [251] S. Sarji et al. Failed magnetic resonance imaging examinations due to claustrophobia. *Australasian radiology*, 42(4):293–295, 1998.
- [252] P. Joseph et al. Principles of image formation. In *Magnetic resonance imaging of the brain and spine*. 1991.
- [253] J. Parra-Robles et al. Theoretical signal-to-noise ratio and spatial resolution dependence on the magnetic field strength for hyperpolarized noble gas magnetic resonance imaging of human lungs. *Medical physics*, 32(1):221–229, 2005.
- [254] F. Reid et al. (ab) normal saline and physiological hartmann’s solution: a randomized double-blind crossover study. *Clinical science*, 104(1):17–24, 2003.
- [255] MR-tips. Coil loading. <https://www.mr-tip.com/serve1.php?type=ab1&db=Coil\%20Loading>, 2020.
- [256] J. Harkin. Development of upright, multimodal, respiratory mri. *Nottingham eTheses*, 2020.
- [257] T. L. Peck et al. Design and analysis of microcoils for nmr microscopy. *Journal of Magnetic Resonance, Series B*, 108(2):114–124, 1995.
- [258] K. W. Miller et al. Xenon nmr: chemical shifts of a general anesthetic in common solvents, proteins, and membranes. *Proceedings of the National Academy of Sciences*, 78(8):4946–4949, 1981.
- [259] C. Jameson. An empirical chemical shielding function for interacting atoms from direct inversion of nmr data. *The Journal of Chemical Physics*, 63(12):5296–5301, 1975.
- [260] A. Venkatesh et al. Temperature measurement using the  $^{129}\text{Xe}$  chemical shift. *ISMRM*, 2001.
- [261] P. Peuravaara et al. Chemical shift extremum of  $^{129}\text{Xe}$  (aq) reveals details of hydrophobic solvation. *Scientific reports*, 8(1):1–11, 2018.
- [262] A. Kantola et al. Direct magnetic-field dependence of nmr chemical shift. *Physical Chemistry Chemical Physics*, 22(16):8485–8490, 2020.
- [263] P. Inglese et al. 3 factors affecting extra-virgin olive oil composition. *Horticultural reviews*, 38:83, 2011.

- [264] E. Woolley. Production of hyperpolarised  $^{129}\text{Xe}$  for nmr spectroscopy and imaging. *Nottingham eTheses*, 2008.
- [265] A Salces et al. *Quality assessment of olive oil by  $^1\text{H-NMR}$  fingerprinting*. INTECH Open Access Publisher, 2012.
- [266] J. Harwood et al. *Handbook of olive oil: Analysis and properties*. Springer, 2000.
- [267] L. Mannina et al. High resolution nuclear magnetic resonance: from chemical structure to food authenticity. *Grasas y Aceites*, 53(1):22–33, 2002.
- [268] A. Sacco et al. Characterization of italian olive oils based on analytical and nuclear magnetic resonance determinations. *Journal of the American Oil Chemists' Society*, 77(6):619–625, 2000.
- [269] R. M. Alonso-Salces et al. Multivariate analysis of nmr fingerprint of the unsaponifiable fraction of virgin olive oils for authentication purposes. *Food Chemistry*, 118(4):956–965, 2010.
- [270] M. Zou et al. Rapid authentication of olive oil adulteration by raman spectrometry. *Journal of agricultural and food chemistry*, 57(14):6001–6006, 2009.
- [271] V. Denolin et al. New insights into the mechanisms of signal formation in rf-spoiled gradient echo sequences. *Magnetic Resonance in Medicine: An Official Journal of the International Society for Magnetic Resonance in Medicine*, 54(4):937–954, 2005.
- [272] W. R. Nitz et al. Contrast mechanisms in mr imaging. *European radiology*, 9(6):1032–1046, 1999.
- [273] Y Zur et al. Spoiling of transverse magnetization in steady-state sequences. *Magnetic resonance in medicine*, 21(2):251–263, 1991.
- [274] M. Wood et al. Optimization of spoiler gradients in flash mri. *Magnetic resonance imaging*, 5(6):455–463, 1987.
- [275] J. Zhong et al. Fast determination of flip angle and  $T_1$  in hyperpolarized gas mri during a single breath-hold. *Scientific reports*, 6:25854, 2016.
- [276] H. Deng et al. Constant-variable flip angles for hyperpolarized media mri. *Journal of Magnetic Resonance*, 263:92–100, 2016.
- [277] B. Gruber et al. Rf coils: A practical guide for nonphysicists. *Journal of magnetic resonance imaging*, 48(3):590–604, 2018.
- [278] R. K. Cacak et al. Magnetic field uniformity around near-helmholtz coil configurations. *Review of Scientific Instruments*, 40(11):1468–1470, 1969.
- [279] A. Kumar et al. Optimized quadrature surface coil designs. *Magnetic Resonance Materials in Physics, Biology and Medicine*, 21(1-2):41, 2008.
- [280] Pulseteq. Pulseteq project 7159 – xenon /  $^1\text{H}$  coil for the lungs for hyperpolarised mri model mnc4-xe + mnc2-1h - lf summary description (feb 2020). pages 1–4, 2020.

- [281] Magnetic Resonance Technology Information Portal. Specific absorption rate. <https://www.mr-tip.com/serve1.php?type=db1dbs=Specific%20Absorption%20Rate:text=MRI%20%2D%20Specific%20Absorption%20R>
- [282] GE Healthcare. Signa hdxt 1.5t. <http://www.g-mr.com/pdf/ExciteHDxt.pdf>, 2008.
- [283] S. Hardy. Study of hyperpolarised 3he mri diffusion on asthma and cystic fibrosis, and development of hyperpolarised 129xe mri lung imaging. phd thesis, university of nottingham. *Nottingham eTheses*, 2016.
- [284] J. Thorpe. Lung mechanics and hyperpolarised gas mri. *Nottingham eTheses*, 2018.
- [285] S. Safavi. Magnetic resonance imaging in respiratory medicine. *Nottingham eTheses*, 2019.
- [286] A Farag et al. Unshielded and asymmetric rf transmit coil for hyperpolarized 129xe human lung imaging at 3.0 t. In *Proceedings of the 20th Annual Meeting of ISMRM, Melbourne, Australia*, page 1233, 2012.
- [287] D. F. Doty et al. Practical aspects of birdcage coils. *Journal of magnetic resonance*, 138(1):144–154, 1999.
- [288] T. Liebig et al. openems—a free and open source equivalent-circuit (ec) fdtd simulation platform supporting cylindrical coordinates suitable for the analysis of traveling wave mri applications. *International Journal of Numerical Modelling: Electronic Networks, Devices and Fields*, 26(6):680–696, 2013.
- [289] Z. I. Cleveland et al. Hyperpolarized 129xe mr imaging of alveolar gas uptake in humans. *PloS one*, 5(8), 2010.
- [290] M. Chen et al. Delayed ventilation assessment using fast dynamic hyperpolarised xenon-129 magnetic resonance imaging. *European radiology*, 30(2):1145–1155, 2020.
- [291] E. Candès et al. Robust uncertainty principles: Exact signal reconstruction from highly incomplete frequency information. *IEEE Transactions on information theory*, 52(2):489–509, 2006.
- [292] D. Donoho. Compressed sensing. *IEEE Transactions on information theory*, 52(4):1289–1306, 2006.
- [293] S. Ajraoui et al. Compressed sensing in hyperpolarized 3he lung mri. *Magnetic Resonance in Medicine: An Official Journal of the International Society for Magnetic Resonance in Medicine*, 63(4):1059–1069, 2010.
- [294] H. Zhang et al. Lung morphometry using hyperpolarized 129xe multi-b diffusion mri with compressed sensing in healthy subjects and patients with copd. *Medical physics*, 45(7):3097–3108, 2018.
- [295] R. Ehman et al. Magnetic resonance imaging with respiratory gating: techniques and advantages. *American journal of Roentgenology*, 143(6):1175–1182, 1984.



- [296] M. Freeman et al. Enabling hyperpolarized  $^{129}\text{Xe}$  mr spectroscopy and imaging of pulmonary gas transfer to the red blood cells in transgenic mice expressing human hemoglobin. *Magnetic resonance in medicine*, 70(5):1192–1199, 2013.

# Appendix A

## Publications

1. Birchall, J.R., Nikolaou, P., Coffey, A.M., Kidd, B.E., Murphy, M., Molway, M., Bales, L.B., Goodson, B.M., **Irwin, R.K.**, Barlow, M.J. and Chekmenev, E.Y., 2020. *Batch-Mode Clinical-Scale Optical Hyperpolarization of Xenon-129 Using an Aluminum Jacket with Rapid Temperature Ramping*. Analytical Chemistry, 92(6), pp.4309-4316.
2. Birchall, J.R., Nikolaou, P., **Irwin, R.K.**, Barlow, M.J., Ranta, K., Coffey, A.M., Goodson, B.M., Pokochueva, E.V., Kovtunov, K.V., Koptyug, I.V. and Chekmenev, E.Y., 2020. *Helium-Rich Mixtures for Improved Batch-Mode Clinical-Scale Spin-Exchange Optical Pumping of Xenon-129*. Journal of Magnetic Resonance, p.106739.
3. Birchall, J.R., **Irwin, R.K.**, Nikolaou, P., Pokochueva, E.V., Kovtunov, K.V., Koptyug, I.V., Barlow, M.J., Goodson, B.M. and Chekmenev, E.Y., 2020. *Pilot Multi-Site Quality Assurance Study of Batch-Mode Clinical-Scale Automated Xenon-129 Hyperpolarizers*. Journal of Magnetic Resonance, p.106755.
4. Birchall, J.R., **Irwin, R.K.**, Nikolaou, P., Coffey, A.M., Kidd, B.E., Murphy, M., Molway, M., Bales, L.B., Ranta, K., Barlow, M.J. and Goodson, B.M., 2020. *XeUS: A second-generation automated open-source batch-mode clinical-scale hyperpolarizer*. Journal of Magnetic Resonance, 319, p.106813.



## Appendix B

# N-XeUS2 automation system and gas handling manifold.

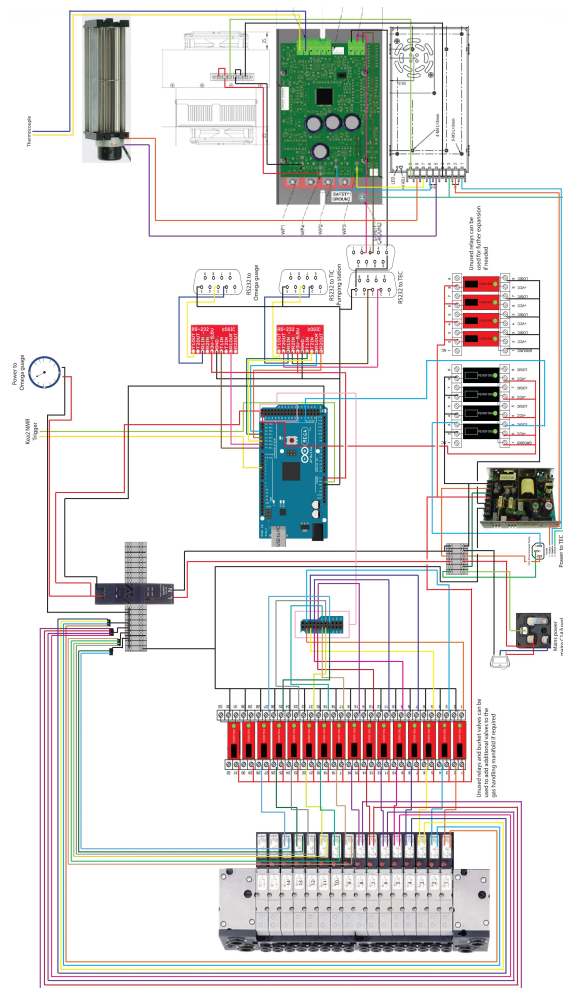


Figure B1: Wiring diagram of the automation system within the N-XeUS2 polariser

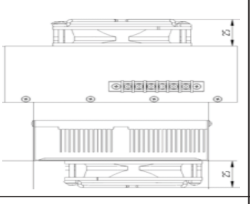
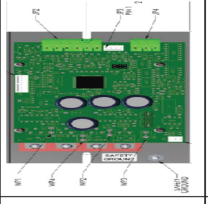
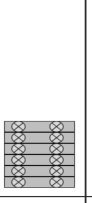


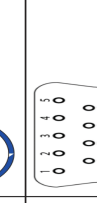
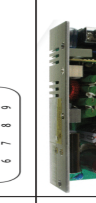





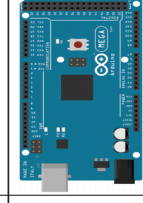


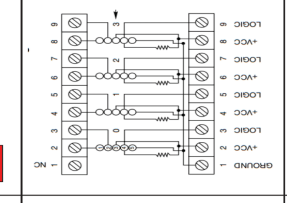
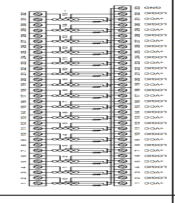

Part Kryotherm Thermoelectric cooling assembly	Part Number 380-24AA	Symbol 
Temperature Controller	397-573	
DIN Terminal blocks	815-666	
AC/DC CONVERTER 5V 10W	285-1228-ND	
Omega High Accuracy Digital Pressure Gauge with Data Logging Capability	DPG4000	
BUS Socket to D9 Female Modular D Adapter	815-666	
AC/DC Converter board	VF-D320-D124A-CF5	
C14 Female Panel Mount Connect	C14-PANEL	
Fused C14 Inlet, Snap-In, 4.8mm, 1.5mm - 6200-4215	6200-4215	
Meanwell AC/DC Enclosed power supply	SP-300-24	
Rotary fan	QG030-148/14R	
Arduino and ReliONE Quick-Modular pneumatic valve unit	Type 8640	
Arduino Microcontroller	Mega 2560	
Grayhill 70-04C Series, 6V SPNO Interface Relay Module, PCB Pin Terminal, PCB Mount	70G-04C54	
Module DC Output 60VDC (Max.); 1 W/A (Typ.); SPST Normally Open	70G-0DC5	
Grayhill Interface Relay Module (4 relays)	70GKCK4R	
Grayhill Interface Relay Module (16 relays)	70GKCK16-DIN	
RS323 to TTL Converter Breakout Board, MAX3232 Transceiver	BOB-1189	

Figure B2: Key for the automation system wiring diagram seen in Figure B1

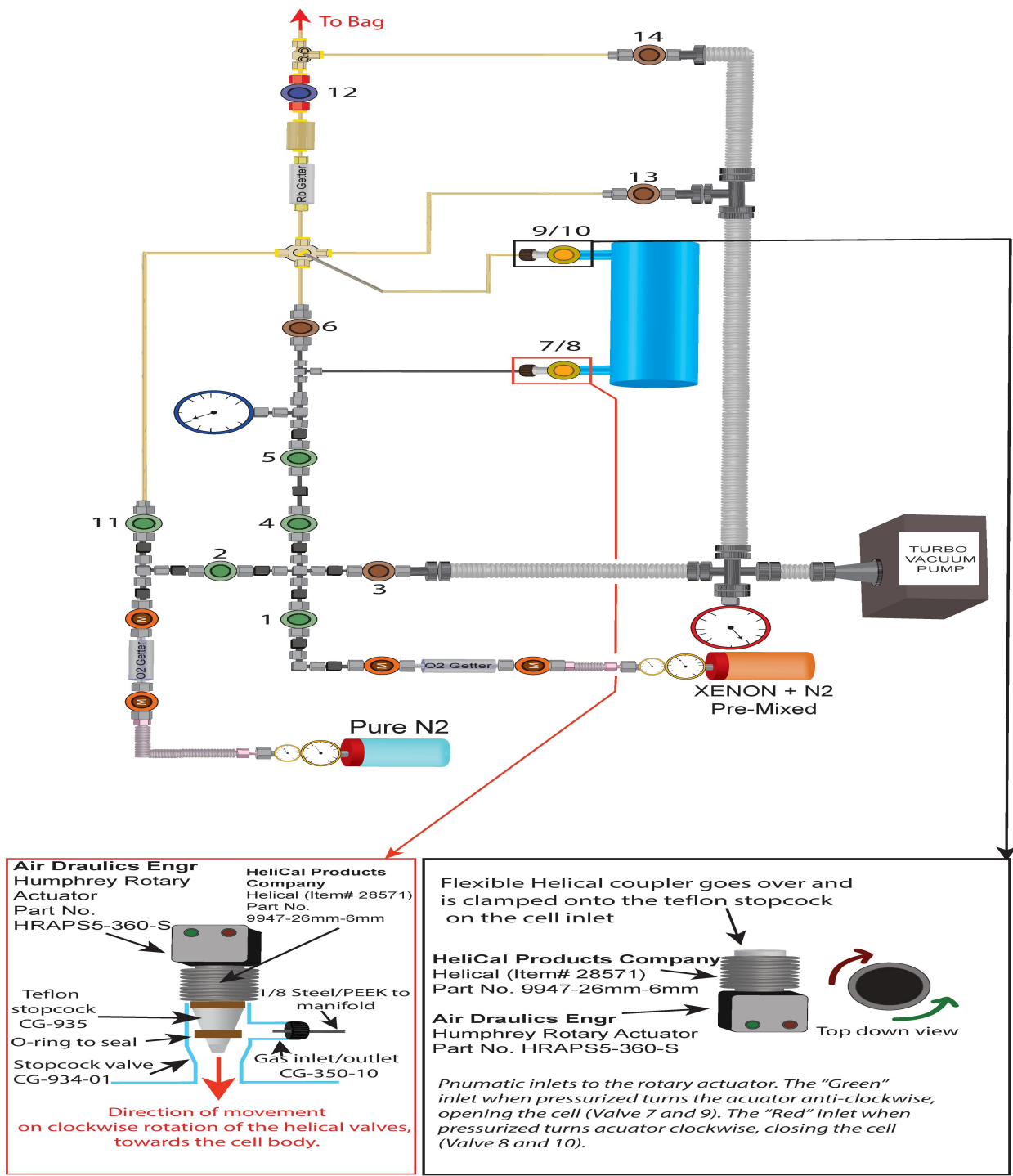


Figure B3: Diagram of the redesigned N-XeUS2 gas handling manifold, including the operation of the helical valves and stopcock





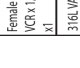
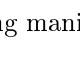


















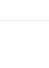






Part/Quantity	Part Number/Supplier	Symbol
316L Stainless Steel Convoluted (FL) Hose, 1/4 in., 321 Stainless Steel Braid, 1/8 in Rotatable Male VCR Fitting	SS-FL4RM4-48H Swagelok	
Regcom Regulator with 1/4" compression fitting outlet	CG4580	
Edwards Active Pirani Vacuum Gauge NW16, KF 16	APG100-3CC x1	
Rotating Female Union VCR	SS-4-WVCR-6-DF Swagelok	
316L Stainless Steel High Purity Bellows Sealed Valve, 1/4 in. Female Swagelok VCR Metal Gasket Face Seal Fitting, Normally Open Actuator	SS-BN51-0 Swagelok	
Stainless Steel High Purity Pressure Diaphragm Sealed Valve, 1/4 in. Female Swagelok VCR Fitting, Round Handle	SS-DSV51 Swagelok	
NuPure THE ELIMINATOR	E040-CAG-VR4-1-PF-SV NuPure	
1/8 VCR Male Union	SS-4-VCR-6-DM Swagelok	
Omega High Accuracy Digital Pressure Gauge	DPG400-300-DC Omega	
316 Stainless Steel VCR Face Seal Fitting, VCR x 1/4 in. FNPT	SS-4-VCR-7-4 Swagelok	
316L WVR Welded VCR Face Seal Fitting, 1/4 in. Female Cross	6L/4-WVCR-CS-FFFF Swagelok	
316L WVR Welded VCR Face Seal Fitting, 1/4 in Female Tee	6L/4-WVCR-FFF Swagelok	
Stainless Steel Swagelok Tube Fitting, Union Tee, 1/8 in.	SS-200-3 Swagelok	
316 Stainless Steel Welded VCR Face Seal Fitting, Swagelok Tube Fitting Connector, 1/4 in. WVCB x 1/8 in. Tube Fitting	SS-4-WVCR-6-200 Swagelok	
KF to Male VCR Metal Gasket Face Seal Fitting	JMWVCR1614 Swagelok	
Seamless 304 Stainless Steel Tubing 1/8" Outside Dia., 0.027" Inside Dia.	3ACR9 Grainger	
Bellows Hose Metal KF-16, Extra Thin Wall Tubing, ISO-KF Flange Size NW-16, Stainless Steel	P103700 Ideal Vacuum Products	
KF crosses KF small flange connections NW 16	C10512422 Edwards	
Reducer Conical KF-16 to KF-25 Vacuum Fittings, ISO-KF Flange Size NW-16 to NW-25, Stainless Steel	P101227 Ideal Vacuum Products	
Edwards Vacuum Inc Turbo Pump Station EXT75DX Turbo Pump with NW-40 Flange RVS Dual Stage Vane Backing Pump TIC Controller for Remote Operation	TSM121002 Edwards	
Helical Products Company Helical Coupler	a) 8947-26mm-6mm Item# 28571 Helical Products Company	
Rotary Actuator	b) HRAPSS-360-S Humplery	
Simplified representation of the valve	c) N/A	
Tree KF-16 Vacuum Fittings, ISO-KF Flange Size NW-16, Stainless Steel	P101209 Ideal Vacuum Products	
316L Stainless Steel High Purity Bellows Sealed Valve, 1/4 in. Female Swagelok VCR Metal Gasket Face Seal Fitting, Normally Closed Actuator	SS-BN51-C Swagelok	
PEEK Tubing OD x ID, 1/8 in. x 0.062 in, natural	54995 Sigma Aldrich	
Tube Fitting, Flangeless nut and female 1/4-28 male upouch for tubing 1/8 in. OD	S8686 Sigma Aldrich	
PEEK Manifold Assembly 5 Port for 1/8" OD	P-155 Western Analytical	
Tee Assy 1/8 in PEEK USF thru	P-713 Western Analytical	
One way Peak valve BID-CHEM 973 363-3001	CF-5C BioChem Fluidics	
Entegris GT Plus in-line gas filter	WGFC01K P3 Entegris	
Rb Getter		
IPS VCR valve	Part Number/Supplier MTV22CRR1 International Polymer Solutions	Symbol 
Teflon Stopcock	CG-935 ChemGlass	
Pyrex glass body with 2 in. ID, 2.125 in. OD, and a length of 9.75 in., capped off with a 2 in. diameter Pyrex optical window on each end.	MKG350-10 Midwest Glass Blowing	
The side stems are constructed of 1/8 in. Pyrex tubing joined to Chem-glass pieces. a) The piece used to seal the OP-cell is a Teflon Stopcock valve. b) Attached perpendicular to that, valve is a Chemthread stem containing a compression O-ring used to connect 1/8 in. OD Teflon tubing	a) CG-934-01 ChemGlass b) CG-350-10 ChemGlass	
Brass Nut for 1/8 in. Swagelok Tube Fitting	B-202-1 Swagelok	
PTFE Female Set (1 Front Ferrule 1 Back Ferrule) for 1/8 in. Swagelok Tube Fitting (For RB Filter)	T-200-SET Swagelok	Not Pictured
Centering Ring KF-16 Vacuum Fittings, ISO-KF Flange Size NW-16, Stainless Steel & Viton O-ring	P101242 Ideal Vacuum Products	Not Pictured
Centering Ring KF-25 Vacuum Fittings, ISO-KF Flange Size NW-25, Stainless Steel & Viton O-ring	P101243 Ideal Vacuum Products	Not Pictured
Copper VCR Face Seal Fitting, 1/4 in. Gasket, Non-Retained Style	CU-4-VCR-2 Swagelok	Not Pictured

Figure B4: Parts list for the N-XeUS2 gas handling manifold diagram

## Appendix C

# Protocol for HP $^{129}\text{Xe}$ clinical drug production

HP  $^{129}\text{Xe}$  has been classified as an investigational drug by the MRHA, meaning it is subject to the same scrutiny as any MHRA controller investigational medicinal product (IMP). Each bag produced must have clear GMP traceability so that all of its details can be traced in the unlikely event that a healthy volunteer or patient negatively responds to the HP  $^{129}\text{Xe}$ . This makes it possible to see whether protocol was adhered to, if any anomalous results were present and the batch from which the Tedlar bag and other consumables came.

There are four people involved in the manufacture of HP  $^{129}\text{Xe}$  in the QMC. Working together, they ensure it can be delivered to subjects safely. The first member of the team is the polariser operator, who must be fully trained in its operation. The next individual handles quality control and confirms by way of signature that the operator has adhered to the SOP and has recorded all critical production parameters. Both individuals must be fully trained in Good Clinical Practice and GMP. The third member of the team is a qualified person (QP), who must be a certified expert in pharmaceutical manufacture and distribution. Their duty is to check the production paperwork to verify that all procedures have been followed. They are also the only one who can issue a batch release for use in human studies. The final person is a clinician, who screens the patient before the day of scanning to make sure they meet the studies selection criteria. Outside of the scanner, they monitor and record the subject's vital signs before and after each scan. They also train the subject on the protocol for breathing in the HP  $^{129}\text{Xe}$ . They also test the subject's ability to tolerate Xe by giving them an unpolarised bag of medical-grade Xe to inhale. In the scanner room, the clinician is responsible for instructing the subject on when to inhale the HP  $^{129}\text{Xe}$ . In the case of an emergency or adverse response to the Xe, the clinician can stop the scan and remove the patient from the scanner. 24 hours after the visit, the clinician contacts the subject by phone to check on them and record any adverse events they may have experienced.

When making HP  $^{129}\text{Xe}$  for clinical use using the 9810, a pre-approved SOP has to be adhered to, and the process must be fully documented. The SOP is detailed in the "Batch Record and Certificate of Release - Hyperpolarised Xenon-129. MAN 001 Master Batch Record. Version G" form. A part-by-part



description of the SOP is detailed below, with the relevant page pictured before an itemised description of that part.

Part 1: Routine start up checks

STANDARD OPERATING PROCEDURE	Master Batch Record		
Batch Record and Certificate of Release - Hyperpolarised Xenon-129			
Batch Number		Date of Manufacture	
Part 1: Routine Startup Checks		Check Box	Initials
SOP MAN 004 Checks 1 – 6 carried out and satisfactory		<input type="checkbox"/>	_____
SOP MAN 004. Check 7 – Measurement Station NMR coil test check		<input type="checkbox"/>	_____
SOP MAN 004 Check 8 – Release of Tedlar bags & labels for production		<input type="checkbox"/>	_____
SOP MAN 004 Check 9 – Sufficient Lq Nitrogen in dewar		<input type="checkbox"/>	_____
SOP MAN 004 Check 10 - Polarean 9810 systems all on		<input type="checkbox"/>	_____
SOP MAN 004 Check 11a – Purge cold finger Vac / N2 three times		<input type="checkbox"/>	_____
SOP MAN 004 Check 11b – Purge Tedlar Bag Vac / N2 three times		<input type="checkbox"/>	_____
SOP MAN 004 Check 11c –Start gas flow to avoid pressure build up		<input type="checkbox"/>	_____
SOP MAN 004 Check 11d- Start laser with cold cell & record transmission		<input type="checkbox"/>	_____
SOP MAN 004 Check 11e –Heat optical cell>100C then pre-sat, record trans		<input type="checkbox"/>	_____
Manufacturing Setup	Equipment Checks Confirmed by:		
	Line Clearance Checks Completed by: (Production area cleared)		
	Label Check by:		
<p><i>Attach copies of labels and orders</i></p> <p style="text-align: center;">CONTROLLED DOCUMENT: SPMIC-QMC, MEDICAL SCHOOL, UNIVERSITY OF NOTTINGHAM</p> <p style="text-align: center;">MAN 001 Master Batch Record <span style="float: right;">Version: G</span></p>			

Figure C1: STANDARD OPERATING PROCEDURE Master Batch Record-Part 1: Routine start-up checks

- The batch number and date are recorded so the bags of Xe can be matched to the relevant paperwork. This information is recorded on all pages of the batch release form and on labels attached to the bag.
- The each stage of the polariser start-up is checked off and initialled by the polariser operator upon completion. This ensures all the equipment

needed to perform the clinical run is present. These checks also make sure process is performed correctly to avoid damage and poisoning of the optical cell. Once the purge and evacuation cycles are complete, the gas is allowed to flow through the system. Finally, the laser is powered up and the relevant variables are recorded.

These checks begin up to an hour before the subject arrives to give time for any minor issues to be overcome. It also allows the visit to be cancelled before scanner time is wasted should a more serious problem be identified.

- These checks are then signed off by the polariser user once they are complete, stating the polariser is fit for service.

Part 2: Batch release checks – production start – 1<sup>st</sup> sample

STANDARD OPERATING PROCEDURE		Master Batch Record		
<b>Part 2: Batch Release checks – production start – 1<sup>st</sup> sample.</b>				
<b>Materials checks</b>	Cylinder Ref Number			
	Bag Ref Number			
	Valve Ref Type			
<b>In-process checks</b>	Cylinder Operating Pressure ( psig) (min 25)	psi		
	Flow-rate (Ltr per min)– A (Acc. Range 0.1 – 2.5)	L/min		
	Collection Time (min) – B	Min	Volume collected (Xe% $\times$ min $\times$ 100) $\times$ A $\times$ B	L
	Cell Temperature (DegC) (Range 100 – 180C)	$^{\circ}$ C	Pre-saturator Temp (Range 100–240C)	$^{\circ}$ C
	Cold Cell HR4000 Spectrometer Reading – C		HR4000 Spectrometer wavelength @	nm
	Hot Cell HR4000 Spectrometer Reading - D		% transmission ratio (Photodiode)	%
	Checked by		Date	
<b>Test Results</b>	Polarisation Reading 1	%	On Resonance: YES / NO	
	Polarisation Reading 2	%		
	Polarisation Reading 3	%	Average	%
	<b>Disposition</b>			
Disposition : PASS / FAIL		Deviation report		
Comments				
QC Release by:		Date:		
Initial QP Release		Date:		

CONTROLLED DOCUMENT: SPMC-QMC, MEDICAL SCHOOL, UNIVERSITY OF NOTTINGHAM

MAN 001 Master Batch Record

Version: G

Figure C2: STANDARD OPERATING PROCEDURE Master Batch Record-Part 2: Batch release checks – production start – 1<sup>st</sup> sample

- As HP <sup>129</sup>Xe is constantly depolarising, the gas should be delivered to the patient as quickly as possible after production. It is therefore not practical to have the QP release each bag for human use individually. A special IMP licence was obtained so that the QP could issue a batch release using the QC results from only the first bag. The first bag has to undergo the following checks:

- **Materials checks:** These are unique to the batch release checks. The gas cylinder serial number is recorded along with the batch numbers of the bags and bag clips so that they can be traced back if needed.
- **In-process checks:** These checks are used to record the values of the polariser's operational parameters. This makes it easy to observe any anomalous values both during production and in a later review. They can also inform parameter selection in future studies. This check is completed by the polariser operator.
- **Test results:** After the HP  $^{129}\text{Xe}$  is released to a bag, its polarisation is then measured on the 3777 measuring station. The polarisation is recorded three times, and the average is calculated. The average polarisation is also recorded on a sticker attached to the bag, one is placed on Part 3. A third is placed on the clinician's patient report to enhance traceability between production and clinical use.
- **Disposition:** The average polarisation is checked to see if it is higher than 3%. If it fails, the bag cannot be given to the patient and is rejected. At this point, the production run must cease. Any information explaining what might have contributed to the failure and other details that deemed important are recorded in the comments section. A deviation report and (out of specification) OOS investigation need to be completed before production of the next bag.  
If no issues are encountered, and if the polarisation is above the 3% limit, "Good fill" is written. This is signed then off by the person performing QC.
- **Once completed,** Part 1 and Part 2 are sent to the QP to be checked. If the QP is satisfied, they sign off the batch release and give verbal assent to release the batch. The clinician is then able give the subject the first bag HP  $^{129}\text{Xe}$  if they are satisfied it is safe to do so.

Part 3: Patient bag filling record - Hyperpolarised Xenon-129

STANDARD OPERATING PROCEDURE		Master Batch Record		
Part 3: Patient Bag Filling Record - Hyperpolarised Xenon-129		Page __ of __		
Batch Number		Bag Number		
		Date of Manufacture		
<b>In-process checks</b>	Cylinder Operating Pressure ( psig) (min 25)	psi		
	Flow-rate (Ltr per min)- A (Acc. Range 0.1 – 2.5)	L/min		
	Collection Time (min) – B	Min	Volume collected (Xe% <i>m</i> ix/100) <i>x</i> A <i>x</i> B	L
	Cell Temperature (DegC) (Range 100 – 180C)	°C	Pre-saturator Temp (Range 100–240C)	°C
	Cold Cell HR4000 Spectrometer Reading – C		HR4000 Spectrometer wavelength @	nm
	Hot Cell HR4000 Spectrometer Reading – D		% transmission ratio (Photodiode)	%
Checked by		Date		
<b>QC Test Results</b>	Polarisation Reading 1	%	On Resonance: YES / NO	
	Polarisation Reading 2	%		
	Polarisation Reading 3	%	Average	%
QC by		Date		
<b>Disposition</b>	Disposition : PASS / FAIL		Deviation report	
	Comments			
QC Release by:			Date:	
<b>CEASE MANUFACTURE IF IN-PROCESS RESULTS FALL OUTSIDE LIMITS</b>				
<b>Patient Label Copy</b>				

CONTROLLED DOCUMENT: SPMIC-QMC, MEDICAL SCHOOL, UNIVERSITY OF NOTTINGHAM  
 MAN 001 Master Batch Record Version: G

Figure C3: STANDARD OPERATING PROCEDURE master batch record - Part 3: patient bag filling record - Hyperpolarised Xenon-129

- Although the QP does not release each bag, GMP still needs to be adhered to. The IMP licence therefore requires QA and QC to be performed on every bag intended to be given to a subject. Each bag, including the first, must have a “patient bag filling record”, which records the same in-process checks, QC test results and disposition. The failure protocol for insufficient polarisation is also the same as that detailed in Part 2.

- Patient label copy: As noted in Part 2, a duplicate to the label on each bag is placed on the sheet to enhance traceability and a third copy to the clinician for the patient record. This creates full traceability from production to administration.

## Batch review and QP certification

STANDARD OPERATING PROCEDURE		Master Batch Record	
Batch Review and QP Certification			
<i>SPMIC-QMC, MEDICAL SCHOOL, UNIVERSITY OF NOTTINGHAM</i>			
Batch Number		Date of Manufacture	
Study Number		Number of Patient Bags	

**RELEASE TESTS:**

Minimum 3% POLARISATION LIMIT PASS / FAIL	BAG Number	AVERAGE RESULT
--	------------	----------------

QP REVIEW AND FINAL RELEASE BY: \_\_\_\_\_ DATE: \_\_\_\_\_

PRINT: \_\_\_\_\_

I hereby certify that the above information is authentic and accurate. This batch of product has been manufactured at the *SPMIC-QMC, MEDICAL SCHOOL, UNIVERSITY OF NOTTINGHAM*, in full compliance with GMP and the relevant Product Specification File for Investigational Medicinal Products. The batch processing, packaging and analysis records were reviewed and found to be in compliance with GMP.

---

CONTROLLED DOCUMENT: SPMIC-QMC, MEDICAL SCHOOL, UNIVERSITY OF NOTTINGHAM

MAN 001 Master Batch Record Version: G

Figure C4: STANDARD OPERATING PROCEDURE Master Batch Record - Batch review and QP certification

- Release tests: A summary of the polarisation measured for each bag produced.
- The QP checks through the “patient bag filling record” associated with each bag used in the batch and signs off that the polarisation values are correct and that the SOP was followed. This can occur after clinical work is completed, typically within 24 hours.